Faculté des Sciences **Département d'Astrophysique, Géophysique et Océanographie**

Space-variant optical phase retarders in liquid crystal polymers and their applications

THÈSE

présentée pour l'obtention du diplôme de

Docteur en Sciences

par

Pierre Piron

Soutenue publiquement le 10 février 2014 devant le Jury composé de :

Président :	Pr. Jean SURDEJ
Directeur de thèse :	Pr. Serge HABRAKEN
Examinateurs :	Dr. Olivier ABSIL Pr. Mikael KARLSSON Dr. Cédric LENAERTS Dr. Dimitri MAWET

HOLOLAB - Optics Laboratory

Mis en page avec la classe thloria.

Remerciements

Tout d'abord, je remercie mon promoteur Monsieur Serge Habraken pour le vif intérêt qu'il a porté à mes recherches, pour les précieux conseils qu'il m'a donnés et pour toutes les informations qu'il a partagées avec moi. Je pense plus spécialement aux nombreux articles à propos des nouvelles méthodes d'enregistrement et des perspectives d'applications nouvelles. Je le remercie pour ses encouragements dynamiques. Après chacune de nos réunions de travail, je me sentais reboosté pour attaquer le chapitre suivant et, ainsi petit à petit, finaliser toutes mes recherches.

Mes chaleureux remerciements vont aussi à Monsieur Yvon Renotte. Merci Monsieur pour tout le temps et toute l'attention que vous m'avez consacrés. Pendant ces quatre années, vous avez toujours été disponible pour répondre à mes questions d'ordre scientifique à propos de l'holographie ou à mes questions d'ordre pratique pour mieux identifier les problèmes expérimentaux et leur trouver une solution "élégante".

Je tiens aussi à remercier Dimitri Mawet pour l'attention qu'il a portée à mes recherches et pour l'aide qu'il m'a apportée pour le calcul de l'atténuation produite par les retardateurs. Sans son aide, je serais toujours en train de patauger dans les méandres des transformées de Fourier.

Je remercie également Cédric Lenaerts pour son aide efficace lors du nettoyage du spin-coater. Sans lui, il n'y aurait pas eu de vortex réalisé par holographie de polarisation et la partie expérimentale de ma thèse aurait été grandement réduite ou fortement retardée.

Je remercie aussi tous les collègues qui se sont succédés au Hololab pendant ces quatre années: Caro, le seul élément féminin du laboratoire, Aïssa, Bernard, Fabian, Georges et Grégory.

Je remercie Pascal pour les "apéros bières" qu'il organisait. Ils m'ont permis de découvrir bon nombre de nos bonnes bières belges. Plus sérieusement, je remercie "mon compagnon de galère" pour ces quatre années de fructueuse collaboration, l'un aidant l'autre dans ses recherches scientifiques ou plus prosaïquement dans ses préparations culinaires à base de LCP. Merci donc pour tous ces moments d'intense réflexion qui commençaient invariablement par "à ton avis, que va-t-il se passer si ...". Ces discussions ont permis à chacun de nous de faire le point sur ce qu'on sait et ce qu'on ne sait pas mais qu'on doit savoir pour continuer, sur ce qui marche même si on ne sait pas trop bien pourquoi et surtout sur ce qui ne marche pas et pourquoi ça ne marche pas! Merci aussi pour ta patience quand j'arrivais avec mes "Je ne comprends plus, pourquoi ...". Pascal, je te souhaite beaucoup de courage pour la dernière ligne droite de ta thèse ...

Je voudrais aussi remercier Christian pour ses encouragements dans ma dernière ligne droite, pour nos pauses "cafééééés" ainsi que pour ta relucture et ses judicieux commentaires.

Mes mercis sont aussi pour Marc. Je le remercie pour son aide quand j'avais besoin de mains supplémentaires ou quand mes mains étaient un peu maladroites suite à mes blessures aux bras. Je le remercie aussi pour ses ... béquilles qui m'ont beaucoup aidé dans ma dernière ligne droite. Marc, j'espère que tu araus la chance d'écrire le même genre de remerciements dans un avenir proche

Je voudrais aussi remercier "mes" étudiants-stagiaires pour leur collaboration. Ils m'ont permis d'avoir de nombreuses mains pour préparer mes recettes à base de LCP. Merci Chloé, Ophélie, Jean-Patrick, Eric, Antoine et Loïc.

Je ne peux pas oublier de remercier Grégoire pour son amitié lui qui a instauré les "vendredi-baguette". J'en profite pour saluer les habitués c'est-à-dire Pic-Pic, François, Marc, Géraldine ainsi que tous les autres. Nous avons passé d'agréables pause-midi à discuter de tout et de rien et surtout de l'étude comparative du goût des frites en fonction de la sauce du voisin et de son attitude face au partage dont la conclusion est "la meilleure frite est celle volée dans l'assiette du voisin".

Je ne peux pas non plus oublier mes amis qui ont souvent dû subir mes indisponibilités et mes passages à vide. Merci Alice, Pierre-Emmanuel, Sylvain, François et Nicolas pour votre soutien inconditionnel, vos encouragements et votre patience. Merci aussi pour mon anniversaire surprise en décembre 2013, pour nos soirées "jeux de société" et les belles vacances, en un mot, pour tous ces moments qui m'ont permis de me détendre, de penser à autre chose et ainsi de recharger mes batteries plus ou moins régulièrement.

And last but no least, merci aux membres de ma famille pour m'avoir subi et supporté toutes ces années. Merci à eux du fond du cœur pour l'intérêt qu'ils ont toujours porté à mes études, pour les encouragements qu'ils m'ont toujours donnés surtout pendant les moments difficiles (mes deux blessures successives aux bras, ma récente blessure au genou) et pendant les moments de grand découragement.

This research was supported by a fellowship of the Belgian National Foundation
("Bourse FRIA") and by the University of Liège.

Contents

Acronyms and notations

Notations

Λ	grating period
θ_i	incident angle
λ_r	recording wavelength
ϕ	phase retard between two components of polarization
ψ	phase retard for a beam due to geometric considerations
ϕ_p	Pancharatnam phase
c^{ste}	a constant
α	orientation of the fast axis in a retarder or orientation of the electric field
r	radial coordinate
θ	polar angle
ι	imagninary unit
$\mathbf{K}$	grating vector
p	period of a retarder
ζ	orientation of the lines of same intensity in the polarization analyzer
N	complex refractive index
ρ	ratio of complex reflection coefficient
s	transverse electric component
p	transverse magnectic component
l	topologial charge
∇	gradient of a function
I_{dir}	directional intensity
d_p	directional parameter
R_{mis}	maximum radius of misalignment area
s_{mis}	ratio of the misaligned surface on the total surface of the retarder
I_{mis}	transmitted intensity where areas of misoriented LC are computed
ϵ_i	difference between the orientation of the polarization components active axis i and its ideal orientation
d	separation of the beams at the exit of the Savart plate
r_S	radius of the circle due to the Savart plate separation

Acronyms

AGPM	Annular Groove Phase Mask
LC	Liquid Crystal
LCP	Liquid Crystal Polymer
RCWA	Rigourous Coupled Wave Analysis
SR	Space-variant Retarder
VR	Vortex Retarder
ZOG	Zeroth Order Grating

Conventions

angle in °	angle for a geometrical orientation (unless explicit mention)
angle in *rad*	angle for a phase retard or a phase difference

Introduction

On ne voit bien qu'avec le coeur, l'essentiel est invisible pour les yeux.

Antoine de Saint Exupéry, "Le Petit Prince" (1943)

Among the properties of light, polarization is very hard to observe with our eyes. Indeed, everyone can see the difference between a red beam or a blue one, a collimated or a diverging beam by looking at the spot size at different places; even a grasp of coherence is reachable with the naked eye but we are unable to see polarization differences without the help of instrumentation. We can't tell the difference in polarization between light emitted by the sun or by a computer screen: one is not polarized while the other one is polarized. However this invisible property of light is already used in our everyday life. Last decade, polarization has been extensively researched and methods to create light beams with a specific variation of polarization were discovered. These beams lead to an astronomical amount of applications in several domains such as military, industry, astronomy, medical sciences and many others.

To create a space-variant polarized beam, one of the simplest method is to use a Space-variant retarder (SR): an optical retarder with a constant phase retard and a variation of its fast axis and a uniformly polarized beam. The uniformly polarized beam meets a different fast axis orientation and becomes a polarized beam with a specific variation of its polarization.

The initial goal of this thesis was to build with liquid crystal polymers a space-variant retarder for a specific application: coronagraphy. During our first manipulation to record simple retarders, we discovered an article concerning the recording of a space-variant retarder with liquid crystals polymers using differently polarized beams. We were impressed by this technique and realization, our first reaction was :"Waw, they are skilled, they can achieve that! It is really awesome!" but this article led to several questions like:

- How does it work?
- Can we do the same?
- Can this concept be used for other applications?
- Is it possible to record a retarder for coronagraphy using this technique?
- What are the limitations of this technique?
- Is it cheap?
- ...

The present thesis will answer at these questions in a quite concise way.

The first chapter, will present the space-variant retarders, their applications and several recording methods.

Chapter 2 will explain the original recording method based on the superimposition of differently polarized beams using liquid crystals. The mathematical model will be detailed, several examples with two beams will be presented and the expansion to a four-beam superimposition will be described.

Next, in chapter 3, our first application will be shown. It is a dynamic polarization analysis method using space-variant retarders recorded by two circularly polarized beams of opposite handedness. The mathematical description and the experimental aspects such as the recording of the retarder and the measurement process will be detailed. We will conclude with the analysis of the measurements and the presentation of the possible upgrades and extensions of the method.

Chapter 4 will introduce a second application. It consists in a polarization states separator based on retarders similar to the polarization analyzer but with a shorter period. The mathematical principle will be exposed as well as the use of the retarders to shearography.

Afterwards, during chapter 5, we will focus on the recording of a specific kind of retarders: the Vortex Retarders (VR). It will introduce their distinctive features and their classification. The systems based on the superimposition of differently polarized beams will be exposed and analyzed thanks to numerical simulations. The first prototypes of VR recorded using polarization holography will be presented and a short sensitivity analysis will be performed to determine the effect of the experimental conditions.

Then, in chapter 6, we will come back to coronagraphy. After a short presentation of the concept and evolution, the computed performances of several retarders used as coronagraphs will be shown and compared to the actual experimental setup.

As a conclusion, we will synthesize the main results of the thesis and expose some of the many upgrades as well as future applications that this technology will enable.

Part I

Space-variant retarders in liquid crystal polymers

1

Space-variant retarders: their applications and their building method

Contents

In this chapter, we present the space-variant retarders. We decribe the common characteristics of space-variant retarders and the specificities of several particular retarders[1]*. Due to their specificities, some retarders are extremely well suited for some applications while others retarders are extremely useful for another type of applications. Since a very large number of applications exist, during the thesis we focused on a few of them. The selected applications will be presented in the present chapter and they will be completely detailed in the next chapters. Finally, several materials and manufacturing methods will be exposed.*

---

[1] The reader can find a short resume of the polarization formalisms wich will be used in Appendix A.

1.1 Theoretical background

As their name suggests, space variant retarders are characterized by a variation of their optical axis orientation. Due to this definition, a large amount of different configurations can be imagined. As a first step into the world of space-variant retarders (SR), let us classify these retarders by looking at the structure of their optical axis variation.

- The first distinctive feature is the law which governs the optical axis orientation. Some methods are used to synthesize retarders with a specific orientation of their optical axis (Fig.1.1(a)) while other methods are used to obtain retarders with a random orientation (Fig.1.1(b)). The applications of the retarders are also very different between these two types. Retarders with a specific structure are designed to achieve a specific non uniform orientation of the polarization in the beam while the others are more likely to be used as simulators of unpolarized beam or as failures of the first kind.

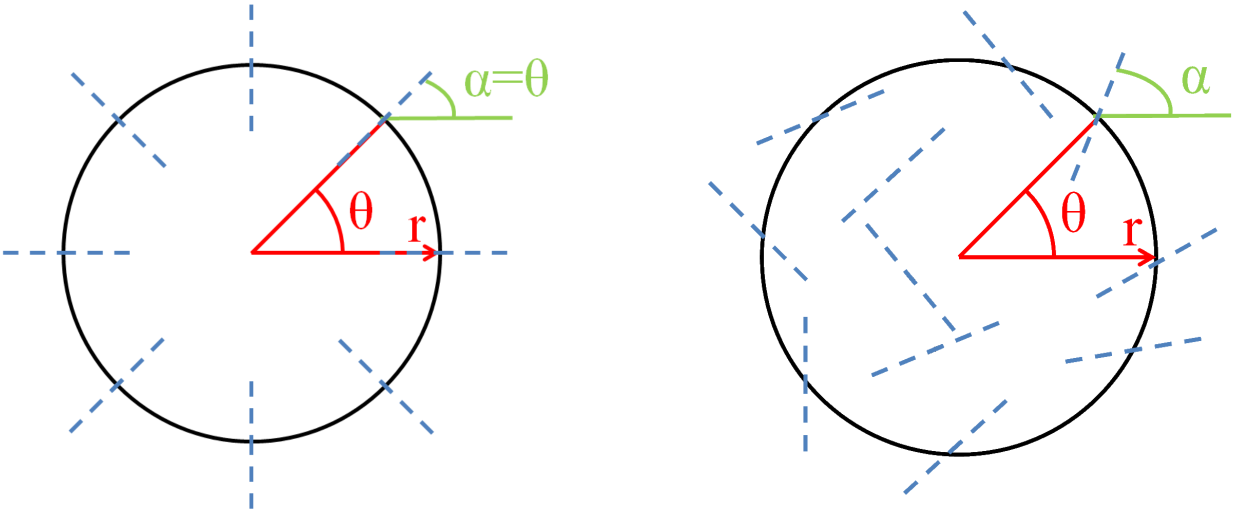

(a) (b)

Figure 1.1: (a) Scheme of an ordered retarder where the orientation of the fast axis is a function of the position of the retarder: $\alpha = \theta$ where α is the orientation of the fast axis and (r, θ) are the polar coordinates in the retarder. (b) Scheme of a retarder with a random orientation of its fast axis. The fast axis is pictured by dashed blue lines.

For the structured retarders other classifications can be made:

  - The variation can be a 1D or a 2D variation. A 1D variation means that in one direction the fast axis is modified while its orientation is conserved along the perpendicular direction (Fig.1.2(a)). A 2D variation means that the variation occurs in the 2 perpendicular directions (Fig.1.2(b)).

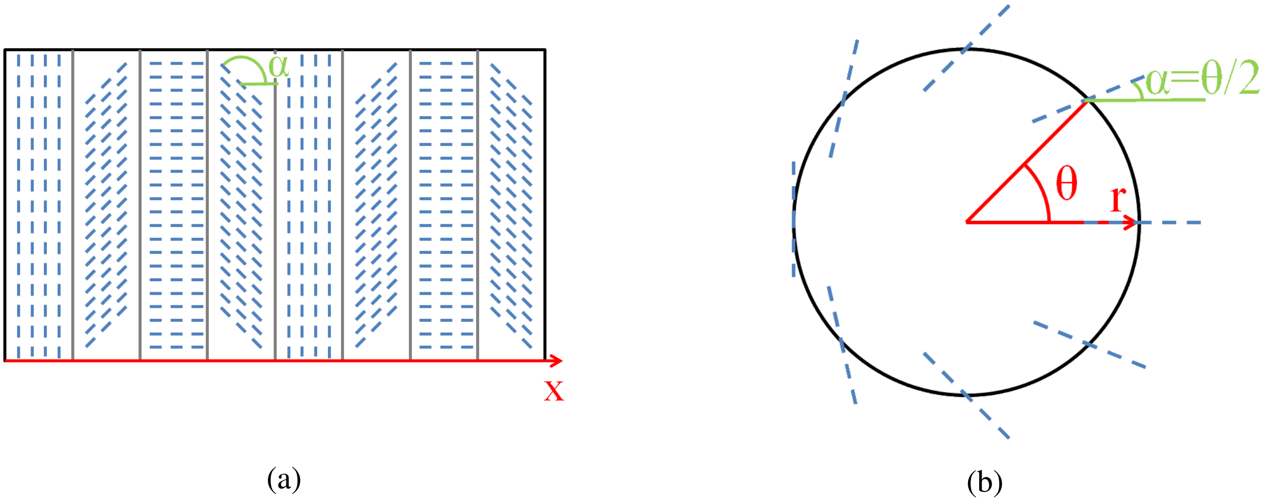

(a) (b)

Figure 1.2: (a) Scheme of a retarder with a 1D variation of its fast axis orientation. (b) Scheme of a retarder with a 2D variation of its fast axis orientation. α is the orientation of the fast axis, x is the direction of variation in the 1D SR, (r, θ) are the polar coordinates in the 2D SR.

- 2 types of variation can also be defined: discrete and continuous variation. Discrete retarders (Fig.1.3(a)) can be viewed as a junction of several retarders with a uniform orientation of the fast axis while the other ones exhibit a smooth variation for the orientation from one point to its neighbors (Fig.1.3(b)).

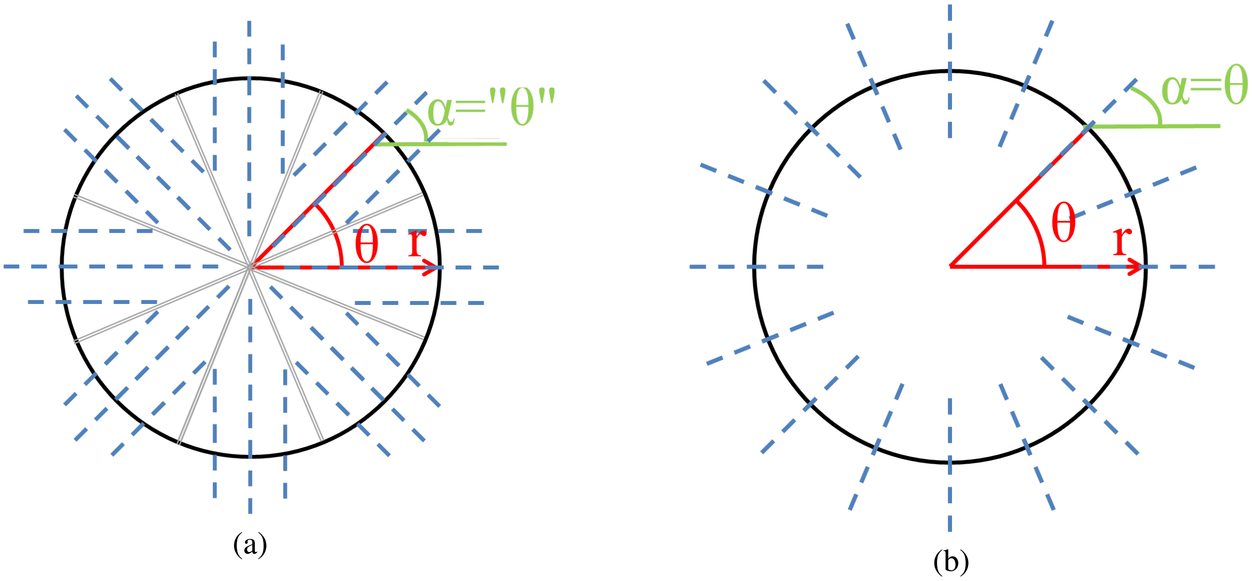

(a) (b)

Figure 1.3: (a) Scheme of a retarder with a discrete variation, each area is characterized by a uniform orientation of the axis. (b) Scheme of a retarder where the variation is continuous. α is the local orientation of the fast axis and (r, θ) are the polar coordinates.

As we will see in the next sections, depending on the structure of the variations, the building methods and the efficiency for some applications are different.

1.2 Applications

Until now, several applications of SR have been developed in a lot of domains.
In the present work, several applications of SR with liquid crystals polymers have been investigated. The following paragraphs will introduce them while the development of the specific application is related in the application chapter. Some applications like polarization analysis, polarization gratings or polarization converters lead to more advanced applications (e.g. ellipsometry for polarization analysis, shearography for polarization gratings, optimal focusing with polarization converters). The advanced applications will also be described in the chapter related to the basic application.

- A first application of SR is a dynamic method of polarization analysis using a 1D SR and a linear polarizer [1, 2, 3].
  An incident uniformly polarized beam will exhibit a 1D variation of its polarization after the retarder. Therefore, the beam transmitted by the retarder and a linear polarizer exhibits intensity variations. By studying the variation of the intensity, one can compute the polarization parameters of the incident beam.
- SR with a periodical variation of approximately ten times the wavelength of the incident beam acts as polarization gratings [1, 4, 5].
  An incident beam is separated into several beams differently polarized the same way a beam is diffracted by a grating. The angle between the beams and the intensity of each beams depend on the characteristics of the SR and the polarization state of the incident beam.
- Specific 2D SR can be used as phase mask coronagraphs [6, 7, 8, 9, 10].
  The goal of coronagraphy is to reduce the light of a central star to enable the visual detection of its fainter companions. Phase masks are used to shape the phase of the incident light to obtain the reduction of the central star intensity. The required phase shaping is achieved by the orientation of the fast axis.
- Several 2D SRs are used as polarization converters [11, 12].
  Thanks to the structure of their optical axis, they are able to convert a uniformly polarized beam into a radially (Fig.1.4(a)) or azimuthally polarized one (Fig.1.4(b)). The structure of the retarder must be adapted to the incident polarization: the structure being different for a circularly or a linearly polarized beam and a converter designed to achieve a radial orientation from one polarization converts the orthogonal polarization to the azimuthal one.

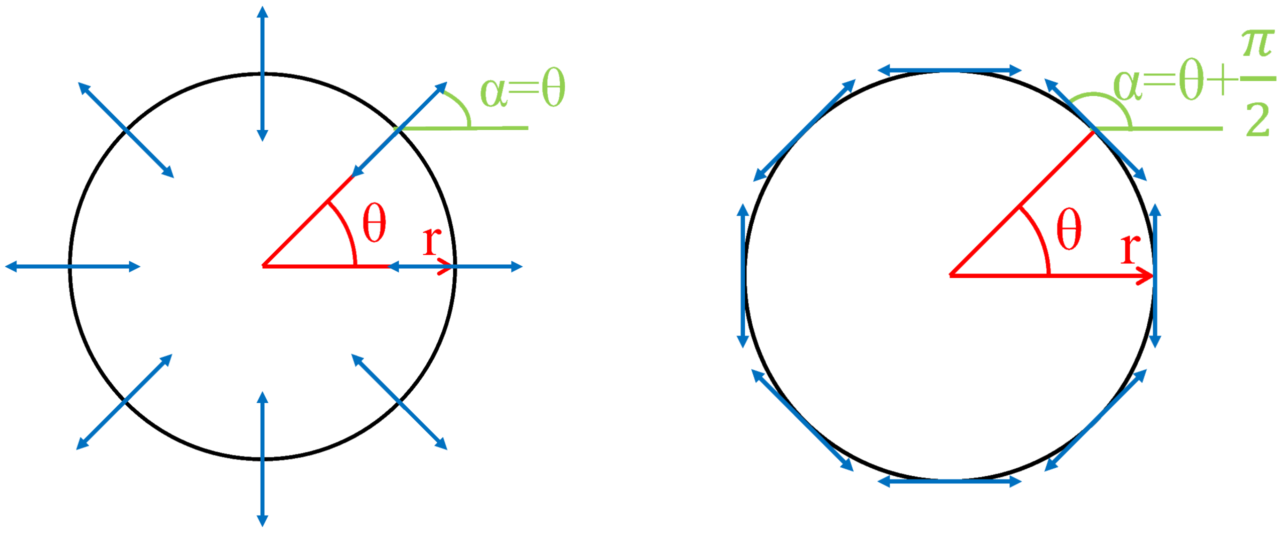

(a)

(b)

Figure 1.4: Schemes of a radially polarized beam (a) and an azimuthally polarized one (b). The polarization being pictured by blue arrows, α is the local orientation of the polarization and (r, θ) are the polar coordinates.

- SR could be used to simulate an unpolarized beam from one completely polarized incident beam. Several 1D SR will be stacked to create a large amount of different polarization states. Scanning the retarders with a small spot and moving the spot will allow to change the polarization state of the transmitted beam. Using a temporal averaging on the transmitted beam enables to simulate an unpolarized beam.

1.3 Building methods

As stated before, there are different kinds of SRs: 1D/2D variation, discrete or continuous variation of the fast axis orientation.
This section is a brief overview of the methods and materials used to record SR.

1.3.1 Birefringent plate

The easiest way to build a SR is to put together several retarders of uniform orientation to obtain a discrete SR [12, 13]. Space-variant half-wave plates have already been realized by laterally gluing together several half-wave plates of uniform orientation.

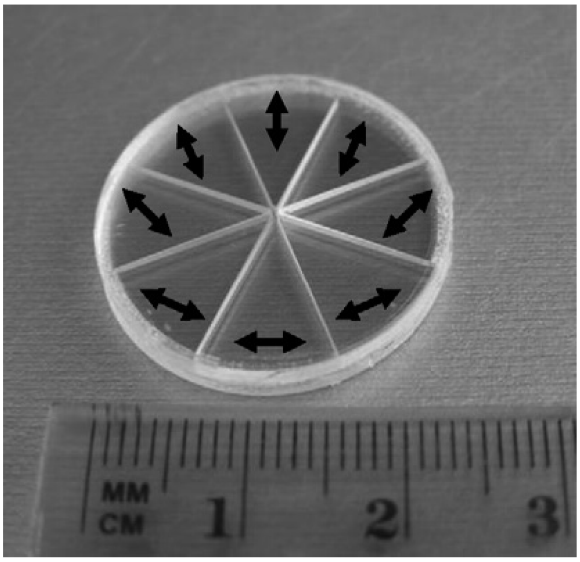

Figure 1.5: Picture of a manufactured SR composed by eight sectors of a $\lambda/2$ plate each one with its proper orientation of its fast axis, the arrows represent the direction of the slow axis of each sectors (picture from Machavariani et al. [13]).

Unfortunately, due to the discrete variation, the obtained polarization is roughly the desired one. This deviation from a continuous variation of the polarization orientation may affect the performance for several applications or may require an appropriate polarization filter to conserve them [12, 14]. Moreover at the interfaces, the beam exhibits zones with no transmitted light: dead zones. The presence of the dead zones will also affect the quality of the retarder. As an example, for an imagery application such as coronagraphy, the presence of the dead zones leads to a serious decrease of the performance since the planet can not be detected if the light is completely blocked.

1.3.2 Zeroth-order gratings

Another way to record SR is to use specific gratings: zeroth-order gratings (ZOGs). ZOGs are particular case of diffraction gratings, they only diffract the zeroth order of the incident beam. To exhibit the ZOG property, the following condition must be respected [6, 15, 16]:

$$\frac{\Lambda}{\lambda} \leq \frac{1}{n_I \sin\theta_i + max(n_I, n_{III})}. \tag{1.1}$$

Where Λ is the grating period, λ is the wavelength of the incident beam, θ_i is the incident angle and (n_I, n_{III}) are the refractive indices of the media (see Fig. 1.6 for gratings with different periods).

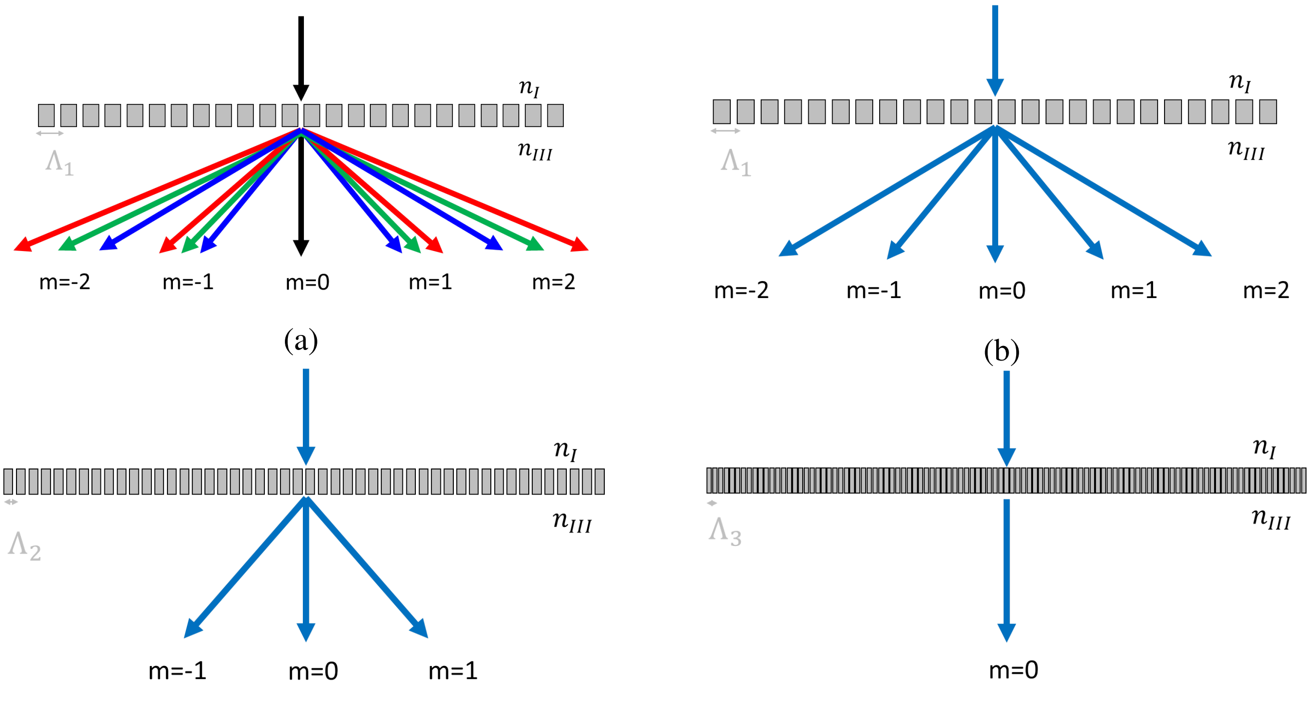

(a) (b)

(c) (d)

Figure 1.6: Several gratings with different groove periods $\Lambda_1 > \Lambda_2 > \Lambda_3$. (a) Diffraction pattern for a white incident beam (in black on the picture) and a grating with a groove period of Λ_1. (b) Diffraction pattern for a monochromatic beam and a grating with a groove period of Λ_1. (c) Diffraction pattern for a monochromatic beam and a grating with a groove period of Λ_2. (d) Diffraction pattern for a monochromatic beam and a grating with a groove period of Λ_3 respecting the ZOG condition. Pictures from Mawet et al. [17].

Theoretically and experimentally, it has been demonstrated that these gratings can be used as birefringent plates. Using the Rigorous Coupled Wave Analysis (RCWA) [9, 18], one can compute the properties of the equivalent birefringent plate knowing the gratings characteristics. To briefly summarize, for a 1D surface-relief grating:

- The refractive indices for the directions of polarization parallel and perpendicular to the grating grooves are function of the structure real indices and of the filling factor.
- The fast axis orientation is parallel to the grating vector **K**. **K** is perpendicular to the grating grooves and $|\mathbf{K}| = \frac{2\pi}{\lambda}$.

Therefore a ZOG with a non-uniform orientation of **K** can be viewed as a SR.
Two kinds of variation exist: discrete and continuous variation.

- Discrete gratings can be viewed as the grating version of the plates joining. They are composed of several areas characterized by a uniform **K** and the orientation of **K** changes from one area to the other one (see Fig. 1.7). Once again, due to the discreteness, the transmitted beam may exhibit dead zones at the edges of the areas of uniform orientation and for a small number of areas the beam may slightly deviate from the desired one reducing the performances for several applications

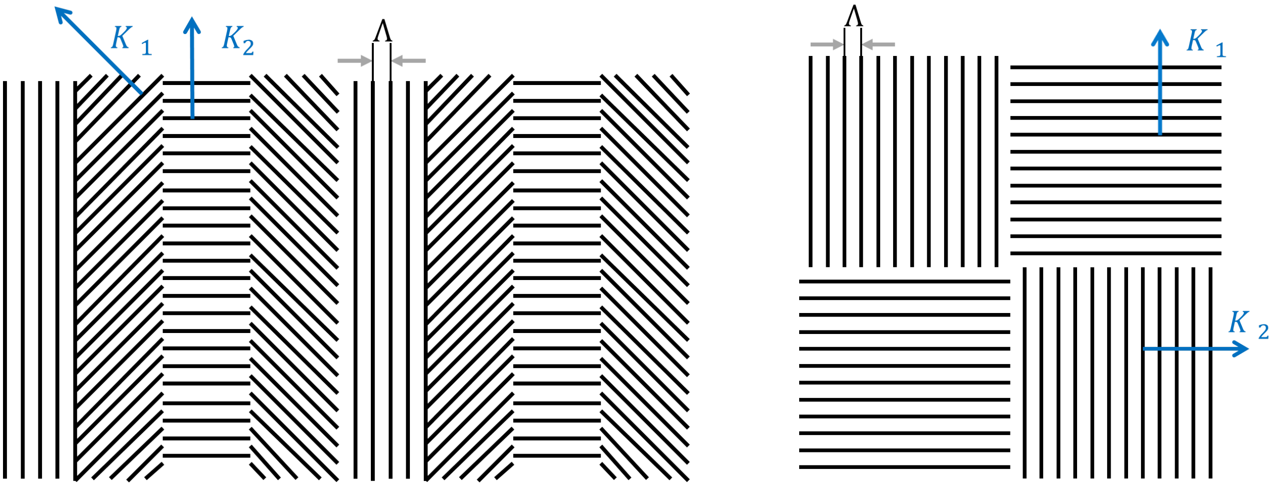

(a) (b)

Figure 1.7: Top views of SR using ZOG with a discrete variation of their grating vector. (a) represents a 1D SR; (b) represents a 2D SR.

- Continuous gratings are characterized by a continuous variation of **K** module or orientation. The continuity is assured by $\nabla \wedge \mathbf{K} = 0$. These gratings are more complicated to build for complex optical axis pattern. During the recording process, it is difficult to achieve the optimal gratings parameters (optimal shape of the grooves, optimal size parameters, optimal filling ...) while achieving the desired orientation of the grooves and preserving the continuity of the grating structure.

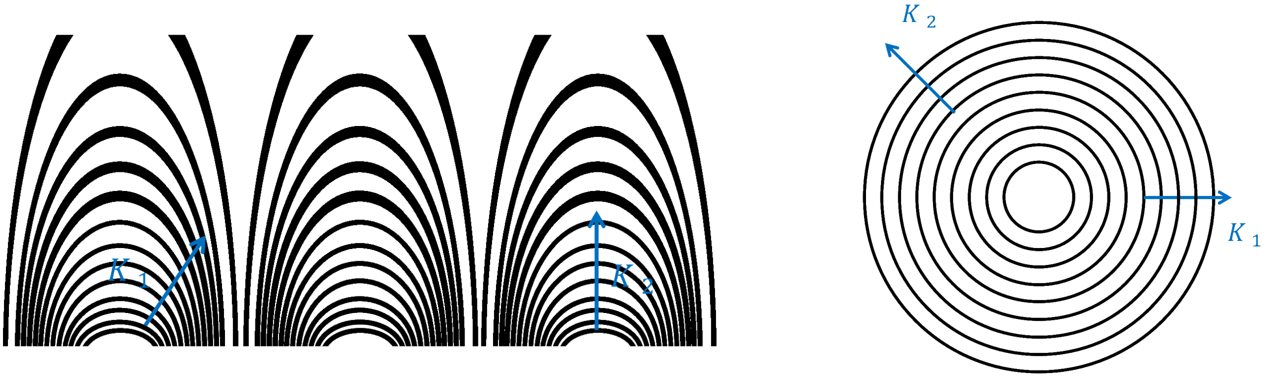

(a) (b)

Figure 1.8: Top views of SR using ZOG with a continuous variation of their grating vector. (a) represents a 1D SR; (b) represents a 2D SR. (a) is inspired by the grating structure desribed in [16]

1.3.3 Liquid crystals

As a brief reminder, the liquid crystal phase is an intermediate phase between the crystal and the liquid phases [19, 20, 21]. As a liquid the molecules are able to diffuse but as a crystal the same molecules exhibit an orientational order and in some cases a positional order too.

The liquid crystal molecules are called mesogens, the most simple one can be viewed as a rod like molecule. A liquid crystal phase contains these molecules with their long axis pointing to a preferred direction during the diffusion, the preferred direction being called the director, designed by the vector **n** (see Fig. 1.9). In the present work, two major properties of liquid crystals were used.

- Due to their anisotropy, LCs exhibit birefringent properties: the light polarized parallel to the director propagates at a different speed from the light polarized perpendicular to the director. The speed difference induces a phase retard between the two polarization components. Therefore, the orientation of the liquid crystals define the orientation of the retarder fast axis.
- The LCs are able to align when submitted to an electromagnetic field. LCs have electric dipoles: one end of the molecules exhibits a net negative charge while the other end is characterized by a positive one. When submitted to an electric field, the molecules with an electric dipole will orient themselves along the direction of the electric field. If the molecules are not characterized by a permanent dipole, the field produces a re-arrangement of the electrons and protons in the molecule resulting in an induced electric dipole. Even though the effect is weaker than the permanent dipole, the orientation along the electric field still occurs.

Thanks to these properties, recording a SR containing LCs can be achieved by submitting the LCs to the appropriate electric field to achieve the desired optical axis pattern.

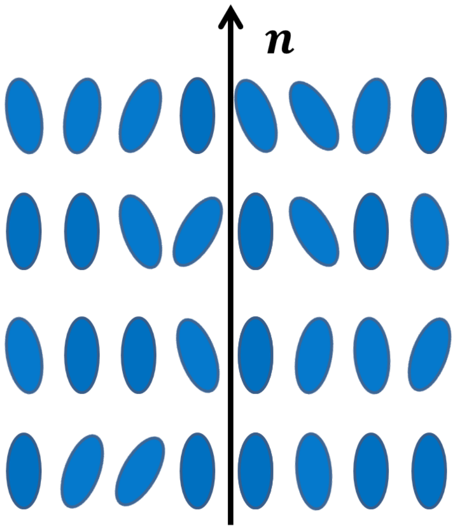

Figure 1.9: Representation of liquid crystals with a vertical director.

A lot of retarders made from LC already exist, a classification of the retarders and several examples are presented in Appendix B. In this thesis, our goal was to fabricate SRs with an uniform orientation of the LC along their thickness and a frozen orientation of the LC. Therefore the following recording methods are mainly used to record this kind of retarders. Several recording ways exist, they can be classified into three categories:

- rubbing the LCs or an alignment layer with a magnetic rod to imprint the fast axis pattern [11, 22],
- sending an electric current using an electrode [23],
- exposing the LCs layer or an alignment layer to a linearly polarized recording beam [3, 4, 8, 22, 24].

The common point of these methods is that they own a second step where the LC are fixed to prevent a variation of their orientation when exposed to a polarized light.

- Rubbing an alignment layer or the LCs layer with a magnetic rod will submit the LCs to a specific electromagnetic field and it will orient them. A uniform retarder is created if the rod possesses the same orientation in the retarder while a SR will be realized if the orientation of the rod changes during the alignment process. Unfortunately, any pattern with a continuous variation of the fast axis orientation cannot be achieved and some areas of misorientation of the LCs may appear after the recording process.

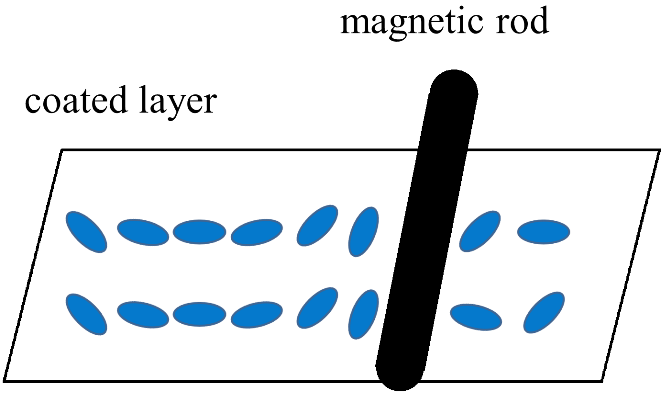

Figure 1.10: Representation of a retarder with an alignment using a magnetic rod

- Using a LC gel, an electrode under the substrate and a needle on top of the LC layer allow to submit the LC to a radial electric field (see Fig. 1.11). After the alignment, the LC gel will be cooled and exposed to UV beam to fix the LC to reach a frozen orientation of the fast axis. This method allows the recording of a retarder with a rotation of 360° of the fast axis orientation only.

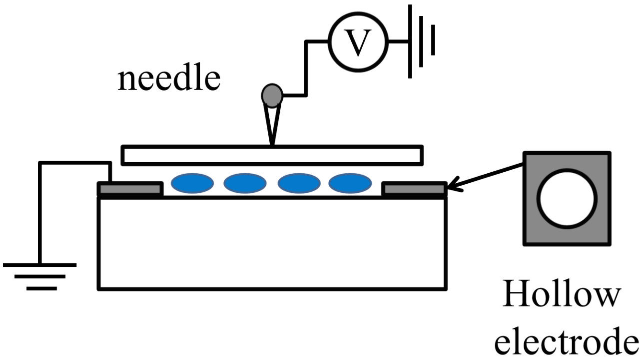

Figure 1.11: Representation of a retarder with an alignment using a hole electrode to create a radial electric field

- Using a linearly polarized light to expose an alignment layer and modifying the orientation the polarization also allows the recording of SRs in LCs.
  Two techniques exist to obtain the required variation of the recording polarization for the first layer.
  - The first one is based on mechanical action. Using a wedge aperture and rotating mounts containing a linear polarizer and the substrate enable the recording of an artificial space-variant linear polarization [8, 24]. The polarizer and the substrate are continuously rotated to expose each parts of the retarder through a different orientation of the recording polarization (see Figure 1.12). The method is able to produce SRs with continuous rotation of their fast axis with different amount of total rotation. The total rotation is a function of the relative speed of the mounts: if the polarizer and substrate exhibit the same rotating speed, the total rotation of the fast axis will be of 360° while a rotation of the substrate 2 times slower than the rotation the polarizer record a retarder with a rotation of 180° of the fast axis orientation. Unfortunately, due to the rotation, the center of the retarder may exhibit area with disoriented LCs.

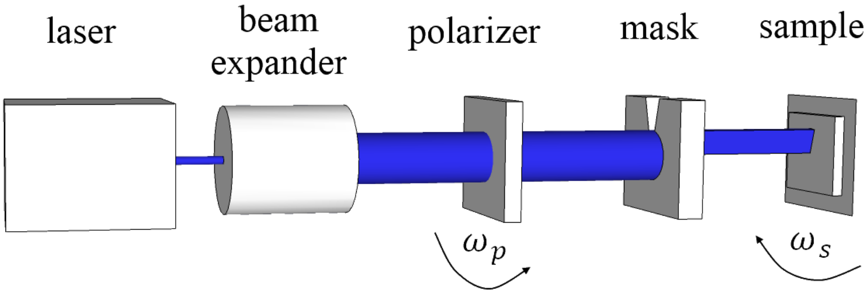

Figure 1.12: Scheme of the exposure process for the recording with mask and rotating mounts.

  - The second method uses polarization holography. The interference between two orthogonally polarized beams to create a 1D variation of the recording polarization [25, 26]. Since two different beams are superimposed only 1D SR can be realized with this method [3, 4, 22].
    Our contribution is to expand polarization holography to four beams in order to record 2D SR retarders for coronagraphy or polarization converting.

For this method, after the exposure to the beam with a non uniform polarization, the LCs are fixed using UV curing and the retarder can be exposed to another polarized beam without a variation of its fast axis orientation.

1.4 Conclusions

In this introductory chapter, we described the space-variant retarders and we classified them following their properties (1D, 2D, continuous, discrete ...). We also exposed a short review of their applications and their recording methods. In the next chapter, we will present the principle of polarization holography and its expansion to four beams. We will also describe our material: the liquid crystal polymers, the recording process of retarders and one measuring system.

Chapter 1 references

[1] F.Gori, “Measuring stokes parameters by means of a polarization grating,” *Opt. Lett.* **24**(9), 584–586 (1999).

[2] G.Biener, A.Niv, V.Kleiner, and E.Hasman, “Near-field fourier transform polarimetry by use of a discrete space-variant subwavelength grating,” *J. Opt. Soc. Am. A* **20**(10), 1940–1948 (2003).

[3] P.Piron, P.Blain, and S.Habraken, “Polarization measurement with space-variant retarders in liquid crystal polymers,” in [*Proc.SPIE*], **8160**, 81600Q–81600Q–7, Society of Photo-Optical Instrumentation Engineers SPIE (2011).

[4] S.R.Nersisyan, N.V.Tabiryan, D.M.Steeves, and B.R.Kimball, “Optical axis gratings in liquid crystals and their use for polarization insensitive optical switching,” *Journal of Nonlinear Optical Physics Materials* **18**(01), 1–47 (2009).

[5] P.Blain, P.Piron, Y.Renotte, and S.Habraken, “An in-line shearography setup based on circular polarization gratings,” *Optics and Lasers in Engineering* **51**, 1053–1059 (2013).

[6] D.Mawet, P.Riaud, J.Surdej, and J.Baudrand, “Subwavelength surface-relief gratings for stellar coronagraphy,” *Appl. Opt.* **44**(34), 7313–7321 (2005).

[7] D.Mawet, P.Riaud, O.Absil, and J.Surdej, “Annular groove phase mask coronagraph,” *Astrophys. J.* **633**(2), 1191–1200 (2005).

[8] D.Mawet, E.Serabyn, K.Liewer, C.Hanot, S.McEldowney, D.Shemo, and N.O’Brien, “Optical vectorial vortex coronagraphs using liquid crystal polymers theory, manufacturing and laboratory demonstration,” *Opt. Express* **17**(3), 1902–1918 (2009).

[9] C.Delacroix, *Exoplanet imaging with mid-infrared vector vortex coronagraphs: design, manufacture, validation and first light of the annular groove phase mask*, PhD thesis, University of Liège (2013).

[10] S.R.Nersisyan, N.V.Tabiryan, D.Mawet, and E.Serabyn, “Improving vector vortex waveplates for high contrast coronagraphy,” *Opt. Express* **21**(7), 8205–8213 (2013).

[11] M.Stalder and M.Schadt, “Linearly polarized light with axial symmetry generated by liquid-crystal-polarization converters,” *Opt. Lett.* **21**(23), 1948–1950 (1996).

[12] Q.Zhan, “Cylindrical vector beams: from mathematical concepts to applications,” *Adv. Opt. Photon.* **1**(1), 1–57 (2009).

[13] G.Machavariani, Y.Lumer, I.Moshe, A.Meir, and S.Jackel, “Spatially-variable retardation plate for efficient generation of radially- and azimuthally-polarized beams,” *Opt. Commun.* **281**(4), 732–738 (2008).

[14] R.Dorn, Quabis, S., and G.Leuchs, “Sharper focus for a radially polarized light beam,” *Phys. Rev. Lett.* **91**, 2339011–2339014 (2003).

[15] D.Mawet, P.Riaud, O.Absil, and J.Surdej, “Annular groove phase mask coronagraph,” *Astrophys. J.* **633**(2), 1191–1200 (2005).

[16] E.Hasman, Z.Bomzon, A.Niv, G.Biener, and V.Kleiner, "Polarization beam-splitters and optical switches based on space-variant computer-generated subwavelength quasi-periodic structures," *Opt. Commun.* **209**(1-3), 45–54 (2002).

[17] D.Mawet, P.Riaud, A.Boccaletti, P.Baudoz, J.Baudrand, O.Absil, J.L.Beuzit, P.Labeye, and J.Surdej, "Optical vortex coronagraph with subwavelength gratings." `http://exep.jpl.nasa.gov/TPF/tpfcDocs/27c+Optical+vortex+coronagraph.ppt` (2006). Accessed: 2013-05-04.

[18] D.Mawet, *Subwavelength gratings for extrasolar planetary system imaging and characterization*, PhD thesis, University of Liège (2006).

[19] T.Scharf, "Organic optical materials," in [*Polarized light in liquid crystals and polymers*], 110–121, Wiley (2007).

[20] P.J.Collings and M.Hird, "Introduction to a special phase of matter," in [*Introduction to liquid crystals chemistry and physics*], G.W.Gray, J.W.Goodby, and A.Fukuda, eds., 1–16, Taylor and Francis (1997).

[21] Case Western Reserve University, "Virtual textbook of polymers & liquid crystals." `http://plc.cwru.edu/tutorial/enhanced/files/textbook.htm` (2004). Accessed 2013-07-02.

[22] G.P.Crawford, J.N.Eakin, M.D.Radcliffe., A.Callan-Jones, and R.A.Pelcovits, "Liquid-crystal diffraction gratings using polarization holography alignment techniques," *J. Appl. Phys.* **98**(12) (2005).

[23] H.Ren, T.-H.Lin, and S.-T.Wu, "Linear to axial or radial polarization conversion using a liquid crystal gel," *Appl. Phys. Lett.* **89**(5) (2006).

[24] S.-W.Ko, C.-L.Ting, A.Y.-G.Fuh, and T.-H.Lin, "Polarization converters based on axially symmetric twisted nematic liquid crystal," *Opt. Express* **18**(4), 3601–3607 (2010).

[25] L.Nikolova and T.Todorov, "Diffraction efficiency and selectivity of polarization holographic recording," *Optica Acta: International Journal of Optics* **31**(5), 579–588 (1984).

[26] B.Kilosanidze and G.Kakauridze, "Polarization-holographic gratings for analysis of light. 1. analysis of completely polarized light," *Appl. Opt.* **46**(7), 1040–1049 (2007).

2

Techniques and materials

Contents

In the previous chapter, we introduced the space-variant retarders, several applications and recording methods. In the present work, polarization holography was used to record SRs made out of liquid crystal polymers without mechanical action. This chapter concerns the polarization holography. It exposes the mathematical model, it develops several examples of the superimposition of two differently polarized beams and it presents the expansion of polarization holography to the case of a four-beam superimposition. Afterwards, our material, the Liquid Crystal Polymers (LCP) is presented as well as the experimental and recording process of a simple retarder.

2.1 Polarization interferometry

Usually, when interference phenomena are discussed, the beams inducing the interference are characterized by the same polarization state as stated by the Arago-Fresnel laws [1, 2, 3, 4].

- Two waves with the same polarization state can interfere.
- Two waves orthogonally polarized cannot interfere.
- Two orthogonally polarized waves coming from orthogonal components of unpolarized light and brought to the same plane cannot interfere.
- Two orthogonally polarized waves, originating from the same polarization beam and brought to the same polarization state can interfere.

Despite these laws, the superimposition of two orthogonally coherent polarized beams produces an interference "pattern": the resulting electric field exhibits a variation of its orientation instead of a variation of its intensity [5, 6].
Since the 80's, investigations on the superimposition of orthogonally polarized beams have been made and several materials were tested to record the variation of the electric field orientation.

2.1.1 Mathematical model

Kilosanidze et al. [7] developed a mathematical model of the local polarization resulting from the superimposition of two generic coherent beams based on the Jones formalism [8].

Two generic coherent beams A and B are represented by the following equation.

$$A = \begin{pmatrix} A_x \\ A_y \exp(i\phi_A) \end{pmatrix} \exp(i\omega t)\ B = \begin{pmatrix} B_x \\ B_y \exp(i\phi_B) \end{pmatrix} \exp(i\delta)\exp(i\omega t) \tag{2.1}$$

Where A_x and B_x are the amplitude modules of the horizontal component of A and B, A_y and B_y the amplitude modules of the vertical components, ϕ_A and ϕ_B the phase differences between the horizontal and vertical components. ω is the pulsation of the beams and δ is the phase difference between the two beams.

At the overlap plane, the resulting electric field: Σ can be written as equation 2.2.

$$\Sigma = \begin{pmatrix} A_x + B_x \exp(i\delta) \\ A_y \exp(i\phi_A) + B_y \exp(i\phi_B + i\delta) \end{pmatrix} \exp(i\omega t) \tag{2.2}$$

The local polarization ellipse is described by the real part of the electric field and is written as

$$\Re(\Sigma) = \mathbf{p}\cos(\omega t) + \mathbf{q}\sin(\omega t) \tag{2.3}$$

where $\mathbf{p} = \begin{pmatrix} A_x + B_x\cos(\delta) \\ A_y\cos(\phi_A) + B_y\cos(\phi_B + \delta) \end{pmatrix}$ and $\mathbf{q} = -\begin{pmatrix} B_x\sin(\delta) \\ A_y\sin(\phi_A) + B_y\sin(\phi_B + \delta) \end{pmatrix}$.

To describe the local polarization ellipse, three parameters must be provided: I_1 the intensity along the largest axis, I_2 the intensity along the smallest axis and α the angle between the horizontal and the largest axis of the ellipse (see Fig.2.1).

These parameters are given by

$$\begin{aligned}
I_{1,2} &= \tfrac{1}{2}\left[(p_x^2+p_y^2)+(q_x^2+q_y^2)\right] \pm \tfrac{1}{2}\sqrt{\left[(p_x^2-p_y^2)+(q_x^2-q_y^2)\right]^2+4\left(p_xp_y+q_xq_y\right)^2},\\
\sin(2\alpha) &= \frac{2(p_xp_y+q_xq_y)}{\sqrt{\left[(p_x^2-p_y^2)+(q_x^2-q_y^2)\right]^2+4\left(p_xp_y+q_xq_y\right)^2}},\\
\cos(2\alpha) &= \frac{(p_x^2-p_y^2)+(q_x^2-q_y^2)}{\sqrt{\left[(p_x^2-p_y^2)+(q_x^2-q_y^2)\right]^2+4\left(p_xp_y+q_xq_y\right)^2}}.
\end{aligned} \tag{2.4}$$

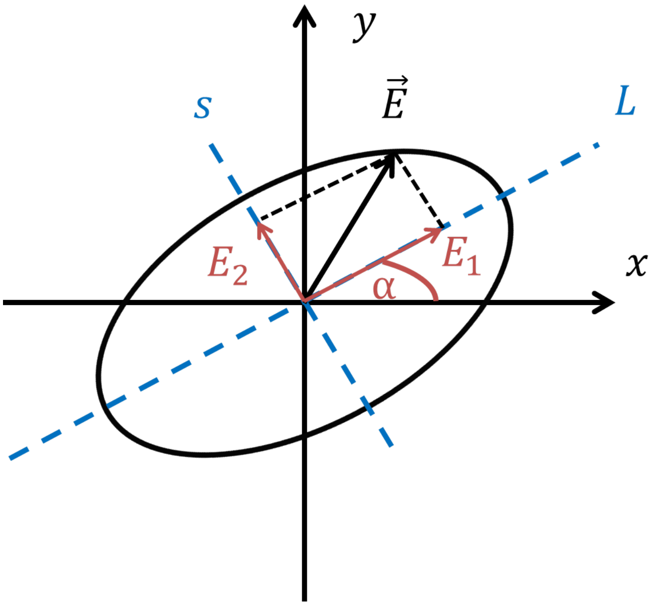

Figure 2.1: Representation of the local polarization ellipse, the largest (L) and the smallest (s) axis are pictured by dashed blue lines.

Let us notice that $I_2 = 0$ and $I_1 \neq 0$ always represents a linear polarization and $I_2 = I_1 \neq 0$ represents a circular polarization.

2.1.2 Examples

To illustrate the model, several simple cases can be studied.

- the classical case of two linearly polarized beams with the same polarization,
- two circularly polarized beams with the same handedness
- two linearly polarized beams orthogonally polarized
- two circularly polarized beams of opposite handedness

***a*: 2 linearly polarized beams with the same polarization: vertical case**

$$\begin{array}{lcl} A_x = B_x = 0 & & I_1 = 2 \times (1 + \cos(\delta)) \\ A_y = B_y = 1 & \Rightarrow & I_2 = 0 \\ \phi_A = \phi_B = 0 & & \alpha = 90^\circ \end{array}$$

***b*: 2 circularly polarized beam with the same polarization: right handed**

$$\begin{array}{lcl} A_x = B_x = \frac{\sqrt{2}}{2} & & I_1 = 1 + \cos(\delta) \\ A_y = B_y = \frac{\sqrt{2}}{2} & \Rightarrow & I_2 = 1 + \cos(\delta) \\ \phi_A = -\frac{\pi}{2};\ \phi_B = -\frac{\pi}{2} & & \theta \text{ is undefined} \end{array}$$

***c*: 2 linearly orthogonally polarized beams**

$$\begin{array}{lcl} A_x = 1;\ B_x = 0 & & I_1 = 1 + |\cos(\delta)| \\ A_y = 0;\ B_y = 1 & \Rightarrow & I_2 = 1 - |\cos(\delta)| \\ \phi_A = \phi_B = 0 & & sign\,[\cos(\delta)] * \frac{\pi}{4} \end{array}$$

***d*: 2 circularly polarized beams of opposite handedness**

$$\begin{array}{lcl} A_x = B_x = \frac{\sqrt{2}}{2} & & I_1 = 1 + |\cos(\delta)| \\ A_y = B_y = \frac{\sqrt{2}}{2} & \Rightarrow & I_2 = 1 - |\cos(\delta)| \\ \phi_A = -\frac{\pi}{2} : \phi_B a = \frac{\pi}{2} & & \theta = \frac{\delta}{2} \end{array}$$

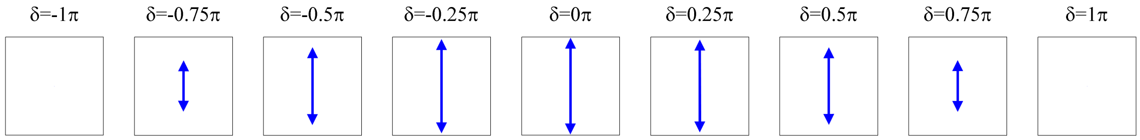

Figure 2.2: Representation of the local polarization ellipse for case *a*.

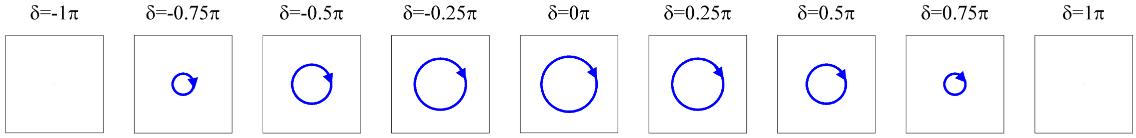

Figure 2.3: Representation of the local polarization ellipse for case *b*.

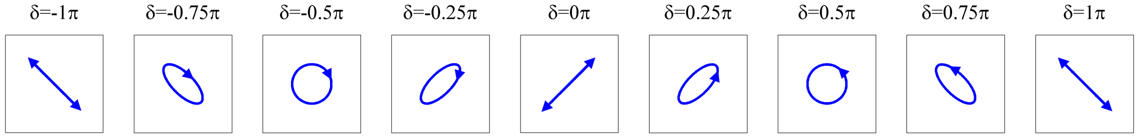

Figure 2.4: Representation of the local polarization ellipse for case *c*.

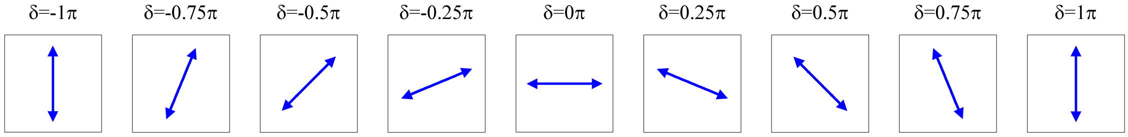

Figure 2.5: Representation of the local polarization ellipse for case *d*.

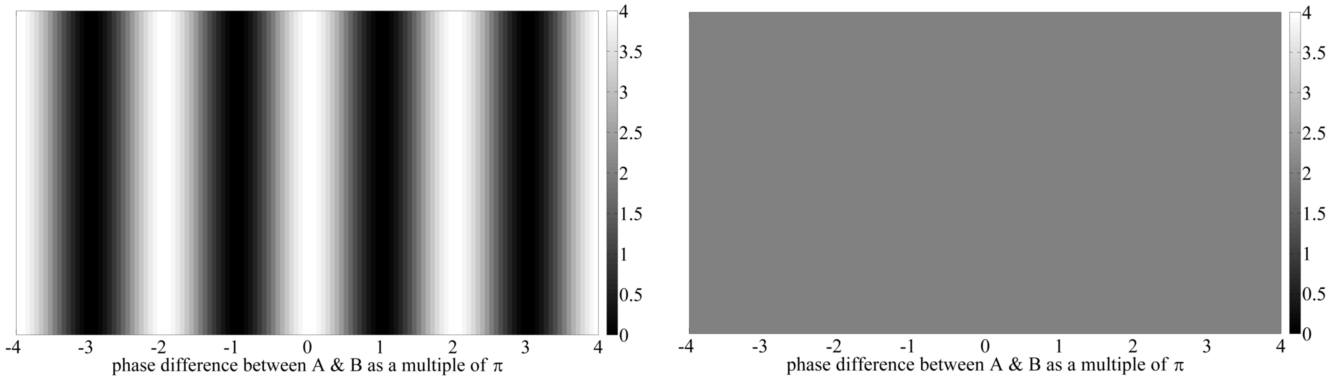

case a and case b

case c and case d

Figure 2.6: Representation of the intensity of the resulting electric fields for the 4 configurations.

2.1.3 Expansion to four beams

One of our contributions is to expand the superimposition to a 4 beam overlap to allow the design of a 2D space variant polarization pattern.
Our goal is to realize 2D SRs with a rotational symmetry of their fast axis. Thus we modeled the four beams superimposition pictured in Figure 2.7.

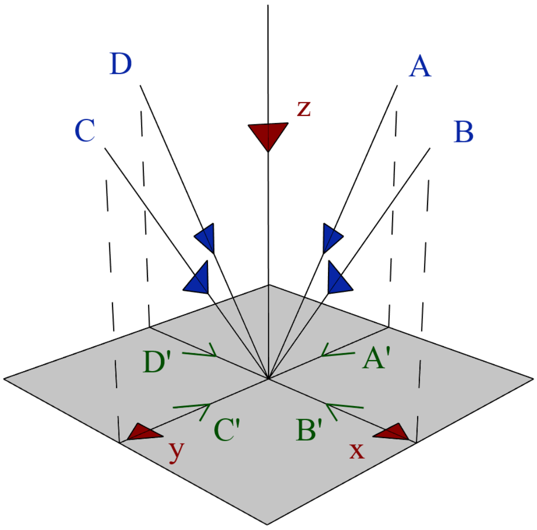

Figure 2.7: Representation of the superimpostion with of beams, possessing the same incident angle.

Using the previous formalism, the four beams are described by:

$$\begin{aligned} A &= \begin{pmatrix} A_x \\ A_y \exp(i\phi_A) \end{pmatrix} \exp(i\delta_A), \quad B = \begin{pmatrix} B_x \\ B_y \exp(i\phi_B) \end{pmatrix} \exp(i\delta_B) \\ C &= \begin{pmatrix} C_x \\ C_y \exp(i\phi_C) \end{pmatrix} \exp(i\delta_C), \quad D = \begin{pmatrix} D_x \\ D_y \exp(i\phi_D) \end{pmatrix} \exp(i\delta_D). \end{aligned} \tag{2.5}$$

An important modification is that the δ_i of each beams are computed as the phase difference between the i plane-wave beam and a virtual beam with a normal incidence. Therefore

$$\begin{aligned} \delta_A &= \frac{2\pi}{\lambda}\sin(\theta_i) \times (y), \quad & \delta_B &= \frac{2\pi}{\lambda}\sin(\theta_i) \times (-x) \\ \delta_C &= \frac{2\pi}{\lambda}\sin(\theta_i) \times (-y), \quad & \delta_D &= \frac{2\pi}{\lambda}\sin(\theta_i) \times (x) \end{aligned}$$

with θ_i is the incident angle.
The two vectors describing the polarization ellipse become:

$$\begin{aligned} \mathbf{p} &= \begin{pmatrix} A_x\cos(\delta_A) + B_x\cos(\delta_B) + C_x\cos(\delta_C) + D_x\cos(\delta_D) \\ A_y\cos(\phi_A+\delta_A) + B_y\cos(\phi_B+\delta_B) + C_y\cos(\phi_C+\delta_C) + D_y\cos(\phi_D+\delta_D) \end{pmatrix} \\ \mathbf{q} &= -\begin{pmatrix} A_x\sin(\delta_A) + B_x\sin(\delta_B) + C_x\sin(\delta_C) + D_x\sin(\delta_D) \\ A_y\sin(\phi_A+\delta_A) + B_y\sin(\phi_B+\delta_B) + C_y\sin(\phi_C+\delta_C) + D_y\sin(\phi_D+\delta_D) \end{pmatrix}, \end{aligned} \tag{2.6}$$

while the ellipse parameters are still described by equation 2.4. The four beams systems will be described and analyzed in the chapter dedicated to the recording of 2D SR (chapter 5. The next section will present our material, the recording process of a simple retarder i.e. a retarder with a uniform orientation of its optical axis and the measuring process of these retarders.

2.2 Retarders in liquid crystal polymers

Liquid crystal polymers are a particular case of liquid crystals. In a nutshell, the mesogens are inserted inside polymer chains [9, 10, 11]. Two kinds of LCPs exist: main-chain LCPs and side-chain LCPs.

- For main-chain LCPs, the mesogens are part of the main chain of polymer (see Fig. 2.8 (a)).
- For side-chain LCPs, the mesogens are connected to the polymer by a flexible bridge called the spacer (see Fig. 2.8 (b)).

Like the previous case, the mesogens will exhibit birefringent properties and their orientation will define the orientation of the optical axis of the retarders. Following the category, the properties are slightly different.

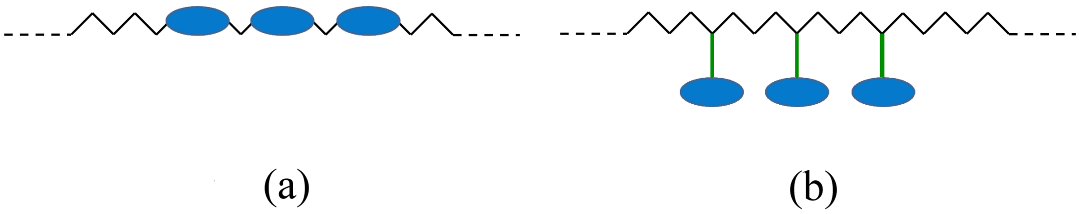

Figure 2.8: Representation of the two kinds of LCPs, (a) main-chain LCP, (b) side-chain LCP. Spacers are represented in green

2.2.1 Recording process

The recording material used during this thesis is from *ROLIC*®: $ROP-103$ and $ROF-5102$.
The generic recording process contains two steps.

- The first one concerns the alignment layer $ROP-103$. The layer is spin-coated on a clean[2] glass substrate to achieve a thickness of $\approx 50\,nm$. Then the substrate is heated to get rid of the solvents and is exposed to UV polarized beam with the recording setup pictured in Figure 2.9.
  During the first exposure, the photo-polymers contained in the first layer will align themselves according to the direction of the recording electric field (see Figure 2.10).
- The second step concerns the LCP $ROF-5103$. The second layer is spin-coated on the first one and the LC will orient themselves according to the orientation of the polymers below.
  The orientation of the LC will define the orientation of the fast axis of the sample. Then the prototype is heated and cooled under a nitrogen flush to avoid oxidation on the LC layer and finally exposed to an unpolarized UV source to fix the LC.
  After the exposure the LC are frozen: the orientation of the fast axis will not change while the retarder is exposed to a polarized beam.
  Changing the spin-coating conditions will change the thickness of the birefringent layer allowing to modify the phase retard induced by the retarder.

---

[2] The cleaning process and a more detailled presentation of the recording process are exposed in Appendix C

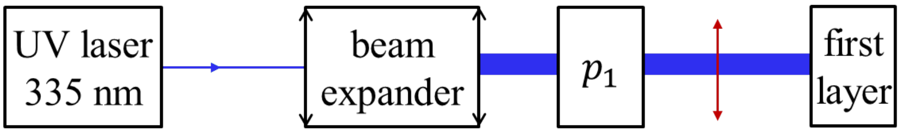

Figure 2.9: Representation of the recording setup for a retarder with a uniform orientation of its fast axis, the beam is pictured in blue and the polarization is pictured in red.

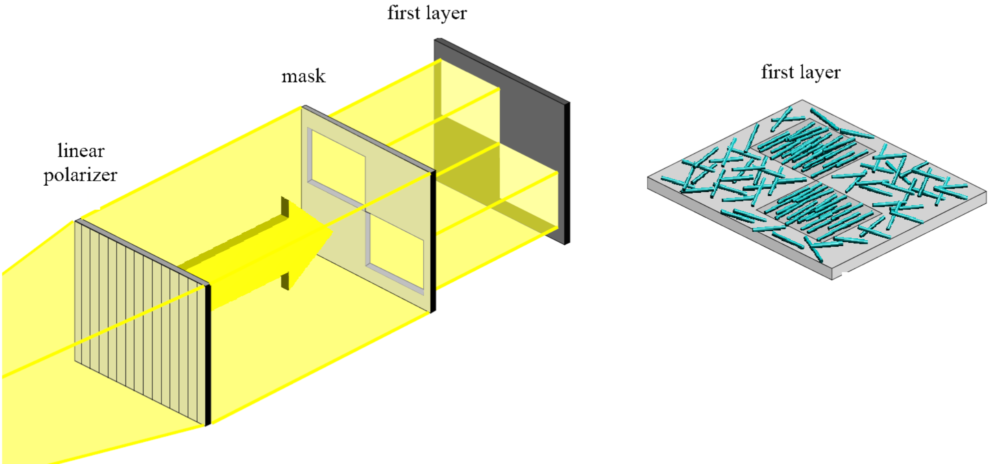

Figure 2.10: Representation of the recording setup for a discrete 2D SR. The polymers in the areas exposed to a polarized light are characterized by the same orientation while the polymers in the unexposed areas are characterized by a random orientation. To finish working with the first layer, the polarizer and the mask must be rotated to expose the other areas. The picture is from the components datasheet [12, 13].

This method is used to produce retarders with a uniform orientation of their fast axis or SR with a discrete variation of their optical if several masks are used (see Figure 2.11 for uniform retarders and Figure 2.12 for retarders with two orientation of its their fast axis).
To record 1D or 2D SR with a continuous variation, polarization holography is used to generate the space-variant recording electric field, the changes of the exposure setup will be presented in their specific section.

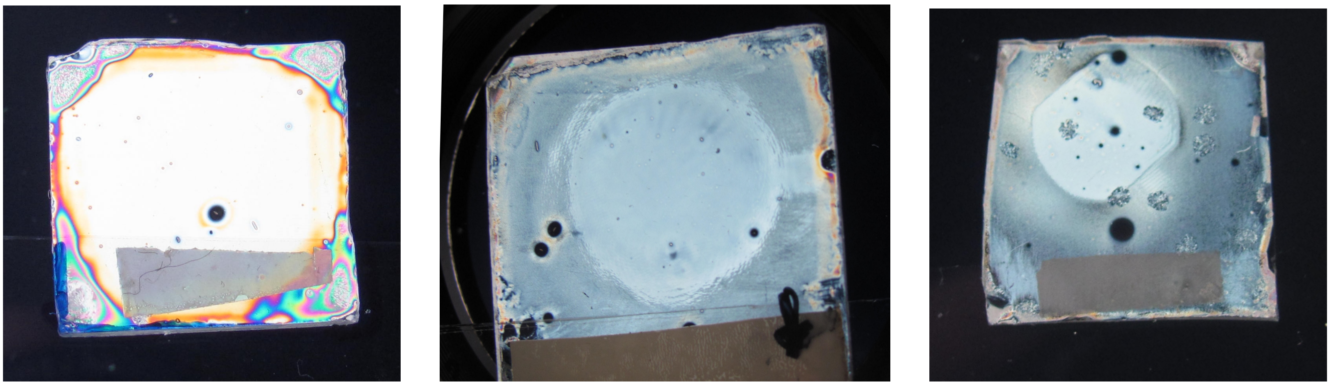

Figure 2.11: Several pictures of the first prototypes of uniform retarders in liquid crystal polymers between two crossed polarizers.

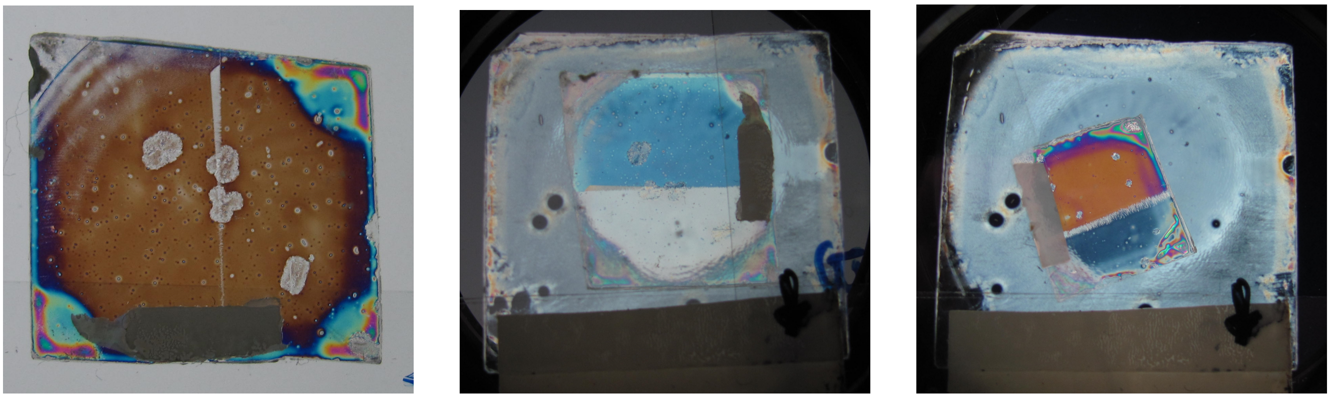

(a) (b) (c)

Figure 2.12: Several pictures of the first retarder with two areas of same orientation of its fast axis between two linear polarizers, the variation of orientation is about 90°. (a) Pictures the intensity of the retarder between two linear polarizers and no obvious variations are present due to the symmetry of the situation. (b) & (c) Present two stacked retarders. The first one is the non-uniform one while the other is a uniform one. The second retarder is used to break the symmetry to achieve a variation of the transmitted intensity which highlights the variation of the fast axis orientation. Therefore the two areas are clearly visible. The line between the two areas is caused by the mask implied during the recording process.

2.2.2 Measuring process

The measuring process of a simple retarder is to compute the phase shift between the ordinary and extraordinary component of the incident polarization (ϕ) and the orientation of its fast axis (α).
To compute these parameters, we used the polarimetric bench at Hololab (see Figures 2.13 and 2.13). The bench is composed of:

- a fibered coupled laser at 660 nm with a diverging beam L
- a collimation lens l
- a diaphragm d
- a linear polarizer P_1
- a quarter-wave plate $\lambda/4$
- 2 linear polarizers on rotation mounts computer controlled P_2 & P_3
- a mono-pixel detector D

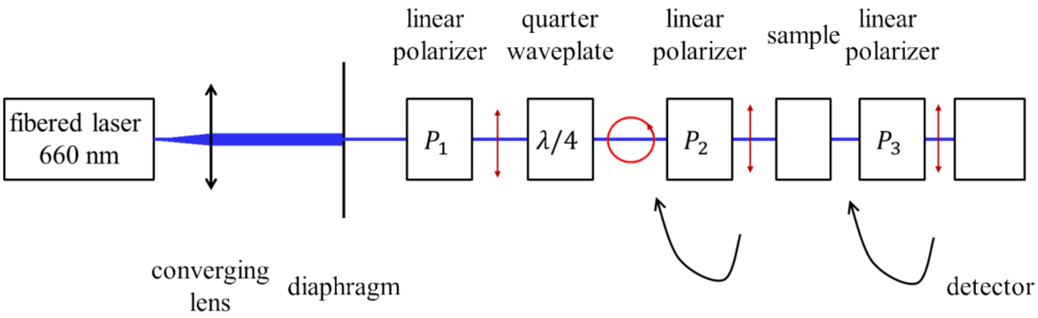

Figure 2.13: Scheme of the polarimetric bench, the polarization is pictured in red.

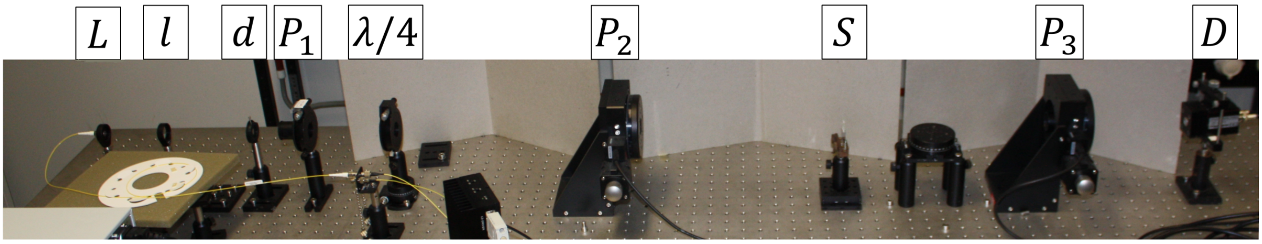

Figure 2.14: Picture of the polarimetric bench.

The fast axis of the quarter-wave plate forms an angle of 45° with the axis of the linear polarizer P_1 to achieve a circular polarization. The principle of measurement is the same as Yang et al.[14], the bench will measure the transmitted intensity for several positions of P_2 each time for two configurations:

- P_3 transmission axis is parallel to P_2 transmission axis $\Rightarrow I_{/\!/}$
- P_3 transmission axis is orthogonal to P_2 axis $\Rightarrow I_\perp$.

The birefringent parameters are given by the next equation.

$$\frac{I_\perp}{I_{/\!/}} = \frac{\sin^2(2(\alpha-\alpha_0))\,\sin^2(\phi/2)}{1-4\left(1-\sin^2(\alpha-\alpha_0)\right)\sin^2(\alpha-\alpha_0)\sin^2(\phi/2)} \tag{2.7}$$

Where ϕ is the phase retard between the ordinary and extraordinary components induced by the retarder, α is the angle between the polarizer and the vertical as defined in Figure 2.15 and α_0 is the angle between the vertical and one of the optical axes of the retarder. The results of our numerical simulations are exposed in Table 2.1 and Figure 2.16 represents the numerical intensity for simulated waveplates.

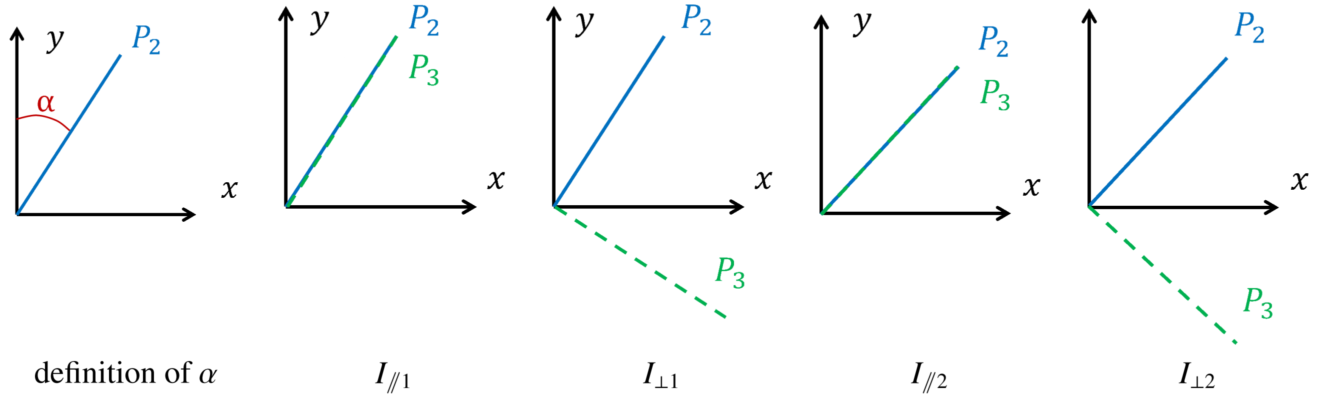

Figure 2.15: Definition of α and representations of several configurations for the measurement of $I_{/\!/}$ and $I_\perp$.

Table 2.1: Simulated parameters for several birefringent plates. ϕ is the phase retard induced by the plate and α is the orientation of one neutral axis. α is degree and exceptionnaly, ϕ is in degree to.

	$\alpha_{fast} = -45$	$\alpha_{fast} = -20$	$\alpha_{fast} = 0$	$\alpha_{fast} = 10$	$\alpha_{fast} = 45$	$\alpha_{fast} = 90$
$\phi_{in} = 45$	$\phi_c = 45$	$\phi_c = 45$	$\phi_c = 445$	$\phi_c = 45$	$\phi_c = 45$	$\phi_c = 45$
	$\alpha_c = 45$	$\alpha_c = 70$	$\alpha_c = 90$	$\alpha_c = 100$	$\alpha_c = 45$	$\alpha_c = 90$
$\phi_{in} = 87$	$\phi_c = 87$	$\phi_c = 87$	$\phi_c = 87$	$\phi_c = 87$	$\phi_c = 87$	$\phi_c = 87$
	$\alpha_c = 45$	$\alpha_c = 70$	$\alpha_c = 90$	$\alpha_c = 100$	$\alpha_c = 45$	$\alpha_c = 90$
$\phi_{in} = 90$	$\phi_c = 90$	$\phi_c = 90$	$\phi_c = 90$	$\phi_c = 90$	$\phi_c = 90$	$\phi_c = 90$
	$\alpha_c = 45$	$\alpha_c = 70$	$\alpha_c = 90$	$\alpha_c = 100$	$\alpha_c = 45$	$\theta_c = 90$
$\phi_{in} = 120$	$\phi_c = 120$	$\phi_c = 120$	$\phi_c = 120$	$\phi_c = 120$	$\phi_c = 120$	$\phi_c = 120$
	$\alpha_c = 45$	$\alpha_c = 70$	$\alpha_c = 90$	$\alpha_c = 100$	$\theta_c = 45$	$\alpha_c = 90$
$\phi_{in} = 180$	$\phi_c = 180$	$\phi_c = 180$	$\phi_c = 180$	$\phi_c = 180$	$\phi_c = 180$	$\phi_c = 180$
	$\alpha_c = 45$	$\alpha_c = 70$	$\alpha_c = 90$	$\alpha_c = 100$	$\theta_c = 45$	$\alpha_c = 90$
$\phi_{in} = 230$	$\phi_c = 130$	$\phi_c = 130$	$\phi_c = 130$	$\phi_c = 130$	$\phi_c = 130$	$\phi_c = 130$
	$\alpha_c = 45$	$\alpha_c = 70$	$\alpha_c = 90$	$\alpha_c = 100$	$\alpha_c = 45$	$\alpha_c = 90$

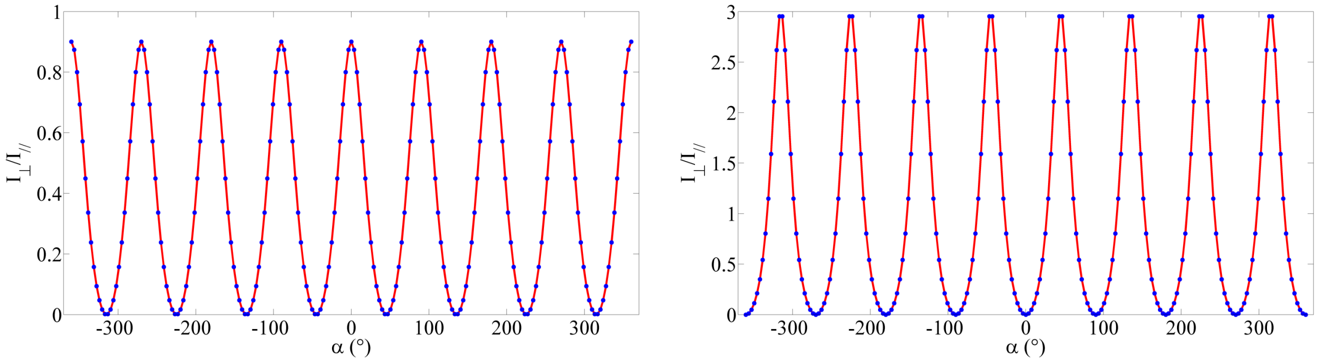

(a) (b)

Figure 2.16: Fit for two simulated waveplates, the red line is the fitted intensity while the blue dots represents the input intensity (a): $\phi = 87°$ $\alpha = 45°$, (b): $\phi = 120°$ $\alpha = 90°$.

One can observe that the phase retard induced by the plate is always accurately computed while the angle θ represents the orientation of the closest neutral axis of the birefringent plates[3].

---

[3] A phase retard of 230° is equivalent to a phase a retard of 130° and the computed angle of orientation is the angle of the fast or of the slow axis of the waveplates.

Several retarders in LCP with a uniform orientation of their fast axis were measured with the bench, the results for three retarders are presented in Table 2.2 and Figure 2.17 presents an example of the fitting by the equation 2.7.

Table 2.2: Results of the phase difference for four retarders measured on the polarimetric bench, the variation of ϕ are due to small variations of the spin-coating parameters, exceptionally the phase retard is in ° for simplicity.

	ϕ (°)	95%confidence interval
retarder A	89.04	[88.59;89.49]
retarder B	87.71	[86.75;87.58]
retarder C	87.72	[85.89;89.58]
retarder D	89.07	[87.18;90.88]

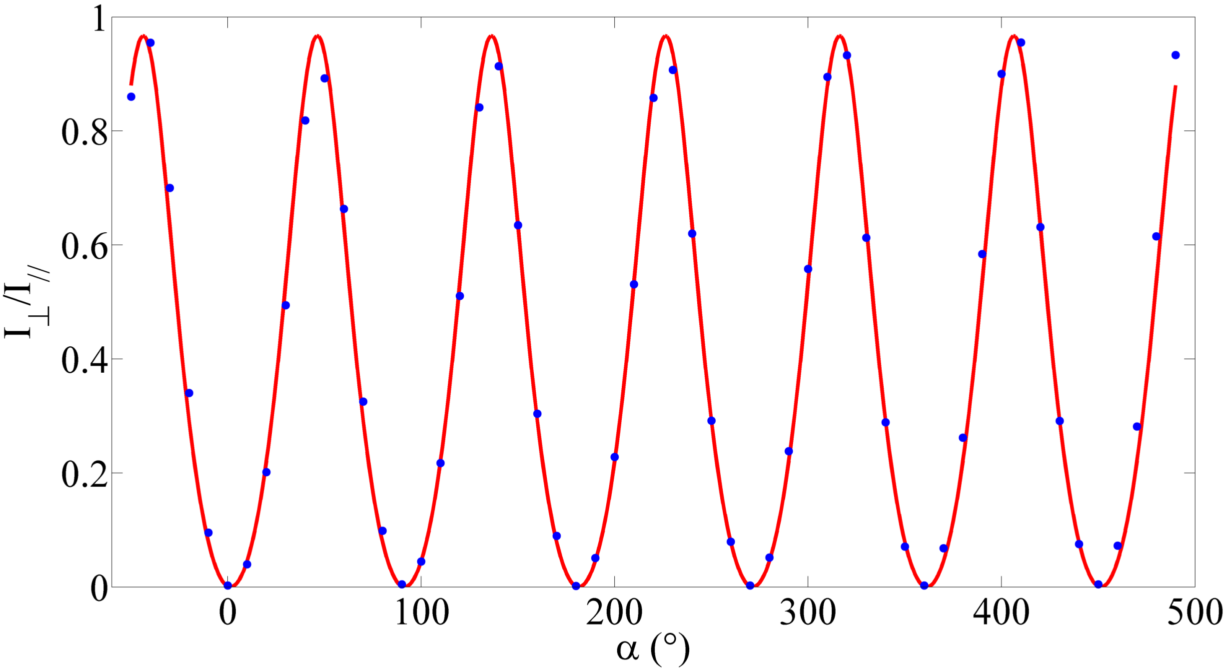

Figure 2.17: Example of the fitting of the measurements. The red line represents the fitted intensity while the blue dots stand for the measured one.

2.2.3 Possible upgrades of the bench

Presently, the measurement of the phase retard and the orientation of one neutral axis is for only pixel per measurement. A useful expansion would be to achieve the measurement for the whole retarder in one measurement process. An idea is to replace the mono pixel detector by a ccd camera and to compute the fitting process for several pixels after the measurement. So a map of ϕ would be available, the map could be useful for other applications such as the polarization analysis method (see section 3.4).

Another upgrade would be to use several fibered sources of different wavelengths or a visible continuum source coupled with wavelength filters to compute the phase retard versus the wavelength for a same point of a retarder. The measured phase retard can be written as

$$\phi = \frac{2\pi\Delta n(\lambda) h}{\lambda}.$$

Where Δn is the difference between the ordinary and the extraordinary refractive indices and h is the thickness of the birefringent layer. Using the computation of ϕ as a function of λ, we will be able to compare the curve of Δn as a function of λ with the datasheet from the supplier (see Figure 2.18).

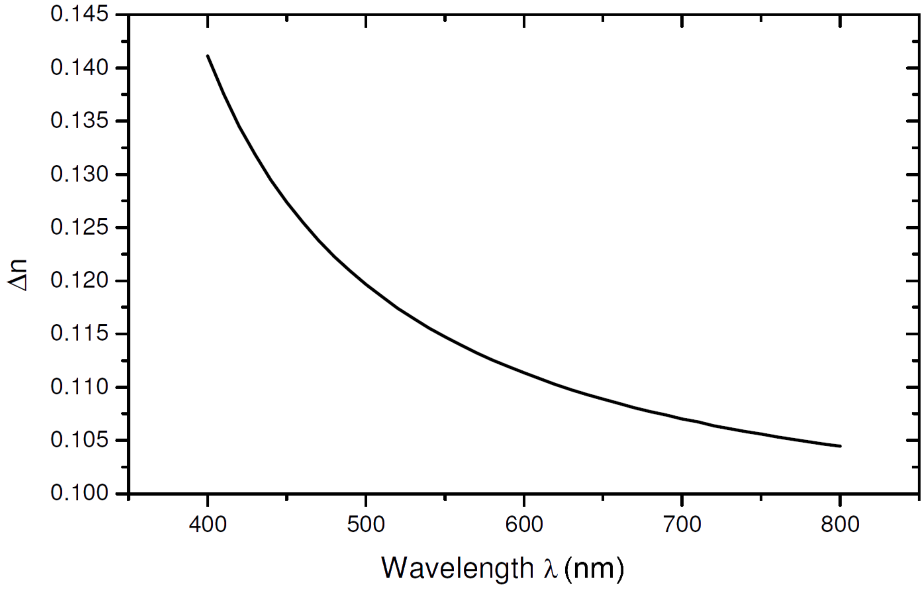

Figure 2.18: Variation of Δn as a function of λ [12, 13].

2.3 Conclusions

In this chapter, we present our recording method based on the superimposition of differently polarized beams, several simple examples were shown and the superimposition with four beams was introduced. Our material, the liquid crystal polymers was introduced and the generic recording was detailed. Finally, the measuring process used to compute the phase retard and the orientation of the fast axis of the retarders and the results for several prototypes were presented.

Chapter 2 references

[1] R.Barakat, "Analytic proofs of the arago-fresnel laws for the interference of polarized light," *J. Opt. Soc. Am. A* **10**, 180–185 (1993).

[2] B.Kanseri, N.Bisht, Kandpal, H., and S.Rath, "Observation of the fresnel and arago laws using the mach-zehnder interferometer," *Am. J. Phys.* **76**, 39–42 (2008).

[3] B.Kanseri and H.C.Kandpal, "Mathematical formulation for verification of the fresnel and arago interference laws using a mach-zehnder interferometer," *Optik-International Journal for Light and Electron Optics* **121**, 1019–1026 (2010).

[4] T.Scharf, "Polarized light," in [*Polarized light in liquid crystals and polymers*], 15–16, Wiley, 1 ed. (2007).

[5] M.Attia and J.M.C.Jonathan, "Anisotropic gratings recorded from two circularly polarized coherent waves," *Opt. Commun.* **47**, 85–90 (1983).

[6] L.Nikolova and T.Todorov, "Diffraction efficiency and selectivity of polarization holographic recording," *Optica Acta: International Journal of Optics* **31**(5), 579–588 (1984).

[7] B.Kilosanidze and G.Kakauridze, "Polarization-holographic gratings for analysis of light. 1. analysis of completely polarized light," *Appl. Opt.* **46**(7), 1040–1049 (2007).

[8] E.Hecht, "Polarisation," in [*Optique*], Addison-Wesley, 4 ed. (2005).

[9] T.Scharf, "Organic optical materials," in [*Polarized light in liquid crystals and polymers*], 110–121, Wiley (2007).

[10] P.J.Collings and M.Hird, "Introduction to a special phase of matter," in [*Introduction to liquid crystals chemistry and physics*], G.W.Gray, J.W.Goodby, and A.Fukuda, eds., 1–16, Taylor and Francis (1997).

[11] Case Western Reserve University, "Virtual textbook of polymers & liquid crystals." `http://plc.cwru.edu/tutorial/enhanced/files/textbook.htm` (2004). Accessed 2013-07-02.

[12] "Linearly photo-polymerisable polymer (lpp) as alignment layer for liquid crystals and retardation film coatings rolic rop-103." technical data sheet (2006).

[13] "Liquid crystal pre-polymer (lcp) for retardation film coatings rolic rop-103." technical data sheet (2006).

[14] C.Yang and P.Yeh, "Artificial uniaxial and biaxial dielectrics with the use of photoinduced gratings," *J. Appl. Phys.* **81**, 23–29 (1997).

Part II

Applications of 1D space-variant retarders

3

Polarization analysis

Contents

In the previous chapter, we introduced our recording method and our material. The first retarders we recorded were 1D continuous SR using the superimposition of two circularly polarized beams of opposite handedness. Thanks to these retarders, we developed a new method of polarization analysis in nearly real time. The principle is to record the variation of the intensity transmitted through a linear polarizer and 1D SR to compute the polarization parameters of the beam. This chapter presents the mathematical model of the method and the results of several numerical simulations. Then, it exposed the experimental aspects such as the recording of the retarder and the measurement process. After, the results are analyzed and several upgrades of the method are mentioned. Finally, a short overview of a possible application of the method is presented.

3.1 Introduction

The first direct application of polarization holography which we developed is a polarization analysis method. As we saw in section 2.1, at a fixed point in space, the end of the electric field describes an ellipse during a period of vibration. Polarization analysis aims to determine the characteristics of polarization. The determination can be used for a lot of applications such as camouflage detection [1], ellipsometry [2, 3], biomedical applications [4, 5], astronomical observations [6], imagery [7] ...
Several methods to measure the Stokes parameters of an incident beam already exist [3, 8, 9, 10, 11, 12, 7, 13, 14].

A usual method consists in measuring the variation of the transmitted intensity after a rotating quarter-wave plate and a linear polarizer [3, 8, 9, 10]. Using the Fourier analysis of the transmitted signal allows to compute the Stokes parameters of the incident beam. Unfortunately, this method is unable to measure dynamic variation of the polarization since it is based on several measurements for different orientations of the quarter-wave plate fast axis.

Another method consists in the splitting of the beam into four beams which could be coupled with several polarization optical elements to compute the Stokes parameters [3, 9, 10, 12]. The drawbacks of this method is the cost of the several detectors, the size of the setup and the sensitivity to statistical errors.

Our method is inspired by a method based on a 1D discrete SR in ZOG [9], the retarder will transform a uniformly polarized beam into a space-variant one and a linear polarizer will convert the variation of the polarization into a space-variant intensity. Using a spatial Fourier analysis of the intensity allows to compute the Stokes parameters. We replaced the 1D discrete SR by a 1D continuous SR containing LCP [15]. The retarder is realized by recording the superimposition of two circularly polarized beams of opposite handedness, the electric field and the retarder are pictured in Figure 3.1 (a) and (b). Due to the continuous variation of the electric field orientation, the retarder exhibits a continuous variation of its fast axis orientation. The orientation being written as: $\alpha = \pi x/p$ where p is the period of the retarder. The period is the distance between two columns where the LC are characterized by the same orientation and depends on the recording wavelength λ_r and the incident angle θ_i: $p = \lambda_r/2\sin(\theta_i)$.

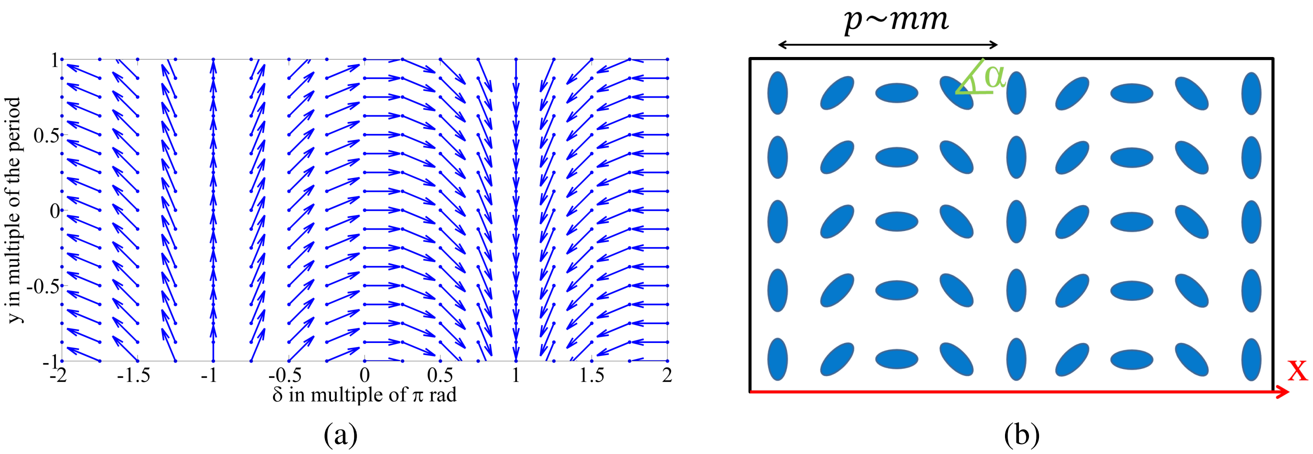

(a) (b)

Figure 3.1: (a) Representation of the electric field resulting from the superimposition of two circularly polarized beams of opposite handedness used to achieve the variation of the fast axis orientation. (b) Representation of the retarder used for polarization analysis.

The principle is the following one: the retarder will transform an incident uniformly polarized beam into a beam with a continuous and periodic variation of its polarization. The linear polarizer will convert the polarization variation into an intensity variation. The camera will record the transmitted intensity and by analyzing its variation, one can compute the polarization state of the incident beam. Our experimental setup is schemed in Figure 3.2. The next section will expose the mathematical model of our method and will show the results of our numerical simulations.

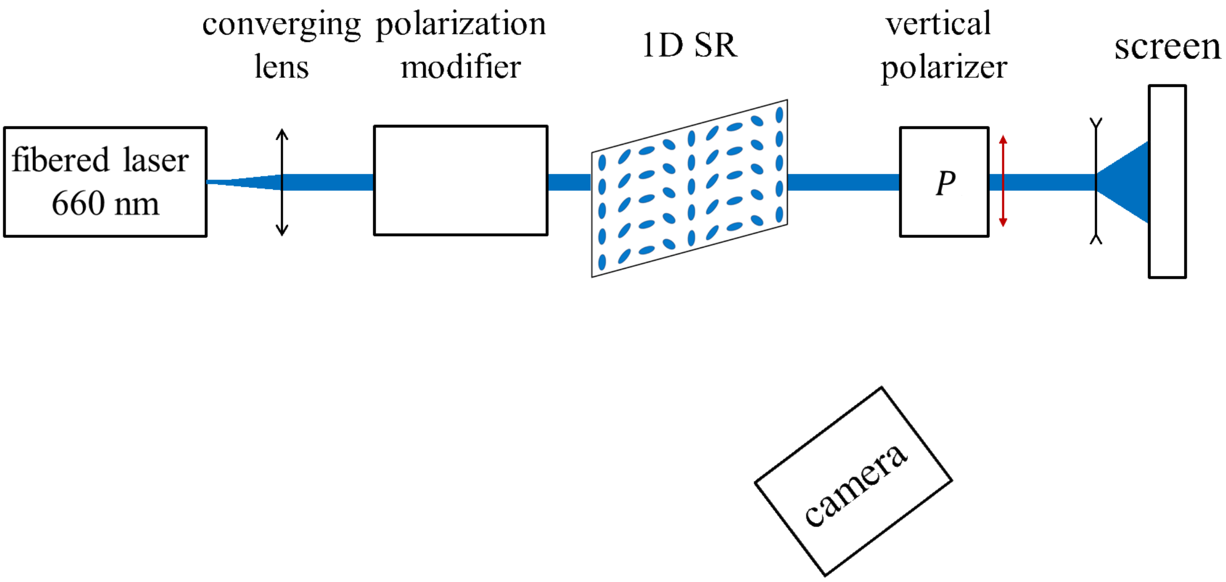

Figure 3.2: Picture of the experimental process, the polarization modifier enables the generation of several polarization states.

3.2 Simulating a mathematical model

3.2.1 Mathematical model

Firstly, concerning polarization measurement, instead of using the Jones formalism presented in the previous chapter, we will use the Stokes-Mueller formalism [16].
The incident beam is written as :

$$S_{in} = \begin{pmatrix} S_0 \\ S_1 \\ S_2 \\ S_3 \end{pmatrix}.$$

Our goal is to compute the S_i of the incident beam. A generic birefringent plate with an arbitrary orientation of its fast axis α and an arbitrary phase retard between the fast and slow axis ϕ is modeled as [16]

$$BP = \begin{pmatrix} 1 & 0 & 0 & 0 \\ 0 & 1-2\sin^2(2\alpha)\sin^2(\phi/2) & 2\cos(2\alpha)\sin(2\alpha)\sin^2(\phi/2) & -\sin(2\alpha)\sin(\phi) \\ 0 & 2\cos(2\alpha)\sin(2\alpha)\sin^2(\phi/2) & 1-2\cos^2(2\alpha)\sin^2(\phi/2) & \cos(2\alpha)\sin(\phi) \\ 0 & \sin(2\alpha)\sin(\phi) & -\cos(2\alpha)\sin(\phi) & \cos(\phi) \end{pmatrix}. \tag{3.1}$$

Our plate is a periodic SR ($\alpha = \pi x/p$) with a period of p[4]. The vertical polarizer P is represented by:

$$P = \frac{1}{2}\begin{pmatrix} 1 & 1 & 0 & 0 \\ -1 & 1 & 0 & 0 \\ 0 & 0 & 0 & 0 \\ 0 & 0 & 0 & 0 \end{pmatrix}.$$

After the linear polarizer, the transmitted beam is described by the following equation.

$$S_{out} = \begin{pmatrix} \frac{S_0}{2} - \frac{S_1}{2}\left(1-\sin^2(2\alpha)\sin^2\left(\frac{\phi}{2}\right)\right) - S_2\cos(2\alpha) sin(2\alpha)\sin^2\left(\frac{\phi}{2}\right) + \frac{S_3}{2}\sin(2\alpha)\sin(\phi) \\ -\frac{S_0}{2} + \frac{S_1}{2}\left(1-\sin^2(2\alpha)\sin^2\left(\frac{\phi}{2}\right)\right) + S_2\cos(2\alpha) sin(2\alpha)\sin^2\left(\frac{\phi}{2}\right) - \frac{S_3}{2}\sin(2\alpha)\sin(\phi) \\ 0 \\ 0 \end{pmatrix} \tag{3.2}$$

At the detector, the intensity $I = S_{out,0}$ is recorded and it is expressed by

$$I = \frac{S_0}{2} - \frac{S_1}{2}\left(\cos(4\alpha)\ \sin^2\left(\frac{\phi}{2}\right) + \cos^2\left(\frac{\phi}{2}\right)\right) - \frac{S_2}{2}\sin^2\left(\frac{\phi}{2}\right)\sin(4\alpha) + \frac{S_3}{2}\sin(2\alpha)\sin(\phi). \tag{3.3}$$

Measuring the variation of the intensity in the x direction allows to compute the Stokes parameters of the incident beam if the parameters of the retarder are known. For a completely polarized beam: $S_0^2 = S_1^2 + S_2^2 + S_3^2$. In the following, completely polarized beams are considered to reduce the number of Stokes parameters from 4 to 3.

---

[4] Indeed, $\alpha_1 = 225°$, $\alpha_2 = 405°$, $\alpha_3 = 585°$ are equivalent represent to an orientation of 45°". Therefore, the mathematical period of our retarder is $p/2$

3.2.2 Numerical simulations

We simulated a measurement process for a beam transmitted by the retarder and a linear polarizer.
Our measurement process consists into two steps The first one is a calibration process used to compute the retarder parameters p and ϕ. The second one is the measurement of the polarization of an unknown beam. Let us also remark that in reality, the first column of the retarder does not necessarily possess an horizontal fast axis, therefore another parameter must be added x_0 and α becomes $\alpha = \pi * (x + x_0)/d$. x_0 will define the orientation of the first pixel in the retarder.
We numerically simulated our method with several polarized beams and one 1D SR characterized by $p = 2048$ pixels, $\phi = 87°$ and 8 periods are contained in the retarder.

Calibration process

To determine the retarder's parameters, calibration measurements must be performed. The retarder will be exposed to beams with a well-known polarization state to compute p and ϕ while imposing the Stokes parameters. We use the horizontal, the vertical and the right circular polarizations.
The beams used for the calibration are the following ones

$$S_a = \begin{pmatrix} 1 \\ 1 \\ 0 \\ 0 \end{pmatrix}; S_b = \begin{pmatrix} 1 \\ -1 \\ 0 \\ 0 \end{pmatrix}; S_c = \begin{pmatrix} 1 \\ 0 \\ 0 \\ 1 \end{pmatrix}.$$

The intensities after the linear polarizer for the three calibration beams are pictured in Figure 3.3.

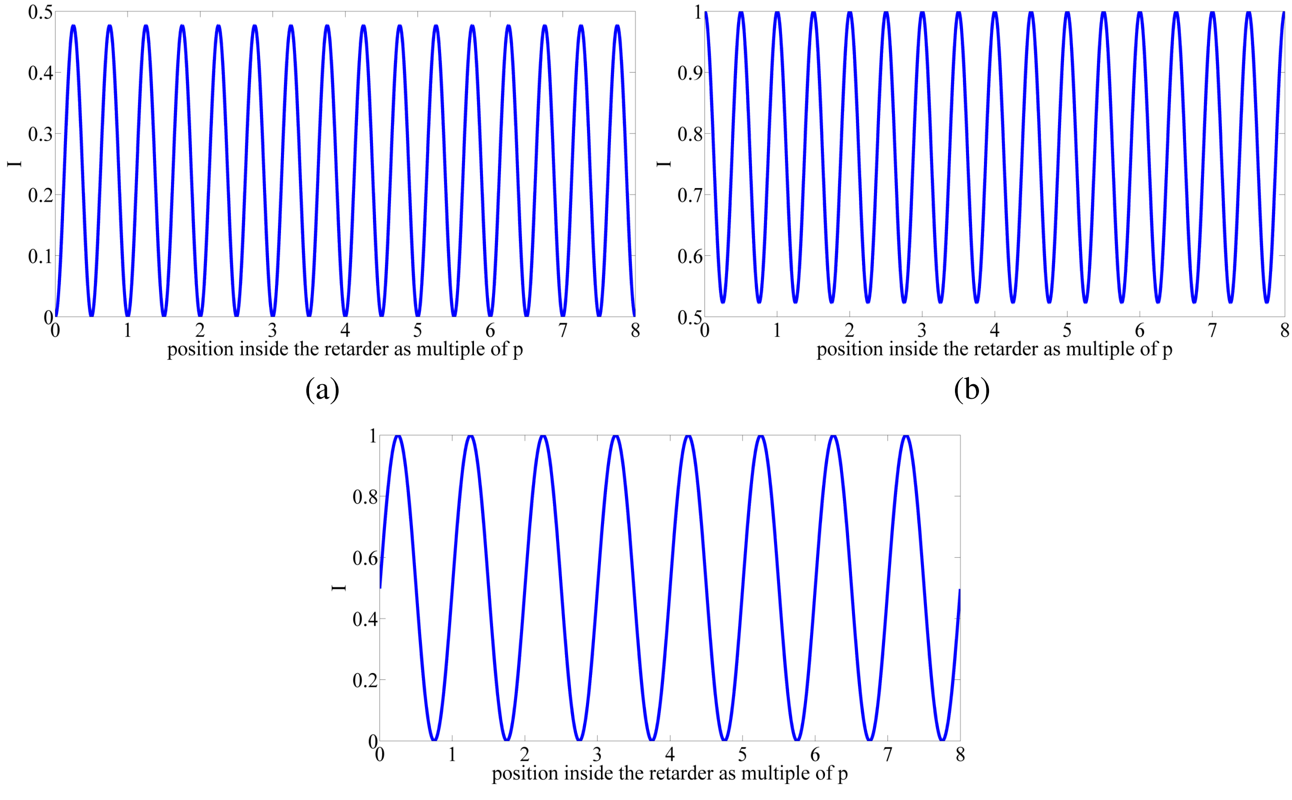

(a) (b)

(c)

Figure 3.3: Computed numerical intensity for the 3 calibrations beams, (a) horizontal polarization, (b) vertical polarization, (c) right handed polarization. For linearly polarized incident beams, the distance peak-to-peak is half of the period, for a circularly polarized incident beam this distance is equal to the period of the retarder.

For the first calibration beam, the Stokes parameters are imposed. The first guess of p is obtained by observation of the apparent period of the transmitted intensity variation and the first guess of ϕ is based on measurements performed by the polarimetric bench (see 2.2.2) of uniform retarders realized with the same spin-coating parameters. Several fits are computed for the first beam with a first guess of p as a multiple of the apparent period.

As an example, Figure 3.4 and Table 3.2 present the results of several fits for an incident horizontal beam where only the starting point of p is changed from one fit to another and the others parameters are summarized in Table 3.1.

Table 3.1: Values of the parameters for the calibration with an horizontally polarized beam

parameters	initial value	lower value	upper value
ϕ	85	-360	360
S_1	1	0.99	1.01
S_2	0	-0.01	0.01
S_3	0	-0.01	0.01
x_0	0.151	$-\infty$	∞

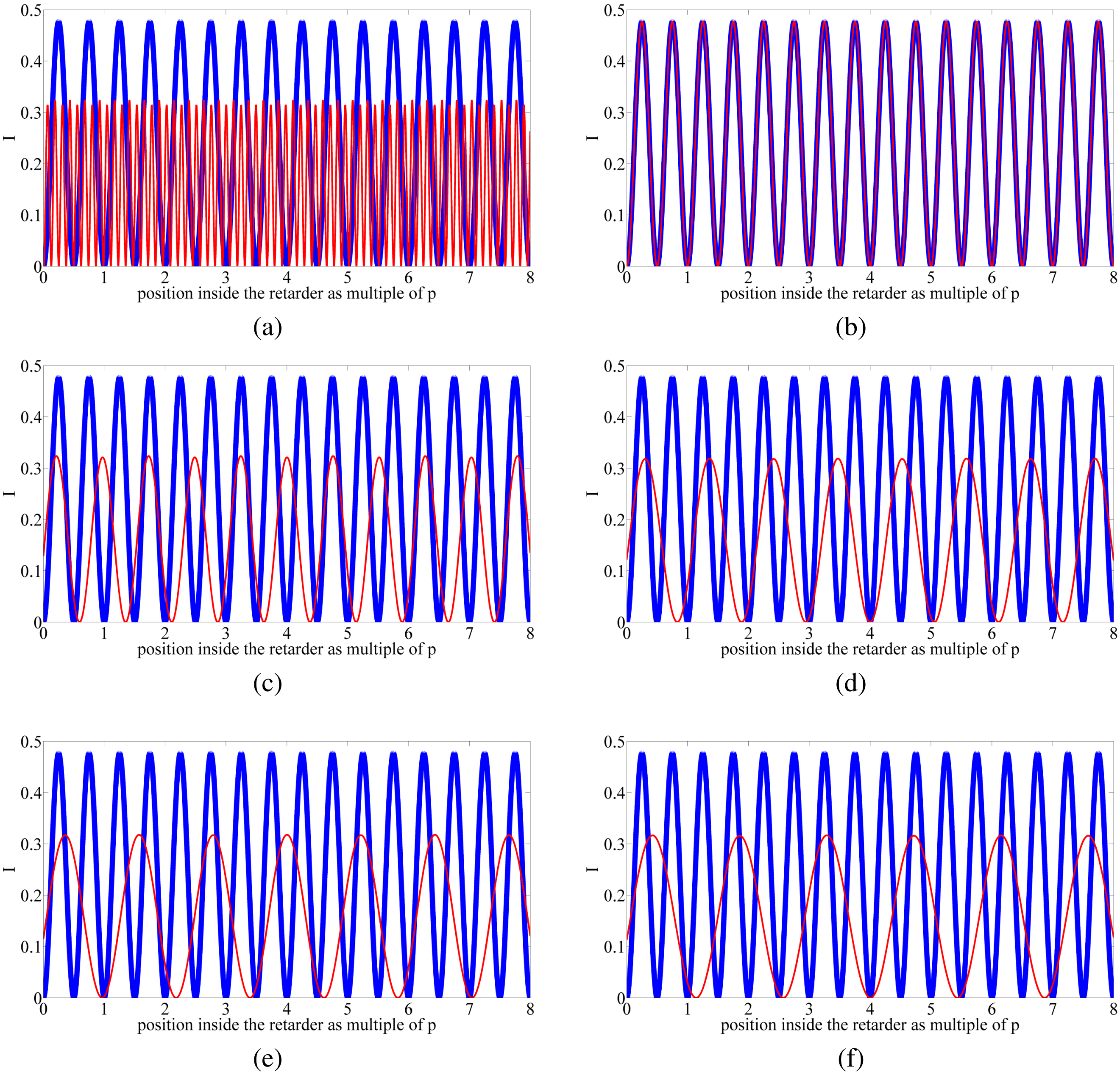

Figure 3.4: Representation of several fitted functions for the calibration intensity. The difference between the graphs is the initial value of the period :p_0. The input intensity is in blue while the fitted intensity is in red. (a) $p_0 = 1000$; (b) $p_0 = 2000$; (c) $p_0 = 3000$; (d) $p_0 = 4000$: (e) $p_0 = 5000$ and (f) $p_0 = 6000$. One can observe that only (b) with $p_0 = 2000$ achieves a good fit. Therefore, if the fit matches the input intensity, no error on the period is possible

Table 3.2: Results of the fits with different startpoint of p

	$p_0 = 1000$		$p_0 = 2000$	
parameters	value	95% confidence interval	val	95% confidence interval
p (pixels)	981.8	$[981.4; 982.3]$	2048	$[2048; 2048]$
ϕ (°)	69.35	$[68.69; 70.02]$	87.35	$[-152; 326.7]$
x_0	-117.2	[-121.7;-112.7]	-0.05122	$[-4.019; 3.916]$
	$p_0 = 3000$		$p_0 = 4000$	
parameters	value	95% confidence interval	val	95% confidence interval
p (pixels)	3101	$[3096; 3105]$	4325	$[4316; 4334]$
ϕ (°)	69.33	$[-1.7\,10^4; 1.7\,10^4]$	68.83	$[-1.4\,10^4; 1.4\,10^4]$
x_0	312.7	[-784.3;1410]	510.8	$[-790.3, 1812]$
	$p_0 = 5000$		$p_0 = 6000$	
parameters	value	95% confidence interval	val	95% confidence interval
p (pixels)	4982	$[4970; 4993]$	5868	$[5851; 5885]$
ϕ (°)	68.7	$[68.05; 69.34]$	68.56	$[-1.3\,10^4; 1.3\,10^4]$
x_0	465	[441.4;488.6]	543.18	$[-1030; 2116]$

The results obtained with $p_0 = 2000$ as the initial value are resumed in Table 3.3.

Table 3.3: Retarder's parameters obtained through the calibration process with $p = 2048$.

parameters	value	95% confidence interval
p	2048	$[2048; 2048]$
$\phi(°)$	87	$[86.95; 87.05]$
x_0	-1	$[-1; -0.9999]$

.

These results will be used for the two others configuration beams to check the values of the parameters.

Results of the numerical simulations

After the calibration, the beams with different polarization states will be computed. The goal is to fit the transmitted intensity with Equation 3.3 while, imposing the retarders parameters. The results of the simulations are presented in Table 3.4 and four plots of the numerical and computed intensities are presented in Figure 3.5.

Table 3.4: Results of the numerical simulations for several completely polarized beams

S_i	input	computed	95% confidence interval	input	computed	95% confidence interval
S_1	0	$4.43\,10^{-11}$	$[-5.92\,10^{-8};\ 5.94\,10^{-8}]$			
S_2	0	$3.10\,10^{-11}$	$[-3.70\,10^{-7};\ -2.50\,10^{-7}]$			
S_3	−1	−1	[−1; −1]			
S_1	0	−0.0005	[−0.0006; −0.0005]	0	0, 0011	[0.008; 0.0013]
S_2	1	0.9997	[0.9997; 0.9997]	−1	−1.001	[−1, 001; −1]
S_3	0	$-3.6\,10^{-10}$	$[-5.5\,10^{-10};\ -1.7\,10^{-10}]$	0	$-3.8\,10^{-9}$	$[-5.9\,10^{-9};\ -1.7\,10^{-9}]$
S_1	1	0.9981	[0.996; 0.9999]	1	1.1017	[1.1017; 1.1017]
S_2	1	0.9998	[0.9996; 1]	−1	−1.002	[−1.002; −1.002]
S_3	0	$-5.54\,10^{-5}$	$[-8.18\,10^{-5};\ -2.91\,10^{-5}]$	0	$-2.62\,10^{-10}$	$[-5.39\,10^{-10};\ 1.45\,10^{-11}]$
S_1	−1	−0.999	[−0.999; −0.999]	1	−0.9976	[−0.9976; −0.9976]
S_2	1	1.002	[1.002; 1.002]	−1	−1.004	[−1.004; −1.004]
S_3	0	$-2.62\,10^{-10}$	$[-3.39\,10^{-10};\ 1.45\,10^{-11}]$	0	$-1.86\,10^{-11}$	$[2.86\,10^{-11};\ -9.6\,10^{-12}]$
S_1	0	$5.69\,10^{-7}$	$[-5.89\,10^{-7};\ -5.45\,10^{-7}]$	0	$-3.72\,10^{-7}$	$[-3.85\,10^{-7};\ -3.59\,10^{-7}]$
S_2	1	1	[1; 1]	1	1	[1; 1]
S_3	1	1	[1; 1]	−1	−1	[−1; −1]
S_1	0	$-3.5\,10^{-8}$	$[-3.6\,10^{-8};\ -3.3\,10^{-8}]$	0	$1.1\,10^{-6}$	$[1.07\,10^{-6};\ -1.1510^{-6}]$
S_2	−1	−1	[−1; −1]	−1	−1	[−1; −1]
S_3	1	1	[1; 1]	−1	−1	[−1; −1]
S_1	1	1	[1; 1]	1	1	[1; 1]
S_2	0	$2.30\,10^{-10}$	$[2.07\,10^{-10};\ 2.52\,10^{-10}]$	0	$5.46\,10^{-9}$	$[5.12\,10^{-9};\ 5.78\,10^{-9}]$
S_3	1	1	[1; 1]	−1	−1	[−1; −1]
S_1	−1	−1	[−1; −1]	−1	−1	[−1; −1]
S_2	0	$-3.54\,10^{-7}$	$[-3.68\,10^{-7};\ -3.40\,10^{-7}]$	0	$1.80\,10^{-12}$	$[-6.10\,10^{-10};\ -6.13\,10^{-10}]$
S_3	1	1	[1; 1]	−1	−1	[−1; −1]
S_1	1	1	[1; 1]	1	1	[1; 1]
S_2	1	1	[1; 1]	1	1	[1; 1]
S_3	1	1	[1; 1]	−1	−1	[−1; −1]
S_1	1	1	[1; 1]	1	1	[1; −1]
S_2	−1	−1	[−1; −1]	−1	−1	[−1; −1]
S_3	1	1	[1; 1]	−1	−1	[1−; −1]
S_1	−1	1	[−1; , 1]	−1	−1	[−1; −1]
S_2	1	1	[1; 1]	1	1	[1; 1]
S_3	1	1	[1; 1]	−1	−1	[1−; −1]
S_1	−1	−1	[−1; −1]	−1	−1	[−1; −1]
S_2	−1	−1	[−1; −1]	−1	−1	[−1; −1]
S_3	1	1	[1; 1]	−1	−1	[−1; −1]
S_1	1	1	[1; 1]	2	2	[2; 2]
S_2	2	2	[2; 2]	−1	−1	[−1; −1]
S_3	3	3	[3; 3]	1	1	[1; 1]
S_1	−0.7	−0.7	[−0.7; −0.7]	−15	−15	[15; 15]
S_2	1.3	1.3	[1.3; 1.3]	−0.25	−0.25	[−0.25; −0.25]
S_3	−2	−2	[−2; −2]	5	5	[−5; −5]

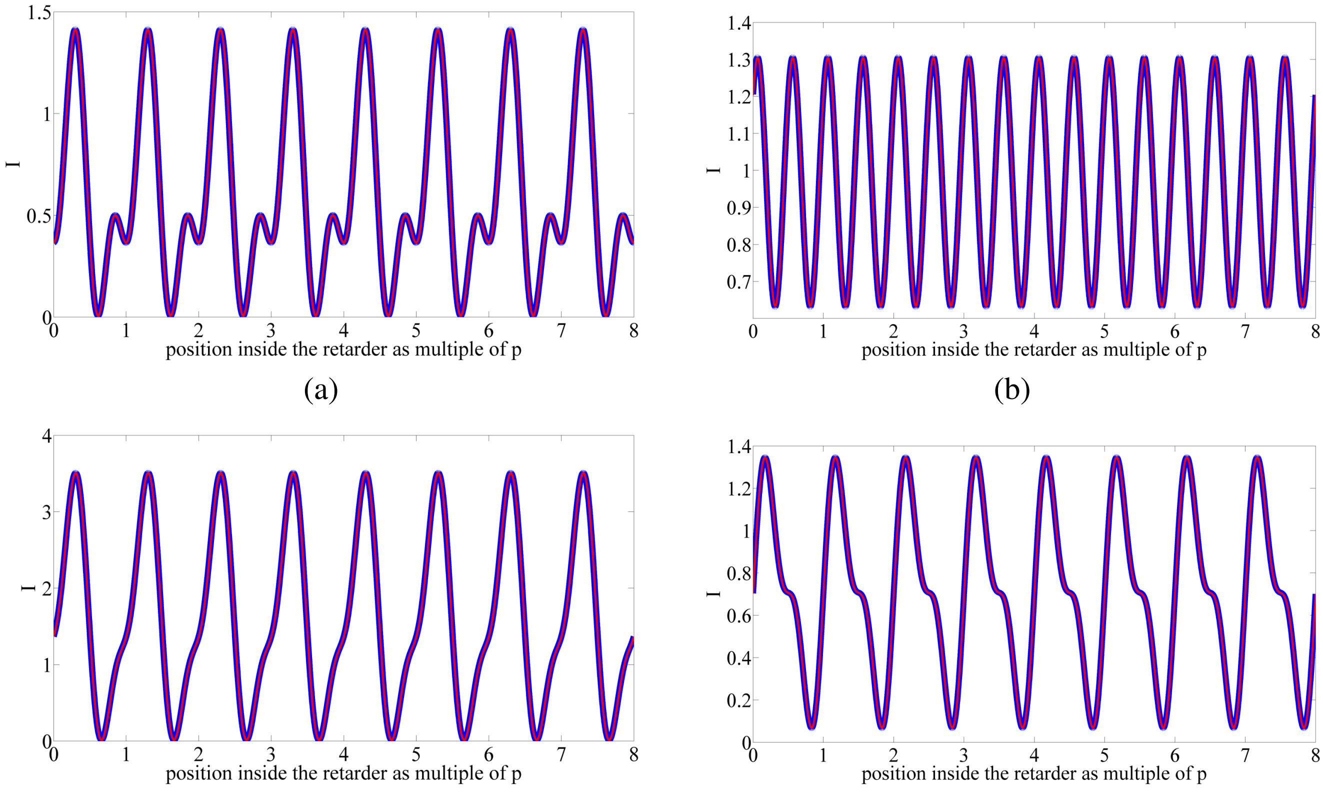

(a) (b) (c) (d)

Figure 3.5: Plots of input intensity (in blue) and fitted intensity (in red) for four completely polarized beam. (a) $S_{in} = (1\ 1\ 1)$, (b) $S_{in} = (-1\ -1\ 0)$, (c) $S_{in} = (1\ 2\ 3)$, (d) $S_{in} = (0\ -1\ 1)$

Conclusions of the numerical part

As we can observe, the computed parameters are the same as the introduced one and the fitted intensities are also extremely close to the computed ones. Thanks to those promising results, we can assume that our method computes the Stokes parameters for the ideal case: a retarder with an uniform phase retard ϕ and a perfect sampling of the intensity variation. In the following section, we will detail the experimental aspects of the method: the recording of the retarder, the measurement process and the analysis of the results.

3.3 Experimental process

3.3.1 Recording

To obtain the expected variation of the fast axis orientation, the recording setup of the first layer is modified compared to the case of a uniform retarder while the recording of the second layer stays the same. To achieve the recording of the superimposition of two circularly polarized beams of opposite handedness, several elements are added on the experimetal setup (see Figure 3.6) such as:

- a quarter-wave plate,
- a Savart plate [17, 18],
- a quarter-wave plate.

The Savart plate is a pair of identical birefringent crystals where the fast axis forms an angle of 45° with the normal of the crystals and the axis is rotated of 90° from one crystal to the other one. The utility of the Savart plate is to divide one incident polarized beam into two linearly orhtogonally polarized beams. Assuming an incident beam uniformly polarized under normal incidence, the emerging beams are also at normal incidence with respect to the Savart plate and there is no phase difference between them.
The goal of the first quarter-wave plate is to generate an incident circularly polarized beam on the Savart plate to obtain two orthogonally polarized beams with the same intensity exiting the Savart plate. Finally, the second quarter-wave plate will circularize the incident beams to record the superimposition of two circularly polarized beams of same intensity and opposite handedness.

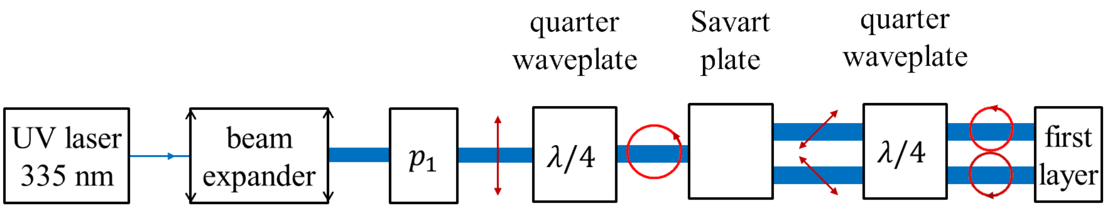

Figure 3.6: Scheme of the recording setup for the polarization analyzer, beams are pictured in blue and the polarization in red.

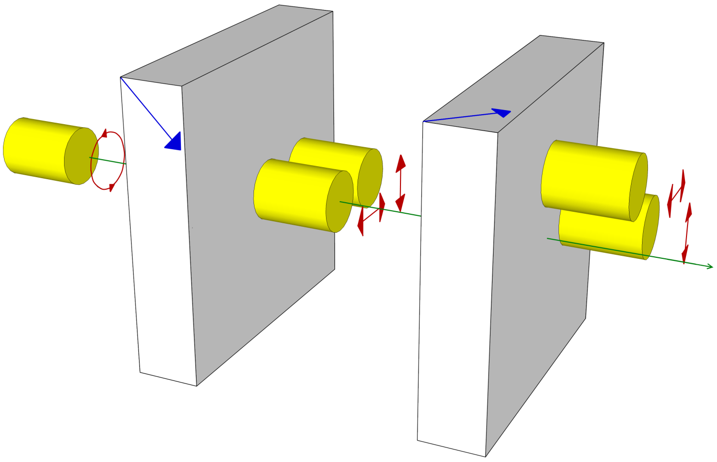

Figure 3.7: Scheme of a decemented Savart plate, the fast axis of the crystals are pictured in blue, the polarization in red and the direction of propagation in green.

A picture of the retarder is exposed in Figure 3.8
Between two polarizers, the transmitted intensity exhibits the predicted variation according to the theory. The color variation for the white source are linked to the variation of the phase shift ϕ induced by the retarder which is dependent of the incident wavelength.

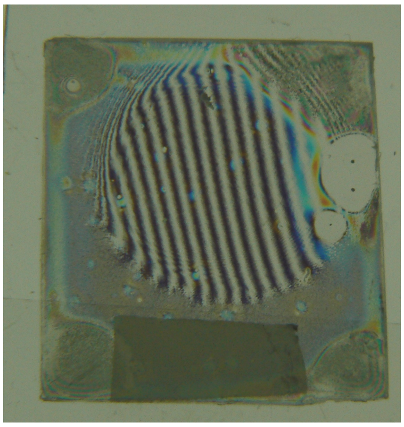

Figure 3.8: Picture of the retarder between two linear polarizers.

3.3.2 Measuring

Our experimental setup contained:

- a red laser at 633 nm L,
- two converging lenses to expand and collimate the beam l_1, l_2,
- a linear polarizer and a quarter-wave plate with an angle of 45° between their fast axes P_1, $\lambda/4$,
- a linear polarizer on a rotation mount which will be turned to achieve several linearly polarized beams with different orientation of their polarization P_2,
- the retarder S,
- a linear polarizer with its transmission axis aligned on the vertical P_3
- a screen and a camera.

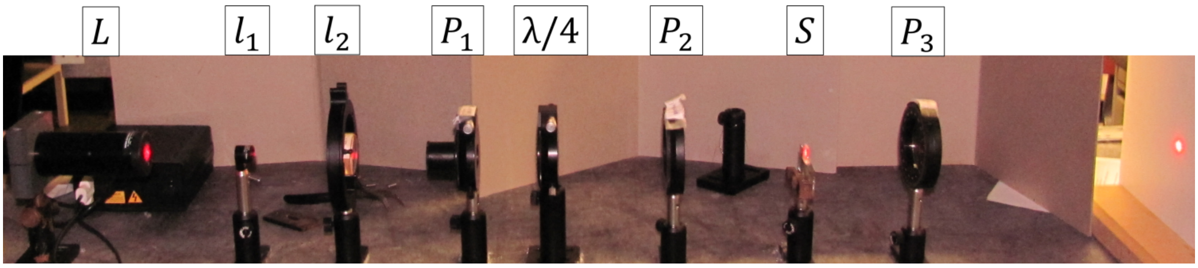

Figure 3.9: Picture of the retarder between two linear polarizers

Our experimental process can be sum up in 7 points:

1. computation of the normalized intensity for all pictures,
2. determination of the orientation of the lines of same intensity (ζ) using one picture,
3. rotation of the pictures to obtain vertical lines of same intensity,
4. determination of the area of interest using one picture,
5. selection of the area of interest and meaning of the lines inside this area for every pictures,
6. determination of the retarder's parameters with the pictures correspoding to the calibration beams,
7. computation of the Stokes for the measuring pictures.

1. Computation of the normalized intensity

To measure the polarization state of a beam, videos are recorded for three different configurations (see Figure 3.10) :

- one with the whole setup (see Figure 3.2) ⇒ Im,
- one without the last linear polarizer ⇒ Ref,
- one with the laser turned off ⇒ D.

Next, pictures are extracted from the videos and the mean transmitted intensity is computed (see Figure 3.10).

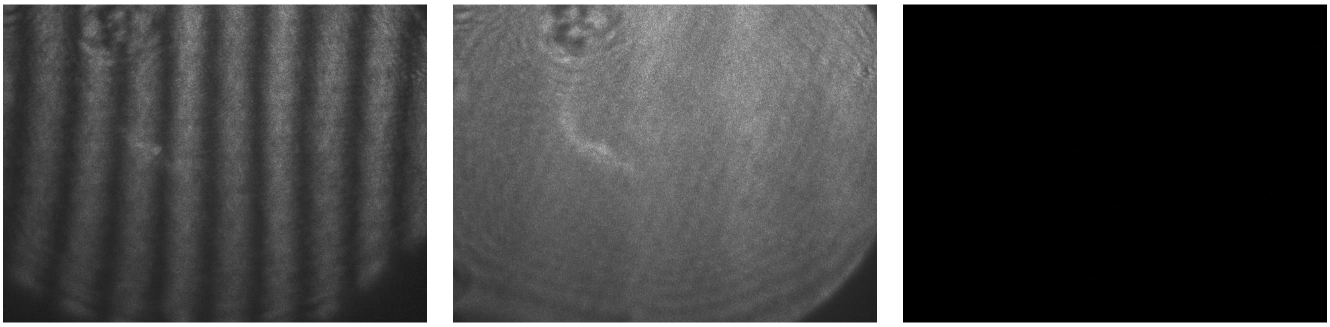

(a) (b) (c)

Figure 3.10: Pictures of the transmitted intensity for −45°, (a) is Im, (b) is Ref and (c) is D.

Then a normalized image is computed $Norm = \dfrac{Im - D}{Ref - D}$ to reduce the effect of intensity variation due to optical aberrations independent of polarization (see Figure 3.11).

We can observe that the pictures are very similar. The transmitted intensity exhibits the expected periodic variation for the real retarder.

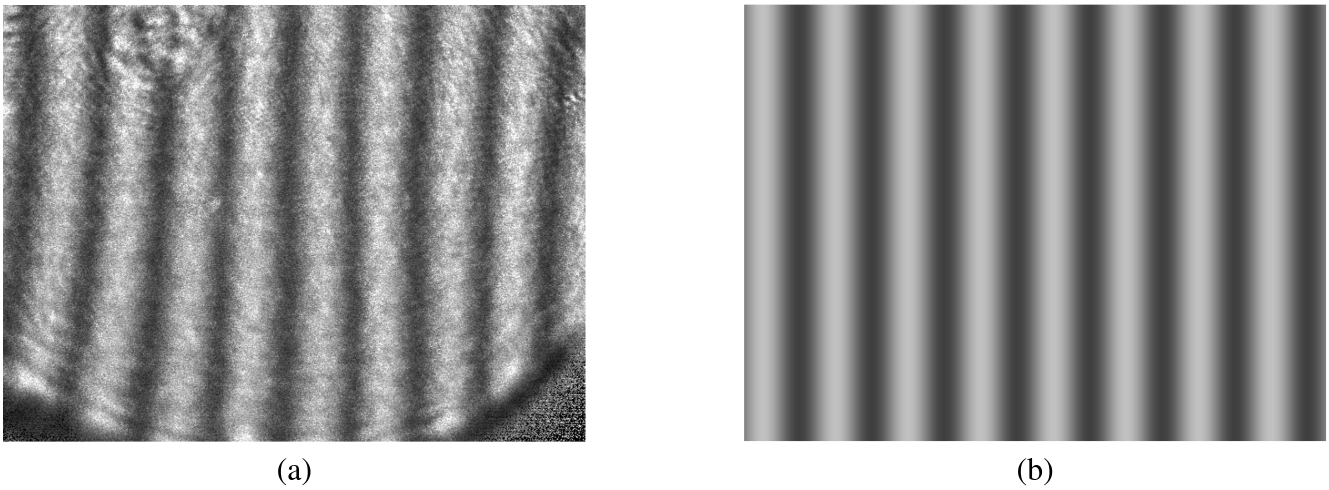
(a) (b)

Figure 3.11: (a) Picture of the normalized intensity for an angle −45° (b) numerical map of the transmitted intensity for an ideal birefringent plate with the same characteristics.

2&3. Determination of ζ and rotation of the pictures

Since the orientation of the intensity variation depends on the direction of the fast axis variation, experimentally the areas of same intensity could be tilted with respect to the horizontal (Figure 3.12 (a)). Therefore the computation of this angle and the rotation of the pictures are mandatory to achieve vertical lines of uniform orientation. Using the Hough transform [19, 20], the angle is computed and the pictures are rotated using MATLAB© (Figure 3.12 (b)).

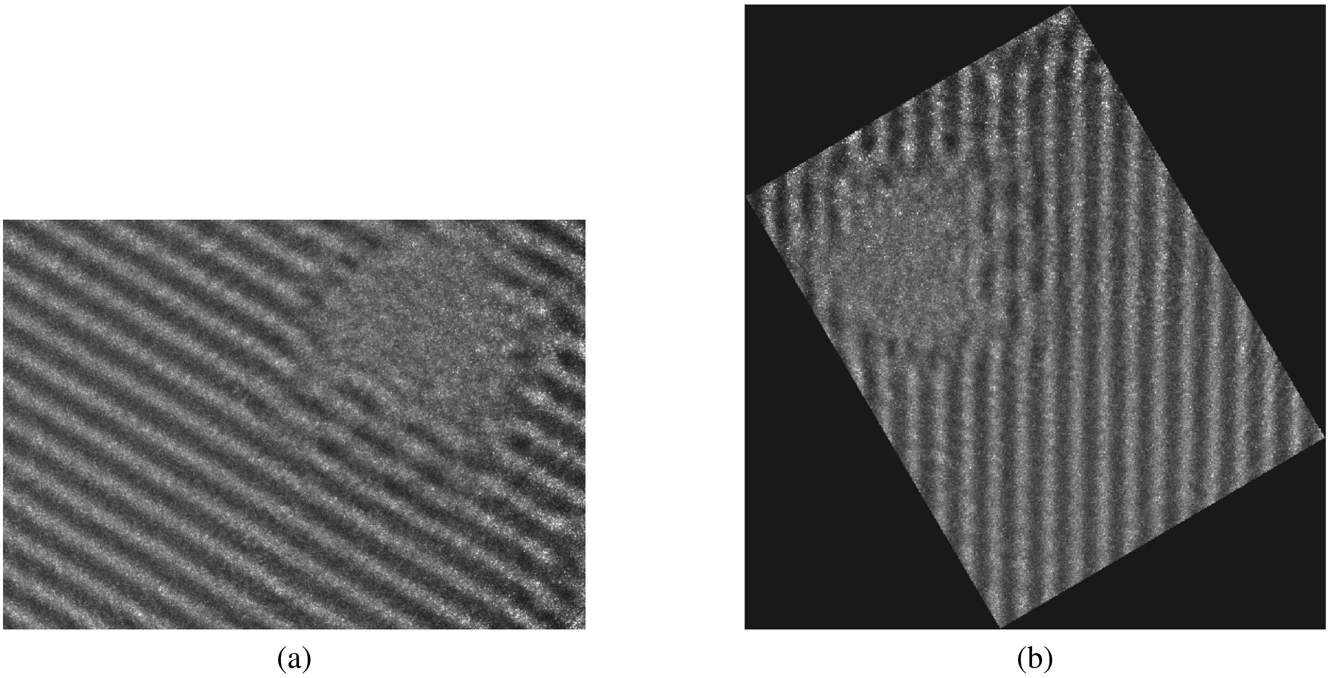
(a) (b)

Figure 3.12: (a) Picture of the transmitted intensity, the areas of same intensity are not vertical due to the orientation of the retarder (b) rotated picture with the angle computed using the Hough transform.

4&5. Determination of the area of interest and computation of the mean line

After the rotation of the pictures, an area of interest is selected (see Figure 3.13) based on several criteria.

- The area must contain several periods of variation of the intensity.
- The area must be near the retarder center to avoid important variations of ϕ.
- The area must avoid diffraction patterns due to dust or oxidation on the retarder.

Then a mean is performed on the line of the picture to compute the mean intensity which will be fitted afterwards.

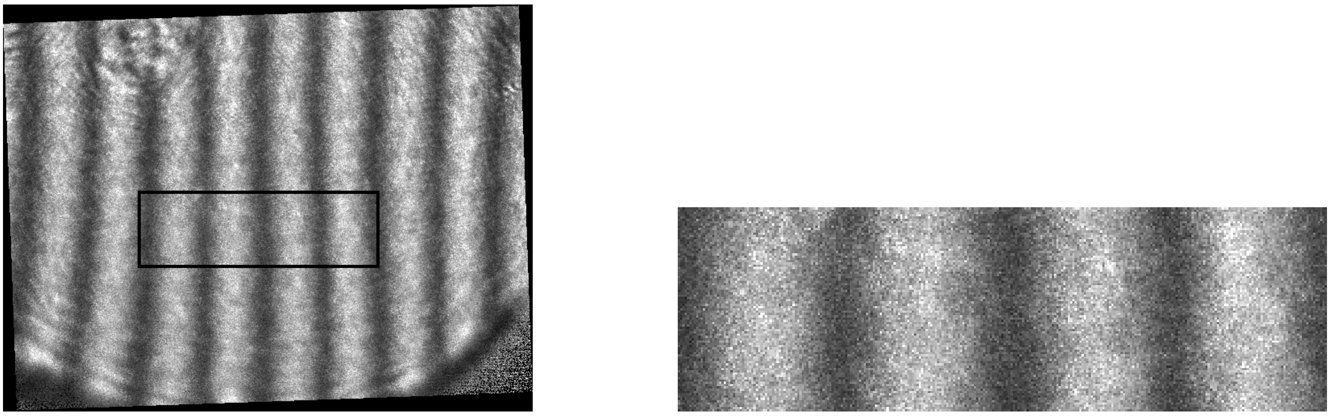
(a) (b)

Figure 3.13: (a) Picture of the rotated intensity and the selection of the region of interest. (b) Region of interest where the mean intensity per column will be computed.

6. Determination of the retarder' parameters

The mean intensity for the vertical and horizontal polarization are used for the calibration. The transmitted intensity will be fitted by equation 3.4 while imposing the values of the Stokes parameters to find the values of the retarder's parameters (ϕ, d, x_0) and the parameters due to the recording (A, off). A represents the gain of the camera and off stands for the offset.

$$A\left\{\sqrt{S_1^2+S_2^2+S_3^2}-S_1\left[\cos\left(\frac{4\pi*(x+x_0)}{d}\right)\sin^2\left(\frac{\phi}{2}\right)+\cos^2\left(\frac{\phi}{2}\right)\right]\right.$$
$$\left.-S_2\sin\left(\frac{4\pi(x+x_0)}{d}\right)\sin^2\left(\frac{\phi}{2}\right)+S_3\sin\left(\frac{2\pi(x+x_0)}{d}\right)\sin(\phi)\right\}+off \quad (3.4)$$

Figure 3.14 presents the results of the calibration process.

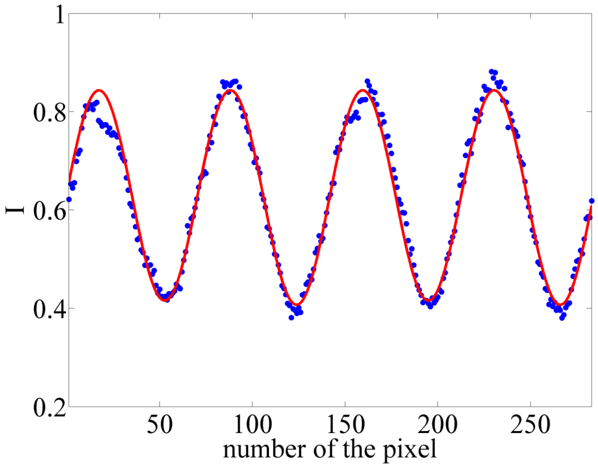

(a)

parameters	value	95% confidence interval
A	0.43	[0.41; 0.44]
d	142.2	[141.5; 143]
off	0	[0; 0.05]
ϕ	91.43°	[90.5; 92.5]
x_0	53.88	[53; 54.5]

(b)

Figure 3.14: Results for the calibration using the horizontally polarized beams. (a) Represents the calibration fit of the transmitted intensity for an incident vertically polarized beam, the blue dots represent the experimental intensity, the red line the computed intensity with the parameters. (b) Values of the retarder and camera parameters obtained thanks to the calibration process.

These parameters will be imposed with the other beam to compute the Stokes parameters.

7. Computation of the Stokes parameters for the measured beams

Finally, while imposing the parameters of the retarder and the camera, the mean transmitted intensity will be fitted to compute the Stokes parameters of the incident beam. Several linearly polarized beams were measured. To change the polarization state from one beam to another, the polarizer was rotated. The experimental results are summarized in Table 3.5 and Figure 3.15 presents fits for two beams.

Table 3.5: Experimetal results of the polarization analyzer. α is the orientation of the polarization, the S_{norm} column represents the Stokes parameters when for a beam with $S_0 = 1$ and RMSE is the value of the Root Mean Square Error obtained using the curve fitting tool of MATLAB©.

$\alpha(°)$	S_{in}	$S_{computed}$	confidence interval	S_{norm}	RMSE
−67.5	$\begin{pmatrix}-\sqrt{2}/2\\-\sqrt{2}/2\\0\end{pmatrix}$	$\begin{pmatrix}-0.68\\-0.71\\-0.05\end{pmatrix}$	[−0.80; −0.55] [−0.81; −0.61] [−0.12; −0.06]	$\begin{pmatrix}-0.69\\-0.72\\-0.05\end{pmatrix}$	0.02
−45	$\begin{pmatrix}0\\-1\\0\end{pmatrix}$	$\begin{pmatrix}-0.11\\-1\\-0.03\end{pmatrix}$	[−0.15; −0.08] [−1.02; −0.98] [−0.05; −0.01]	$\begin{pmatrix}-0.11\\-0.99\\-0.03\end{pmatrix}$	0.05
−22.5	$\begin{pmatrix}\sqrt{2}/2\\-\sqrt{2}/2\\0\end{pmatrix}$	$\begin{pmatrix}0.94\\-1\\0.00\end{pmatrix}$	[0.88; 1.01] [−1.03; −0.97] [−0.04; 0.04]	$\begin{pmatrix}-0.69\\0.73\\0\end{pmatrix}$	0.09
22.5	$\begin{pmatrix}\sqrt{2}/2\\\sqrt{2}/2\\0\end{pmatrix}$	$\begin{pmatrix}0.98\\1.01\\0.05\end{pmatrix}$	[0.90; 1.07] [1; 1.02] [−0.06; 0.07]	$\begin{pmatrix}0.7\\0.72\\0.03\end{pmatrix}$	0.02
45	$\begin{pmatrix}0\\1\\0\end{pmatrix}$	$\begin{pmatrix}-0.15\\1.01\\0.05\end{pmatrix}$	[−0.17; −0. − 0.11] [1; 1.02] [0.02; 0.08]	$\begin{pmatrix}-0.14\\0.97\\0.05\end{pmatrix}$	0.07
67.5	$\begin{pmatrix}-\sqrt{2}/2\\\sqrt{2}/2\\0\end{pmatrix}$	$\begin{pmatrix}-0.65\\0.83\\0.02\end{pmatrix}$	[−0.73; −0.52] [0.6; 1.02] [−0.05; 0.05]	$\begin{pmatrix}-0.62\\0.79\\0.02\end{pmatrix}$	0.02

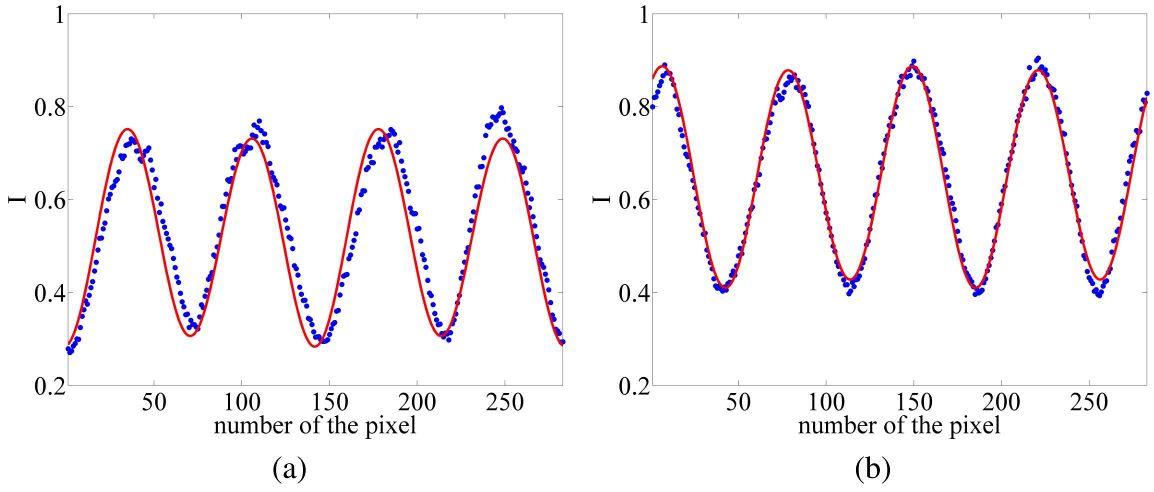

(a) (b)

Figure 3.15: Fits of the transmitted intensity for two different linearly polarized beams, the blue dots represent the experimetal intensities, the red line the computed intensities with the parameters. (a) Is for a −45° polarized beam with the horizontal. (b) Pictures a beam with a polarization at 67.5° with the horizontal.

3.3.3 Results analysis

As we can observe, our method does not perfectly compute the Stokes parameters. The computed parameters are different from the real ones but the general orientation of the polarization is respected. The major difference between the Stokes parameters is obtained for the orientation of 45°, where the polarization can be viewed as a nearly linear polarization at 49°. Several origins are possible for the error on the computed Stokes parameters.

- A variation of the phase retard inside the retarder:
  The phase retard induced by the retarder between the components of the polarized light may present variations. Due to the spin-coating process, the thickness of the birefringent layer may vary, altering the phase retard: $\phi \neq c^{ste} \Rightarrow \phi = \phi(x, y)$ while ϕ is considered a constant during the calibration and computation processes.
- The speckle phenomenon:
  Since we project the intensity on a screen, the speckle phenomenon occurs [16, 21]. It induces another variation of the intensity which may lead to errors on the determination of the angle of orientation of same intensity lines and on the computed parameters.
- Several optical defaults:
  As we can see in Figure 3.11, our system is not free from optical defaults. Our pictures present circular and diffraction patterns due to small misalignment of the lenses and dust particles present on the LCP layer of the retarder. The variation of intensity and the reduction of the small usable area of the retarder may reduce the accuracy of the computation.
- Error on the angle of lines of same intensity:
  During the numerical treatment, the Hough transform is used to compute the orientation of the lines of same intensity. However, in several cases the computation of the angle leads to several angles contained in an interval about 2°. This error may cause a mixing of different regions when the mean intensity is computed reducing the accuracy of the parameters computation. Moreover, the rotation of the image performed with MATLAB©uses an interpolation algorithm to compute the rotated image which may cause some loss of information.
- Sampling problem:
  Another possible source of error is the sampling. Our pictures only contain a small number of periods and a small number of pixels per period. The sampling conditions could lead to a poor computation of the Stokes parameters.

To determine the effect of the errors, several simulations were made. To simulate the effect of a ϕ variation, two parabolic profiles were computed with a maximum variation of 3 and 9° (see Figure 3.16 (a) & (b)). A speckle intensity was computed and multiplied to the perfect case intensity (Figure 3.16 (c)). An intensity map was also computed for an error of 1° on ζ and the mean line was computed (Figure 3.16 (d)). Finally an intensity map with a reduced number of periods and pixels per periods was also computed.

Table 3.6: Results for several error sources.

S_{in}	$S_{\Delta\phi=3°}$	$S_{\Delta\phi=9°}$	S_{speck}	$S_{\Delta\zeta=1°}$	S_{samp}
$\begin{pmatrix} -\sqrt{2}/2 \\ -\sqrt{2}/2 \\ 0 \end{pmatrix}$	$\begin{pmatrix} -0.694 \\ -0.720 \\ 1.56\,10^{-4} \end{pmatrix}$	$\begin{pmatrix} -0.60 \\ -0.80 \\ 4.34\,10^{-4} \end{pmatrix}$	$\begin{pmatrix} -0.81 \\ -0.60 \\ 1.74\,10^{-3} \end{pmatrix}$	$\begin{pmatrix} -0.71 \\ -0.71 \\ -6.32\,10^{-8} \end{pmatrix}$	$\begin{pmatrix} -0.68 \\ -0.74 \\ -1.18\,10^{-7} \end{pmatrix}$
$\begin{pmatrix} 0 \\ -1 \\ 0 \end{pmatrix}$	$\begin{pmatrix} 3.13\,10^{-3} \\ -1.00 \\ 1.82\,10^{-4} \end{pmatrix}$	$\begin{pmatrix} 0.02 \\ -1.00 \\ 5.24\,10^{-4} \end{pmatrix}$	$\begin{pmatrix} -0.06 \\ -1.00 \\ 3.91\,10^{-4} \end{pmatrix}$	$\begin{pmatrix} -5.56\,10^{-3} \\ -1.00 \\ 2.33\,10^{-7} \end{pmatrix}$	$\begin{pmatrix} -1.81\,10^{-3} \\ -1.00 \\ -8..47\,10^{-8} \end{pmatrix}$
$\begin{pmatrix} \sqrt{2}/2 \\ -\sqrt{2}/2 \\ 0 \end{pmatrix}$	$\begin{pmatrix} 0.71 \\ -0.71 \\ 1.41\,10^{-3} \end{pmatrix}$	$\begin{pmatrix} 0.71 \\ -0.71 \\ 4\,10^{-3} \end{pmatrix}$	$\begin{pmatrix} 0.70 \\ -0.71 \\ 6.88\,10^{-4} \end{pmatrix}$	$\begin{pmatrix} 0.82 \\ 0.57 \\ -9.24\,10^{-5} \end{pmatrix}$	$\begin{pmatrix} 0.71 \\ -0.70 \\ -2.9\,10^{-8} \end{pmatrix}$
$\begin{pmatrix} \sqrt{2}/2 \\ \sqrt{2}/2 \\ 0 \end{pmatrix}$	$\begin{pmatrix} 0.71 \\ 0.71 \\ -1.56\,10^{-3} \end{pmatrix}$	$\begin{pmatrix} 0.71 \\ 0.71 \\ -4\,10^{-4} \end{pmatrix}$	$\begin{pmatrix} 0.72 \\ 0.70 \\ 2.23\,10^{-3} \end{pmatrix}$	$\begin{pmatrix} 0.70 \\ 0.72 \\ 6.48\,10^{-8} \end{pmatrix}$	$\begin{pmatrix} 0.71 \\ 0.71 \\ -2.05\,10^{-7} \end{pmatrix}$
$\begin{pmatrix} 0 \\ 1 \\ 0 \end{pmatrix}$	$\begin{pmatrix} 1.78\,10^{-3} \\ 1.00 \\ -1.80 \end{pmatrix}$	$\begin{pmatrix} 0.02 \\ 1.00 \\ -5\,10^{-4} \end{pmatrix}$	$\begin{pmatrix} 0.07 \\ 1.00 \\ 2.32\,10^{3} \end{pmatrix}$	$\begin{pmatrix} -5.97\,10^{3} \\ 1.00 \\ -2.33\,10^{-7} \end{pmatrix}$	$\begin{pmatrix} -5.42\,10^{-3} \\ 1.00 \\ -7.08\,10^{-9} \end{pmatrix}$
$\begin{pmatrix} -\sqrt{2}/2 \\ \sqrt{2}/2 \\ 0 \end{pmatrix}$	$\begin{pmatrix} -0.70 \\ 0.71 \\ 1.41\,10^{-3} \end{pmatrix}$	$\begin{pmatrix} -0.69 \\ 0.73 \\ 4.07\,10^{4} \end{pmatrix}$	$\begin{pmatrix} -0.61 \\ 0.80 \\ 2.63\,10^{-3} \end{pmatrix}$	$\begin{pmatrix} -0.71 \\ 0.71 \\ -0.07\,10^{-7} \end{pmatrix}$	$\begin{pmatrix} -0.71 \\ 0.71 \\ -1.32\,10^{-9} \end{pmatrix}$

One can observe that the polarization states are not affected the same way by the errors. Three cases are not much affected ($S_{in} = (0\ -1\ 0)$, $S_{in} = \sqrt{2}/2\ \sqrt{2}/2\ 0)$ and $S_{in} = (0\ 1\ 0)$) while the others present significant errors. For these cases, the major contributions are the variation of the phase of 9°, the presence of the speckle and the error on ζ. Therefore, a reduction of these error sources could lead to better results.

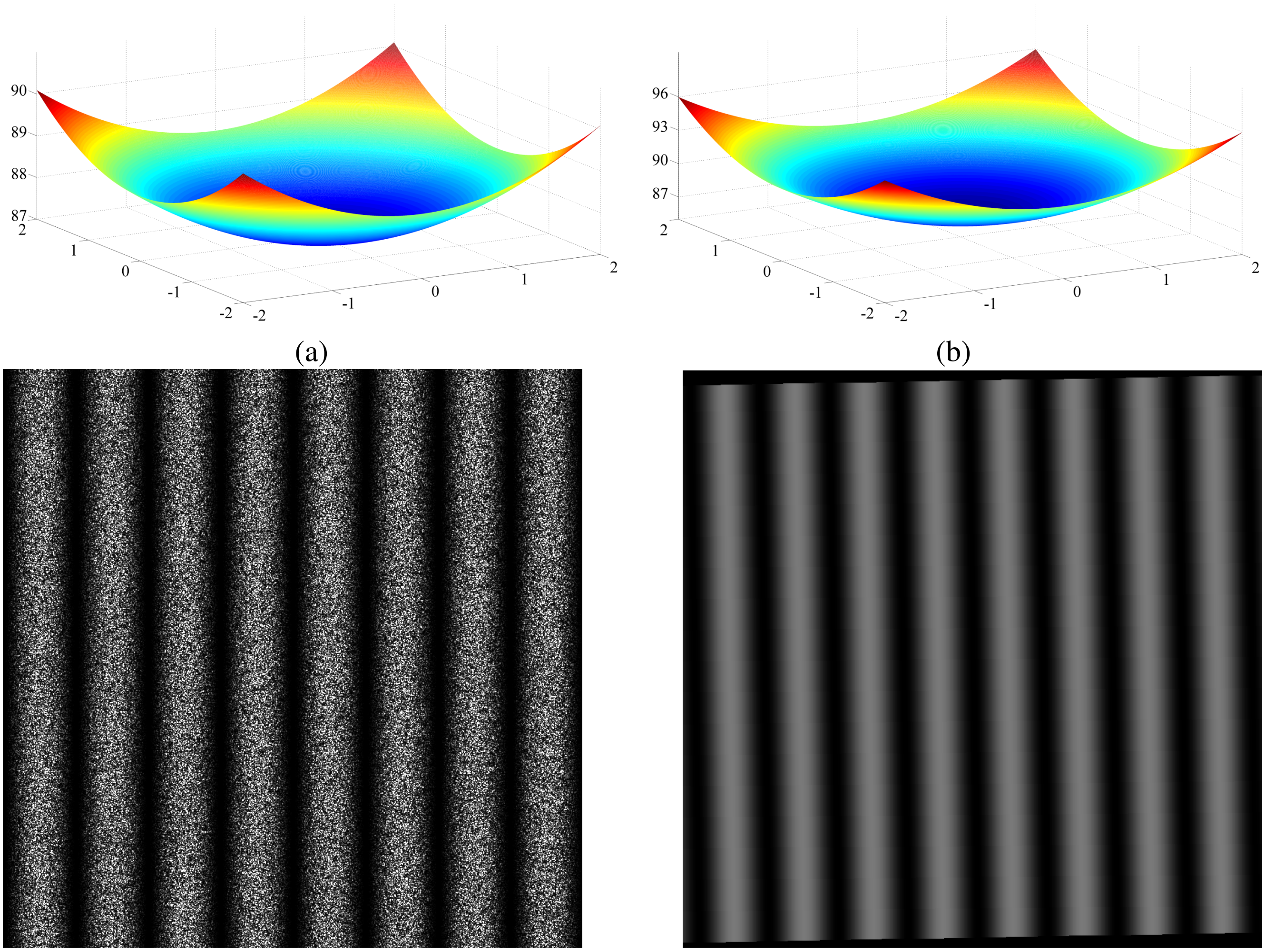

(a) (b)

(c) (d)

Figure 3.16: Presentation of the several error sources. (a) & (b) Represent the variation of ϕ inside the retarder, as a function of the position in the retarder as a multiple of the period. (a) Stands for a maximum variation of 3° and (b) for 9° with a base value of 87°. (c) Represents an example of the intensity when speckle is also computed. (d) Depicts the intensity where the area of interest will be selected with an error on ζ.

3.4 Conclusions and perspectives

3.4.1 Conclusions

In this chapter, we presented an original polarization analysis method using a 1D continuous SR. Thanks to the superimposition of two circularly polarized beams of opposite handedness, we are able to record a retarder with a continuous and periodical variation of its fast axis. The variation of the fast axis will transform an incident uniformly polarized beam into a space-variant one. This variation will be used to compute the Stokes parameters of the incident beam thanks to a linear polarizer and a recording camera. We presented the mathematical model of the measuring process and several numerical simulations with completely polarized beams. We also described the experimental steps: the recording and the measuring processes. The computed parameters are different from the real ones but the general orientation of the polarization is respected.

3.4.2 Perspectives

Several upgrades are possible to achieve a better accuracy and quality of the computed parameters.

- Including phase retard variation in the computation process:
  As we stated before, a variation of ϕ inside the retarder may reduce the accuracy of the parameters computation. In order to solve this problem, the whole retarder should be measured on the polarimetric bench to compute a map of ϕ. A new fitting algorithm should be implemented to allow the computation of the Stokes parameters using three variables x, y and $\phi(x, y)$. Since the polarimetric bench compute a map of α and ϕ, the calibration will be replaced by the measurement of the retarder and a verification measurement will be perfomed using a beam with a well known polarization state.
- Reducing the importance of the speckle phenomenon:
  Using a high speed rotating disk between the vertical polarizer and the projection screen and performing a temporal meaning would allow to reduce the effect of the speckle phenomenon.
- Upgrading the optical system:
  Presently, the optical system used to collimate the beam is not optimized for imagery. An optical system free from aberrations due to misalignment will achieve a better quality of the pictures leading to a better accuracy on the parameters computation. Moreover, the camera used for the recording of the picture is not optimized neither, a large suface of the detector is not used because the beam is quite small at the minimum distance between the screen and the camera for clean pictures. An optimization of the size of the beam, the size of the retarder and the used size of the detector would lead to a more accurate computation of ζ and more relevant results.

3.4.3 Expansion of the method to ellipsometry measurements

One application of our polarization analysis method could be ellipsometry [2, 3]. The goal of this subsection is to briefly present ellipsometry and to show how our polarization analyzer could be used.

Ellipsometry is a contact free technique that measures several characteristics of an interface using the variation of the polarization state of the reflected beam. In a nutshell, a monochromatic beam with a well-known polarization state is incident to the surface with an angle θ_i (see Figure 3.17), due to surface properties (like the material, the state of its surface ...) the polarization of the reflected beam changes. By studying these variations, one can determine several surface properties.

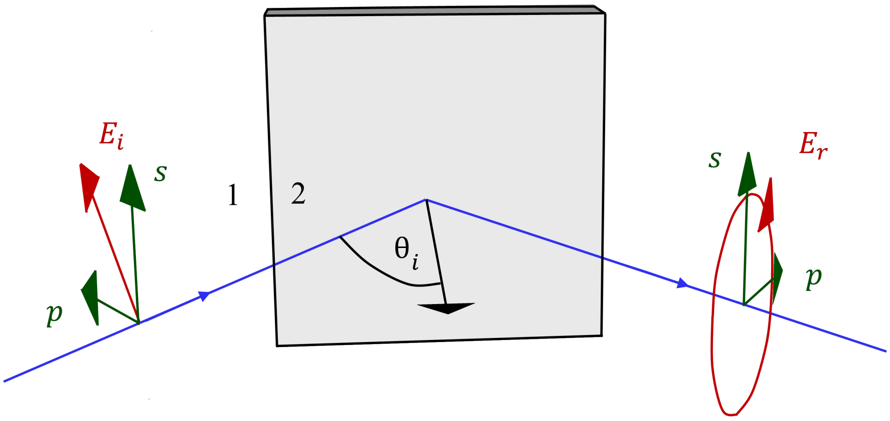

Figure 3.17: Scheme of the ellipsometry principle. The polarization of the incident and reflected beam are represented in red (E_i E_r) and the decomposition in the s and p components are pictured in green.

The principle of the measurement is to determine a ratio of complex reflection coefficients: ρ which will be used to determine the interface properties using several models [3]. The electric field of the incident and reflected beams are decomposed following the s and p components[5].
The complex amplitudes of the beams can be written as

$$E_{rp} = R_p\, E_{ip},\ E_{rs} = R_s\, E_{is}. \tag{3.5}$$

Where E_{ip} and E_{is} respectively are the complex amplitudes following the p and s components of the incident beam, E_{rp} and E_{rs} stands for the reflected beam and R_p and R_s are complex reflexion coefficients. ρ can be defined as the ratio of the complex reflection coefficients $\rho = \dfrac{R_p}{R_s}$, it can also be defined as a ratio of two coefficients χ_i and χ_r: $\rho = \dfrac{\chi_i}{\chi_r}$ which represents the ratio of the s component on the p component $\chi_i = \dfrac{E_{is}}{E_{ip}}$ and $\chi_r = \dfrac{E_{rs}}{E_{rp}}$.

---

[5] The s components represents an electric field perpendicular to the incidence plane while p stands for an electric field comprised in the incidence plane.

Several physical models exist to describe the phenomenon of the reflection: two-phases model, three-phases, multilayer ...
Their common point is to express the physical properties of the interface as a function of ρ. As an example, we present the two-phases model which expresses n as a function of ρ.
It represents a single interface between two homogenous and isotropic semi-infinite media (1, 2).
The reflection coefficients are given by

$$\begin{aligned} r_{12,p} &= \frac{\epsilon_2\Omega_1 - \epsilon_1\Omega_2}{\epsilon_2\Omega_1 + \epsilon_1\Omega_2} \\ r_{12,s} &= \frac{\Omega_1 - \Omega_2}{\Omega_1 + \Omega 2} \end{aligned} . \tag{3.6}$$

Where $\epsilon_i = N_i^2$ is the dieclectric function of the medium i, N is the complex refractive index and $\Omega = \left(\epsilon_i - \epsilon_1 \sin^2(\theta_i)\right)^{1/2}$. The measured ρ is given by equation 3.7:

$$\rho = \frac{\sin(\theta_i)\tan(\theta_i) - \left[\epsilon \sin^2(\theta_i)\right]^{1/2}}{\sin(\theta_i)\tan(\theta_i) + \left[\epsilon \sin^2(\theta_i)\right]^{1/2}} \tag{3.7}$$

with $\epsilon = \frac{\epsilon_2}{\epsilon 1}$.

Finally, ϵ_2 can be written as a function of ρ and ϵ_1 as

$$\epsilon_2 = \epsilon_1 \left\{ \sin^2(\theta_i) + \sin^2(\theta_i)\tan^2(\theta_i)\left[\frac{1-\rho}{1+\rho}\right]^2 \right\}. \tag{3.8}$$

Using an incident beam from a medium with a well-known ϵ_1 allows the computation of ϵ_2 at a given wavelength. Several methods exist to analyze the polarization of the reflected beam in ellipsometry such as the nulling ellipsometry, the photometric ellipsometry and the return path ellipsometry ... One method is particularly interesting since it uses the Stokes parameters of the reflected beams to compute ρ.
Indeed, the coefficients χ_i and χ_t can be written as:

$$\chi = \frac{S_2 + \imath S_3}{S_0 + S_1} = \frac{S_0 - \imath S_1}{S_2 - \imath S_3}. \tag{3.9}$$

Typical setups used to compute the Stokes parameters with ellipsometry are based on four detectors devices (see Figure 3.18)

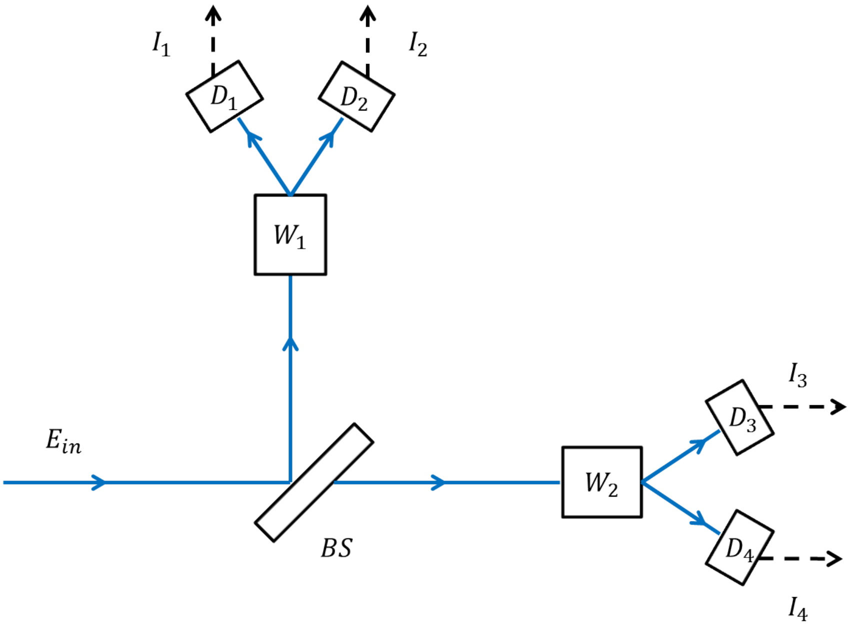

Figure 3.18: Representation of the four Stokes parameters measurement using four detectors and two wollaston prisms (W).

The beam is divided into four different beams and each beam is transmitted through different polarization elements to record 4 different intensities: I_1, I_2, I_3, I_4. The recorded intensities depend on the Stokes parameters of the incident beam and the optical elements:

$$I = A\,.S,$$

where A is 4 by 4 matrix which represents the optical elements and is obtained by performing calibration measurements with a linearly polarized beam and quarter-wave plate.

We believe that our retarder could be used for ellipsometric measurements. The advantages would be a compact and simple setup since our method only requires the retarder and a linear polarizer. It would be also possible to monitor dynamic variations of the state using an appropriate camera.

Chapter 3 references

[1] J.Mudge and M.Virgen, "Near-infrared simultaneous stokes imaging polarimeter: integration,field acquisitions, and instrument error estimation," in [*Proc.SPIE*], **8160**, 81600B–81600B–14, Society of Photo-Optical Instrumentation Engineers SPIE (2011).

[2] H.G.Tompkins and E.A.Irene, "Polarized light and ellipsometry," in [*Handbook of ellipsometry*], *Handbook of Optics*(vol. 1), William Andrew and Springer, 2 ed. (2005).

[3] M.Bass and Optical Society of America, "ellipsometry," in [*Handbook of Optics: devices, measurement and properties*], McGraw-Hill, ed., *Handbook of Optics*(vol. 2), McGraw-Hill, 2 ed. (1994).

[4] B.Baumann, S.O.Baumann, T.Konegger, M.Pircher, E.Götzinger, H.Sattman, M.Listschauer, and C.K.Hitzenberger, "Polarization sensitive optical coherence tomography of melanin provide tissue inherent contrast based on depolarization," *Proc.SPIE* **7554**, 75541M–75541M–6, Society of Photo-Optical Instrumentation Engineers SPIE (2010).

[5] V.Sankaran, M.J.Everett, J.Duncan, J.T.Maitland, and J.T.Wals, "Comparaison of polarized light propagation in bilogical tissue and phantoms," *Opt. Lett.* **24**(15), 1044–1046 (1999).

[6] M.Bass and Optical Society of America, "polarimetry," in [*Handbook of Optics: devices, measurement and properties*], McGraw-Hill, ed., *Handbook of Optics*(vol. 2), McGraw-Hill, 2 ed. (1994).

[7] Society of Photo-Optical Instrumentation Engineers SPIE, [*Spectrally broadband channeled imaging polarimeter using polarization gratings*], **8160** (2011).

[8] B.Schaefer, E.Collet, R.Smyth, D.Barret, and B.Fraher, "Measuring the stokes polarization parameters," *Am. J. Phys.* **75**, 163–168 (2007).

[9] G.Biener, A.Niv, V.Kleiner, and E.Hasman, "Near-field fourier transform polarimetry by use of a discrete space-variant subwavelength grating," *J. Opt. Soc. Am. A* **20**(10), 1940–1948 (2003).

[10] Y.Gorodetski, G.Biener, V.Kleiner, and E.Hasman, "Space-variant polarization manipulation for far-field polarimetry by use of subwavelength dielectric gratings," *Opt. Lett.* **30**(17), 2245–2247 (2005).

[11] Z.Bomzon, G.biener, V.Kleiner, and E.Hasman, "Spatial fourier-transform polarimetry using space-variant subwavelength metal-stripe polarizers," *Opt. Lett.* **26**(21), 1711–1713 (2001).

[12] A.Bouzid, M.A.G.Abushagur, A.El-Sabar, and R.M.A.Azzam, "Fiber-optic four-detector polarimeter," *Opt. Commun.* **118**(3–4), 329–334 (1995).

[13] R.M.A.Azzam, "Arrangement of four photodetectors for measuring the state of polarization of light," *Opt. Lett.* **10**(7), 309–311 (1985).

[14] R.M.A.Azzam, "Integrated polarimeters based on anisotropic photodetectors," *Opt. Lett.* **12**(8), 555–557 (1987).

[15] P.Piron, P.Blain, and S.Habraken, "Polarization measurement with space-variant retarders in liquid crystal polymers," in [*Proc.SPIE*], **8160**, 81600Q–81600Q–7, Society of Photo-Optical Instrumentation Engineers SPIE (2011).

[16] E.Hecht, “Polarisation,” in [*Optique*], Addison-Wesley, 4 ed. (2005).

[17] M.Françon and S.Mallick, [*Polarization interferometers: applications in microscopy and macroscopy*], Wiley-Interscience London, New York (1971).

[18] P.Blain, F.Michel, Y.Renotte, and S.Habraken, “Using a savart plate in optical metrology,” in [*Proc. SPIE*], **7791**, 779107–779107–8, Society of Photo-Optical Instrumentation Engineers SPIE (2010).

[19] A.Boucher, “Détection de contours.” `http://www2.ifi.auf.org/personnel/Alain.Boucher/cours/traitement_images/05-Contours.pdf` (2012). Accessed: 2013-12-08.

[20] MathWork, “Hough transform.” `http://www.mathworks.nl/help/images/ref/hough.html` (2013). Accessed:2013-12-08.

[21] M.Bass and Optical Society of America, “General principles of geometric optics,” in [*Handbook of Optics: Fundamentals, techniques, and design*], McGraw-Hill, ed., *Handbook of Optics*(vol. 1), ch. General principles of geometric optics, McGraw-Hill, 2 ed. (1994).

4

Polarization states separator

Contents

The second application which we developed at Hololab for 1D continuous SR is a polarization states separator. An incident polarized beam will be separated into several differently polarized beams depending on the polarization state of the beam and the retarder characteristics. The variation of the fast axis follows the same pattern as the analyzer. The difference between these retarders lies in the size their period: the period of the analyzer is ≈ 5 *mm while the period of the separator is* $\approx 20\,\mu m$*. Due to the ratio period/wavelength, the retarder will diffract the incident beam into several orders with specific polarization states. The retarder was developed with Pascal Blain a PhD student at Hololab. It will be extensively described and analyzed in his forthcoming Ph.D. thesis. This chapter will be a brief overview of it. We will present the mathematical principle and the application we worked on.*

4.1 Introduction

The polarization state separator is nearly the same retarder as the polarization analyzer. It exhibits the same variation of the fast axis orientation but its period is way smaller: $15\,\mu$m instead of 6 mm for the analyzer. Due to the period/wavelength ratio, the retarder will exhibit diffraction properties in the visible. Three orders of diffraction will appear each with a unique polarization state depending on the retarder's characteristics and the polarization of the incident beam.

The principle of the separator will be described in the following section.

4.2 Diffraction analysis

This time, the retarder will be modeled using the Jones formalism. The polarization separator (PS) is represented by [1]:

$$PS = \begin{pmatrix} \cos\left(\frac{\phi}{2}\right) - \imath\cos(2\alpha)\sin\left(\frac{\phi}{2}\right) & -\imath\sin(2\alpha)\sin\left(\frac{\phi}{2}\right) \\ -\imath\sin(2\alpha)\sin\left(\frac{\phi}{2}\right) & \cos\left(\frac{\phi}{2}\right) + \imath\cos(2\alpha)\sin\left(\frac{\phi}{2}\right) \end{pmatrix}, \tag{4.1}$$

α and ϕ being the orientation of the fast axis and the phase retard induced by the retarder.

The electric field E_{out} simply being: $E_{out} = PS\ E_{in}$.

With the far-field condition and a period/wavelength ratio about 30, diffraction occurs [2] and the field after the retarder E_{diff} is represented by Equation 4.2 [3].

$$E_{diff} = \begin{pmatrix} FT\left(E_{out,x}\right) \\ FT\left(E_{out,y}\right) \end{pmatrix} \tag{4.2}$$

It can be shown that only three orders of diffraction are present D_0, D_R, D_L [4] with their own diffraction efficiency η_0, η_R, η_l [5, 6, 7].

$$\begin{aligned} \eta_0 &= \cos^2\left(\frac{\phi}{2}\right) \\ \eta_R &= \frac{1}{2}\left(1 - S'_3\right)\sin^2\left(\frac{\phi}{2}\right) \\ \eta_L &= \frac{1}{2}\left(1 + S'_3\right)\sin^2\left(\frac{\phi}{2}\right) \end{aligned} \tag{4.3}$$

Where S'_3 is the fourth normalized Stokes parameters of the incident beam: $S'_3 = S_3/S_0$.

We can observe that:

- for a perfect half-wave plate: $\phi = \frac{\pi}{2}$ thus $\eta_0 = 0$ and only two diffraction orders exist,
- for an incident circularly polarized beam and half-wave plate, only one diffraction order is present and it is orthogonally polarized with respect to the incident one.

The behavior of the retarder in these configurations is pictured in Figure 4.1 and a prototype is presented in Figure 4.2.

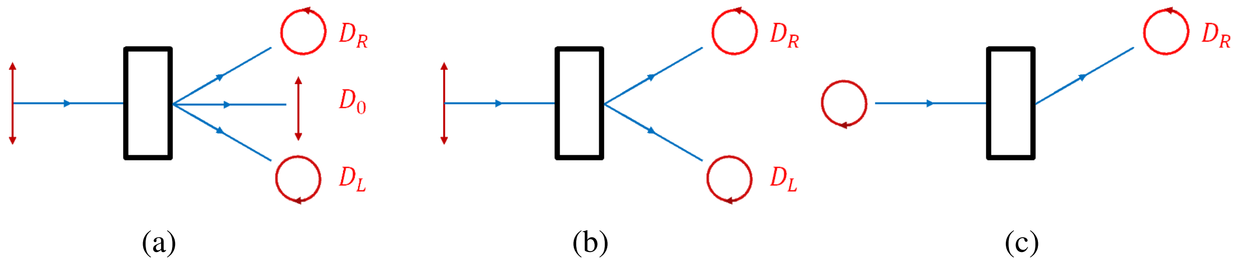

Figure 4.1: Schemes of the effect of the polarization state separator for several configurations. The polarization of the beams is pictured in red and the variation of the fast axis orientation is vertical like the separation direction. (a) Pictures the general case where three orders of diffraction are present. (b) Represents the case of a perfect half-wave plate where only two diffraction orders exist. (c) Stands for a half-wave plate and a circularly polarized incident beam where only one diffraction order exists.

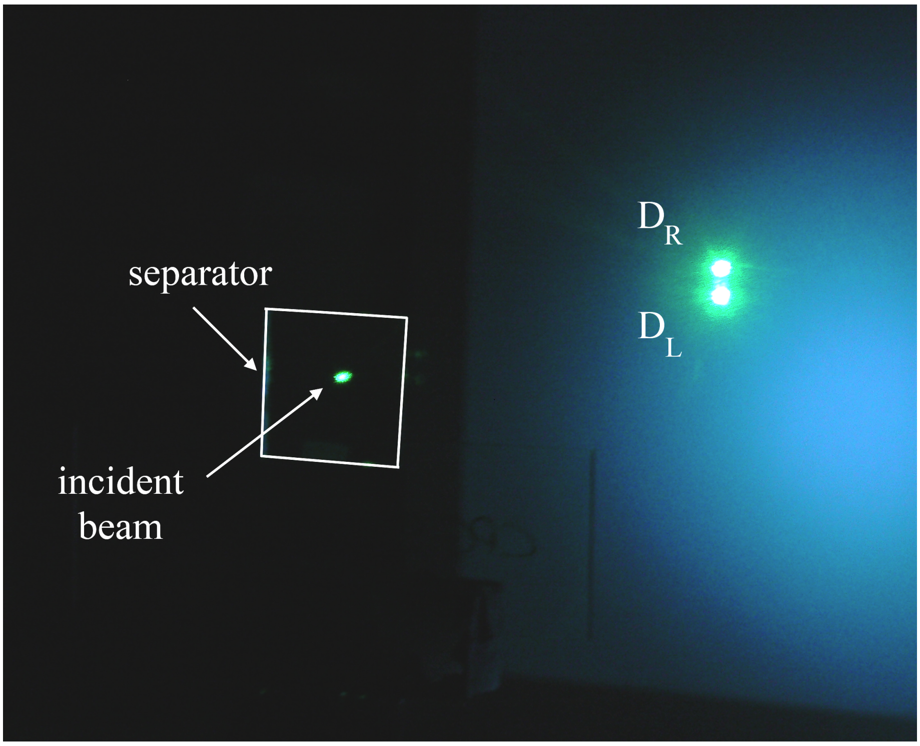

Figure 4.2: Picture of the beam after a polarization state separator for a phase retard of π.

4.3 Application to shearography

In the following paper [8], the polarization separator is used for shearography. The goal is to detect defaults on a surface, the surface is illuminated by a collimated beam and the retarder is placed before the camera, the separator will be designed to be act as a half-wave plate. The retarder will diffract the beams diffused by the studied surface into two circularly polarized beams of opposite handedness and same intensity. A linear polarizer will be placed between the separator and the camera to produce a fringe pattern. By submitting the surface to a slight deformation of a few wavelength , the fringe pattern will change and by recording its variation, one can determine the surface default. In the article, the principle of the method is explained, several numerical simulations and their analysis are exposed. Our first prototypes are presented as well as the proof of the concept and an analysis of the experimental limits is performed. Finally, several improvement of the methods are given.

An in-line Shearography set-up based on Circular polarization gratings

Pascal Blain*, **Pierre Piron, Yvon Renotte and Serge Habraken**

Hololab, Bat. B5a, University of Liège, 17 allée du 6 Août, B-4000 Liège, Belgium
**Corresponding author: pascal.blain@ulg.ac.be*

The shearing amount defines the resolution of a speckle shearing interferometer and the shearing direction defines the sensitivity direction of the setup. The properties of circular (cycloid) holographic polarization gratings recorded in liquid crystal polymers can be used to build a new multi shearing direction and amount shearography set-up. The polarization states of the diffracted beams offer an easy way to produce phase shifts and thus to compute the phase contained in the shearograms. The theoretical bases of such a device are highlighted and an original compact and full in-line set-up is proposed. First experimental results of delamination detection and flaw detection by shearography are presented. A discussion on the importance of the grating recording and the polarization orientation shows the best working requirements.

1. INTRODUCTION

Shearography is widely used in the field of Non-destructive Testing [1]. Many shearing elements for shearographic devices have been proposed [2]. Among these, the most suited with phase shifting techniques (which are the only way to obtain quantitative, i.e. numerical, evaluation of a shearogram [3]) and the most widely used interferometer, is the modified Michelson [3]. The main drawback of this interferometer is that the crossed reference and object beams can be altered differently by external vibrations and environmental disturbances.

To overcome this drawback self-referenced almost common path interferometers based on a diffractive element [4] and on a birefringent element [5] (i.e. a Savart Plate [6]) have been developed for shearography. Unfortunately their constant shearing direction [4] and amount [5] limit their use. Indeed the shearing amount defines the resolution of the interferometer and the shearing direction defines the direction in which the first derivative of the displacement is evaluated. It has also been established that quantitative topological shearography has to be made along the shearing direction [7,8].

A less sensitive interferometer, which allows at the same time phase shifting and variation of the shearing amount and direction, would be ideal for shearography. We propose to associate birefringence together with diffraction. Circular polarization gratings (CPG) recorded in Liquid Crystal Polymers (LCP) [9-14] is the combination which will allow building the first full in line shearography set-up that easily enables phase shifting with the ability to change the shearing direction and amount. After a short reminder of CPGs properties, a new shearography set-up and some experimental results will be proposed.

2. THEORITICAL BACKGROUND

The following results and statements are inspired from previous related works [9-18] on CPGs. In this section we use those results to prove that CPGs can be applied to shearography and that they are well suited for it.

A. Reminder of what a CPG is

A CPG is built by recording an interference pattern of two orthogonal circular polarizations beams. When the beams are overlapping in the horizontal *x* direction, it results in a series of linear polarizations with different orientations in the *x* direction but with uniform illumination intensity [9]. This cycloid pattern is written in a polarization sensitive material. The CPG is then formed in photo-cross-linkable liquid crystal polymers aligned according to this patterned layer [10, 11].

The Jones matrix of such a birefringent plate with spatially varying optical axis is given by Eq. 1.

$$J_{rec} = R^{-1}\left(\frac{2\pi x}{d}\right)\begin{bmatrix} e^{-i2\pi\Delta nh/2\lambda} & 0 \\ 0 & e^{i2\pi\Delta nh/2\lambda} \end{bmatrix} R\left(\frac{2\pi x}{d}\right) \qquad (1)$$

where d is the spatial period of the grating, λ the reading wavelength in free space, $\Delta n = n_e - n_o$ is the birefringence, h the thickness of the layer and *R* a rotation matrix in the plane of the retarder about the normal z-axis.

As elegantly shown in [12], CPGs can only have three diffracted orders (0th and ±1st orders). Eq. 2 gives the efficiencies of the diffracted beams [13].

$$\begin{aligned} \eta_0 &= \cos^2\left(\frac{\pi\Delta nh}{\lambda}\right) \\ \eta_{\pm 1} &= 0.5\left(1 \pm P.\sin(2\chi)\right)\sin^2\left(\frac{\pi\Delta nh}{\lambda}\right) \end{aligned} \qquad (2)$$

where P is the degree of polarization in Stokes formalism, and $\chi = \tan^{-1}(\pm b/a)$ is the ellipticity angle of the input beam with a the longest and b the shortest axis of the polarization ellipse.

B. Application to shearography

The ±1 order separation will be used as symmetric sheared beams. To get rid of the 0th order for shearography the CPG has to be built as a half-wave plate, i.e. $\eta_0 = 0$ in Eq. 2. For a linear or a non-polarized input beam entering the grating, the two diffracted beams will have crossed circular polarization states.

The intensities of the two sheared beams must be equal in order to enhance the contrast of the shearograms. The contrast ratio is given by the following equation

$$C = \frac{I_{\max} - I_{\min}}{I_{\max} + I_{\min}} = \frac{2A_1A_2}{|A_1|^2 + |A_2|^2} \qquad (3)$$

Where I_{max} and I_{min} are the maximum and the minimum of the intensity of the interference pattern of two electric field E_1 and E_2 with the respective amplitudes A_1 and A_2.

Thanks to the relation between $\eta_{\pm 1}$ and χ in Eq. 2, this condition is reached if the input beam is linearly polarized.

C. Rotation of the CPG for changing the shearing direction

The effect of the CPG rotation about its normal for beam shearing orientation variation has been tested by computer simulation. A Gaussian vertically polarized beam E_{in} enters a half-wave plate CPG. The output field can be written as [14]:

$$E_{out} = J_{rec} E_{in} = \begin{pmatrix} E_{out,x} \\ E_{out,y} \end{pmatrix} \qquad (4)$$

Considering far field [15] and a grating period greater than 10λ [16], the diffracted field E_{diff} is given in [14]:

$$E_{diff} = \begin{pmatrix} FFT(E_{out,x}) \\ FFT(E_{out,y}) \end{pmatrix} \qquad (5)$$

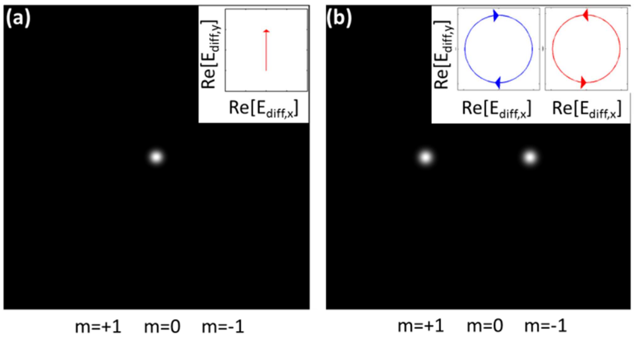

Fig. 1. Simulation of the intensity distributions of the output beams exiting a half-wave plate CPG and their respective polarization state. (a) Input beam with a vertical linear polarization, λ=532nm. (b) Intensities of the diffracted beams behind the CPG with a period d=15µm. The beams polarization states are shown in the upper right corner of each picture: clockwise and counter-clockwise circular polarizations for the diffracted beams.

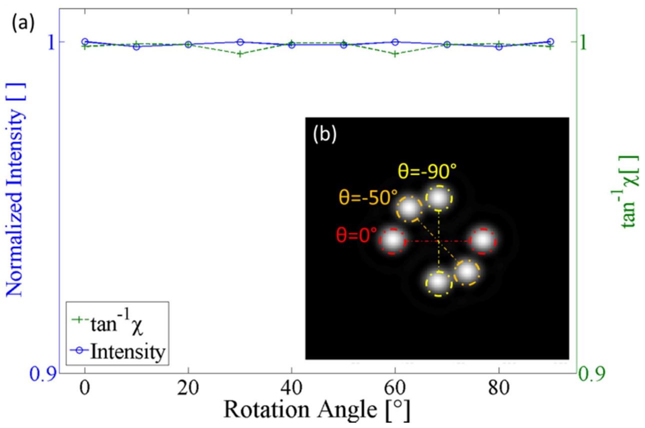

Fig. 2. (Color online) (a) Variation of the intensity and ellipticity of the diffracted beams while the grating is rotated about its normal with a maximal error of 0.0015. (b) Diffracted beams intensities for different grating orientations θ = 0, -50 and -90°.

Eq. 2 leads to the intensity distribution shown in Fig. 1 where the grating equation $d \sin\theta_m = m\lambda$ governs the diffraction angles, where θ_m is the diffraction angle of the mth order.

No change in the intensity or the polarization state of the output beams occurs when rotating the grating about its normal (see Fig. 2). Thus by placing the CPG in a precision rotating mount, one should be able to control the shearing beam direction.

D. Variation of the shearing amount

There are two different ways for varying the shearing amount. The first one consists in a multi-period grating (at least three or four areas with different periods). Thus by laterally translating the CPG, the input beam will be diffracted at different angles.

The second one uses two successive parallel CPGs with the same orientation and period. The first grating diffracts two beams with circular polarization of opposite handedness. Their ellipticity angle χ are $-\pi/4$ and $\pi/4$, and their Stokes parameters are respectively (1,0,0,-1) and (1,0,0,1). The second grating further diffracts the two beams. But as one can deduce in the relation between the parameters $\eta_{\pm 1}$, χ and P in Eq. 2, only one beam is further diffracted for each incoming beam. Thanks to the principle of reversibility of light, the diffracted beam restores the initial propagation direction. Fig. 3 sums up those concepts.

The idea is not new and it has been established that the distance

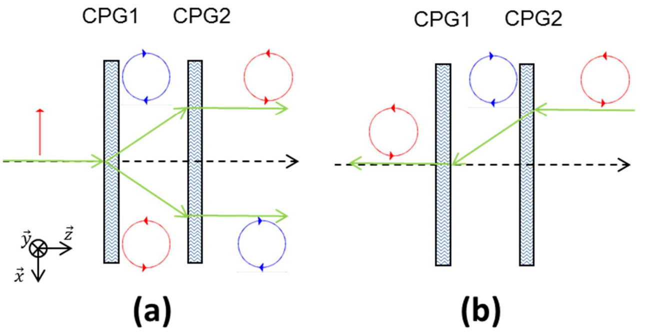

Fig. 3. (Color online) Polarization conversion [14] and beam propagation [18] trough two successive CPGs with (a) a linearly vertical polarized input input beam and (b) a counterclockwise circular polarized input.

between the two diffracted beams is given by $\Delta x = \Delta z \tan(\theta_{\pm 1})$ [17], where Δz is the displacement of the grating along the propagation axis, Δx the lateral displacement of the diffracted beams and $\theta_{\pm 1}$ is the diffraction angle for the ±1 orders.
Thus by applying this concept to shearography, changing the distance between the two gratings will change the shearing amount. One more advantage of the previous statement is that the shearing amount can be cancelled out [18], making easier the preliminary step of camera lens focusing.

E. Phase shifting

Phase shifts are convenient for interferometry. Inteferograms with different phase shifts are compared in order to calculate their phase. Here we can take advantage of the orthogonal circular polarized output beams [19]. The Jones matrix of the CPG can be rewritten as two opposite circular polarizers with a phase difference ϕ between them:

$$J_{out} = \frac{i}{2}\left\{\begin{bmatrix} 1 & +i \\ -i & 1 \end{bmatrix} + e^{i\phi}\begin{bmatrix} 1 & +i \\ +i & 1 \end{bmatrix}\right\} \qquad (6)$$

Considering a vertical initial polarization and an analyzer P2 of polarization orientation φ with respect to the x direction, the interference intensity distribution is given by Eq. 7:

$$I_{2\varphi} = I_0\left(1 + \cos(\phi + 2\varphi)\right) \qquad (7)$$

By placing a motorized rotating polarizer after the CPG, phase shifting techniques will be achievable. In order to avoid any mechanical movement, a polarizer array [20] or a calibrated liquid crystal variable retarder (LCVR) [5] placed between a quarter-wave plate (QWP) and a polarizer could be used. The orientation of the fast and slow axis of the LCVR must be oriented at 45° to the orientation of the QWP axis. The orientation of the polarizer can be parallel or orthogonal to the QWP axis. With such elements temporal phase shifting and temporal phase transforms [21,22] are achievable.

3. DESIGN OF A SHEAROGRAPHY SET UP BASED ON THE ASSOCIATION OF TWO CPGs

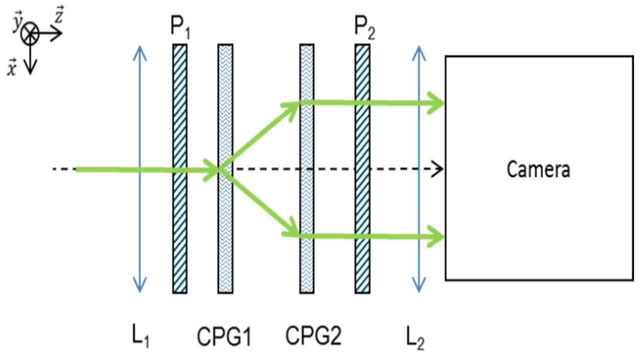

Fig. 4. (Color online) Shearography set up using two CPGs with the same orientation and period

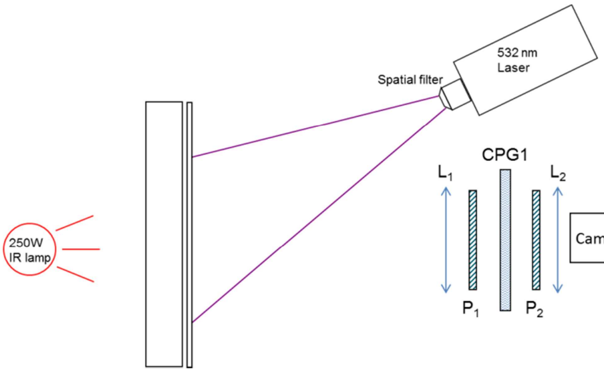

Fig. 5. (Color online) Experimental setup used to detect delamination between two glued aluminium plates.

Thanks to the aforementioned properties of CPGs, a new shearography setup which allows phase shifting, shearing direction and amount modulation is proposed in Fig. 4. A first lens L1 is used to collect the light diffused by the object under test. A polarizer P1 ensures a linear input polarization. CPG1 is on a rotation stage and CPG2 can be translated in the z direction as long as it endures the same rotation as CPG1. P2 can be a rotating polarizer or a polarizer array. L2 is the objective lens of the camera.

4. EXPERIMENTAL SETTINGS & RESULTS

A. Recording CPGs

Our CPGs are built with Liquid Crystal Polymers (LCP) which are Liquid Crystals connected to chain polymers from Rolic®. A near 50 nm photo-alignment layer (Rolic® ROP103) is spin-coated on a 15 x 15 x 1.5 mm³ glass substrate and baked during 5 minutes at a temperature of 150°C. Then the alignment is set through exposure to a series of linear polarizations pattern with a 325 nm laser light and a dose of 200 mJ/cm². The cycloid pattern is obtained by polarization holography [9], i.e. the superimposition of two circularly polarized beams of opposite handedness, in order to have a grating period of ~15 µm. For that purpose, we selected a Mach-Zender interferometer bench [13]. The LCP precursor (Rolic® ROF5102), which orients itself according to the photo-alignment layer, is then spin-coated, heated to get rid of solvents (during 3 minutes at 50°C under nitrogen flushing) and subsequently polymerized by UV curing. In fact, the LCP reaches a stable solid state. The coating thickness of the LCP precursor is chosen to obtain a half-wave plate at 532 nm, i.e. ~2.3 µm.

B. Proof of concept with one CPG

First experimental results were obtained from an optical workbench assembly without CPG2 and with a motorized rotating polarizer as P2. CPG1 was oriented so that there is a vertical shearing direction. The experiment (see Fig. 5) consists in detecting delamination between two thin glued sheets of aluminum. The glue between the two layers is purposely non-homogeneously applied. The thermal loading is made with a 250 W IR lamp located at about ten centimeters behind the plates. The loading is applied during 5 s. The phase maps are calculated at different thermal relaxation times after switching off the lamp. The reference time and phase map is set before switching on the lamp. Fig. 6 shows some phase maps recorded by a 4 image

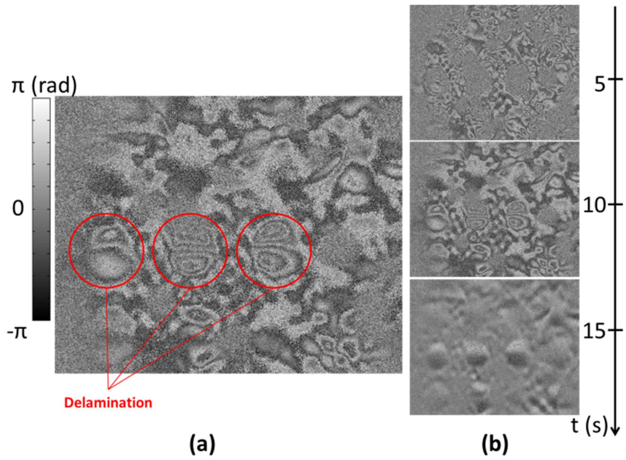

Fig. 6. (Color Online)(a) Wrapped phase map difference between a phase map before heating and a phase map 10s after the heating has started. It shows delamination between two glued thin layers of metal over an area of 4 x 3 cm^2. (b) Temporal evolution of the difference phase maps during the relaxation time.

temporal phase shifting algorithm (the 4 frames correspond to I_{0°, I_{90°, I_{180°, I_{270° in Eq. 7).

C. Checking the two CPG arrangement

Instead of a diffuse input light in our shearographic head in Fig. 5, a collimated 532nm laser diode beam (50 mW) is used. The camera is replaced by a diffusive screen. Thus instead of having a shearogram interferometer we have an interferometric fringe projector. This trick allows checking the theories mentioned in section 2.C and 2.D:

- Moving CPG2 away from CPG1 leads to a decrease of the fringes period (cf. Fig. 7). This period is inversely proportional to the distance between the two CPGs. This corroborates the relation between the shearing amount and Δz between the two CPGs.
- Rotating both the CPGs about the system optical axis generates a rotation of the fringes orientation in Fig. 7. The shearing direction is determined along the perpendicular to the orientation of the fringes.
- Rotating of the polarization orientation of P2 results in a spatial shift of the fringes. If as suggested in section 2.E, no mechanical movements are preferred to a rotating polarizer, the fringes projector configuration enables an easy way to calibrate a liquid crystal variable retarder coupled with a quarter-wave plate.

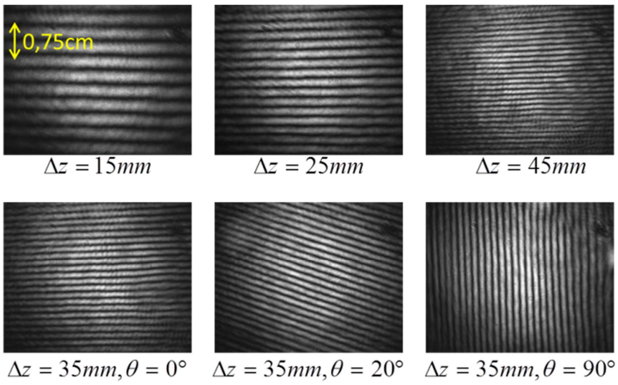

$\Delta z = 15mm$ $\Delta z = 25mm$ $\Delta z = 45mm$

$\Delta z = 35mm, \theta = 0°$ $\Delta z = 35mm, \theta = 20°$ $\Delta z = 35mm, \theta = 90°$

Fig. 7. (Color online) Adjustments of the set-up by using a fringe projector configuration. The distance between the camera and the screen is fixed (50 cm). The only changing parameters are the distance between the CPG and their orientations. The pictures in the top line are recorded with $\theta = 0°$.

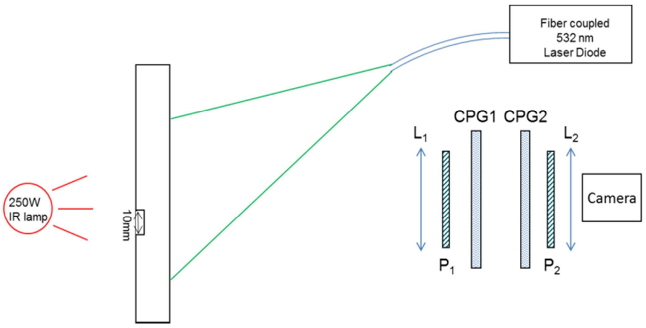

Fig. 8. (Color online) Experimental setup used to detect a hidden defect on an aluminium plate with a two CPG configuration.

D. Results obtained with the two CPG design

The interferometer is set as described in section 3 (Fig. 5). The experiment consists of detecting a hidden defect made in an aluminum plate. The plate thickness is 2 mm. The defect volume is 10 x 10 x 1 mm^3. The thermal loading conditions are the same as earlier with a 4 s heating. A 300 mW fiber coupled laser diode brings a wide uniform laser beam on the plate (cf. Fig. 8). The unwrapped difference phasemaps are obtained by subtracting a phase map recorded before the loading with one recorded 30 s after it. The filtering method is the sine-cosine filtering [23]. The area covered by each picture is approximately 4 x 3 cm^2.

The top line of Fig. 9 shows that the sensitivity of our set-up can be changed. This sensitivity improvement is due to the increase of the shearing amount and in our case with the growing of the distance between the two CPGs.

The bottom line of Fig. 9 shows that the set up really offers the possibility to change the shearing direction by rotating both CPGs about the set-up optical axis.

5. DISCUSSION

A. Criticality of the CPG recording

We will first discuss the criticality of the CPG recording. In order to diffract 2 beams only the CPG has to work as a half wave-plate. The coated thickness depends on the precision with which the spin coating is made. The recorded gratings might not have

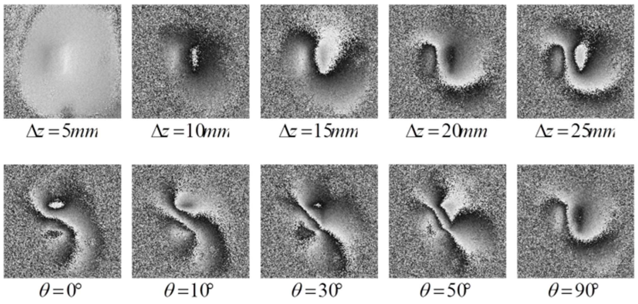

$\Delta z = 5mm$ $\Delta z = 10mm$ $\Delta z = 15mm$ $\Delta z = 20mm$ $\Delta z = 25mm$

$\theta = 0°$ $\theta = 10°$ $\theta = 30°$ $\theta = 50°$ $\theta = 90°$

Fig. 9. Wrapped phase maps obtained with the two CPG shearography set-up with different amounts and orientations of the shearing. The phasemaps in the top line are recorded with $\theta = 90°$ and the one in the bottom line are recorded with $\Delta z = 20$ mm.

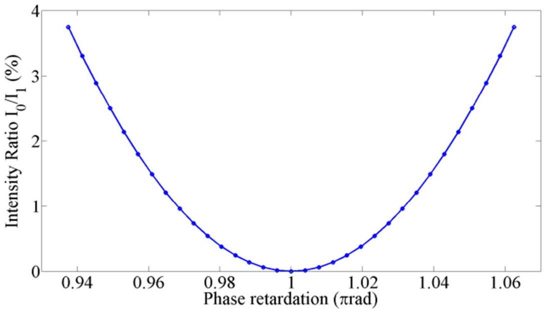

Fig. 10. (Color online) Intensity ratio between the 1st order and the 0th order according to the phase retardance of the CPG.

exact π phase retardation. Different CPGs with different phase retardation were simulated thanks to Eq. 5. As shown in Fig. 10, the intensity ratio of the 0th order grows as the phase retardation of the CPG deviates from π. Thus a 0th order of CPG1 exists and when this linearly polarized beam reaches the 2nd CPG under normal incidence, it is diffracted into three new orders. Meanwhile ±1st orders after the first grating are not diffracted by the second grating and their initial beam propagation direction is restored. By placing a mask the unwanted ±1st orders beams diffracted by CPG2 can be easily prevented. Then 3 beams (+1,-1 and 0,0 in Fig. 11) can be recorded by the CCD camera. Without taking into account the influence of the polarizer P2, this leads to a 3 wave interference pattern, the contrast ratio of which is:

$$C = 2\frac{A_1A_2 + A_1A_3 + A_2A_3}{A_1^2 + A_2^2 + A_3^2} \qquad (8)$$

Let's consider that the intensity ratio between the 0th order and the 1st order is 4% after CPG1. Then after CPG2, $I_{\pm 1}$ is 300 times $I_{0,0}$. As $A_1^2 = A_2^2 = I_{+1} = I_{-1}$ and $A_3^2 = I_{0,0}$, then Eq. 8 is almost equivalent to Eq. 3.

In our lab, we have to coat the LCP precursor layer at a speed of 1600 rev/min during 30 s for a π phase retardation. Knowing that the rotation accuracy of our spin-coater is ±50 rev/min and considering that the coated thickness is decreasingly proportional to the number of revolution, then the approximated phase retardation of our CPGs are between 0.96π and 1.03π. By reporting those values in Fig. 11, one can see that the intensity ratio is below 1%, thus after CPG2, $I_{\pm 1}$ is 4500 times $I_{0,0}$. Eq. 8 is thus equivalent to Eq. 3 and the influence of $I_{0,0}$ can be neglected.

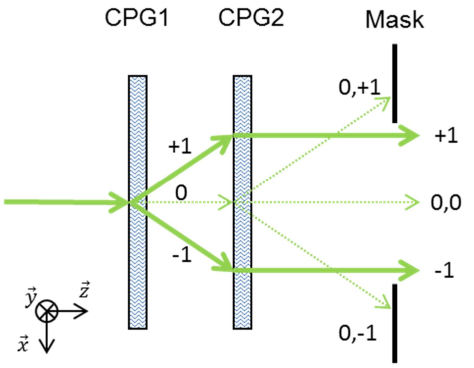

Fig. 11. (Color online) Shearography set up using two CPGs with the same orientation and period

Using 2 successive CPGs and a mask compensates the fact that those are not accurately made as half wave-plates. Even if a third beam reaches the CCD camera, its impact is negligible on the overall result.

B. Criticality of the polarization orientation

For previous set-ups [4,5] the orientation of the input polarizer was of great importance because it defined the intensity ratio between the two generated beams. For a good fringe contrast the intensities of the two beams have to be as equal as possible. In this new set-up, the polarization orientation incident on CPG1 is of no importance as long as it is a linear polarization.

When using a rotating polarizer as P2, the initial orientation of the polarizer is of no importance too. As two opposite circular polarization states exit from CPG2, whatever the orientation of P2 is, the same amount of amplitude will be projected according to its orientation.

If a liquid crystal phase modulator is used, the orientation of its axis does not matter, but the orientation of the following polarizer must be oriented at 45° according to the retarder axis. Indeed the polarization states exiting the LCVR are orthogonal and linear, thus to project the same amount of intensity on the same polarization state the polarizer has to be accurately oriented. If as described in Fig. 12, an error angle ε occurs between the ideal orientation of 45° and the real orientation of the polarizer P2 Eq. 3 becomes Eq. 9:

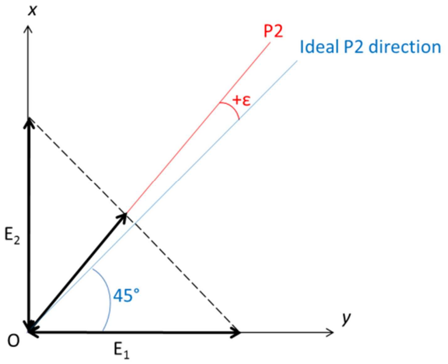

Fig. 12. (Color online) Adjustments of the set-up by using a fringe projector configuration. The distance between the camera and the screen is fixed (50cm). The only changing parameters are the distance between the CPG and their orientations.

$$C = \frac{2A_1A_2\cos(2\varepsilon)}{|A_1|^2 + |A_2|^2 + 0.5\left(|A_1|^2 - |A_2|^2\right)\cos(2\varepsilon)} \qquad (9)$$

Assuming A_1 and A_2 are equal after CPG1, thus $C = \cos(2\varepsilon)$. A Taylor series development allows to approximate this contrast ratio by $C \approx 1 - 2\varepsilon^2$. Thus a small error angle ε leads to a decrease of twice the square of its value on the contrast ratio.

6. CONCLUSIONS

CPGs have outstanding features that facilitate a really compact setup with few optical elements. Thanks to polarization states separation, an in line set-up is made possible. Thus the installation suffers less from misalignment tilt and is easier to build. As it is a symmetrical common path interferometer, short coherence length source can be used. Although great care must be taken that the spatial coherence of the source is guaranteed. The output polarization states of the diffracted beams even ease phase shifting methods with a rotating polarizer or a polarizer array. We believe that the suggested interferometer is versatile and could be used for example in fringe projection profilometry, imaging spectrometry or Fourier transform spectrometry.

In this work we also outline the main drawbacks that could occur during the manufacturing of the device. Further work should compare the performances of such a shearographic device with more traditional shearography set-ups.

A further step in this approach would be to use Achromatic Polarization Gratings [24] and broadband polarizers to be able to easily change the source depending on the absorption/reflection of the object under investigation.

Thanks to F. Languy and G. Martin for their precious help. The authors are grateful to the financial support of the MINT Project from the Marshall program of the Walloon Government.

References

1. D. Malacara, “Optical Shop Testing” (Wiley series in Pure and applied Optics, 2007), Chap. 16.
2. D. Francis, R. P. Tatam and R. M. Groves, “Shearography technology and applications: a review”, Meas. Sci. Technol. 21 (10), 2001-2029 (2010).
3. W. Steinchen, L. Yang, “Digital Shearography: Theory and Application of Digital Speckle Pattern Shearing Interferometry” (SPIE Press Book, USA, 2004), Chap. 2 & Chap 4.
4. V. Rosso, Y. Renotte, S. Habraken, Y. Lion, F. Michel, V. Moreau, and B. Tilkens, “Almost-common path interferometers using the separation of polarization states for digital phase-shifting shearography”, Opt. Eng. 46, 105601 (2007).
5. P. Blain, F. Michel, Y. Renotte, and S. Habraken, “Using a Savart plate in optical metrology”, Proc. SPIE 7791, 779107 (2010)
6. M. Born and E. Wolf, “Principles of Optics”, 830-831 (Cambridge University Press, 2003).
7. F. Michel, Y. Renotte and S. Habraken, “Measurement of the defect size by shearography or other interferometric techniques”, Optical Engineering, Opt. Eng. 51, 033602 (2012)
8. H. M. Shang, F. S. Chau, C. J. Tay and S. L. Toh, “Estimating the depth and width of arbitrarily-oriented disbonds in laminates using shearography”, Journal of Nondestructive Evaluation 9 (1), 19-26 (1990).
9. B. Kilosanidze and G. Kakauridze, “Polarization-holographic gratings for analysis of light. 1.Analysis of completely polarized light,” Appl. Optics 46, 1040–1049 (2007).
10. M. Schadt, H. Seiberle, and A. Schuster, “Optical patterning of multi-domain liquid crystal displays with wide viewing angles," Nature 381, 212-215(1996).
11. T. Scharf, “Polarized light in liquid crystals and polymers” (Wiley Inter science, 2007).
12. F. Gori, “Measuring Stokes parameters by means of a polarization grating”, Opt. Lett. 24 (9), 584-586 (1999).
13. C. Oh and M. J. Escuti, "Time-domain analysis of periodic anisotropic media at oblique incidence: an efficient FDTD implementation", Opt. Express 14, 11870-11884 (2006).
14. H. Ono, M. Nakamura and N. Kawatsuki, “Conversion of circularly polarized light into linearly polarized light in anisotropic phase gratings using photo-cross-linkable polymer liquid crystals”, Appl. Phys. Lett. 90, 231107(2007).
15. C. G. Someda, “Far field of polarization gratings”,Opt. Lett. 24 (23), 1657-1659 (1999)
16. I. Kallioniemi, T. Ammer and M. Rossi, “Optimization of continuous profile blazed gratings using rigorous diffraction theory”, Opt. Commun., 177, 15–24 (2000)
17. S. R. Nersisyan, N. V. Tabiryan, D. M. Steeves and B. R. Kimball, “Optical axis gratings in liquid crystals and their use for polarization insensitive optical switching”, Journal of Nonlinear Optical Physics & Materials, 18 (1), 1–47 (2009).
18. S. R. Nersisyan, N. V. Tabiryan, L. Hoke, D. M. Steeves and B. Kimball, “Polarization insensitive imaging through polarization gratings”, Opt. Express, 17 (3), 1817-1830 (2009).
19. J. A. Davis, B. Melvin L. Pascoguin, I. Moreno, and A. Nava-Vega, “Circular-polarization-splitting common-path interferometer based on a zero-twist liquid-crystal display”, Opt. Lett. 34 (9), 1486-1488 (2009).
20. J. Millerd, N. Brock, M. North-Morris, M. Novak and J.Wyant, “Pixelated Phase-Mask Dynamic Interferometer” , Proc. SPIE 5531, 304-314 (2004)
21. G. H. Kaufmann, “Phase measurement in temporal speckle pattern interferometry using the Fourier transform method with and without a temporal carrier”, Opt. Commun. 217, 141–149 (2003).
22. M. Cherbuliez, P. Jacquot and X. Colonna de Lega, “Wavelet processing of interferometric signals and fringe patterns”, Proc. SPIE, 3813,692-702 (1999).
23. H.A. Aebischer, S. Waldner, “A simple and effective method for filtering speckle-interferometric phas fringe patterns”, Opt. Commun. 162, 205-211 (1999).
24. C. Oh and M. J. Escuti, Achromatic diffraction from polarization gratings with high efficiency, Opt. Lett. 33 (20), 2287-2289 (2008).

4.4 Conclusions and perspectives

In this chapter, we presented the polarization states separator. It is a 1D continuous SR characterized by a period of approximately 15μ m. The retarder diffracts the incident beam into several polarization orders with their own polarization states. The number of diffracted beams depends on the polarization state of the incident beam and the birefringence of the retarder. Its application to shearography was presented with the numerical simulations and the experimental tests.

In the future, two major upgrades could be performed. Using liquid crystals which allow a variation of their orientation in the thickness would achieve achromatic polarization gratings [6, 9]. A new setup allowing fringe projection and shearography with the same element could be implemented [10].

Chapter 4 references

[1] S.Huard, [*Polarisation de la lumière*], Masson, 1 ed. (1993).

[2] I.Kallioniemi, T.Ammer, and M.Rossi, "Optimization of continuous-profile blazed gratings using rigorous diffraction theory," *Opt. Commun.* **177**(1), 15–24 (2000).

[3] H.Ono, M.Nakamura, and N.Kawatsuki, "Conversion of circularly polarized light into linearly polarized light in anisotropic phase gratings using photo-cross-linkable polymer liquid crystals," *Appl. Phys. Lett.* **90**(23) (2007).

[4] F.Gori, "Measuring stokes parameters by means of a polarization grating," *Opt. Lett.* **24**(9), 584–586 (1999).

[5] S.R.Nersisyan, N.V.Tabiryan, D.M.Steeves, and B.R.Kimball, "Optical axis gratings in liquid crystals and their use for polarization insensitive optical switching," *Journal of Nonlinear Optical Physics Materials* **18**(01), 1–47 (2009).

[6] C.Oh and M.J.Escutti, "Achromatic polarization gratings as highly efficient thin-film polarizing beamsplitters for broadband light," in [*Proc.SPIE*], **6682**, 668211–668211–12, Society of Photo-Optical Instrumentation Engineers SPIE (2007).

[7] M.J.Escutti, C.Oh, C.Carlos, C.Bastiaansen, and D.J.Broer, "Simplified spectropolarimetry using reactive mesogen polarization gratings," in [*Proc.Spie*], **6302**, 630207–630207–11, Society of Photo-Optical Instrumentation Engineers SPIE (2006).

[8] P.Blain, P.Piron, Y.Renotte, and S.Habraken, "An in-line shearography setup based on circular polarization gratings," *Optics and Lasers in Engineering* **51**, 1053–1059 (2013).

[9] C.Oh and J.Escutti, "Achromatic diffraction polarization gratings with high efficiency," *Opt. Lett.* **33**, 2287–2289 (2008).

[10] P.Blain, F.Michel, P.Piron, Y.Renotte, and S.Habraken, "Combining shearography and interferometric fringe projection in a single device for complete control of industrial applications," *Optical Engineering* **52**(8), 084102–084102 (2013).

Part III

Applications of 2D space-variant retarders

5

Vortex retarders

Contents

In the previous chapters, we exposed applications of 1D SR recorded using the superimposition of 2 differently polarized beams. This chapter will present the vortex retarders. They are specific kind of 2D SR characterized by a rotation of their fast axis.
The retarders will be described and classified. The recording systems based on polarization holography will be shown. The first vortex retarders recorded only by polarization holography will be detailed and finally a small sensitivity analysis will be performed to present the variations due to experimental conditions.

5.1 Introduction

Vortex retarders are specific retarders which convert an incident beam into an optical vortex.
Optical vortices are particular beams characterized by a phase singularity at their center just like a whirlpool. The form of the phase over the wavefront is the same as a screw dislocation $\phi = \exp \imath\theta$ [1, 2, 3], where θ is the azimuthal coordinate.
Just like a whirlpool, at the center of the vortex beam, the phase is undefined and the intensity of the beam is null.
To generate a vortex beam, two kinds of retarders exist: scalar retarders and vectorial retarders.
For the scalar retarders, the variation of the phase is achieved thanks to a variation of the thickness of the retarder. While transmitted through an helix shaped retarder, the beam acquires the desired wavefront.
The vectorial retarders do not implement a material ramp. They locally manipulate the polarization of the beam to create the required wavefront. Usually, vectorial vortex retarders are made of birefringent material characterized by a rotation of their optical axis (see Fig 5.1).

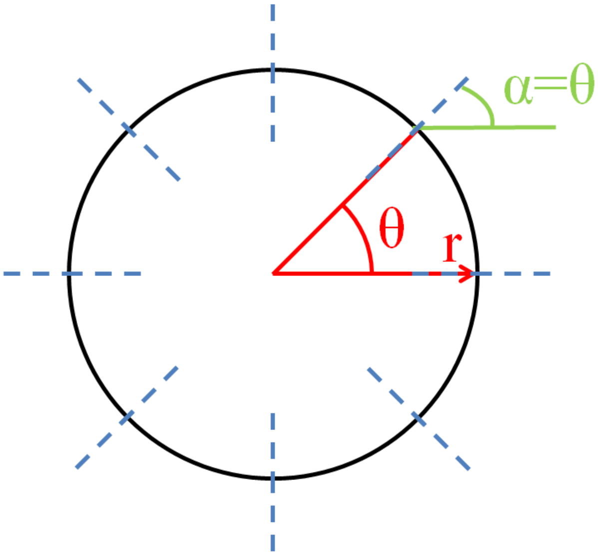

Figure 5.1: Representation of the rotation of the fast axis in a vortex retarder, the orientation of the fast axis is pictured by blue dashed lines.

Since scalar retarders implement a material phase ramp, the difficulty is to achieve an accurate and continuous etching of the surface. The thickness of the retarder must be accurate to a very small fraction of λ/n. Moreover, scalar vortices exhibit a strong dependence on the wavelength, the phase retard $\Delta\psi$ being a function of the wavelength [4]

$$\Delta\psi = \frac{2\pi}{\lambda}\left[n(\lambda) - 1\right] h, \tag{5.1}$$

where h is the thickness of the material. As a consequence, this dependence to the wavelength restricts the usage of scalar retarders to applications with a short spectral band or a monochromatic light.

In the present thesis, we worked on the recording of vectorial vortex retarders using polarization holography and LCP. We will shape the recording electric field to achieve the desired rotation of the fast axis of the retarder. The next section will describe the origin of the phase and the mathematical model of the vortices.

5.2 Mathematical description

5.2.1 Pancharatnam phase and topological charge

The distinctive feature of a vortex retarder is the rotation of the fast axis. It will convert a uniformly polarized beam into a space-variant one.
Two points of the beam possess a phase difference: the Pancharatnam phase ϕ_P.
It was described by Pancharatnam as a geometric phase during the observation of the superimposition of two differently polarized beams [5]. He associated the variation of the observed intensity to a phase difference between the beams.

Two modern descriptions exist [2, 4, 6, 7, 8]. The first one is more geometrical while the other one is based on the Jones formalism.

- The geometrical description relies on the Poincaré sphere of polarization and is used to compute the phase difference between two beams with a variation of the polarization state of one of them.
  It was demonstrated that a cyclic change of the polarization state of a beam generates a phase retard. The retard depends on the polarization states achieved. It is equal to half of the area comprised between the polarization states on the Poincaré sphere [9].
  As an example, we will study the case of a linearly polarized beam transmitted by two quarter-wave plates and a half-wave plate. The incident polarization is a linear one and it is represented by point A (see Figure 5.2). After the quarter-wave plate with an angle of 45° between the incident polarization and the orientation of the fast axis, the beam becomes circularly polarized (point B). The other quarter-wave plate converts the circular polarization into a linear one with a different orientation (point C). Finally, the beam recovers its initial polarization state thanks to the half-wave plate. It can be shown that the beam acquires an extra phase retard compared to a beam transmitted by the same birefringent plates with their fast axis aligned to the incident polarization. The extra phase retard is equal to half of the solid angle subtended by the trajectory $ABCA$: Ω

$$\phi_P = \Omega/2. \tag{5.2}$$

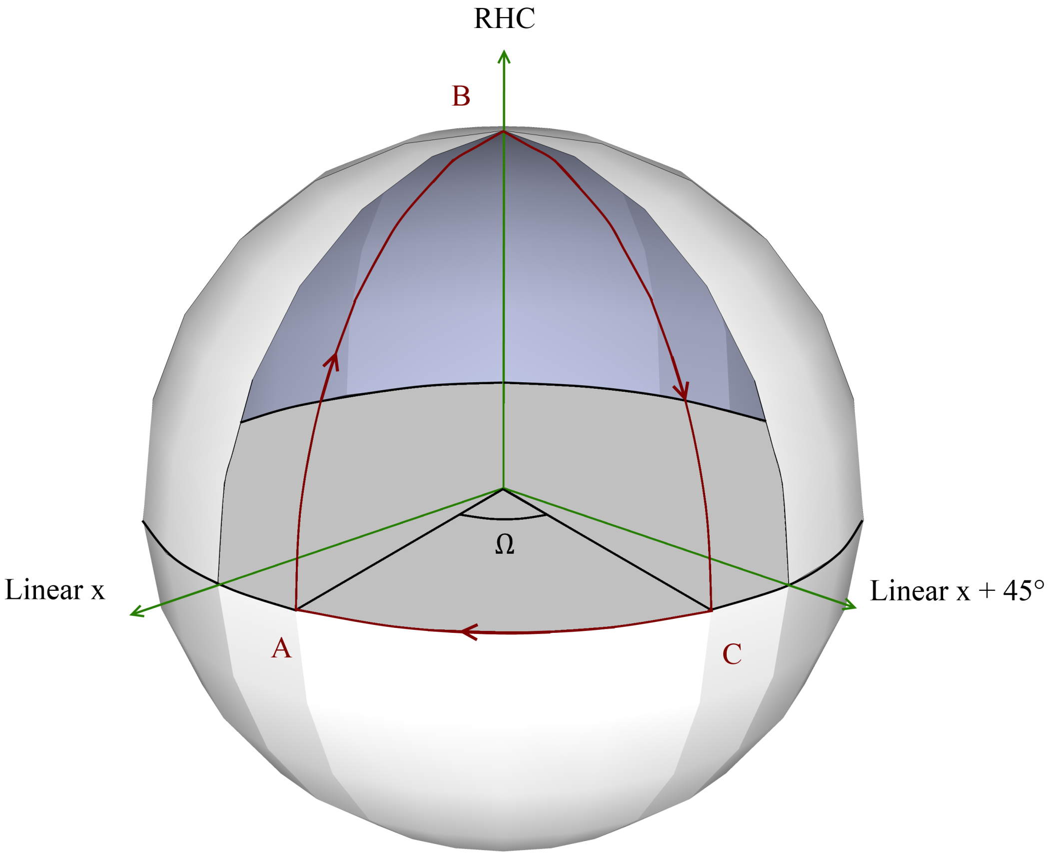

Figure 5.2: Representation of a cyclic change of polarization state, the red lines on the Poincaré sphere represents the path of the beam.

- The other description is more appropriate for the phase difference between two points in a non uniformly polarized beam originated from a uniformly polarized one [10].
  In this configuration, the Pancharatnam phase is computed as the inner product of the polarization of the beams using the Jones formalism and the helical base [2, 11].
  For example, for two points A and B of the same beam:

$$\phi_P = \arg \langle J_B, J_A \rangle . \tag{5.3}$$

Since we are working with space-variant retarders and space-variant polarization, the second description will be used.

Another characteristic of the vortex beam is the topological charge l. It is defined as the number of times the Pancharatnam phase accumulates 2π along a closed path surrounding the singularity [2, 4]:

$$l = \frac{1}{2\pi} \oint \nabla \phi_P ds. \tag{5.4}$$

The next subsection will present the mathematics of a coronagraph and its Panchartnam phase.

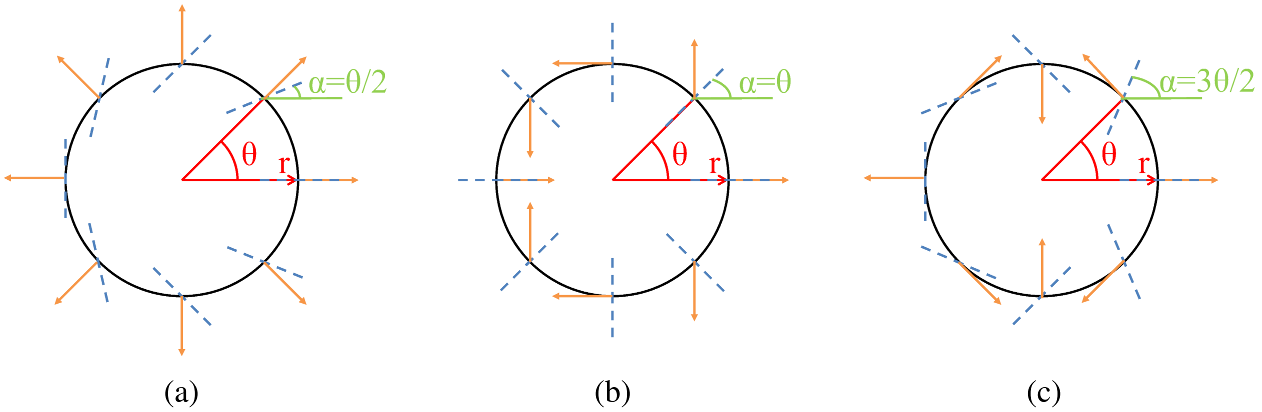

Figure 5.3: Representation of several vortex retarders. The orientation of the fast axis is represented by dashed blue lines. The polarization of the transmitted beams for an incident horizontaly polarized beam is pictured by orange arrows: (a) describes a retarder with a rotation of 180° of its fast axis leading to $l = 1$. (b) Stands for a rotation of 360° and $l = 2$. (c) Represents a rotation of 540° and $l = 3$.

5.2.2 Vortex nature of retarders with a rotating fast axis

The vortex nature of our retarder will be presented under the Jones formalism.
A uniform birefringent wave-plate characterized by a horizontal optical axis is represented by the following equation [12, 13].

$$HP = \begin{pmatrix} \eta_e e^{-\frac{\imath\phi}{2}} & 0 \\ 0 & \eta_o e^{\frac{\imath\phi}{2}} \end{pmatrix} \tag{5.5}$$

where η_o is the transmittance along the ordinary direction of polarization, η_e is the transmittance along the extraordinary direction of polarization and ϕ is the ordinary-extraordinary phase shift. For a perfect half-wave plate $\eta_e = \eta_o = 1$ and $\phi = \pi$.

To represent a SR, the previous matrix is rotated by an angle α depending on the position in the retarder $\alpha = \alpha(r, \theta)$ with r and θ the polar coordinates in the retarder and α the angle between the optical axis and the horizontal.

$$SR = R^{-1}[\alpha(r,\theta)]\, HP\ R[\alpha(r,\theta)] \tag{5.6}$$

Where $R[\alpha(r,\theta)]$ represents the rotation matrix, $R = \begin{pmatrix} \cos\alpha(r,\theta) & -\sin\alpha(r,\theta) \\ \sin\alpha(r,\theta) & \cos\alpha(r,\theta) \end{pmatrix}$.

For a theoretical lossless birefringent plate($\eta_o = \eta_e = 1$), the space-variant retarder is finally represented by

$$\cos(\frac{\phi}{2})\begin{pmatrix} 1 & 0 \\ 0 & 1 \end{pmatrix} - \imath\sin(\frac{\Delta\phi}{2})\begin{pmatrix} -\cos(2\alpha) & \sin(2\alpha) \\ \sin(2\alpha) & \cos(2\alpha) \end{pmatrix}. \tag{5.7}$$

The model is splitted into two different parts:

- the imaginary part represents a perfect polarization rotator,
- the real part represents a system which does not modify the polarization of the beam.

For a perfect half-wave plate, $\phi = \pi$, the real part is null. By simplifying the imaginary part, the retarder is represented by

$$SV = \begin{pmatrix} -\cos(2\alpha) & \sin(2\alpha) \\ \sin(2\alpha) & \cos(2\alpha) \end{pmatrix} \tag{5.8}$$

For small phase errors, $\phi = \pi + \epsilon$. By multiplying by $\imath$ the equation 5.7, the retarder is represented by

$$\begin{pmatrix} -\cos(2\alpha) & \sin(2\alpha) \\ \sin(2\alpha) & \cos(2\alpha) \end{pmatrix} + \imath\epsilon \begin{pmatrix} 1 & 0 \\ 0 & 1 \end{pmatrix}. \tag{5.9}$$

For a nearly perfect half-wave plate the effect of the phase error is proportionnal to the phase default ϵ and its effect can be reduced by an appropriate polarization filtering. To highlight the vortex nature of the retarder, the SR is projected on the helical basis thanks to the matrix $U = \frac{1}{\sqrt{2}} \begin{pmatrix} 1 & 1 \\ -\imath & \imath \end{pmatrix}$.
In the helical basis, the retarder is represented by

$$SR_{helic} = U^{-1} SR\ U = \frac{1}{2} \begin{pmatrix} \eta_e e^{-\frac{\imath\phi}{2}} + \eta_o e^{\frac{\imath\phi}{2}} & \left(\eta_e e^{-\frac{\imath\phi}{2}} - \eta_o e^{\frac{\imath\phi}{2}}\right) e^{2\imath\alpha} \\ \left(\eta_e e^{-\frac{\imath\phi}{2}} - \eta_o e^{\frac{\imath\phi}{2}}\right) e^{-2\imath\alpha} & \eta_e e^{-\frac{\imath\phi}{2}} + \eta_o e^{\frac{\imath\phi}{2}} \end{pmatrix}. \tag{5.10}$$

In this basis, the retarder can still be divided into two terms. The first one will affect the phase and the polarization of the incoming beam while the second term does not affect the polarization state of the incoming beam and is a function of the mask's defaults ($\eta_e \neq 1\, \eta_o \neq 1$, $\phi \neq \pi$). This decomposition is obtained thanks to the definition of two coefficients M and D depending on the birefringent properties of the retarder. M will multiply the *mask* matrix and D will multiply the *default* matrix.
With $M = \frac{1}{2}(\eta_e e^{-\frac{\imath\phi}{2}} - \eta_o e^{\frac{\imath\phi}{2}})$ and $D = \frac{1}{2}(\eta_e e^{-\frac{\imath\phi}{2}} + \eta_o e^{\frac{\imath\phi}{2}})$, the retarder becomes

$$SR_{helic} = M \begin{pmatrix} 0 & e^{2\imath\alpha} \\ e^{-2\imath\alpha} & 0 \end{pmatrix} + D \begin{pmatrix} 1 & 0 \\ 0 & 1 \end{pmatrix}. \tag{5.11}$$

For a perfect half-wave ($\eta_e = \eta_o = 1$ and $\phi = \pi$) $M = -\imath$ and $D = 0$. By simplifying the $-\imath$ factor, the retarder is represented by the following equation:

$$\begin{pmatrix} 0 & e^{2\imath\alpha} \\ e^{-2\imath\alpha} & 0 \end{pmatrix}. \tag{5.12}$$

For a radial orientation of the fast axis $\alpha = \theta$[6], the retarder becomes

$$\begin{pmatrix} 0 & e^{2\imath\theta} \\ e^{-2\imath\theta} & 0 \end{pmatrix}. \tag{5.13}$$

In the helical basis, the unit vectors are the right and left handed circular polarization states:

$$RC_{in} = \begin{pmatrix} 1 \\ 0 \end{pmatrix}, \ LC_{in} = \begin{pmatrix} 0 \\ 1 \end{pmatrix}.$$

After the retarder, these two beams become

$$RC_{out} = \begin{pmatrix} 0 \\ e^{-2\imath\theta} \end{pmatrix}, \ RL_{out} = \begin{pmatrix} e^{2\imath\theta} \\ 0 \end{pmatrix}.$$

---

[6] A radial orientation of the optical axis for a half-wave plate will generate a vortex with topological charge of 2 while higher rotation speed of the fast axis will generate higher topological charges.

The transmitted beam is orthogonally polarized to the incident beam and possesses a phase modification of 2θ.
The Pancharatnam phase between two points in the resulting beam at the same radius but at a different angle $A(r_1, \theta = 0)$ and $B(r_1, \theta = \theta_B)$ is $2\theta_B$. Thanks to this result, we are able to plot the Pancharatnam phase for the whole retarder and conclude that a retarder with a radial orientation of its optical axis is indeed a vortex generator.

In this thesis we focused on vortex retarders with a topological charge of one and two. For these retarders, the orientation of the fast axis is given b: $\alpha = \theta/2$ for $l = 1$ and $\alpha = \theta$ for $l = 2$. The next pictures will present their main characteristics such as a representation of their fast axis orientation (Figures 5.4 and 5.5), the transmitted intensity when the retarder is between two parallel polarizers (Figure 5.6) and the Pancharatnam phase inside the vortex beam (Figure 5.7).

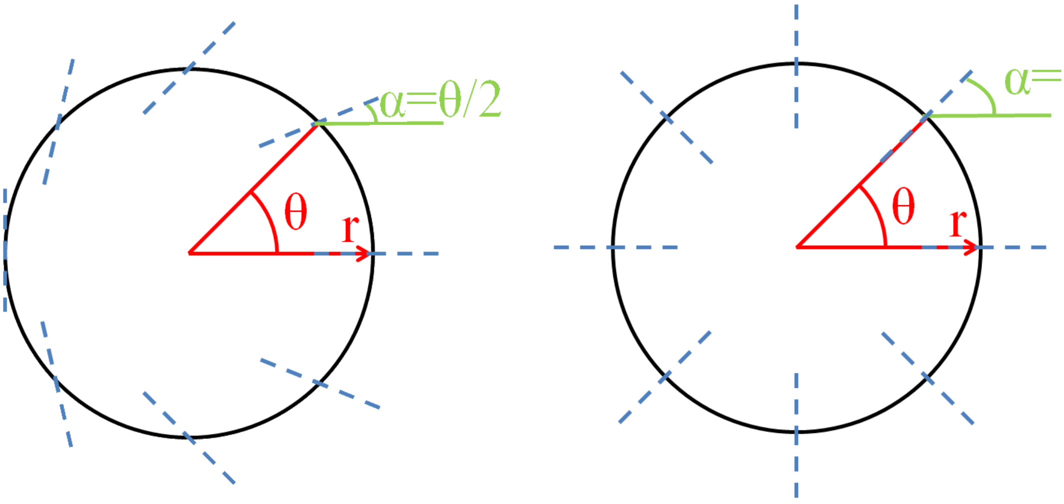

(a) (b)

Figure 5.4: Representation of the fast axis orientation (dashed blue) for two vortices of different topological charges: (a) is characterized by a rotation of its fast axis equal to π generating vortices with $l_p = 1$. (b) Is characterized by a rotation of its fast axis equal to 2π generating vortices with $l_p = 2$.

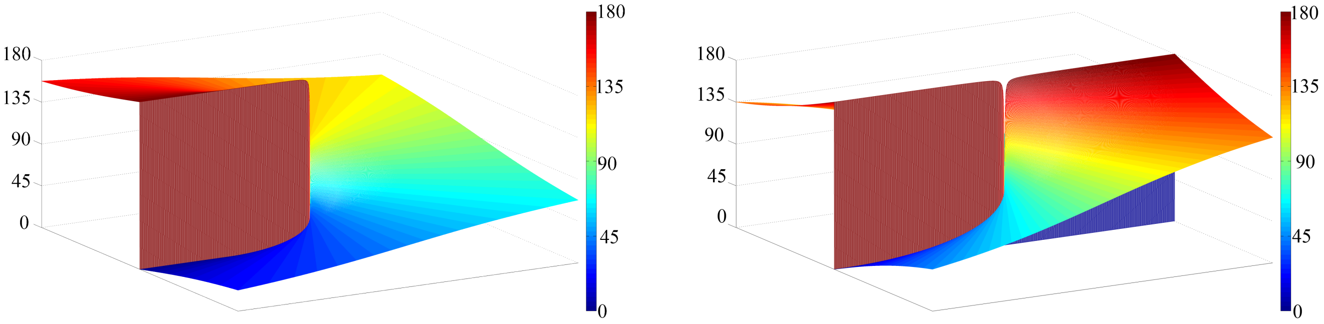

(a) (b)

Figure 5.5: Representation of the retarders fast axis orientation in degrees: (a) represents a total rotation of 180°, (b) represents a total rotation of 360°. The discontinuity at the right side of (b) is caused by the chosen scale, the orientation being a continuous function in reality.

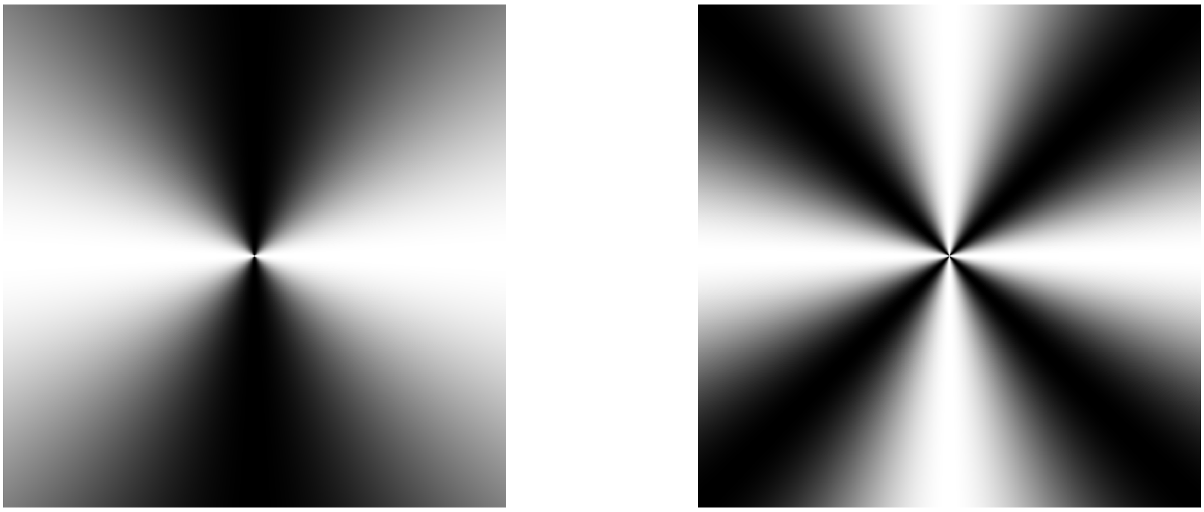
(a) (b)

Figure 5.6: Representation of the transmitted intensity for the vortex retarders between two parallel linear polarizers: (a) is characterizd by 2 bright and two dark areas while (b) is characterized by four bright and four dark areas.

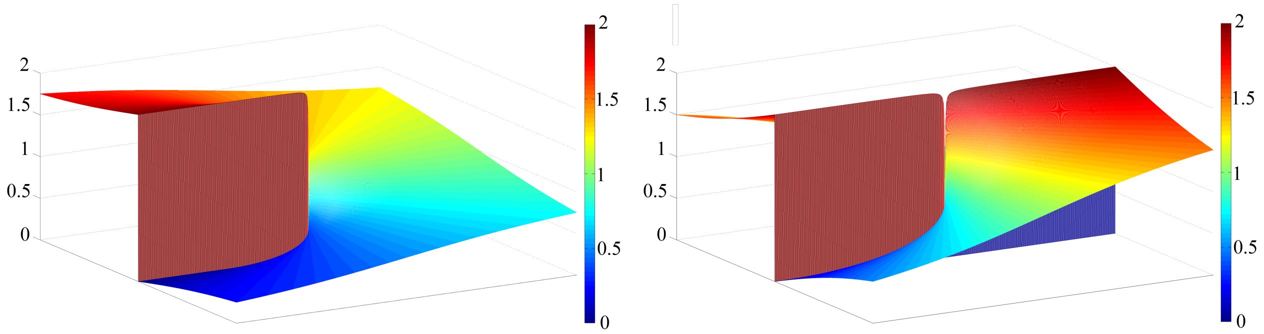

(a) (b)

Figure 5.7: Representation of the Pancharatnam phase inside the beam transmitted by the vortex retarders as a multiple of π. The maximum phase retard is 2π for (a) and 4π for (b). Once again the discontinuity on the left side of (b) is caused by the scale, the phase varying smoothly from 0 to 4π.

The following section will present several systems of 4 beams differently polarized which are able to record vortex retarders.

5.3 Recording using polarization holography

As mentioned in 2.1.3, we expanded polarization holography to 4 beams. Several systems achieve the recording of vortex retarders with $l = 1$ and $l = 2$. Their resulting electric fields deviate from the ideal one: the intensity or the directionality of the fields drop down to zero near the phase singularity. The composition of the systems, the analysis of the recording electric fields and the first determination of the experimental limits are presented in the following article [14].

Polarization holography for vortex retarders recording

Pierre Piron,[1],* Pascal Blain,[1] Serge Habraken,[1] and Dimitri Mawet[2]
[1]Hololab, University of Liège, 17 Allée du 6 Août, 4000 Liège, Belgium
[2]European Southern Observatory, Alonso de Córdova 3107, Vitacura 7630355, Santiago, Chile
*Corresponding author: pierre.piron@ulg.ac.be

Received 9 July 2013; revised 8 September 2013; accepted 10 September 2013;
posted 11 September 2013 (Doc. ID 193331); published 1 October 2013

We present an original static recording method for vortex retarders (VRs) made from liquid crystal polymers (LCPs) using the superimposition of several polarized beams. VRs are birefringent plates characterized by a rotation of their fast axis about their center. The new method is based on polarization holography and photo-orientable LCP. Combining several polarized beams induces the polarization patterns required for the recording process of VRs without mechanical action. A mathematical description of the method, the outcomes of the numerical simulations, and the first experimental results are presented.

OCIS codes: (090.0090) Holography; (090.2880) Holographic interferometry; (260.5430) Polarization; (160.3710) Liquid crystals.
http://dx.doi.org/10.1364/AO.52.007040

1. Introduction

Our goal is to develop a new method to produce vortex retarders (VRs) without mechanical action using the superimposition of several polarized beams. VRs are particular space-variant retarders (SRs), i.e., birefringent plates characterized by a nonuniform orientation of their fast axis (see Fig. 1). The fast axis in a VR rotates around the center of the plate inducing a phase dislocation of the form $\exp(il\theta)$, where l is the topological charge and θ the azimuthal angle (see Fig. 2).

The topological charge is defined as the number of times the Pancharatnam phase (ϕ_p) accumulates 2π along a closed path surrounding the phase singularity [1,2]:

$$l = \frac{1}{2\pi} \oint \nabla \phi_p \mathrm{d}s.$$

The Pancharatnam phase between two points (Γ and Ω) in a nonuniformly polarized beam is defined as the argument of the inner product of their Jones vectors, $\phi_p = \arg\langle\Gamma|\Omega\rangle$ [1,3,4].

Nowadays, there are many applications of SR and VR, as follows:

- SRs are used as polarization analyzers or polarization states separators. A SR modifies the polarization parameters of the beam or diffracts it in specific polarization states. By analyzing the intensity of the transmitted or diffracted beams, one can compute the Stokes parameters of the incoming beam [5,6].
- VRs can be used as polarization converters to transform a uniformly linearly polarized beam into a radially polarized one [7–9]. Radially polarized beams lead to several applications such as tighter focusing [10–12], optimal surface plasmon excitation by a focusing beam [12,13], and optical tweezers [12,14].
- SR and VR have already been used in phase mask coronagraphy [2,15–19]. The goal of coronagraphy is to dim the light of a star to diminish the contrast between the star and its fainter companions.

Presently, to our knowledge, no method is able to build VR with different topological charges without mechanical action (e.g., rotation of a mask, translation of lenses, etc.) or multiple exposures of the alignment layer. In this paper, we propose a purely optical and versatile method based on polarization

1559-128X/13/287040-09$15.00/0

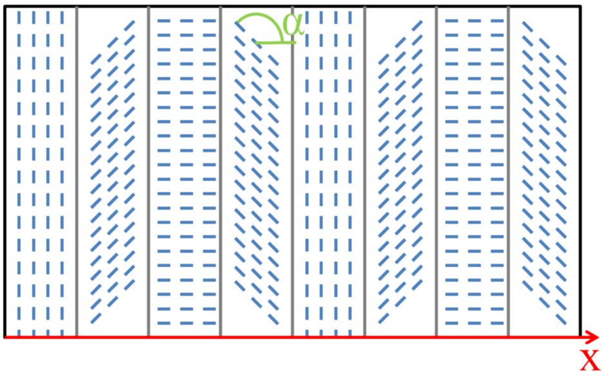

Fig. 1. Schematic representation of the fast axis (in dashed blue) for a SR, x being the direction of variation of the fast axis in the SR and α the orientation of the fast axis.

holography and liquid crystal polymers (LCPs). Using the superimposition of several polarized beams, we will shape the polarization of the resulting beam to obtain the required polarization pattern of the recording beam.

The paper contains the following sections. In Section 2, we briefly detail several methods of SR and VR building. In Section 3, we present the theory of polarization holography, its application for two circularly polarized beams of opposite handedness, and its expansion to four beams with arbitrary polarization states. In Section 4, we describe the parameters of the polarization ellipse resulting from the superimposition and the analysis of the resulting beams as recording ones. In Section 5, we expose our first experimental results.

2. Current Recording Methods

Several materials and methods are already used to build SR and VR: assembling several birefringent plates with different fast axis orientations [20], building of zero order gratings (ZOG) characterized by a variation of the grating structure orientation [16,17,21], and designing the fast axis pattern by aligning liquid crystals (LCs) [2,6–8,19,22–24].

- The easiest way to produce a SR is to laterally join together several half-wave plates with a variation of their fast axis orientation to form one birefringent plate characterized by a discrete variation of its fast axis [12,20]. Unfortunately, due to the discreteness, the polarization is hardly the desired one. Moreover, the transmitted beam exhibits dead zones, i.e., zones with no transmitted light due to the glued interfaces [12].
- Another way to produce SR and VR is to use ZOG. ZOG only diffract the zeroth-order due to their groove period Λ. The ZOG condition [16,17,21] is

$$\frac{\Lambda}{\lambda} \leq \frac{1}{n_{\mathrm{I}} \sin \chi + \max(n_{\mathrm{I}}, n_{\mathrm{III}})}, \tag{1}$$

where λ is the wavelength, χ is the angle of incidence, and n_{I}, n_{III} are the refractive indices of the incident and output media, respectively.

Theoretically and experimentally, it was demonstrated that ZOG can be used as birefringent plates [17,21]. The birefringent properties of the identical plate depend on the grating parameters, such as the grating period, the filling factor, the refractive indices, and the grating vector $\mathbf{K}$, perpendicular to the grating grooves with $|\mathbf{K}| = 2\pi/\Lambda$.

To achieve the fast axis variation, the orientation of the grating vector must be nonuniform. Two kinds of variation exist: discrete and continuous variation.

Discrete gratings contain several areas of uniform $\mathbf{K}$, the vector's orientation being modified from one area to the other one. Due to the discrete variation, the transmitted beam can exhibit dead zones at the edges reducing the performances of the retarder for several applications [5,15]. Continuous gratings exhibit a continuous variation of the length or of the orientation of $\mathbf{K}$, the continuity being assured by $\nabla \wedge \mathbf{K} = 0$. The drawback of continuous gratings is the difficulty to achieve the optimal grating parameters while preserving the continuity of the grating structure [17,21].

- LCs are already used to record SR and VR. Their ability to easily achieve a nonuniform orientation implies a simple recording process of continuous SR. Subject to an electromagnetic field, LC orient themselves according to this field. Several recording methods already use this property, e.g., rubbing an alignment layer with a magnetic rod to imprint the fast axis pattern [7,22], sending an electric current through a hole electrode under the substrate to create a radial electric field [23], or exposing piece by piece an alignment layer to several uniformly polarized beams using rotation mounts, apertures, or cylindrical lenses [2,8,19].

These techniques have already been used but none of them is able to achieve the recording of VR of different topological charges without mechanical action or areas containing disoriented LC.

A static method based on polarization holography and LC is already used to record SR with a one-dimensional variation of their fast axis orientation [6,22,24–26]. Inside the area of superimposition, the resulting electric field is characterized by a variation of its orientation. The LC will be used to record the variation to realize a unidimensional SR. We propose to expand polarization holography to four beams like Ruiz *et al.* [27] to record retarders with a 2D variation of their fast axis. To be specific, we will record VR with topological charges of 1 and 2.

3. Polarization Holography

Our goal is to produce VR with topological charges of 1 and 2 (see Fig. 2). Using LCP allows for the recording of the orientation of the local electric field. Polarization holography is used to shape the resulting electric fields to imprint a specific fast axis pattern. Kilosanidze and Kakauridze [28] developed a mathematical description of the local polarization ellipse for the superimposition of two generic coherent beams A and B

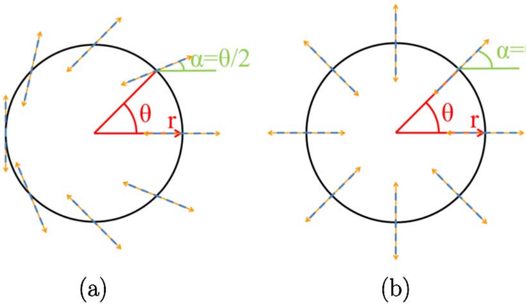

(a) (b)

Fig. 2. Schematic representation of the fast axis (in dashed blue). (a) A VR with $l = 1$ and (b) a VR with $l = 2$, α being the orientation of the fast axis and (r, θ) the polar coordinates. The orange arrows represent the ideal electric field required to record the retarders with LCP.

$$A = \begin{pmatrix} A_x \\ A_y \ \exp(i\phi_A) \end{pmatrix} \exp(i\omega t),$$
$$B = \begin{pmatrix} B_x \\ B_y \ \exp(i\phi_B) \end{pmatrix} \exp(i\delta)\exp(i\omega t), \tag{2}$$

where A_x and B_x are the amplitude modules of the horizontal component of A and B, A_y and B_y are the amplitude modules for the vertical components, ϕ_A and ϕ_B are the phase differences between the horizontal and vertical components, ω is the pulsation of the beams, and δ is the phase difference between the two beams. At the recording plane, the resulting electric field Σ can be written as

$$\Sigma = \begin{pmatrix} A_x + B_x \ \exp(i\delta) \\ A_y \ \exp(i\phi_A) + B_y \ \exp(i\phi_B + i\delta) \end{pmatrix} \exp(i\omega t). \tag{3}$$

The local polarization ellipse is described by the real part of the electric field and is written as

$$\Re(\Sigma) = \mathbf{p} \cos(\omega t) + \mathbf{q} \sin(\omega t), \tag{4}$$

where

$$\mathbf{p} = \begin{pmatrix} A_x + B_x \cos(\delta) \\ A_y \cos(\phi_A) + B_y \cos(\phi_B + \delta) \end{pmatrix}$$

and

$$\mathbf{q} = -\begin{pmatrix} B_x \sin(\delta) \\ A_y \sin(\phi_A) + B_y \sin(\phi_B + \delta) \end{pmatrix}.$$

The ellipse is characterized by three parameters: I_1 the intensity along the largest axis, I_2 the intensity along the smallest axis, and θ the angle between the largest axis and the horizontal direction (see Fig. 3).

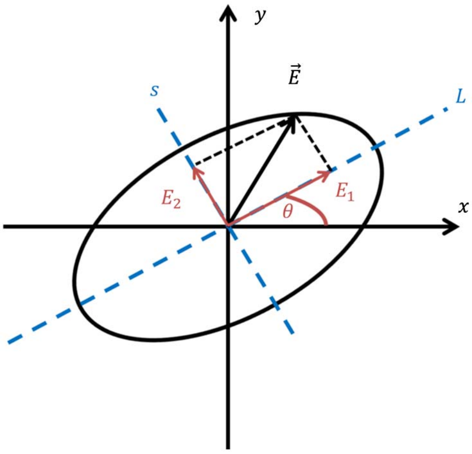

Fig. 3. Schematic representation of the local polarization ellipse. The largest (L) and the smallest (s) axis are pictured in dashed blue.

These parameters are given by

$$\begin{aligned} I_{1,2} &= \frac{1}{2}[(p_x^2 + p_y^2) + (q_x^2 + q_y^2)] \\ &\quad \pm \frac{1}{2}\sqrt{[(p_x^2 - p_y^2) + (q_x^2 - q_y^2)]^2 + 4(p_x p_y + q_x q_y)^2}, \\ \sin(2\theta) &= \frac{2(p_x p_y + q_x q_y)}{\sqrt{[(p_x^2 - p_y^2) + (q_x^2 - q_y^2)]^2 + 4(p_x p_y + q_x q_y)^2}}, \\ \cos(2\theta) &= \frac{(p_x^2 - p_y^2) + (q_x^2 - q_y^2)}{\sqrt{[(p_x^2 - p_y^2) + (q_x^2 - q_y^2)]^2 + 4(p_x p_y + q_x q_y)^2}}. \end{aligned} \tag{5}$$

As an example, it can be shown that the superimposition of two circularly polarized beams of opposite handedness results in an electric field of uniform intensity and characterized by a variation of its orientation.

Circularly polarized beams of opposite handedness are characterized by

$$A_x = A_y = B_x = B_y = \sqrt{2}/2,$$
$$\phi_A = -\pi/2, \qquad \phi_B = \pi/2.$$

With these parameters, $\mathbf{p}$ and $\mathbf{q}$ are given by

$$\mathbf{p} = \sqrt{(2)}/2\begin{pmatrix} 1 + \cos(\delta) \\ -\sin(\delta) \end{pmatrix},$$
$$\mathbf{q} = -\sqrt{(2)}/2\begin{pmatrix} 1 + \sin(\delta) \\ -1 + \cos(\delta) \end{pmatrix}.$$

Finally, the local polarization ellipse is described by

$$I_1 = 2, \ \ I_2 = 0, \ \ \sin(2\theta) = \sin(\delta), \ \ \cos(2\theta) = \cos(\delta). \tag{6}$$

Using these parameters, the resulting electric field inside the superimposition area can be characterized.

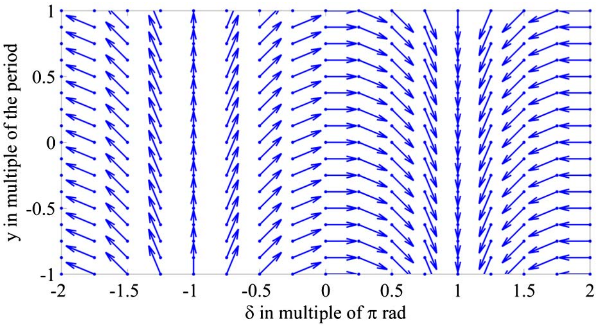

Fig. 4. Orientation of the electric field for the superimposition of two circularly polarized beams of opposite handedness, δ being the phase retard between the two beams.

- $I_2 = 0$ and $I_1 \neq 0$ means the electric field can be pictured by vectors everywhere.
- $I_1 = 2$ signifies a constant intensity inside the electric field.
- $\tan(2\theta) = \tan(\delta)$ describes a variation of the electric field orientation.

Combining these statements, it can be assumed that at the recording plane, the local polarization is linear and its orientation depends on the phase difference between the superimposed beams.

The electric field pattern resulting from the beams superimposition is represented in Fig. 4.

Our goal is to record VR with $l = 1$ and $l = 2$, therefore the resulting electric field must exhibit 2D variation and rotational symmetry (see Fig. 2) which is impossible with only two beams. To obtain the desired electric field, we expanded polarization holography to a four beam overlap (A, B, C, D) in a tetrahedral configuration, represented in Fig. 5.

The four beams are described by

$$A = \begin{pmatrix} A_x \\ A_y \exp(i\alpha) \end{pmatrix} \exp(i\delta_A),$$

$$B = \begin{pmatrix} B_x \\ B_y \exp(i\beta) \end{pmatrix} \exp(i\delta_B),$$

$$C = \begin{pmatrix} C_x \\ C_y \exp(i\gamma) \end{pmatrix} \exp(i\delta_C),$$

$$D = \begin{pmatrix} D_x \\ D_y \exp(i\delta) \end{pmatrix} \exp(i\delta_D)$$

with $\delta_A = (2\pi/\lambda)\sin(\theta_i) \times (y)$, $\delta_B = (2\pi/\lambda)\sin(\theta_i) \times (-x)$, $\delta_C = (2\pi/\lambda)\sin(\theta_i) \times (-y)$, $\delta_D = (2\pi/\lambda)\sin(\theta_i) \times (x)$, and θ_i is the incident angle.

With this configuration, the parameters of the local polarization are the same function of $\mathbf{p}$ and $\mathbf{q}$ and these vectors become

$$\mathbf{p} = \begin{pmatrix} A_x \cos(\delta_A) + B_x \cos(\delta_B) + C_x \cos(\delta_C) + D_x \cos(\delta_D) \\ A_y \cos(\alpha + \delta_A) + B_y \cos(\beta + \delta_B) + C_y \cos(\gamma + \delta_C) + D_y \cos(\delta + \delta_D) \end{pmatrix},$$
$$\mathbf{q} = -\begin{pmatrix} A_x \sin(\delta_A) + B_x \sin(\delta_B) + C_x \sin(\delta_C) + D_x \sin(\delta_D) \\ A_y \sin(\alpha + \delta_A) + B_y \sin(\beta + \delta_B) + C_y \sin(\gamma + \delta_C) + D_y \sin(\delta + \delta_D) \end{pmatrix}. \tag{7}$$

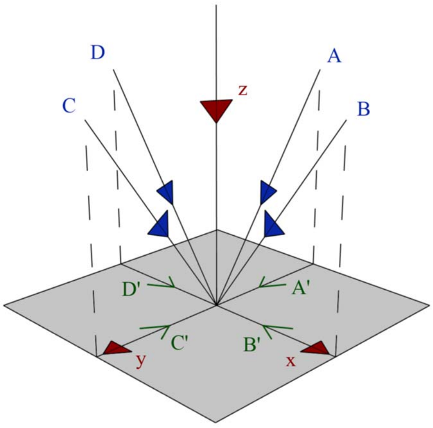

Fig. 5. Schematic representation of the polarization overlap, the four beams possess the same incident angle on the surface.

4. Vectorial Vortex Recording

Our final goal is to record a radial electric field to achieve a VR with $l = 2$. We found several systems of four beams fitting this purpose. In this paper, the most interesting ones are presented. The first system $(\mathcal{A})$ is composed of four linearly polarized beams. The second one $(\mathcal{B})$ is composed of two linearly and two circularly polarized beams. Finally, the third system $(\mathcal{C})$ is composed of four linearly polarized beams with a beam retarded by a quarter wavelength. $\mathcal{A}$ results in a locally radially electric field $l = 2$, while $\mathcal{B}$ and $\mathcal{C}$ resulting electric fields are characterized by a rotation of 180° about a vortex center: $l = 1$. These plates with $l = 1$ will be used as polarization converters to achieve the desired radially polarized beam required for the recording of $l = 2$ VR.

$\mathcal{A}$ is characterized by

$$A = \begin{pmatrix} 0 \\ 1 \end{pmatrix}, \qquad B = \begin{pmatrix} 1 \\ 0 \end{pmatrix},$$
$$C = \begin{pmatrix} 0 \\ 1 \end{pmatrix}, \qquad D = \begin{pmatrix} 1 \\ 0 \end{pmatrix}. \tag{8}$$

$\mathcal{B}$ is characterized by

$$A = \begin{pmatrix} 0 \\ 1 \end{pmatrix}, \qquad B = \frac{\sqrt{2}}{2}\begin{pmatrix} 1 \\ -i \end{pmatrix},$$
$$C = \begin{pmatrix} 1 \\ 0 \end{pmatrix}, \qquad D = \frac{\sqrt{2}}{2}\begin{pmatrix} 1 \\ i \end{pmatrix}. \tag{9}$$

$\mathcal{C}$ is characterized by

$$A = \begin{pmatrix} 1 \\ 0 \end{pmatrix}, \qquad B = \frac{\sqrt{2}}{2}\begin{pmatrix} 1 \\ 1 \end{pmatrix},$$
$$C = \begin{pmatrix} 0 \\ i \end{pmatrix}, \qquad D = \frac{\sqrt{2}}{2}\begin{pmatrix} 1 \\ -1 \end{pmatrix}. \tag{10}$$

Figures 6–8 represent the intensity of several plates between two parallel linear polarizers.

To achieve an ideal VR of $l = 2$, the electric field must be similar to the electric field of a perfectly radially polarized beam with a uniform intensity. The electric fields resulting from our simulations approach this ideal field but they are different in terms of uniformity of the intensity or directionality of the local polarization ellipse. In the following, we will analyze and compare our resulting electric fields.

The local polarization ellipse resulting from $\mathcal{A}$ is perfectly linear. The superimposition area contains several vortex centers and along a vortex center the orientation of the polarization rotates about 360°. However, the system presents a major drawback: the intensity drops down to zero at the vortex center. Due to the lack of recording intensity, the orientation of the fast axis near the center of the retarder may be random after the recording process.

For $\mathcal{B}$ and $\mathcal{C}$, the superimposition area also contains several vortex centers but unlike $\mathcal{A}$, the fast axis of the local polarization rotates only about 180° instead of 360°. A retarder recorded using $\mathcal{B}$ or $\mathcal{C}$ will exhibit only a half of the desired fast axis rotation. However, a half-wave plate characterized by this orientation of fast axis acts a polarization converter: it transforms a horizontally polarized beam into a radially polarized one. Therefore, these systems are not direct recording of VR with $l = 2$ but a two step recording process. The first step is a four beam overlap to record a half-wave plate at the recording wavelength (325 nm) characterized by a total rotation of its fast axis of 180° (VR with $l = 1$). The second step uses a UV (325 nm) collimated beam transmitted through the nonuniform half-wave plate to record a VR of $l = 2$. With these systems, the electric field resulting from the superimposition does not undergo the drastic drop of intensity at the center but the directionality of the local polarization ellipse decreases near the center and the local polarization is perfectly circular at a vortex center.

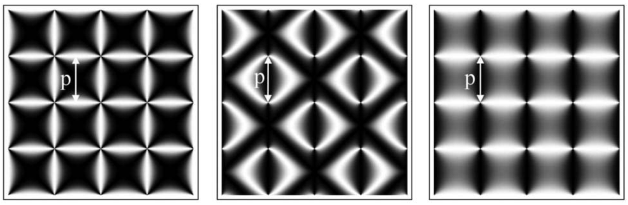

($\mathcal{A}$) ($\mathcal{B}$) ($\mathcal{C}$)

Fig. 6. Transmitted intensities of the half-wave plates obtained by polarization holography with several vortex centers. The smallest distance between two vortex centers will be defined as the period p, with p being a function of the incident angle and the recording wavelength, θ_i and λ_r, respectively, with $\lambda_r = 325$ nm. Our simulations were made with $\theta_i = 5$ arcsec; therefore $p = 20{,}626\lambda_r$. The value of θ_i was chosen due to experimental results.

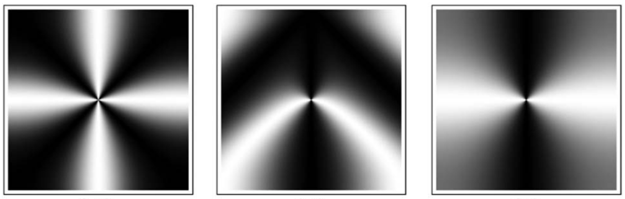
($\mathcal{A}$) ($\mathcal{B}$) ($\mathcal{C}$)

Fig. 7. Transmitted intensities of the half-wave plates obtained by polarization holography between two parallel polarizers for a size of p.

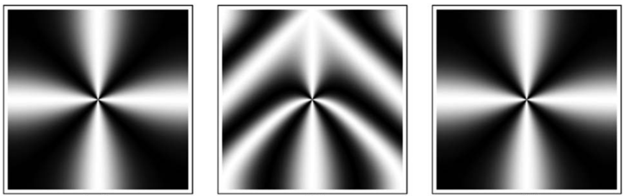
($\mathcal{A}$) ($\mathcal{B}$) ($\mathcal{C}$)

Fig. 8. Transmitted intensities of VR of $l = 2$ obtained by polarization holography between two parallel polarizers for a size of p. $\mathcal{B}$ and $\mathcal{C}$ are obtained by the recording a collimated beam transmitted by the intermediate plates.

Since our resulting electric fields deviate from the ideal one, the orientation of the polymers contained in the first layer may not be the predicted one, causing an area with disoriented LC at the end of the recording process. Indeed, to achieve a perfect orientation of the LC, the alignment layer must be submitted to an electric field with an important intensity and directionality. Our resulting fields present drops of intensity or directionality, to characterize them two criteria were established.

- $I_{\mathrm{dir}} = (I_1 - I_2)/I_T$, with I_T being the sum of the intensity of the beams used in the overlap. I_{dir} represents the percentage of the directional intensity. For the ideal recording electric field, $I_{\mathrm{dir}} = 1$ everywhere in the sample, while $I_{\mathrm{dir}} = 0$ means the LC cannot properly align because the beam is circularly polarized: $I_1 = I_2$ or the intensity is null $I_1 = I_2 = 0$.
- $d_p = 1 - (I_2/I_1)$ is the directionality parameter. For a linear polarized beam $d_p = 1$, while $d_p = 0$ is for a circularly polarized beam.

The criteria will be used to numerically compute areas where the recording electric field is not strong or directional enough to achieve a proper orientation of the polymers in the first layer. Therefore, after the recording process, the LC contained in these areas may not have the predicted orientation. To easily represent the variation of these criteria, maps with a size equal to p were computed and are presented in Figs. 9 and 10.

Near the vortex centers, the variation of these parameters exhibits rotational symmetry. However, for $\mathcal{B}$, I_{dir} exhibits an asymmetry in the y direction

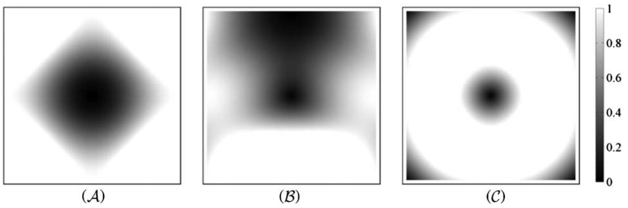

Fig. 9. Maps of I_{dir} for the three systems.

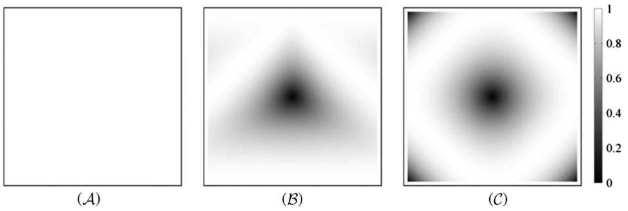

Fig. 10. Maps of d_p for the three systems.

but the drop of intensity being in the region with a strong deviation from the ideal angle, this region is not of great interest in VR and will not be extensively analyzed.

To obtain accurate values on the evolution of the characteristics of our beam, I_{dir} and d_p were computed along the line containing the vortex center and calculations were made to determine the radii of the circles where these parameters are under several thresholds. The thresholds were selected on an experimental base. They represent I_{dir} and d_p for a linearly polarized beam transmitted by a quarter-wave plate with an angle α between the direction of the incident polarization and its fast axis. We chose several values of α: 22.5°, 30°, 37.5°, 42.5°, 44.5°, and 44.9°. The results are summarized in Table 1.

Several pictures of possible disorientation area are presented in Fig. 11. The evolution of I_{dir} and d_p are shown in Figs. 12 and 13 and the numerical values of the radii are in Tables 2 and 3, respectively.

The systems with an intermediate plate are characterized by the same loss of directionality. Consequently, the criterion of choice will be the directional intensity. Based on this criterion, the best system is $\mathcal{C}$ because the radius where the directional intensity is below a threshold is smaller than in the other systems. Another advantage of $\mathcal{C}$ is that the distribution of its fast axis orientation is very similar to the perfect case unlike $\mathcal{B}$ where the areas of same orientation do not follow straight lines but are curves. However, the recording setup of $\mathcal{C}$ is complicated to implement because the D beam must be accurately retarded by a quarter-wave with respect to the other beams.

Table 1. Table of I_{dir} and d_p for Several Values of α

α(°)	I_{dir}	d_p
22.5	0.701	0.824
30	0.5	0.6667
42.5	0.2588	0.1603
44.5	0.0872	0.0343
44.9	0.0035	0.007

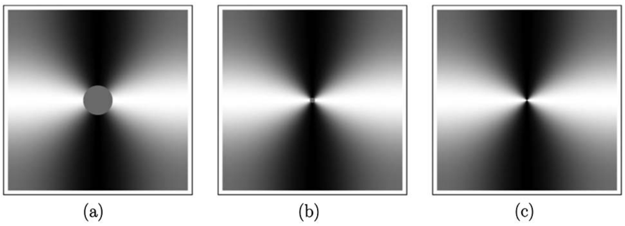

Fig. 11. Maps of transmitted intensities of half-wave plates obtained with $\mathcal{C}$ between two parallel polarizers with an area of disorientation of the LC. The intensity in the area of disorientation is pictured by the transmitted intensity of an unpolarized beam after a linear polarizer. Thus, the area of disorientation pictured by a gray disk depend on the criterion. (a) $I_{\mathrm{dir}} < I_{\mathrm{dir}30°}$, (b) $I_{\mathrm{dir}} < I_{\mathrm{dir}42.5°}$, and (c) $I_{\mathrm{dir}} < I_{\mathrm{dir}44.9°}$.

5. First Experimental Results

Our method presents two major differences with the classical method used to record uniform retarders.

- Our recording electric fields are not the ideal electric field with a uniform intensity and where the local polarization is linear everywhere. Our recording fields present drops I_{dir} and d_p.
- Our recording electric fields result from the superimposition of differently polarized beams.

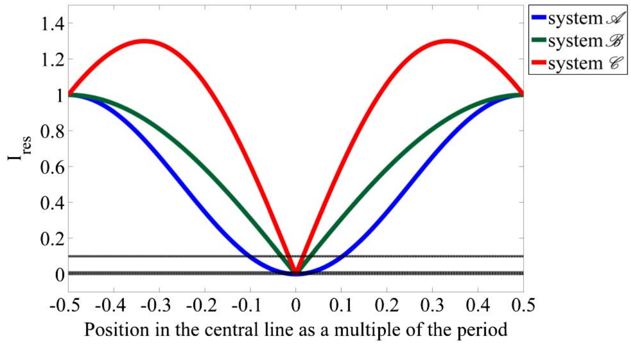

Fig. 12. Evolution of I_{dir} along the central line. The dashed lines represent several limit values selected in our analysis: $I_{\mathrm{dir}30°}$, $I_{\mathrm{dir}42.5°}$, and $I_{\mathrm{dir}44.9°}$.

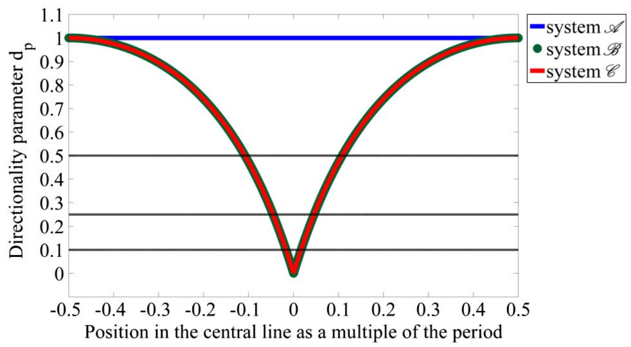

Fig. 13. Evolution of d_p along the central line. The dashed lines represent several limit values selected in our analysis: $d_{p30°}$, $d_{p42.5°}$, and $d_{p44.9°}$, with $\mathcal{B}$ and $\mathcal{C}$ being superimposed.

Table 2. Table of Radii for the Resulting Intensities (in λ_r Units) for a Size of a Sample of $\approx$20,626λ_r

	$\mathcal{A}$	$\mathcal{B}$	$\mathcal{C}$
$I_{\text{dir}} < I_{\text{dir}}(22.5°)$	6557	5155	2462
$I_{\text{dir}} < I_{\text{dir}}(30°)$	5155	3437	1687
$I_{\text{dir}} < I_{\text{dir}}(37.5°)$	3503	1718	856
$I_{\text{dir}} < I_{\text{dir}}(42.5°)$	1966	574	286
$I_{\text{dir}} < I_{\text{dir}}(44.5°)$	869	116	57
$I_{\text{dir}} < I_{\text{dir}}(44.9°)$	387	24	11

Table 3. Table of Radii for the Ratio of Intensities (in λ_r Units) for a Size of a Sample of $\approx$20,626λ_r

	$\mathcal{B}$	$\mathcal{C}$
$d_p < d_p(22.5°)$	5155	5155
$d_p < d_p(30°)$	3436	3436
$d_p < d_p(37.5°)$	1718	1718
$d_p < d_p(42.5°)$	572	572
$d_p < d_p(44.5°)$	116	116
$d_p < d_p(44.9°)$	24	24

Before recording a VR with $l = 2$, we realized two sets of experiments to separately test the deviations from the ideal case. The first set allowed us to determine a first approximation of the lower limit of I_{dir} and d_p to obtain an upper approximation of the area containing disoriented LC. The goal of the other set was to achieve the recording of 1D SR using the superimposition of two circularly polarized beams of opposite handedness. It allowed us to implement a simple full in-line recording process.

A. Determination of the Lower Limits of I_{dir} and d_p

To determine the lower limits of I_{dir} and d_p, several retarders were recorded using elliptical polarization. The recording setup contained a UV laser at 325 nm, a UV linear polarizer (p_1), a UV quarter-wave birefringent plate on a rotation mount (l_1), and a beam expander (see Fig. 14). To change the polarization of the recording beam from one retarder to the other, l_1 was rotated along its normal. Several retarders were recorded with an angle from 0° to 45° between the axes of p_1 and l_1.

The recording process of our samples contains two successive steps.

- First, a photalignment layer (Rolic *ROP*103) of approximately 50 nm is spin-coated on a glass substrate. Then, the layer is submitted to the elliptical recording polarization with a dose of 200 mJ/cm^2.
- Second, the LCP precursor (Rolic *ROF*5102) is spin-coated on the previous one and heated to remove the solvents. The LCs will orient themselves according to the orientation of the polarization sensitive elements of the first layer. Then, the sample is submitted to UV curing. Therefore, the LCs are fixed so the fast axis of the sample is frozen. The coating thickness of the second layer is determined to produce an half-wave plate at 660 nm.

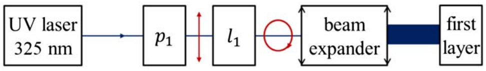

Fig. 14. Scheme of the exposing process, polarization in red and beam in blue.

To characterize the uniformity of the fast axis orientation, the following property was used: when the fast axis of a uniform retarder is parallel or perpendicular to the incident polarization, the polarization remains unchanged. The retarder is inserted between two linear polarizers which are continuously rotated and the transmitted intensity is recorded. On one hand, when the fast axis of a uniform retarder is aligned with the axis of one of the polarizers, the transmitted intensity must be null. On the other hand, a retarder with a variation of its fast axis orientation will never exhibit a null intensity between two crossed polarizers. Therefore, the transmitted intensity will be used as a criterion of uniform directionality of the fast axis.

The experimental setup was composed of a visible collimated beam (660 nm), a linear polarizer (P_1), a quarter-wave plate with an angle of 45° between its fast axis and the axis of P_1, two linear polarizers on accurate rotation mounts (P_2, P_3), and a camera (see Fig. 15). P_2 and P_3 were in cross configuration and the retarder was inserted between them. They were simultaneously rotated to keep them in cross configuration and the transmitted intensity was recorded.

Presently, several retarders were recorded and the largest angle between the axes of l_1 and p_1 is 45° ± 2°. We observed a nearly uniform transmitted intensity with very small variations due to dust on the LC layer, small polarization variations of the recording beam due to its expanding and imperfections of the polarizers (Fig. 16).

Using these promising results, we can assume that the LC are still properly oriented for an angle of 43° between the axes of l_1 and p_1. The recording ellipse obtained in this configuration is characterized by $I_{\text{dir}} = 0.0698$ and $d_p = 0.1034$. The radii of the area corresponding to these criteria were computed for the systems and the results are pictured in Fig. 17 and summarized in Table 4.

The largest radius of possible disorientation is 1755λ_r for a sample length of 20,626λ_r. It represents an area of $\approx$2.3% of the total area of the retarder. However, it is an upper limit of the radius of

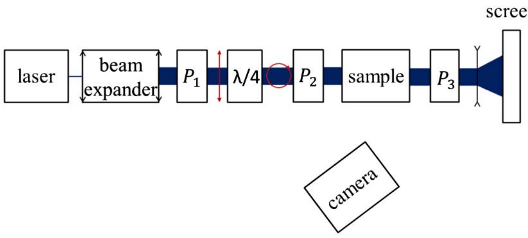

Fig. 15. Scheme of the measuring process, polarization in red and beam in blue.

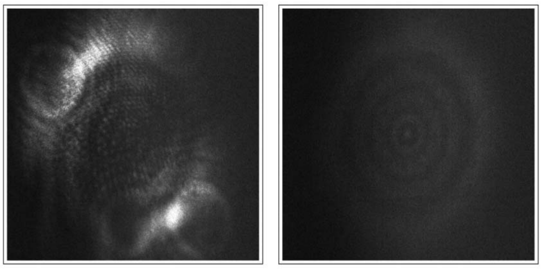
(a) (b)

Fig. 16. (a) Transmitted intensity between two cross polarizers for a uniform retarder recorded with an ellipticaly polarized beam with an angle of 45° ± 2° between the axes of l_1 and p_1. (b) Transmitted intensity for a commercial birefringent plate in the setup. The variations of intensity in (a) are mainly due to dust on the LC layer and on small polarization aberrations due to the expanding process. The two pictures were taken with the same camera and the same exposure time and gain.

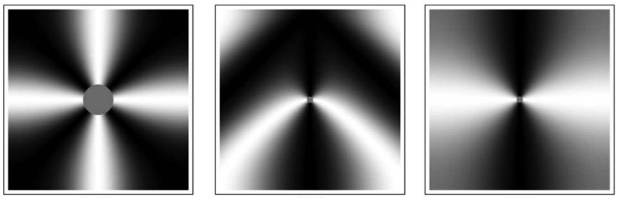
($\mathcal{A}$) ($\mathcal{B}$) ($\mathcal{C}$)

Fig. 17. Transmitted intensities between two parallel polarizers with the largest area of disorientation for each systems with the actual experimental limit ($\alpha = 43°$).

disorientation area and other prototypes will be recorded with a more accurate angle between l_1 and p_1.

B. Recording of 1D SR

To test our capability to record the overlap of several polarized beams, simple prototypes were realized. We exposed the first layer to the superimposition of two circularly polarized beams of opposite handedness to record the electric field pictured in Fig. 1. The recording setup contained the same UV laser, a beam expander, a linear polarizer p_1, a Savart plate [29], and a quarter-wave plate. The Savart plate was used to separate the incident beam into two beams of same intensity with orthogonal linear polarization and l_1 was used to circularize the polarization of these beams in order to generate the two circularly polarized beams of opposite handedness. The exposing setup is pictured in Fig. 18 and pictures of the prototypes are presented in Fig. 19.

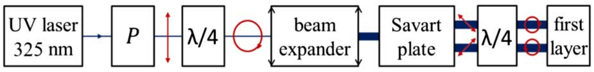

Fig. 18. Scheme of the recording process, polarization in red and beam in blue. The two recording beams possess the same intensity to record a series of linear polarization.

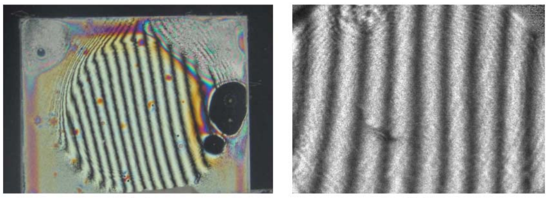
(a) (b)

Fig. 19. (a) Picture of a 1D SR between two crossed polarizers with a white source. Defects are due to dust and small oxidation spots. The retarder was recorded using the superimposition of two circularly polarized beams of opposite handedness. (b) Transmitted intensity of a uniformly linearly polarized beam after the retarder and a linear polarizer.

The prototypes exhibited the expected continuous variation of the fast axis orientation in the area of superimposition. The variation is pictured by the intensity variation of an incident linearly polarized beam transmitted by the retarder and a linear polarizer (see Fig. 19). Changing the expanding process allowed us to record retarders with different periods from 15 μm to 1.3 cm. These retarders were used for two applications depending on their period. Retarders with a small period (≈15 μm) were used as polarization state separators [25], while retarders with a large period (≈3 mm) were used as polarization analyzers [6]. Thanks to these prototypes, we also observed that a period of 20,626λ_r ≈ 6 mm was within our reach. Moreover, the smallest distance between two vortex centers being the same as the period of the 1D SR, we can assume that distances between 15 μm and 1.3 cm are realistic for our VR. Therefore, with our recording setup, a typical size of a VR containing only one center can be from 5 mm to 1.2 cm.

Table 4. Table of Radii for a Recording Polarization Obtained with an Angle of 43° between the Axis of p_1 and the Axis of l_1 (in $\lambda_{\text{recording}}$ Units) for a Size of a Sample of ≈20,626λ_r

	$\mathcal{A}$	$\mathcal{B}$	$\mathcal{C}$
$I_{\text{dir}} < I_{\text{dir}}(43°)$	1755	458	229
$d_p < d_p(43°)$		458	458

6. Conclusions and Perspectives

In this paper, VRs, their applications, and methods of recording were exposed. The theory of polarization holography with two beams was completely developed and its use as a new method to build a VR with four polarized beams was described. The systems used to induce a radially polarized beam were presented. We showed that our systems do not achieve ideal recording electric fields but fields with a drop of intensity or directionality. Our systems were numerically characterized thanks to two parameters I_{dir} and d_p. The first experimental results on the lower acceptable value of these parameters were presented. We computed an upper limit of possible disorientation area. The experimental setup for the recording of a 1D SR and the first prototypes were presented.

In the future, two mains tasks will be achieved: the accurate determination of the limits of d_p and I_{dir} and the recording and testing of several VR.

To accurately determine these limits, the recording setup will be changed: the beam will be collimated before the polarizer and the quarter-wave plate to avoid polarization modifications due to the expanding process and a more complex method will be used to improve the determination of the angle between the axis of the polarizer and the axis of the quarter-wave plate.

To record prototypes with a 2D variation of the fast axis, another Savart plate with its shearing direction perpendicular to the first one will be added, generating four differently polarized beams and allowing the recording of VR prototypes.

This work and the author are funded thanks to a grant of the "Fond pour la formation à la Recherche dans l'Industrie et l'Agriculture" (FRIA).

References

1. A. Niv, G. Biener, V. Kleiner, and E. Hasman, "Manipulation of the Pancharatnam phase in vectorial vortices," Opt. Express **14**, 4208–4220 (2006).
2. D. Mawet, E. Serabyn, K. Liewer, C. Hanot, S. McEldowney, D. Shemo, and N. O'Brien, "Optical vectorial vortex coronagraphs using liquid crystal polymers: theory, manufacturing and laboratory demonstration," Opt. Express **17**, 1902–1918 (2009).
3. M. Berry, "The adiabatic phase and Pancharatnam phase for polarized light," J. Mod. Opt. **34**, 1401–1407 (1987).
4. E. J. Galvez, "Applications of geometric phase in optics," Recent Research Developments in Optics **2**, 165–182 (2002).
5. G. Biener, A. Niv, V. Kleiner, and E. Hasman, "Near-field Fourier transform polarimetry by use of a discrete space-variant subwavelength grating," J. Opt. Soc. Am. A **20**, 1940–1948 (2003).
6. P. Piron, P. Blain, and S. Habraken, "Polarization measurement with space-variant retarders in liquid crystal polymers," Proc. SPIE **8160**, 81600Q (2011).
7. M. Stalder and M. Schadt, "Linearly polarized light with axial symmetry generated by liquid-crystal-polarization converters," Opt. Lett. **21**, 1948–1950 (1996).
8. S.-W. Ko, C.-L. Ting, A. Y.-G. Fuh, and T.-H. Lin, "Polarization converters based on axially symmetric twisted nematic liquid crystal," Opt. Express **18**, 3601–3607 (2010).
9. A. Niv, G. Biener, V. Kleiner, and E. Hasman, "Formation of linearly polarized light with axial symmetry by use of space variant subwavelength gratings," Opt. Lett. **28**, 510–512 (2003).
10. G. M. Lerman and U. Levy, "Effect of radial polarization and apodization on spot size under tight focusing conditions," Opt. Express **16**, 4567–4581 (2008).
11. R. Dorn, S. Quabis, and G. Leuchs, "Sharper focus for a radially polarized light beam," Phys. Rev. Lett. **91**, 233901 (2003).
12. Q. Zhan, "Cylindrical vector beams: from mathematical concepts to applications," Adv. Opt. Photon. **1**, 1–57 (2009).
13. W. Chen, R. L. Nelson, D. C. Abesysinghe, and Q. Zhan, "Optimal plasmon focusing with spatial polarization engineering," Opt. Photon. News **20**, 36–41 (2009).
14. Q. Zhan, "Trapping metallic Rayleigh particles with radial polarization," Opt. Express **12**, 3377–3382 (2004).
15. D. Rouan, P. Riaud, A. Boccaletti, Y. Clénet, and A. Labeyrie, "The four-quadrant phase-mask coronagraph. I. Principle," Publ. Astron. Soc. Pac. **112**, 1479–1486 (2000).
16. D. Mawet, P. Riaud, O. Absil, and J. Surdej, "Annular groove phase mask coronagraph," Astrophys. J. **633**, 1191–1200 (2005).
17. D. Mawet, P. Riaud, J. Surdej, and J. Baudrand, "Subwavelength surface-relief gratings for stellar coronagraphy," Appl. Opt. **44**, 7313–7321 (2005).
18. D. Mawet, E. Serabyn, K. Liewer, R. Buruss, J. Hickey, and D. Shemo, "The vector vortex coronagraph: laboratory results, and first light at palomar observatory," Astrophys. J. **709**, 53–57 (2010).
19. S. R. Nersisyan, N. V. Tabiryan, D. Mawet, and E. Serabyn, "Improving vector vortex waveplates for high-contrast coronagraphy," Opt. Express **21**, 8205–8213 (2013).
20. G. Machavariani, Y. Lumer, I. Moshe, A. Meir, and S. Jackel, "Spatially-variable retardation plate for efficient generation of radially- and azimuthally-polarized beams," Opt. Commun. **281**, 732–738 (2008).
21. E. Hasman, Z. Bomzon, A. Niv, G. Biener, and V. Kleiner, "Polarization beam-splitters and optical switches based on space-variant computer-generated subwavelength quasi-periodic structures," Opt. Commun. **209**, 45–54 (2002).
22. G. P. Crawford, J. N. Eakin, M. D. Radcliffe, A. Callan-Jones, and R. A. Pelcovits, "Liquid-crystal diffraction gratings using polarization holography alignment technique," J. Appl. Phys. **98**, 123102 (2005).
23. H. Ren, T.-H. Lin, and S.-T. Wu, "Linear to axial or radial polarization conversion using a liquid crystal gel," Appl. Phys. Lett. **89**, 051114 (2006).
24. S. R. Nersisyan, N. V. Tabiryan, D. M. Steeves, and B. R. Kimball, "Optical axis gratings in liquid crystals and their use for polarization insensitive optical switching," J. Nonlinear Opt. Phys. **18**, 1–47 (2009).
25. P. Blain, P. Piron, Y. Renotte, and S. Habraken, "An in-line shearography set-up based on circular polarization gratings," Opt. Lasers Eng. **51**, 1053–1059 (2013).
26. S. R. Nersisyan, N. V. Nelson, V. Tabiryan, D. M. Steeves, and B. R. Kimball, "The promise of diffractive waveplates," Opt. Photon. News **21**, 40–45 (2010).
27. U. Ruiz, C. Provenzano, P. Pagliusi, and G. Cipparone, "Pure two-dimensional polarization patterns for holographic recording," Opt. Lett. **37**, 311–313 (2012).
28. B. Kilosanidze and G. Kakauridze, "Polarization-holographic gratings for analysis of light. 1. Analysis of completely polarized light," Appl. Opt. **46**, 1040–1049 (2007).
29. M. Françon and S. Mallick, *Polarization Interferometers: Applications in Microscopy and Macroscopy* (Wiley-Intersciences, 1971).

Complements to the article

After the publication of this article, another set of prototypes was realized to determine with a better accuracy the experimental limits: the minimal value of the directionality parameter d_p and the minimum value of the directional intensity I_{dir}. Several changes were performed on the recording setup:

- The error on the angle formed by the axis of the quarter-wave plate and the linear polarizer was reduced to 0.5°.
- The recording setup was modified: the linear polarizer and the quarter-wave plate were moved after the beam expander (see Figure 5.8).
- The alignment of the beam expander was improved using a reference mirror. The mirror is placed to achieve a normal incidence where no other optics are present. Then the beam expander is positioned, it will be aligned to achieve the best reflected beam.

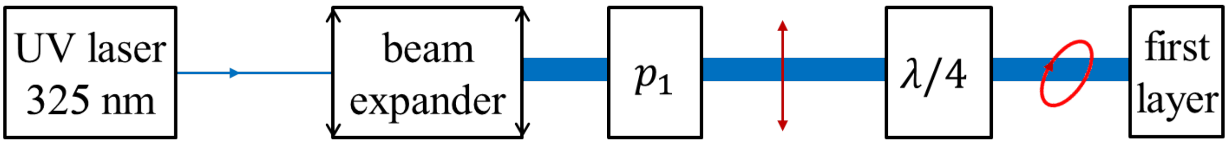

Figure 5.8: Representation of the new recording setup, the beam is pictured in blue and the polarization is represented by red arrows.

Thanks to these prototypes, two major conclusions can be established.

- The maximum acceptable angle between the axes of the polarization components depends on the expanding process. A better alignment of the beam expander will allow a larger angle before depicting visible signs of misorientation of the LCs. Indeed retarders with a poorly aligned expanding process presented a milky veil for an angle larger than 38° while with our better alignment, the coating only appears for angles larger than 43.5°.
- We confirmed that with our best alignment of the beam expander, the maximum angle was 43.5°. Therefore the present experimental limits correspond to the polarization ellipse after a quarter-wave plate with an angle of 45° between its optical axis and the incident polarization

$$d_p = 0.1034;\ I_{dir} = 0.0698.$$

The maximum radius of the misalignment area R_{mis} and the percentage of the ratio between the misaligned surface and the total surface of the retarder s_{mis} are presented in Table 5.1.

Table 5.1: Table of the radii of the expected misalignment area R_{mis} and of the ratios of these areas on the surface of the retarders s_{mis} for the three systems $\mathscr{A}$, $\mathscr{B}$ and $\mathscr{C}$. The size of a sample is ≈ $20626\lambda_r$.

	$\mathscr{A}$	$\mathscr{B}$	$\mathscr{C}$
R_{mis}	1755	458	458
s_{mis}	2.27%	0.15%	0.15%

Nonetheless, one of the reviewers of our article suggested the reading of patent [15] which claims using a neighbor effect to realize micro-arrays of optical vortices with LCs.
Several small areas of the pattern are exposed to a defined polarization state while a large one between the exposed part is never exposed. The orientation of the polymers inside the alignment layer will adjust to ensure continuity with the borders to create a vortex pattern at the center. Presently, the size of the unexposed area is $30\,\mu$m for exposed areas of approximately $10\,\mu$m.

Therefore, we strongly believe that our present experimental limit is a maximum one. It can be reduced by two facts: a better alignment of the beam expander and the neighbor effect.

- Using a UV wavefront sensor will compute the aberrations of the wavefront after the beam expander. Therefore, adding high precision translation components on the beam expander could properly correct the aberrations. Due to the fact that the directionality limits depend on the alignmentand collimation, a proper recording could be achieved with a less directional field with a better aligned beam. Then the recording limits should correspond to a more circularly polarized beam reducing the area of misorientation.
- Since the alignment of the polymers are influenced by the neighbors, even if the polymers near the phase singularity are not exposed to a sufficiently directional field, their neighbors are exposed to a proper field. Therefore, the polymers near the phase singularity will align according to their neighbors orientation and the incoming electric field. This could significantly reduce the area of misalignment. With the same reduction of $15\,\mu$m than the patent [15], the R_{mis} and s_{mis} as a functions of the recording wavelength are given by Table 5.2.

Table 5.2: Table of the radii of the expected misalignment areas R_{mis} and of the ratios of these areas on the surface of the retarders for the three systems s_{mis} when a reduction of $15\,\mu$m ($46\lambda_r$) is taken into account. The size of a sample is $\approx 20626\lambda_r$.

	$\mathscr{A}$	$\mathscr{B}$	$\mathscr{C}$
R_{mis}	1709	412	412
s_{mis}	2.16%	0.13%	0.13%

5.4 Experimental recording

The recording setup of the vortex retarders contains the following elements (Figures 5.9 & 5.10):

- a UV laser at 325 nm,
- a beam expander BE,
- a linear UV polarizer with a vertical orientation P_1,
- two quarter-wave plates $\lambda/4_a$, $\lambda/4_b$,
- two Savart plates Sav_1, Sav_2.

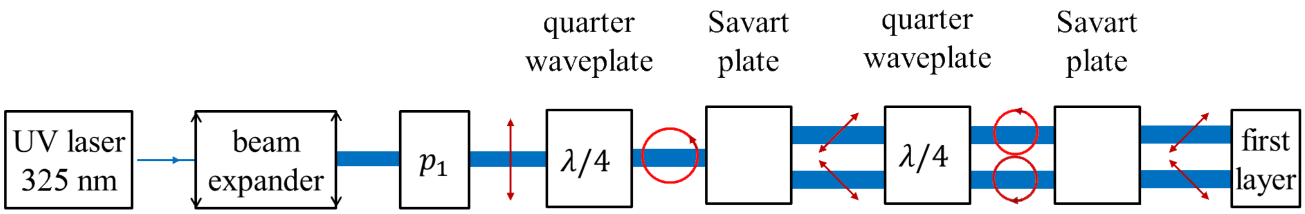

Figure 5.9: Representation of the recording setup, the beams are pictured in blue and the polarization is represented by red arrows.

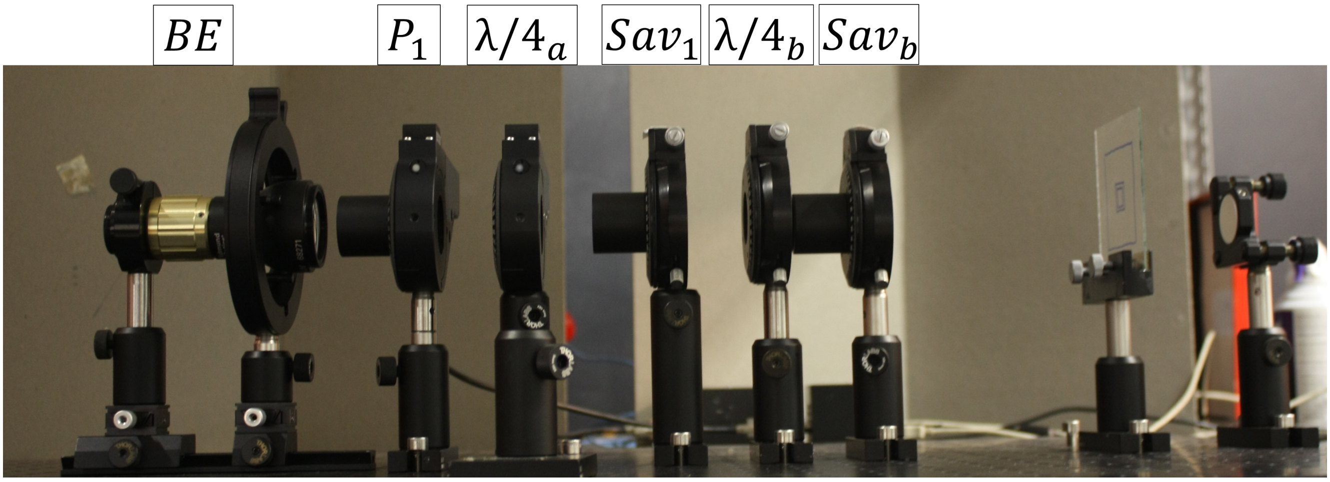

Figure 5.10: Picture of the recording setup.

The first quarter-wave plate converts the incident beam (Figure 5.11 (a)) to a circularly polarized one (Figure 5.11 (b)). The first Savart plate divides the incident beam into two linearly polarized beams with orthogonal linear polarizations (Figure 5.11 (c)), the beams being separated following the vertical. The second quarter-wave plate converts the incident beam into circularly polarized beams of opposite handedness (Figure 5.11 (d)). Finally, the second Savart plate divides the two incident beams into four beams linearly polarized (Figure 5.11 (e)). The separation will follow the horizontal and the beams are in a square configuration.

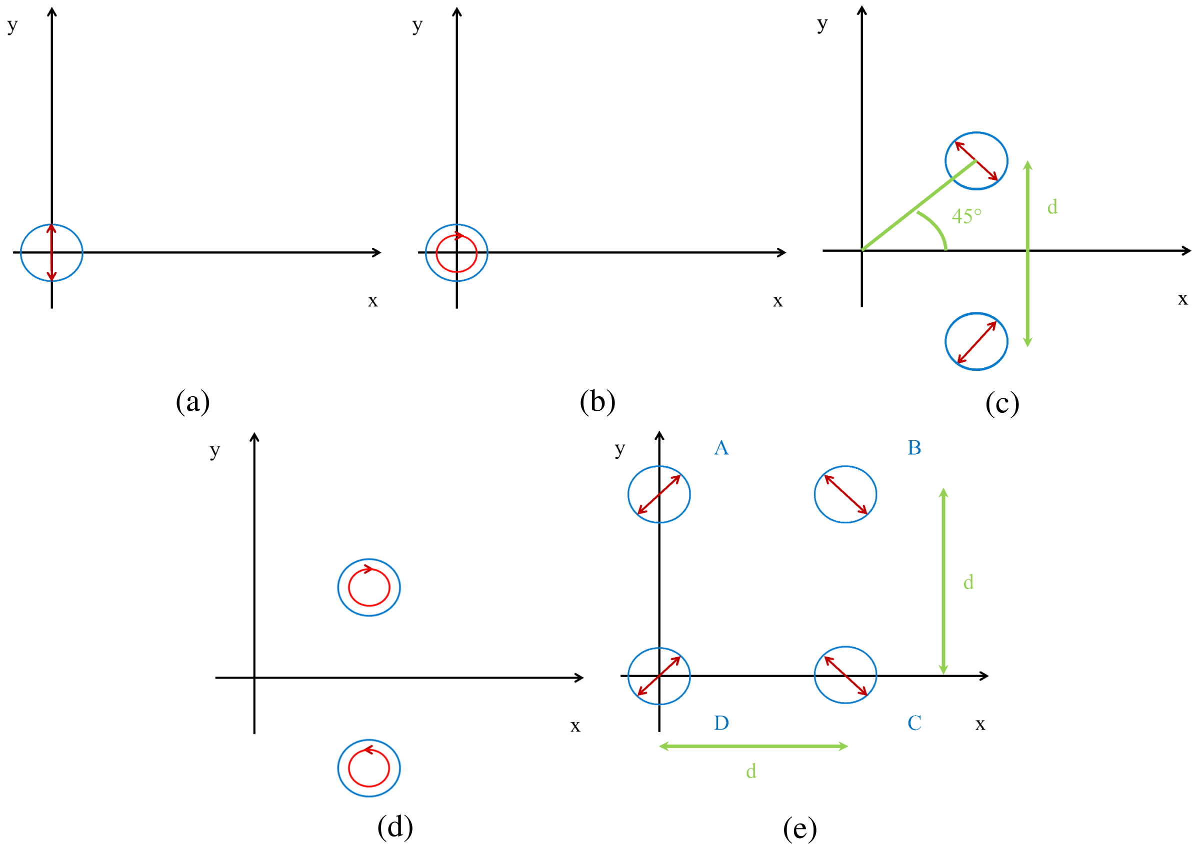

Figure 5.11: Representation of the positions of the beams and their polarization states through the polarization part of the recording setup. The beams are pictured by blue circles and their polarization states by red arrows. The distance between the beams after the Savart plate is *d*. Experimentally, the beams are larger and a superimposition area of the four beams exists.

To determine the characteristics of the local polarization ellipse, the Stokes parameters of the superimposition area were measured. A linear polarizer, a projecting screen and a camera were added on the setup and the transmitted intensity for several orientations of the polarizer axis was recorded to compute the Stokes parameters. The characteristics of the polarization ellipse and the Stokes parameters are linked by the following system of equations [16, 17]:

$$\begin{aligned} S_0 &= I_1^2 - I_2^2 \\ S_1 &= I_1^2 - I_2^2 \cos(2\alpha) \\ S_2 &= I_1^2 - I_2^2 \sin(2\alpha) \end{aligned} \tag{5.14}$$

where I_1 is the intensity following the largest semi-axis of the polarization ellipse, I_2 is the intensity following the smallest one and α is the angle between the largest axis and the horizontal.

Several pictures of the orientation of the largest axis for different viewing angles are presented in Figure 5.12.

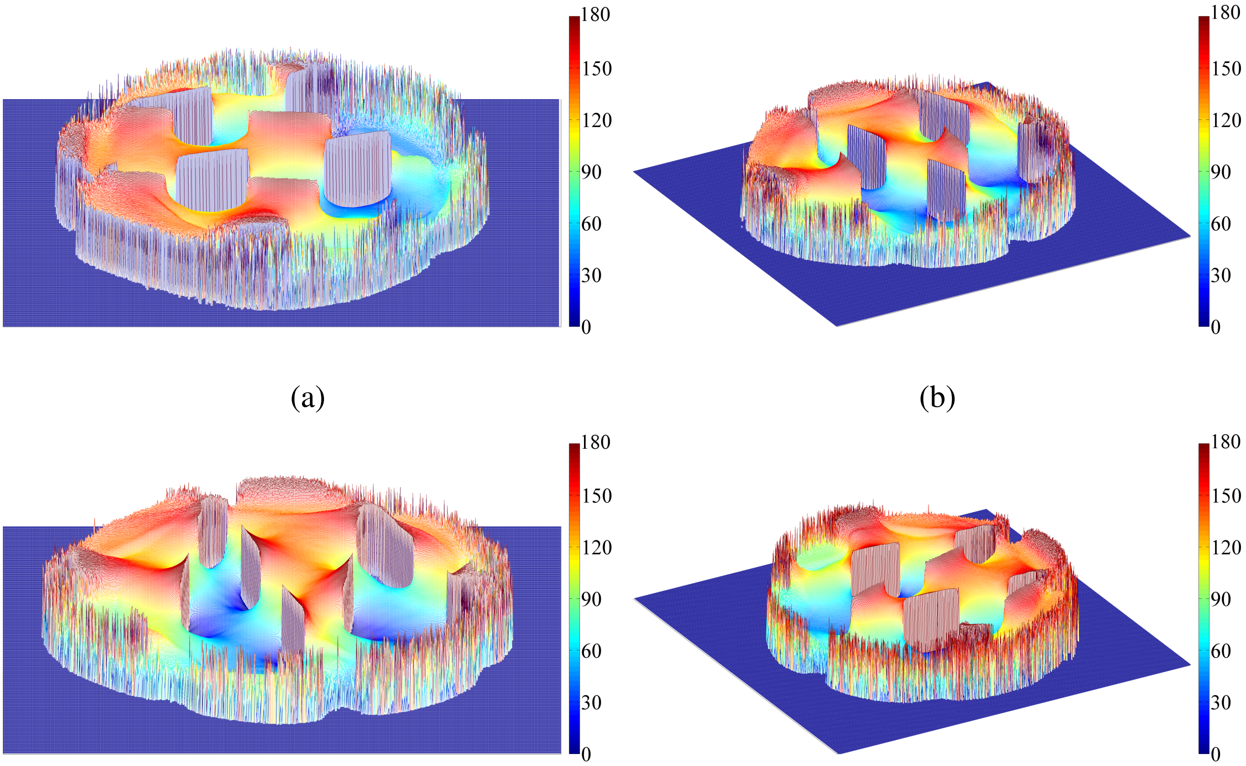

(a) (b)

(c) (d)

Figure 5.12: Representation of the orientation of the largest axis of the local polarization ellipse inside the superimposition area for several angles of view. The orientation of the largest axis varies from 0° to 180°.

We can observe that we have several rotation centers. The axis performs a rotation of 180° corresponding to the recording of charge one vortices. The rotation centers are aligned along several lines of different orientations. Thanks to the measuring of the Stokes parameters, the directionality parameter as well as the residual intensity were also computed. Since the orientation of the fast axis depends of the orientation of the local polarization ellipse, a half-wave plate was simulated with its orientation of fast axis and the transmitted intensity of this plate between two linear polarizers were computed. Figure 5.13 presents these results.

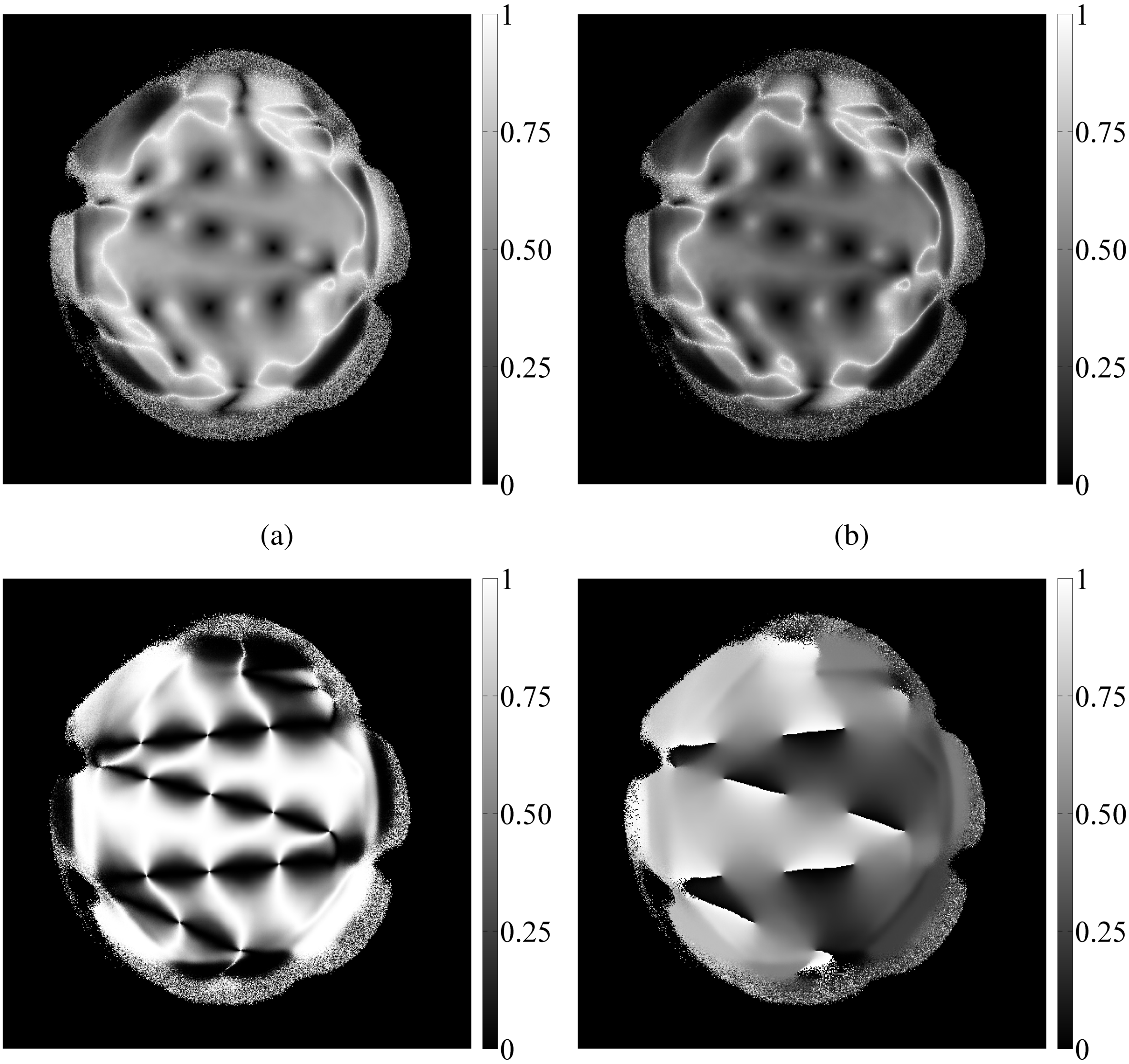

(a) (b)

(c) (d)

Figure 5.13: Representation of the recording field parameters and numerical simulation of a birefringent plate recorded using this electric field: (a) & (b) present the parameters of the electric field; (a) pictures d_p and (b) represents I_{dir}. (c) & (d) present the parameters of the simulated plate: (c) presents the transmitted intensity of the half-wave plate between two linear polarizers and (d) shows the variation of the fast axis orientation as a multiple of 180°.

We can observe that:

- Along a vortex center, the transmitted intensity effectively presents two bright and two dark areas. It was expected since the orientation of the largest axis undergoes a total rotation of 180°.
- The distance between two centers of rotation is approximately 1.5 mm.
- Near a rotation center, the directionality of the electric field decreases. Therefore an area of misorientation of the LC can be expected. Figure 5.14 presents the expected transmitted intensity with misorientation areas I_{mis}.

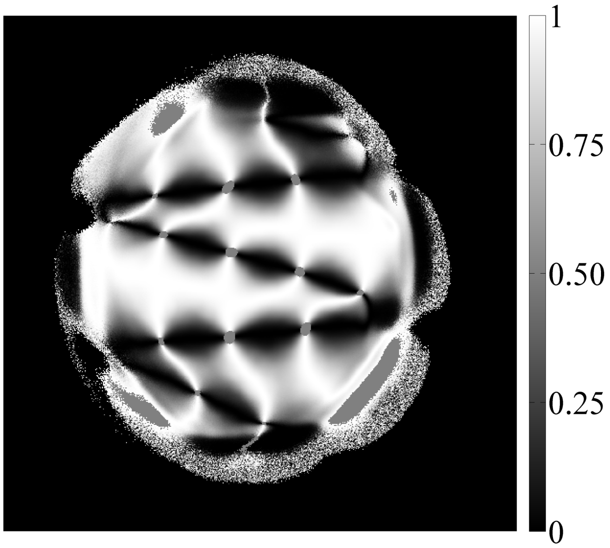

Figure 5.14: Numerical simulation of the transmited intensity with area of misorientation. The polarization of the beam after the disorientation areas was computed as an unpolarized beam. Therefore, the transmitted intensity is equal to half of the incident one and grey disks appear on the picture.

On the picture, we can observe that several areas of misalignment of the LCs appear.
These areas are centered on the future vortices centers, they are different ellipses which can be approximated by circles of different radii. The largest radius of misorientation is approximately 10% of the distance between two centers of rotation. Experimentally, it corresponds to a radius of 150 μm.

Finally, two prototypes were recorded. The thickness of the birefringent layer was chosen to match the half-wave condition near 600 nm. Figure 5.15 presents several pictures of the transmitted intensity of the prototypes between two linear polarizers with a white source.

Figure 5.15: Pictures of the prototypes between two linear polarizers and a white source. The pictures were taken for different orientation between the polarizers.

As expected, the transmitted intensity exhibits the distinctive shape of a retarder containing several charge one vortices. Near a rotation center, there are two dark areas and two bright areas. The distance between two rotation centers is 1.5 mm and the radius of the misorientation area is estimated at approximately 150 μm. Moreover, the pattern of the transmitted intensity for the real case presents no obvious differences with the computed transmitted intensity obtained by the Stokes parameters measurement.

To achieve a better knowledge of the electric field, we changed our numerical model to fit the experimental conditions.

- The four beams are in the square configuration pictured in figure 5.11 (e).
- The beams are gaussian beams instead of infinite beam with uniform intensity.
- The beams are characterized by different intensities corresponding to the measured ones.

The parameters of the local polarization ellipse and the intensity transmitted by the simulated half-wave plate were computed for a sample size of 1.5 cm, they are presented in Figure 5.16.

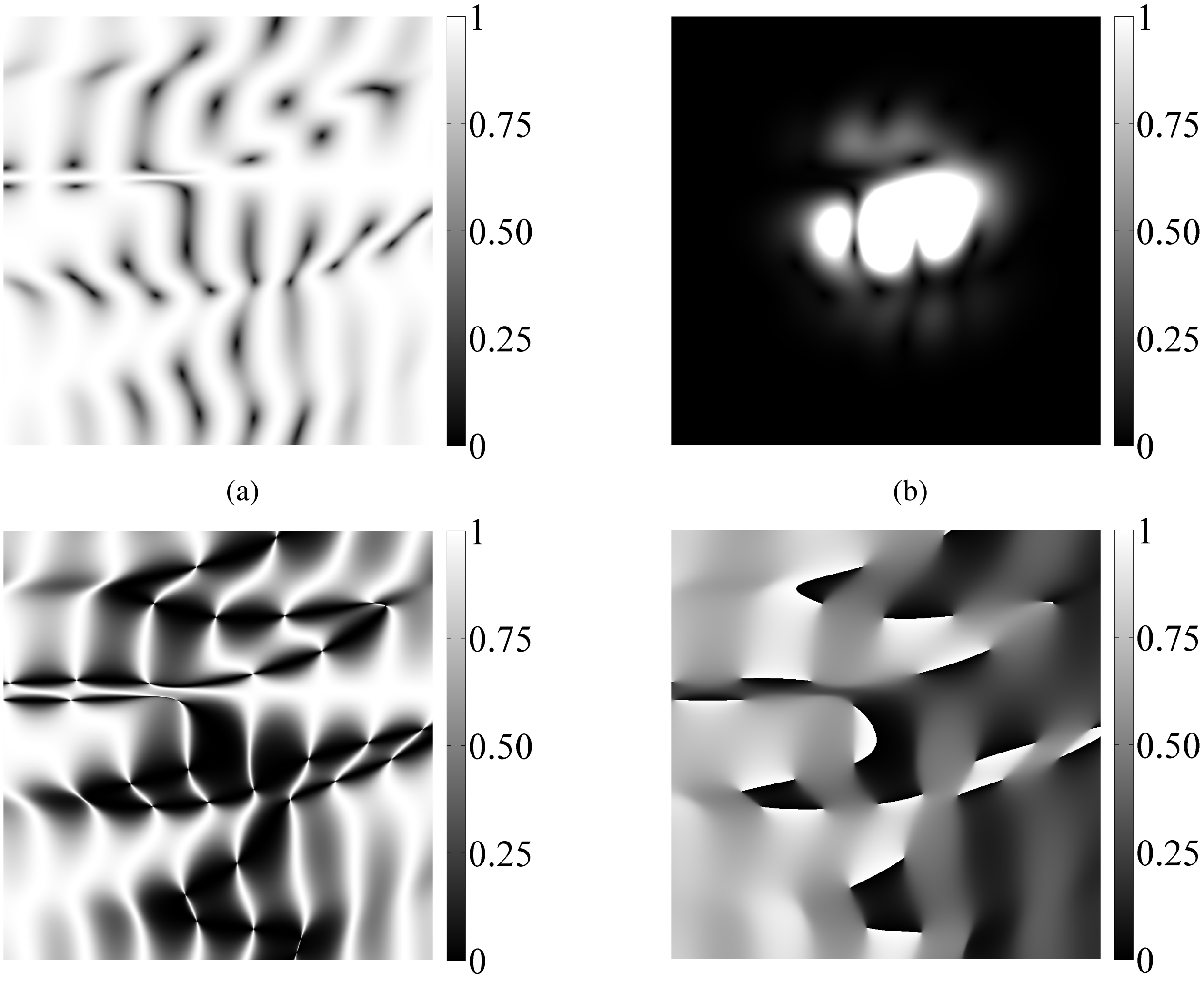

(a) (b) (c) (d)

Figure 5.16: Representation of the simulated electric field with the experimental parameters and simulation of the recorded birefringent plate: (a) & (b) represent the parameters of the electric field; (a) pictures d_p and (b) I_{dir}. (c) & and (d) rxpose the parameters of the simulated plate: (c) presents the transmitted intensity of the half-wave plate between two linear polarizers and (d) shows the variation of the fast axis orientation as a multiple of 180°.

One can observe that the simulations results are similar to the experimental ones. The same pattern of centers is observed, the rotation of the optical axis along a center is also about 180°. The reduction of the electric field directionality near vortex centers also occurs. However, several differences exist: the alignment of the vortex centers is a bit different and the directional intensity is smaller in the simulated case.

To achieve a better knowledge of our experimental model, we performed a sensitivity analysis.

5.5 Sensitivity analysis

The parameters of the sensitivity analysis were separated into two categories, the first ones depending on the orientation of the active axis of the polarization components and the second ones depending on the expanding process.

- The first set contains the difference between the orientation of the optical axis of the components and its ideal orientation. The ideal orientation of the active polarization axis is able to achieve the recording of four beams in a square configuration with identical intensity and the appropriate polarization state (see Figure 5.11 (e)).
- The second set contains the incident angle θ_i and the width of the gaussian beams σ.

5.5.1 Jones representation of the polarization components

The first task to compute the resulting field is to model the polarization components.
Since four components are present, four differences exist $\epsilon_1, \epsilon_2, \epsilon_3, \epsilon_4$. These parameters affect the polarization states of the beams, their intensity and the position of their center which determines the phase relation between them.
The polarization and the intensity of the beams can be computed using the Jones formalism, the vectors representing the exiting beams being obtained by multiplications of the matrices of the polarization components and the incident beam vector.

A generic birefringent plate with a retard of ϕ and orientation α of its fast axis is given by [13].

$$\begin{pmatrix} \cos(\phi/2) + \imath\cos(2\alpha)\sin(\phi/2) & -\imath\sin(2\alpha)\sin(\phi/2) \\ -\imath\sin(2\alpha)\sin(\phi/2) & \cos(\phi/2) - \imath\cos(2\alpha)\sin(\phi/2) \end{pmatrix} \tag{5.15}$$

Since the incident beam (J_{in}) is vertically polarized, the ideal orientation of the first quarter-wave plate (L_1) axis is 45°. Therefore, L_1 is characterized by $\phi = \pi/2$ and $\alpha = 45° + \epsilon_1$ after simplifications it is described by equation 5.16.

$$L_1 = \frac{\sqrt{2}}{2}\begin{pmatrix} 1 - \imath\sin(2\epsilon_1) & -\imath\cos(2\epsilon_1) \\ -\imath\cos(2\epsilon_1) & 1 + \imath\sin(2\epsilon_1) \end{pmatrix} \tag{5.16}$$

The Savart plate can be viewed as two linear polarizers depending on the separation direction of the beams. The transmission axes are at +45° and −45° with respect to the separation direction. A general linear polarizer with a transmission direction of α is represented in equation 5.17.

$$P_\alpha = \frac{1}{2}\begin{pmatrix} 1 + \cos(2\alpha) & -\sin(2\alpha) \\ -\sin(2\alpha) & 1 - \cos(2\alpha) \end{pmatrix} \tag{5.17}$$

Experimentally, the first separation direction is vertical. Thus the polarizers S_{a1} and S_{b1} representing the first Savart plate are oriented at $+45° + \epsilon_2$ and $-45° + \epsilon_2$ (equations 5.18 and 5.19).

$$S_{a1} = \frac{1}{2}\begin{pmatrix} 1 - \sin(2\epsilon_2) & -\cos(2\epsilon_2) \\ -\cos(2\epsilon_2) & 1 + \sin(2\epsilon_2) \end{pmatrix} \tag{5.18}$$

$$S_{a1} = \frac{1}{2}\begin{pmatrix} 1 + \sin(2\epsilon_2) & \cos(2\epsilon_2) \\ \cos(2\epsilon_2) & 1 - \sin(2\epsilon_2) \end{pmatrix} \tag{5.19}$$

The ideal orientation of the axis of the second quarter wave-plate, L_2,is horizontal.
So L_2 is characterized by $\phi = \pi/2$ and $\alpha = \epsilon_3$ (equation 5.20).

$$L_2 = \frac{\sqrt{2}}{2}\begin{pmatrix} 1+\cos(2\epsilon_3) & -\imath\sin(2\epsilon_3) \\ -\imath\sin(2\epsilon_3) & 1-\cos(2\epsilon_3) \end{pmatrix} \tag{5.20}$$

The second ideal separation direction of the Savart plate is the horizontal. Thus the polarizers S_{a2} and S_{b2} representing it are oriented at 135° + ϵ_4 and 45° + ϵ_4 (Equations 5.21 and 5.22).

$$S_{a2} = \frac{1}{2}\begin{pmatrix} 1+\sin(2\epsilon_4) & \cos(2\epsilon_4) \\ \cos(2\epsilon_4) & 1-\sin(2\epsilon_4) \end{pmatrix} \tag{5.21}$$

$$S_{b2} = \frac{1}{2}\begin{pmatrix} 1-\sin(2\epsilon_4) & -\cos(2\epsilon_4) \\ -\cos(2\epsilon_4) & 1+\sin(2\epsilon_4) \end{pmatrix} \tag{5.22}$$

Finally, the four exiting beams can be written as.

$$\begin{aligned} A &= S_{a2}\,L_2\,S_{1a}\,L_1\,J_{in} \\ B &= S_{b2}\,L_2\,S_{1a}\,L_1\,J_{in} \\ C &= S_{a2}\,L_2\,S_{1b}\,L_1\,J_{in} \\ D &= S_{b2}\,L_2\,S_{ba}\,L_1\,J_{in} \end{aligned} \tag{5.23}$$

5.5.2 Position of the beams centers

To compute the phase difference of the beams, the position of their center must be studied.
The action of a Savart plate on the position is a displacement of the beam centers: they are shifted on a circle centered on the incident beam. The radius of this circle r_S depends on distance between the beams at the exit of the Savart plate d, $r_S = \frac{\sqrt{2}}{2}d$ and the angle of rotation depends on the separation direction (see Figure 5.17.

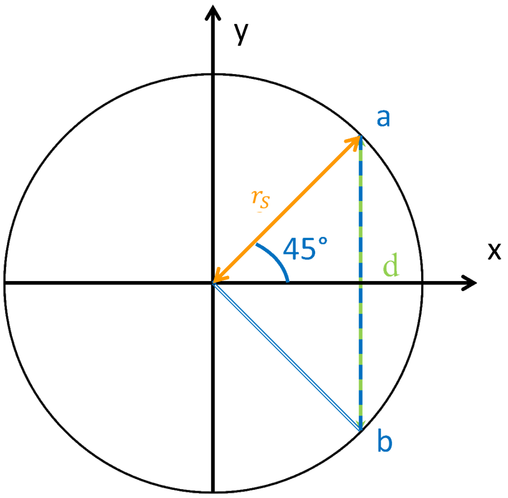

Figure 5.17: Picture of the beams centers exiting the Savart plate for an horizontal separation direction.

For a Savart plate with a perfect vertical direction and a separation of d, the centers of the beams a and b will be

$$\begin{array}{ll} a_x = d/2 & a_y = d/2 \\ b_x = d/2 & b_y = -d/2. \end{array}$$

For a Savart plate with a separation direction of 90° + ϵ_2, the positions of the two centers are given by:

$$\begin{array}{ll} a_x = \cos(45 + \epsilon_2) \times r_S & a_y = \sin(45 + \epsilon_2) \times r_S \\ b_x = \cos(45 + \epsilon_2) \times r_S & b_y = -\sin(45 + \epsilon_2) \times r_S \end{array} .$$

The two configurations are presented on Figure 5.18.

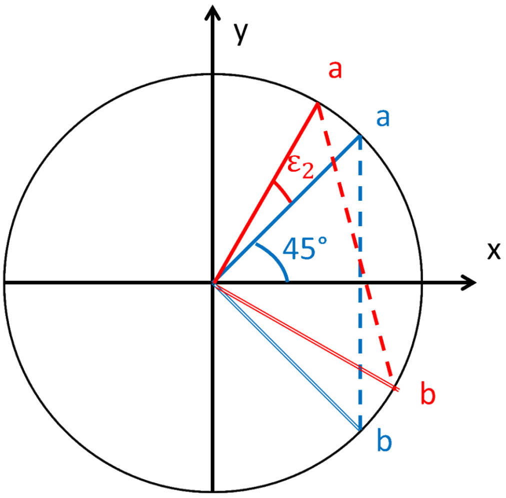

Figure 5.18: Picture of the beams centers exiting the Savart plate, the perfect case is pictured in blue while the case with an alignment error is pictured in red.

The action of the second Savart plate is the same as the first one, the centers of the four beams are on two circles of same radius. The first one is centered in a and the second one is centered in b. A and B originate from a while C and D originate from b (see Figure 5.19).

The ideal case is an horizontal separation direction after a vertical one, the beam positions are (see Figure 5.19 (a)):

$$\begin{array}{ll} A_x = 0 = & A_y = d \\ B_x = d & B_y = d \\ C_x = d & C_y = 0 \\ D_x = 0 & D_y = 0 \end{array} . \tag{5.24}$$

For a case where misalignments occur, the separation direction of the first Savart plate is $90° + \epsilon_2$ and the direction of the second one is ϵ_4. The coordinates of the beams are given by (see Figure 5.19 (b)):

$$\begin{array}{ll} A_x = (\cos(135 + \epsilon_4) + \cos(45 + \epsilon_2)) \times r_S & A_y = (\sin(135 + \epsilon_4) + \sin(45 + \epsilon_2)) \times r_S \\ B_x = (\cos(45 + \epsilon_4) + \cos(45 + \epsilon_2)) \times r_S & B_y = (\sin(45 + \epsilon_4) + \sin(45 + \epsilon_2)) \times r_S \\ C_x = (\cos(45 + \epsilon_4) + \cos(-45 + \epsilon_2)) \times r_S & C_y = (\sin(45 + \epsilon_4) + \sin(-45 + \epsilon_2)) \times r_S \\ D_x = (\cos(135 + \epsilon_4) + \cos(-45 + \epsilon_2)) \times r_S & D_y = (\sin(135 + \epsilon_4) + \sin(-45 + \epsilon_2)) \times r_S \end{array} . \tag{5.25}$$

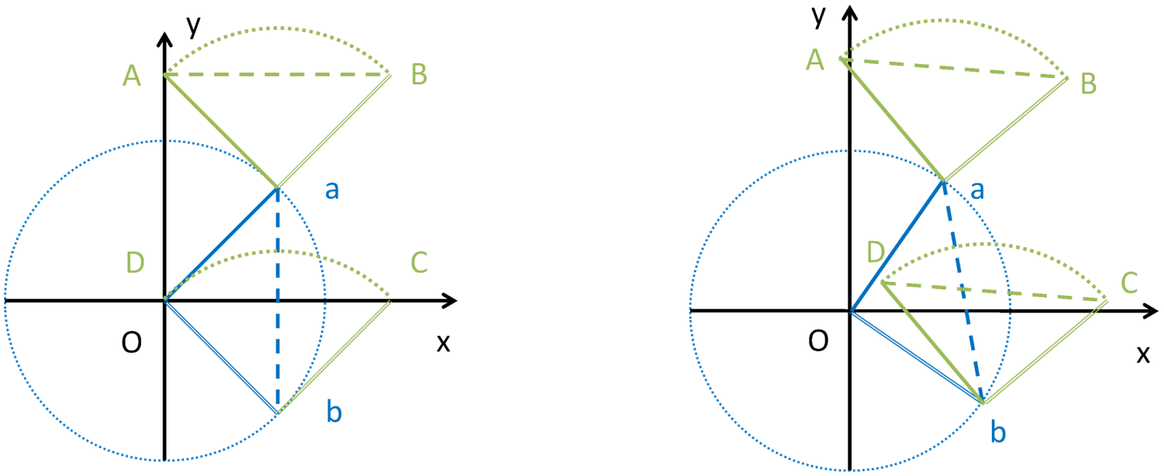

(a) (b)

Figure 5.19: Representation of the beam with two Savart plates: (a) stands for the perfect case where the first separation direction is purely vertical and the second is purely horizontal, (b) stands for a case where small errors on the angles are present. The action of the first plate is pictured in blue while the action of the second one is pictured in green.

5.5.3 Parameters due to the expanding process

To find the parameters due to the expanding process, we measured the beam after the beam expander in two configurations. The first one contains only the beam expander. It measures the intensity of the expanded beam, to compute σ in the gaussian intensity profile $I = I_0 * \exp(-\frac{2*r}{\sigma})$.
The second setup contains the beam expander, a quarter-wave plate, a savart plate and a linear polarizer to convert the polarization variation into an intensity variation to compute θ_i by measuring the distance between two lines of same intensity (Figure 5.20). We found that $\sigma = 2.92$ mm ± 0.04 mm and $\theta_i = 18.57$ arcsec ± 0.2 arcsec.

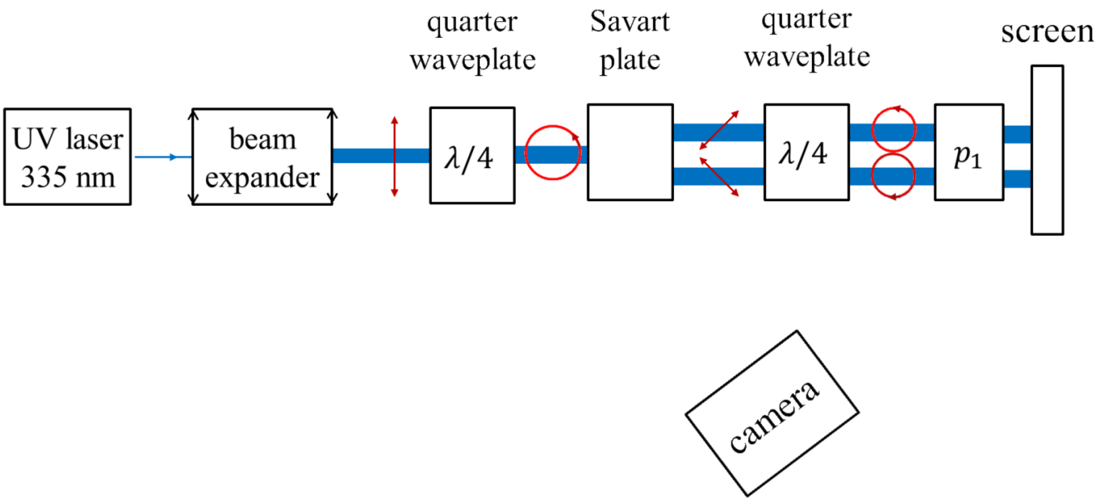

Figure 5.20: Representation of the measuring setup for θ_i, the beams are represented by blue lines and their polarization in red.

5.5.4 Perfect case simulation

Firstly, the perfect case was simulated. It is described by $\epsilon_1 = \epsilon_2 = \epsilon_3 = \epsilon_4 = 0\,, \theta_i = 18.57$ arcsec and $\sigma = 2.92$ mm. The characteristics of the simulation are presented in Figures 5.21 and 5.22.

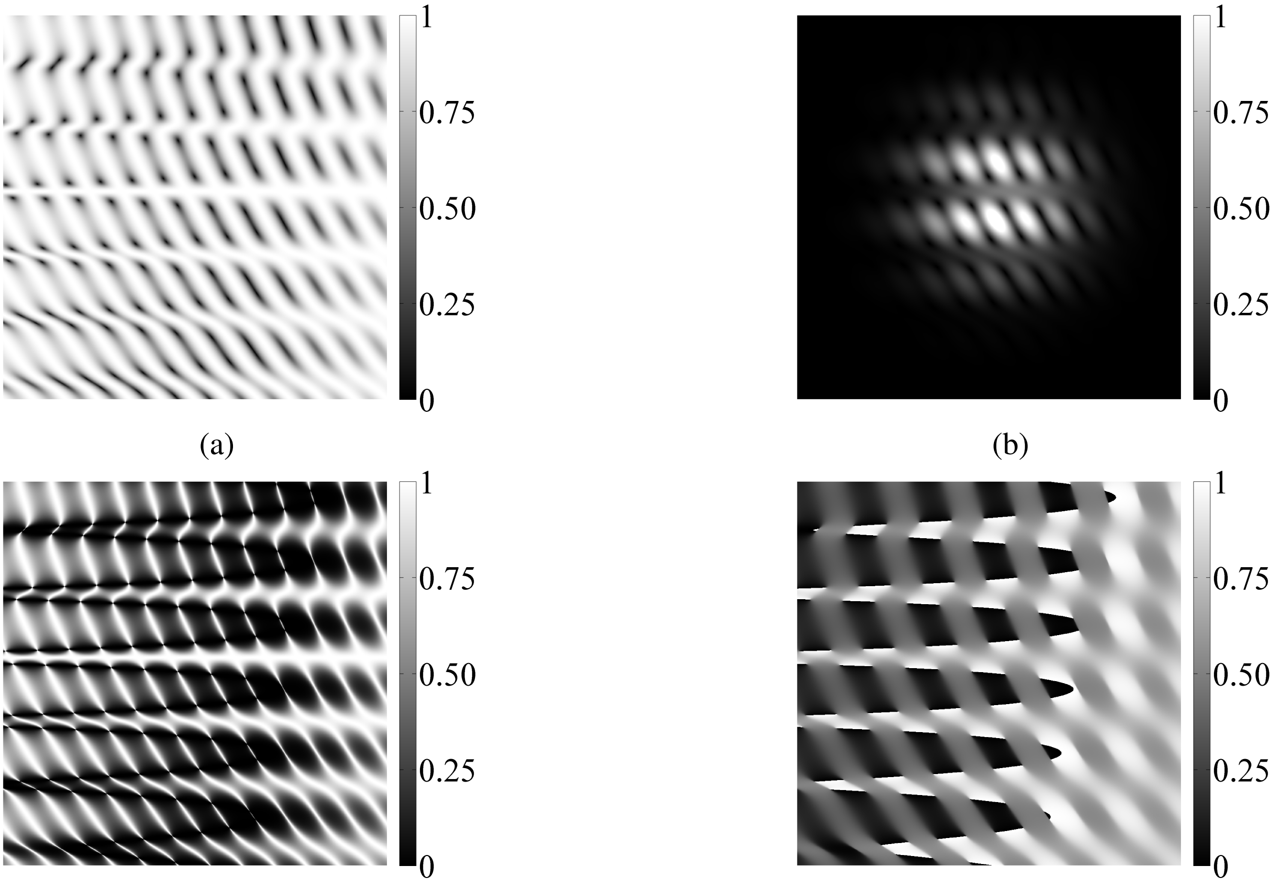

(a) (b) (c) (d)

Figure 5.21: Simulation of the perfect case features for a square of 1.5 cm. (a) Represents the directionality parameter d_p. (b) Pictures the directional intensity I_{dir}. (c) shows the transmitted intensity of the simulated half-wave plate between two perpendicular linear polarizers. (d) Exposes the orientation of the plate fast axis as a multiple of 180°.

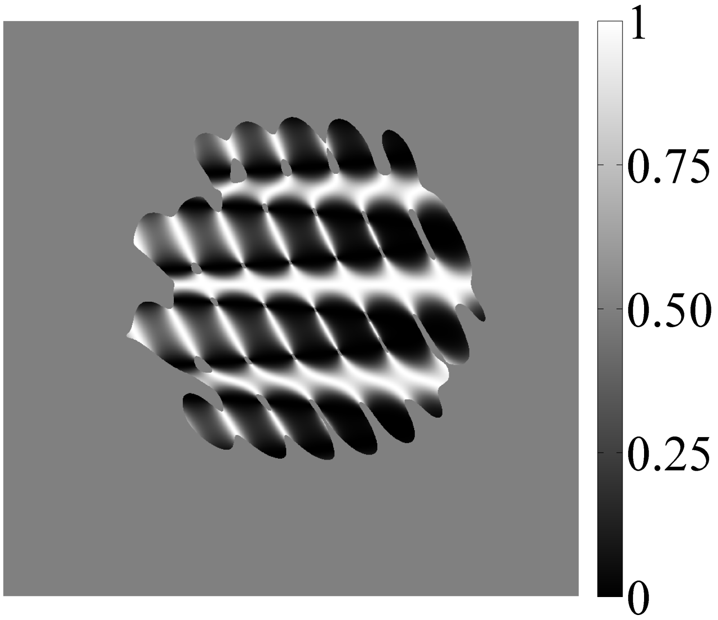

Figure 5.22: Representation of the transmitted intensity for the simulated half-wave plate between two linear polarizers where the areas of misorientation are pictured by grey disks with an intensity of 0.5.

The perfect case captures the essence of the experimental case.

- Several rotation centers are present.
- The rotation of the fast axis along a rotation center is 180°.
- The rotation centers are aligned on several curves.
- The distance between two rotation centers is 13.47 mm with a variation of approximately 0.1 mm, it is approximately the distance between two centers in the experimental case.
- Loss of directionality also appears near the rotation centers for the perfect case.

The major difference is on the directional intensity I_{dir} which is larger in the perfect case simulation than in the simulation of the experimental case.

5.5.5 Definition of the comparison criteria

To simplify the analysis, we defined several comparison criteria

- the dimensions of the frame containing the area submitted to an appropriate recording field,
- the coordinates of four rotation centers (see Figure 5.23),
- the largest and smallest semi-axes of the areas of misorientation for these four centers.

The accuracy of the method for the determination of the coordinates and of the size of the semi-axes is about 1 pixel at the smallest resolution: 1.76 μm.

To compute these parameters, two simulations were realized for each case.

- The first one contains 8 periods of the retarder. It is characterized by a resolution of 7.05 μm and it is used to compute the total rotation of the optical axis, the number of rotation centers and the size of the frame.
- The second one contains 2 periods. It is characterized by a resolution of 1.76 μm and it is used to to compute the position of the centers and the size of the semi-axes.

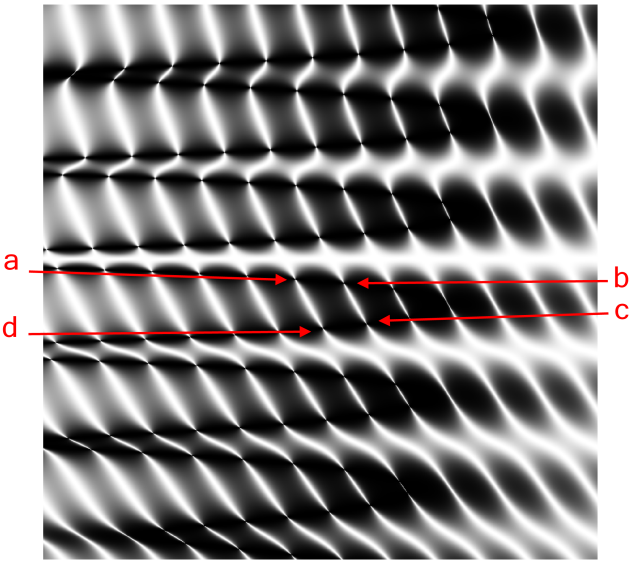

Figure 5.23: Position of the centers used in the sensitivity analysis.

The results of the sensitivity analysis are presented in the following section.

5.5.6 Polarization sensitivity analysis

Our accuracy on the determination of the angle of the polarization axes is about 1°, so the parameters ϵ will vary between $-1°$ and $+1°$ with a step of 0.5°. Since it covers a large amount of cases, we limited our simulation to several physical cases:

- only one component is misaligned,
- all the components present the same error,
- one component is misaligned but the next elements are properly aligned according to it.

Case 1

The polarization axis of the second Savart plate is misaligned.

$$\epsilon_1 = \epsilon_2 = \epsilon_3 = 0 \quad \epsilon_4 \in [-1;\ 1]$$

Table 5.3: Results for an error on the second Savart plate

	$\epsilon_4 = -1$	$\epsilon_4 = -0.5$	$\epsilon_4 = 0$	$\epsilon_4 = 0.5$	$\epsilon_4 = 1$
Frame (pixels)	1297×1344	1296×1388	1296×1257	1295×1369	1295×1374
Coordinates (pixels)					
a	(637,994)	(633,987)	(629,980)	(629,973)	(621,966)
b	(1402,1062)	(1397,1052)	(1392,1043)	(1387,1034)	(1382,1025)
c	(1728,1684)	(1739,1674)	(1741,1683)	(1763,1693)	(1774,1701)
d	(1044,1739)	(1055,1746)	(1066,1753)	(1077,1760)	(1088,1767)
Size of the axes (pixels)					
a	(46,19)	(47,18)	(47,19)	(46,19)	(47,19)
b	(46,14)	(44,14)	(44,15)	(44,14)	(42,16)
c	(65,17)	(64,18)	(62,17)	(63,18)	(62,19)
d	(55,19)	(53,20)	(54,19)	(53,19)	(53,20)

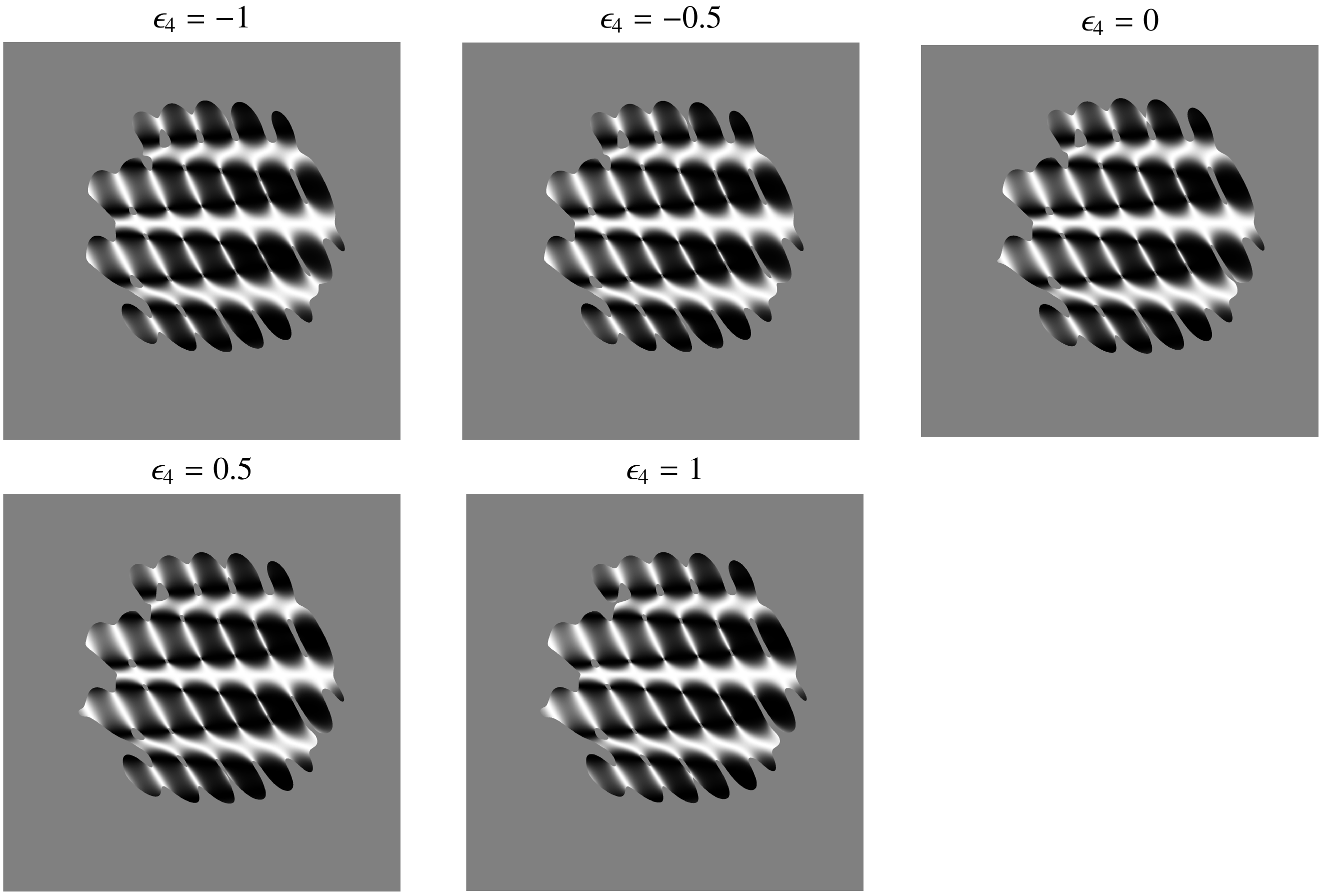
$\epsilon_4 = -1$

$\epsilon_4 = -0.5$

$\epsilon_4 = 0$

$\epsilon_4 = 0.5$

$\epsilon_4 = 1$

Figure 5.24: Representation of I_{mis} with variation of ϵ_4.

Case 2

The polarization axis of the second quarter-wave plate is misaligned.

$$\epsilon_1 = \epsilon_2 = \epsilon_4 = 0 \quad \epsilon_3 \in [-1;\ 1]$$

Table 5.4: Results for an error on the second quarter-wave plate.

	$\epsilon_3 = -1$	$\epsilon_3 = -0.5$	$\epsilon_3 = 0$	$\epsilon_3 = 0.5$	$\epsilon_3 = 1$
Frame (pixels)	1293×1342	1295×1349	1296×1257	1297×1365	1298×1371
Coordinates (pixels)					
a	(620,981)	(625,981)	(629,980)	(633,980)	(637,979)
b	(1382,1041)	(1387,1042)	(1392,1043)	(1396,1044)	(1401,1044)
c	(1755,1702)	(1752,1692)	(1741,1683)	(1749,1674)	(1750,1664)
d	(1068,1769)	(1067,1761)	(1066,1753)	(1065,1745)	(1064,1737)
Size of the axes (pixels)					
a	(47,21)	(48,20)	(47,19)	(46,19)	(46,19)
b	(43,15)	(44,15)	(44,15)	(45,14)	(44,14)
c	(64,18)	(63,18)	(62,17)	(63,18)	(63,15)
d	(55,20)	(55,19)	(54,19)	(54,19)	(53,19)

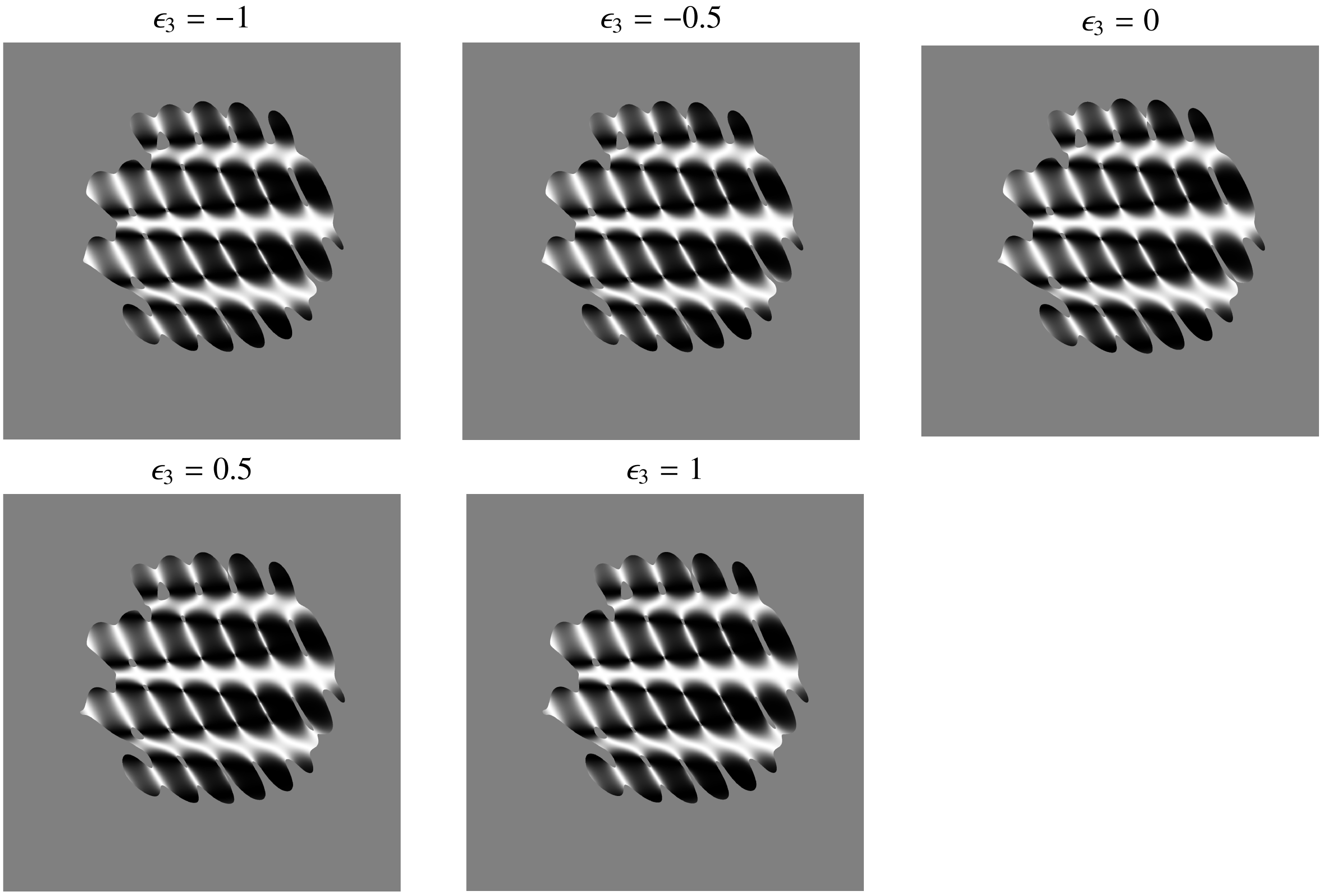

$\epsilon_3 = -1$ $\epsilon_3 = -0.5$ $\epsilon_3 = 0$

$\epsilon_3 = 0.5$ $\epsilon_3 = 1$

Figure 5.25: Representation of I_{mis} with variation of ϵ_3.

Case 3
The polarization axis of the first Savart plate is misaligned.

$$\epsilon_1 = \epsilon_3 = \epsilon_4 = 0 \quad \epsilon_2 \in [-1;\ 1]$$

Table 5.5: Results for an error on the first Savart plate.

	$\epsilon_2 = -1$	$\epsilon_2 = -0.5$	$\epsilon_2 = 0$	$\epsilon_2 = 0.5$	$\epsilon_2 = 1$
Frame (pixels)	1296×1271	1297×1282	1282×1257	1297×1385	1296×1385
Coordinates (pixels)					
a	(638,994)	(634,987)	(629,980)	(624,973)	(620,967)
b	(1400,1061)	(1396,1052)	(1392,1043)	(1387,1034)	(1382,1025)
c	(1738,1693)	(1744,1688)	(1741,1683)	(1757,1679)	(1764,1674)
d	(1036,1739)	(1053,1746)	(1066,1753)	(1081,1759)	(1095,1765)
Size of the axes (pixels)					
a	(47,18)	(46,18)	(47,19)	(47,20)	(47,21)
b	(45,15)	(45,15)	(44,15)	(44,14)	(44,14)
c	(68,20)	(66,18)	(62,17)	(62,18)	(60,17)
d	(56,19)	(55,17)	(54,19)	(54,19)	(53,19)

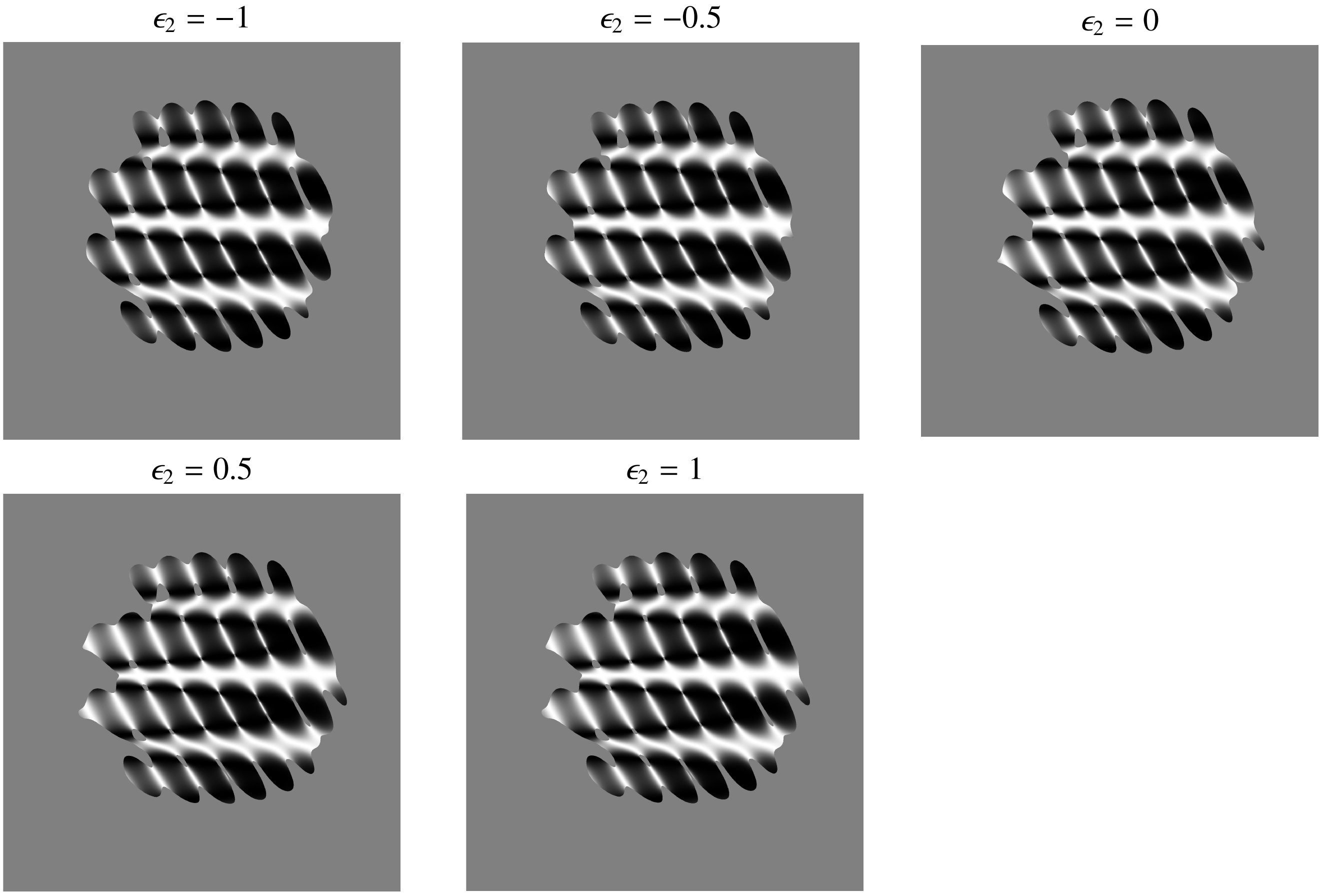

$\epsilon_2 = -1$ $\epsilon_2 = -0.5$ $\epsilon_2 = 0$

$\epsilon_2 = 0.5$ $\epsilon_2 = 1$

Figure 5.26: Representation of I_{mis} with variation of ϵ_2.

Case 4

The polarization axis of the first element is misaligned.

$$\epsilon_2 = \epsilon_3 = \epsilon_4 = 0 \quad \epsilon_1 \in [-1; 1]$$

Table 5.6: Results for an error on the first quarter-wave plate.

	$\epsilon_1 = -1$	$\epsilon_1 = -0.5$	$\epsilon_1 = 0$	$\epsilon_1 = 0.5$	$\epsilon_1 = 1$
Frame (pixels)	1296×1365	1296×1362	1282×1257	1296×1350	1296×1343
Coordinates (pixels)					
a	(628,979)	(629,980)	(629,980)	(630,980)	(631,981)
b	(1392,1043)	(1392,1042)	(1392,1043)	(1392,1043)	(1392,1043)
c	(1758,1683)	(1754,1683)	(1741,1683)	(1748,1684)	(1745,1685)
d	(1075,1754)	(1070,1753)	(1066,1753)	(1062,1753)	(1059,17545)
Size of the axes (pixels)					
a	(47,19)	(46,18)	(47,19)	(46,19)	(47,18)
b	(45,15)	(45,15)	(44,15)	(44,14)	(44,14)
c	(63,18)	(66,18)	(62,17)	(63,18)	(63,19)
d	(55,19)	(55,17)	(54,19)	(54,18)	(54,19)

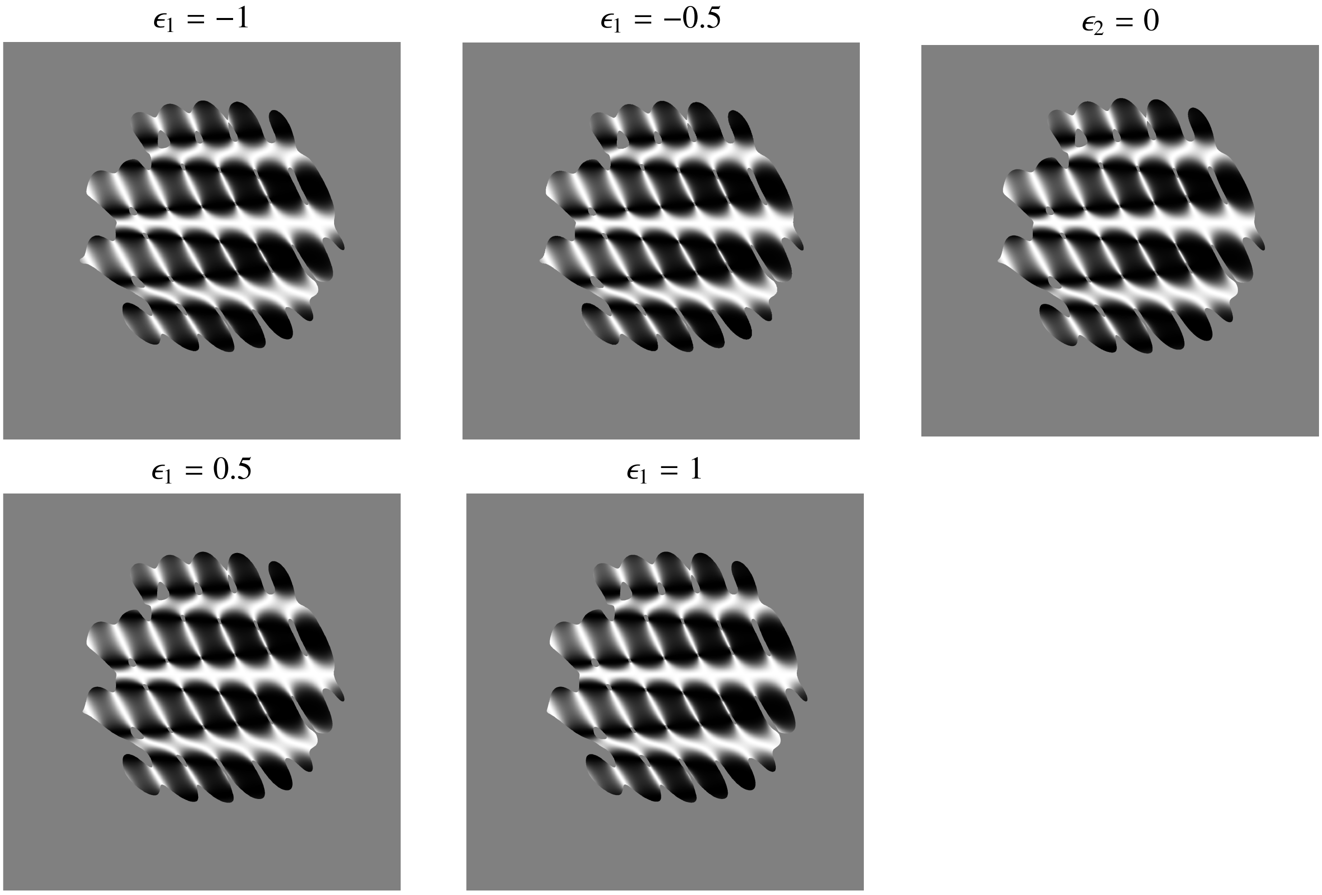
$\epsilon_1 = -1$
$\epsilon_1 = -0.5$
$\epsilon_2 = 0$
$\epsilon_1 = 0.5$
$\epsilon_1 = 1$

Figure 5.27: Representation of I_{mis} with variation of ϵ_1.

Case 5
The error on the alignment of all the elements is the same.

$$\epsilon_1 = \epsilon_2 = \epsilon_3 = \epsilon_4, \in [-1;\ 1]$$

Table 5.7: Results for the same error for all the elements.

	$\epsilon_1 = -1$	$\epsilon_1 = -0.5$	$\epsilon_1 = 0$	$\epsilon_1 = 0.5$	$\epsilon_1 = 1$
Frame (pixels)	1294×1271	1295×1278	1282×1257	1297×1386	1297×1401
Coordinates (pixels)					
a	(628,994)	(629,987)	(629,980)	(629,973)	(629,967)
b	(1391,1059)	(1391,1051)	(1392,1043)	(1391,1034)	(1391,1026)
c	(1748,1711)	(1749,1697)	(1741,1683)	(1753,1670)	(1755,1658)
d	(1046,1756)	(1057,1755)	(1066,1753)	(1075,1751)	(1085,1750)
Size of the axes (pixels)					
a	(48,19)	(46,19)	(47,19)	(47,19)	(47,20)
b	(45,15)	(45,16)	(44,15)	(42,14)	(43,15)
c	(67,20)	(65,19)	(62,17)	(61,16)	(60,17)
d	(57,20)	(57,19)	(54,19)	(52,19)	(51,19)

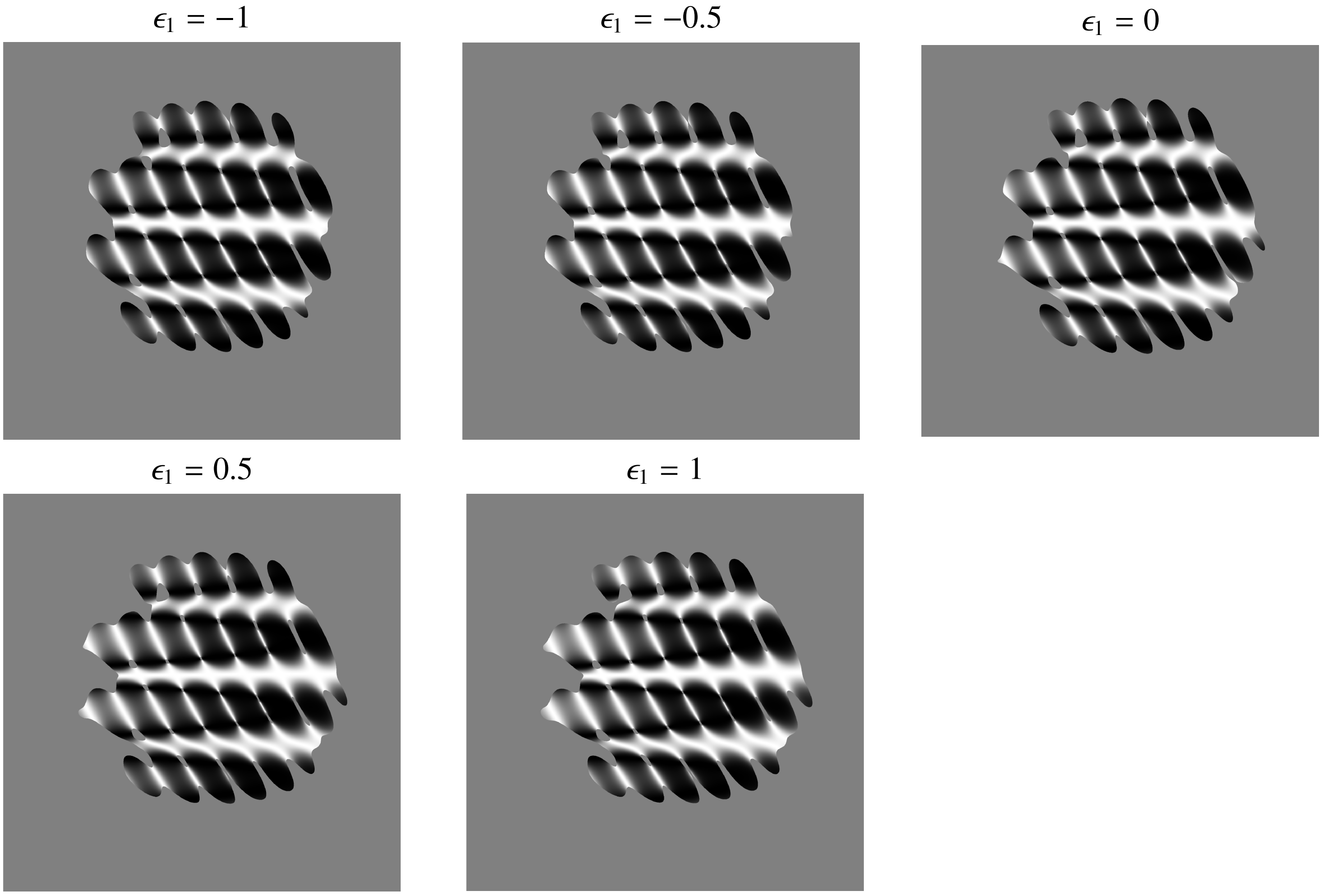

Figure 5.28: Representation of I_{mis} with variation of ϵ.

Case 6

The first Savart plate is misaligned, the next elements possess the same error.

$$\epsilon_1 = 0 \quad \epsilon_2 = \epsilon_3 = \epsilon_4, \in [-1;\ 1]$$

Table 5.8: Results for an error on the first Savart with the same error for the next elements.

	$\epsilon_2 = -1$	$\epsilon_2 = -0.5$	$\epsilon_2 = 0$	$\epsilon_2 = 0.5$	$\epsilon_2 = 1$
Frame (pixels)	1294×1270	1295×1276	1282×1257	1297×1389	1289×1403
Coordinates (pixels)					
a	(629,994)	(629,987)	(629,980)	(628,973)	(629,966)
b	(1390,1059)	(1391,1051)	(1392,1043)	(1391,1034)	(1391,1026)
c	(1741,1712)	(1746,1697)	(1741,1683)	(1756,1670)	(1761,1657)
d	(1038,1755)	(1052,1754)	(1066,1753)	(1080,1752)	(1093,1750)
Size of the axes (pixels)					
a	(47,19)	(46,20)	(47,19)	(46,20)	(47,20)
b	(45,16)	(44,15)	(44,15)	(43,14)	(44,14)
c	(67,20)	(64,19)	(62,17)	(62,17)	(60,16)
d	(56,20)	(56,19)	(54,19)	(53,19)	(52,19)

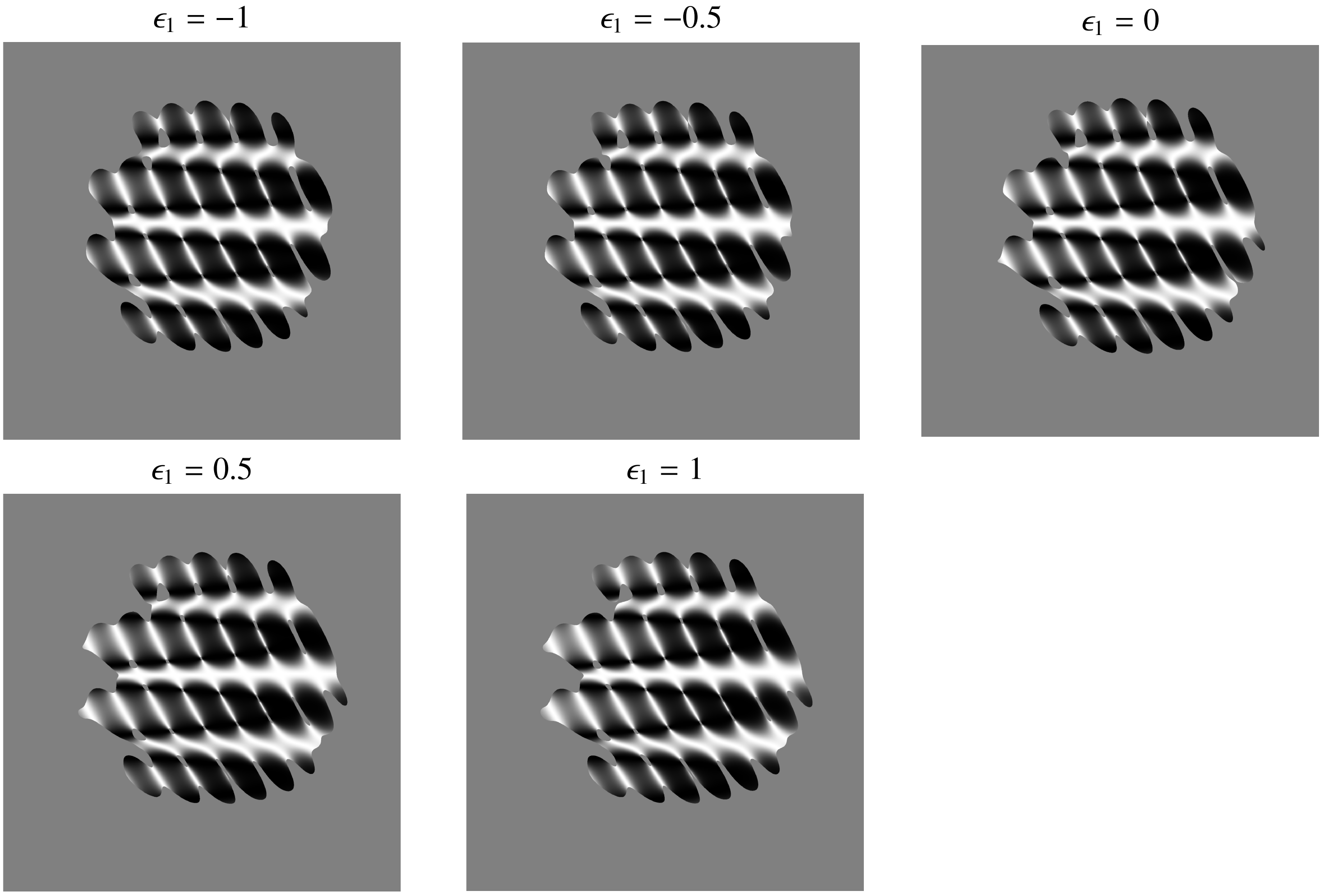

$\epsilon_1 = -1$

$\epsilon_1 = -0.5$

$\epsilon_1 = 0$

$\epsilon_1 = 0.5$

$\epsilon_1 = 1$

Figure 5.29: Representation of I_{mis} with variation of ϵ_2.

Results analysis for the polarization part

When compared to the ideal case, the simulations present small differences with the perfect case.

The variation of the fast axis along a rotation center is always 180° and the pattern of the rotation centers is similar.

The modification of the parameters increases with the error.

The size of the frame exhibits variations. The larger one happens for the case 5 where all the active axes are misaligned with the same error. The difference on the surface of the frame is about 12% of the perfect case.

We can also observe that the centers do not stay at the same place, their displacement also increases with the error on the positioning. The larger displacement is about 30 pixels, it corresponds to 53 μm which is small compared to the size of the simulated retarder which is about 1.5 cm in the simulation.

The semi-axes of the ellipses also present variations, the largest variation exhibits an increased about 10% compared the perfect case. Since the error on the determination of the size of the semi-axes is about 1 pixel, the maximum error on the variation computation is about 4 pixels which is quite important compared to the observed variation. In the future, to increase the result/error ratio, simulations should be performed with a smaller pixel size.

5.5.7 Expanding process simple analysis

Due to the expanding process, σ and θ_i are modified at the same time, they were measured for two configurations.

Table 5.9: Results for the variation of the beam parameters.

	position1	position 2	reference
Parameters			
σ (mm)	2.04	2.88	2.92
θ_i (arcsec)	43.08	23.54	18.57
Frame	1324×1376	1411×1353	1296×1257
Coordinates (pixels)			
a	(1178,1024)	(716,995)	(629,980)
b	(1497,1037)	(1311,1033)	(1392,1043)
c	(1648,1316)	(1602,1560)	(1751,1683)
d	(1342,1329)	(1053,1601)	(1066,1753)
Size of the axes (pixels)			
a	(18,6)	(35,14)	(47,19)
b	(19,8)	(34,11)	(44,15)
c	(21,6)	(43,13)	(62,17)
d	(18,6)	(38,14)	(54,19)

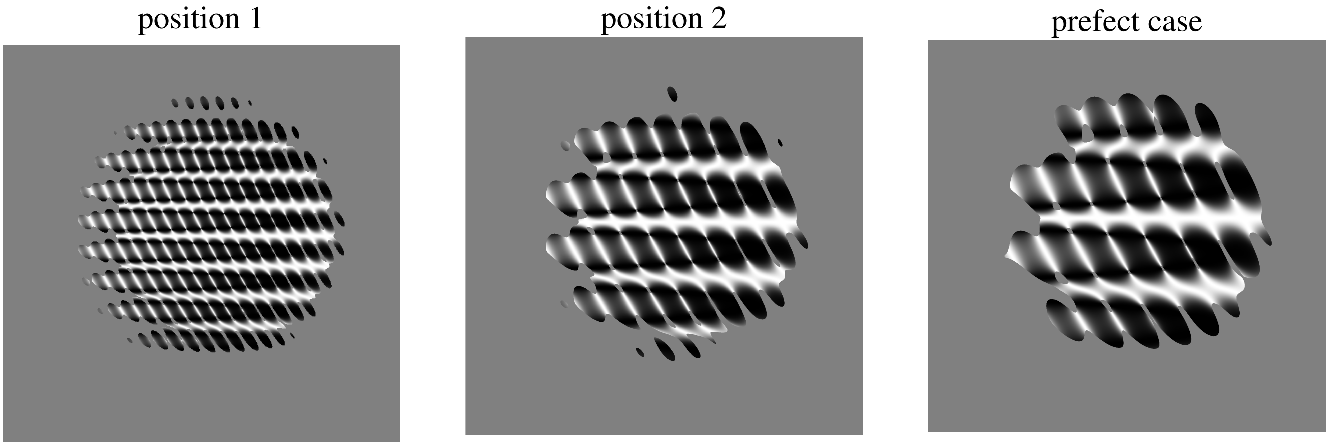

Figure 5.30: Representation of I_{mis} with variation due to the expanding process.

Results analysis for the expanding part

This time, strong modifications exist. The rotation of the fast axis is still 180° along a rotation center but the number of rotation centers drastically changes. However, the pattern of the centers is similar for the three cases.

We can observe that an increase of the width of the Gaussian beam is combined with a reduction of the incident angle. It is shown by a reduction of the frame size and by an increase of the distance between two rotation centers. The reduction of the distance between two centers was expected. Also a decrease of the misorientation ellipses axes exists and it is approximately the same percentage than the reduction of the distance between two rotation centers.

In the future, upgrades will be performed on the measuring setup of the beam parameters to achieve a better accuracy on σ and θ_i using a UV camera at normal incidence instead of a projection screen.

5.5.8 Conclusion of the sensitivity analysis

Two kinds of parameters were selected in the analysis: the errors on the angles formed by the horizontal and the active polarization axes of the elements and the beams parameters σ and θ_i.

The results of the simulations based on the polarization parameters present no obvious variations in our error range. A significant variation of the recorded plate appears when the alignment error is typically five times larger than our experimental one (5° instead of 1°). An example is shown in Figure 5.31. Therefore we are pretty confident with our polarization systems and no upgrade on the determination of the axis seems mandatory.

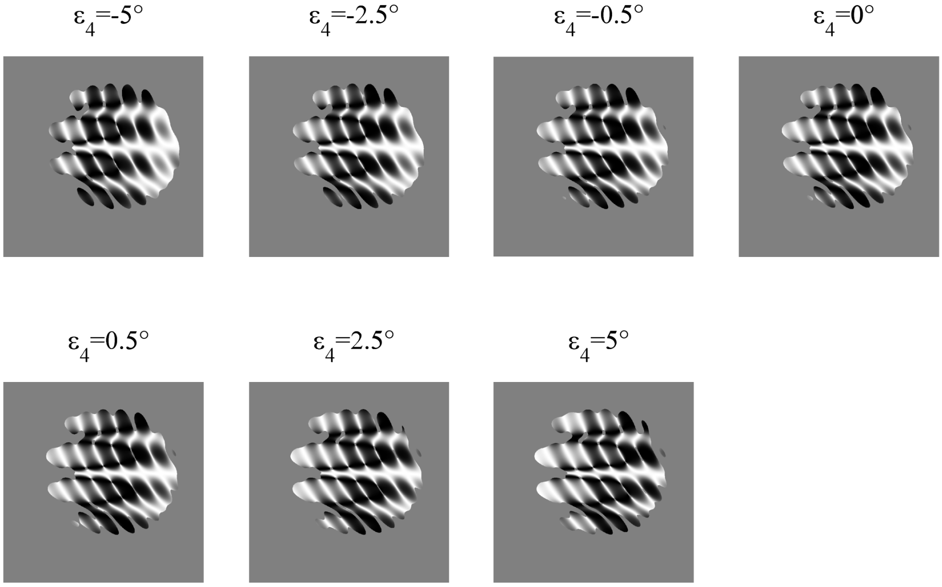

Figure 5.31: Variations of I_{mis} for larger error on the second Savart plate polarization axis. The modification of the fast axis pattern becomes important for angle of 5°.

The parameters depending on the collimating process are modified at the same time. This leads to great variations of the characteristics of the beam like the frame, the number of rotation centers, the distance between them and the size of the semi-axes of the misorientation ellipses. In the future, the measurement systems should be upgraded to achieve a better quality of the measurements and other measurements and simulations will be performed to obtain a better knowledge on the feasible configurations.

5.6 Conclusions and perspectives

In this chapter, the vortex retarders were described. They are characterized by a rotation of their fast axis. Several systems of four differently polarized beams used to record them without mechanical action were exposed and their resulting electric fields were analyzed. Since the fields differ from the ideal case, decreases of intensity or directionality occur and misorientation areas of the liquid crystal could appear. Simple prototypes were realized to determine the experimental limits and the misorientation areas were computed for the numerical simulations. The experimental recording setup was exposed and the first prototypes were presented, analyzed and compared to the simulation of the actual recording setup. Finally, a sensitivity analysis was performed to achieve a better knowledge of the experimental reality.

Several things still need to be investigated. The effect of the neighbors on this particular case must be measured to determine the decrease of the misorientation areas. The wavefront aberrations due to the Savart plates should be simulated, measured and added in the computation of the recording electric field. Accurate measurements of the beams parameters variation should be performed to compute the variation of the electric field when the two parameters change.

Chapter 5 references

[1] D.Mawet, E.Serabyn, K.Liewer, R.Burruss, J.Hickey, and D.Shemo, “The vector vortex coronagraph : laboratory results and first light at palomar observatory,” *Astrophys. J.* **709**(1), 53–57 (2010).

[2] A.Niv, G.Biener, V.Kleiner, and E.Hasman, “Manipulation of the pancharatnam phase in vectorial vortices,” *Opt. Express* **14**(10), 4208–4220 (2006).

[3] A.Niv, G.Biener, V.Kleiner, and E.Hasman, “Rotating vectorial vortices produced by space-variant subwavelength gratings,” *Opt. Lett.* **30**(21), 2933–2935 (2005).

[4] D.Mawet, E.Serabyn, K.Liewer, C.Hanot, S.McEldowney, D.Shemo, and N.O’Brien, “Optical vectorial vortex coronagraphs using liquid crystal polymers theory, manufacturing and laboratory demonstration,” *Opt. Express* **17**(3), 1902–1918 (2009).

[5] S.Pancharatnam, “Generalized theory of interference, and its applications - part i. coherent pencils,” *Proceedings of the Indian Academy of Sciences - Section A* **44**(5), 247–262 (1956).

[6] E.J.Galvez, “Applications of geometric phase in optics,” *Recent Research Developments in Optics* **2**, 165–182 (2002).

[7] Z.Bomzon, G.Biener, V.Kleiner, and E.Hasman, “Space-variant pancharatnam-berry phase optical elements with computer generated subwavelength gratings,” *Opt. Lett.* **27**(13), 1141–1143 (2002).

[8] A.Niv, G.Biener, V.Kleiner, and E.Hasman, “Spiral phase elements obtained by use of discrete space-variant subwavelength gratings,” *Opt. Commun.* **251**(4-6), 306–314 (2005).

[9] Hariharan, P., “The geometric phase,” in [*Progress in optics*], Wolf, E., ed., *Progress in Optics* **48**, 149–201, Elsevier (2005).

[10] Q.Zhan and J.R.Leger, “Interferometric measurement of the geometric phase in space-variant polarization manipulations,” *Opt. Commun.* **213**, 241–245 (2002).

[11] M.Berry, “The adiabatic phase and pancharatnam phase for polarized light,” *Journal of modern optics* **34** (1987).

[12] M.Born and E.Wolf, [*Principles of Optics*], Cambridge University Press, 7 ed. (1999).

[13] S.Huard, [*Polarisation de la lumière*], Masson, 1 ed. (1993).

[14] P.Piron, P.Blain, S.Habraken, and D.Mawet, “Polarization holography for vortex retarders recording,” *Appl. Opt.* **52**(28), 7040–7048 (2013).

[15] D.M.Shemo and S.McEldowney, “Optical vortex retarder micro-array,” (Feb. 12 2013). US Patent 8,373,810.

[16] B.Schaefer, E.Collet, R.Smyth, D.Barret, and B.Fraher, “Measuring the stokes polarization parameters,” *Am. J. Phys.* **75**, 163–168 (2007).

[17] B.Kilosanidze and G.Kakauridze, “Polarization-holographic gratings for analysis of light. 1. analysis of completely polarized light,” *Appl. Opt.* **46**(7), 1040–1049 (2007).

6

Coronagraphy

Contents

In this chapter, we focus on our initial application of vortex retarders: coronagraphy. The goal of coronagraphy is to suppress the light of a central star to make its faint companions visible. The principle of coronagraphy is presented and the use of vortex retarders is mathematically developed. The computation of the performances is explained. The attenuation of on-axis sources will be computed for the theoretical and experimental systems presented in the previous chapters. For each system, several cases will be studied to know the influence of the area of misorientation and the effect of its reduction to the presence of well aligned neighbors. Finally the attenuation for off-axis sources will be computed for several cases and compared to the attenuation of an on-axis one.

6.1 Introduction

Coronagraphy is a method invented by Bernard Lyot [1] to observe the sun's corona. An opaque mask is inserted inside a telescope to block the light from the sun to allow the examination of the sun's corona. Applied to the observation of exoplanets, coronagraphy is used to simulate the eclipse of a star by reducing or suppressing its light. Since the star companions are fainter than the star, they are usually hidden by the central star light. A decrease of this light reduces the contrast between the star and its companions allowing their imaging.

A coronagraph has become a generic term for a system which suppresses or strongly reduces the on-axis light of a central star while allowing the transmission of the light of surrounding sources to allow their detection [2, 3].

The basic principle is pictured in Figure 6.1 for a simple experimental test bench. For the observations with a telescope, the lenses are replaced by the mirrors of the telescope.

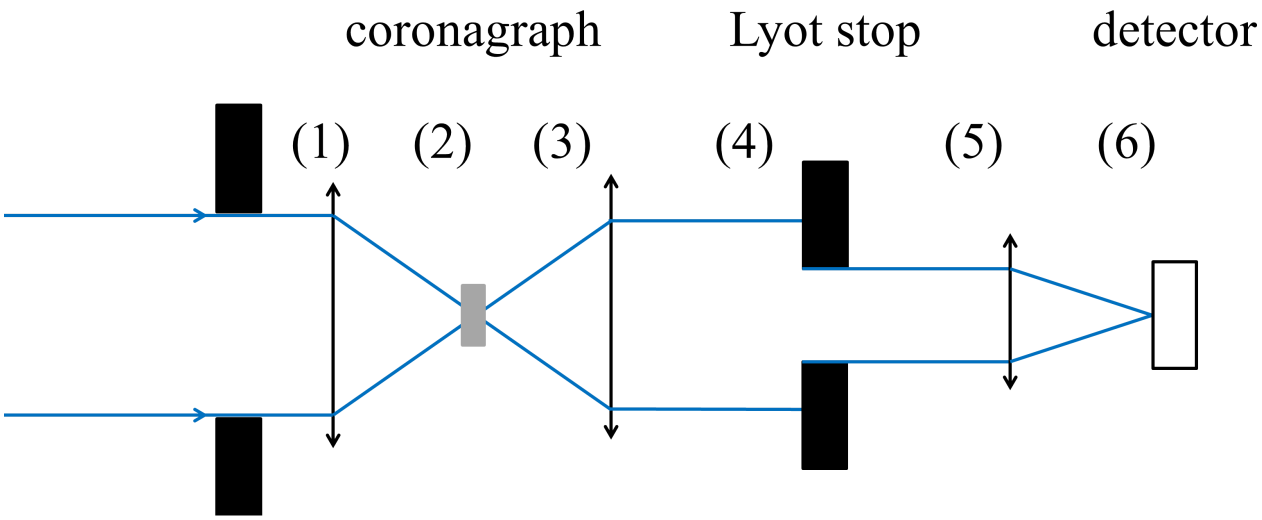

Figure 6.1: Principle of the coronagraphic setup, the numbers present the important steps of the setup. (1) Is a the beginning of the optical setup, (2) before the coronagraph, (3) after the coronagraph, (4) before the Lyot stop, (5) after the Lyot stop, (6) at the detector.

To adapt the coronagraphy principle to the observation of exoplanets, several methods and techniques were investigated [2, 4]. In this chapter we will focus on phase mask coronagraphs.

The principle is the same as the Lyot setup but the coronagraph mask is not an opaque one. It allows the transmission of the central star light but it affects the phase of the wavefront to reject this central starlight outside the Lyot stop. Several designs were proposed [5, 6], realized [7, 8] and tested on telescopes [9, 10].

Roddier phase mask

The mask proposed by Rodier [5] produces a π phase shift on a small part of the center of the central lobe of the Airy pattern. The phase shift is introduced by a thickness difference of the retarder.

The mask presents several drawbacks

- the phase retard depends on the wavelength $\psi = \frac{2\pi}{\lambda}(n-1)h$,
- the size of the central lobe is a function of the wavelength [5].

Therefore, the ideal effect of the mask is obtained for only one wavelength and the performances decrease when used with a large bandwidth.

Four quadrant phase mask

An evolution of the Roddier phase mask was proposed by Rouan in 2000 [6]. The mask divides the focal plane into four symmetrical areas. On one diagonal, the areas will induce a π phase retard caused by a thickness difference with the adjacent parts (see figure 6.2).

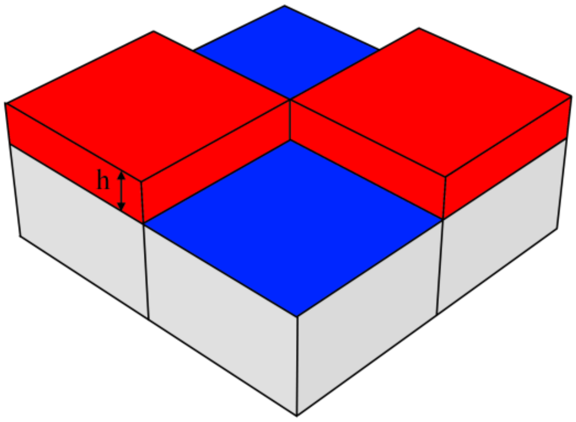

Figure 6.2: Representation of the four quadrant phase mask. The areas in red are characterized by an additional thickness computed to produce an extra π phase retard compared to the blue areas.

Thanks to the π phase retard between two adjacent quadrants, the central light will destructively interfere and it will be rejected outside of the Lyot stop. The advantage of this mask is the absence of geometric chromatism but it still exhibits a variation of the phase retard with the wavelength.

To solve this problem, the use of subwavelength gratings was proposed [11]. The phase retard will be obtained trhough the variation of the grooves orientation instead of a variation of the thickness. The gratings parameters achieve a corresponding half-wave plate and the groove orientation will change about 90° from one area to the other (see figure 6.3).

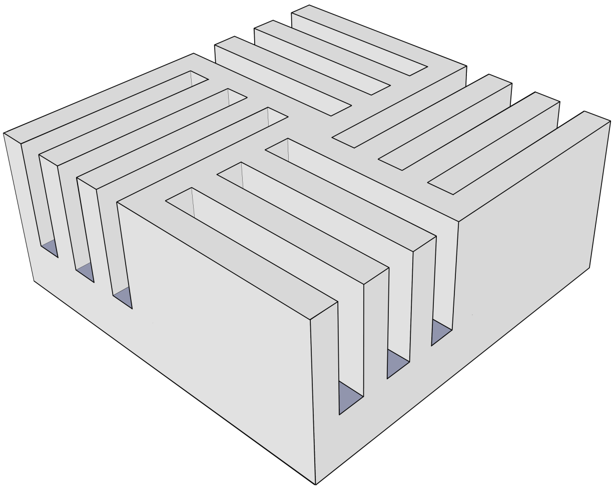

Figure 6.3: Representation of the four quadrant phase mask with subwavelength gratings. The gratings parameters are the same but the groove orientation is rotated from one area to the other.

Unfortunately, due to the rapid change of gratings orientations, phase discontinuities are present on the edges of the quadrants. They will cause dead zones on the final pictures which will prevent the observation of the companion if its light falls on the edges.

Vortex coronagraphs

Since the dead zones are due to the discontinuity of the grooves orientation, a continuous rotation of the fast axis was imagined leading to the use of vortex retarders for coronagraphy. Two avatars exist: the Annular Groove Phase Mask (AGPM) and the Vector Vortex Coronagraph. The AGPM [2, 12, 13] is composed of circular subwavelength gratings while the other one contain liquid crystals polymers oriented to achieve a continuous rotation of the fast axis [8, 10, 14]. Both present specific advantages and drawbacks [2, 15] as the difficulty to achieve the optimal parameters of the grating or the difficulty to achieve a proper orientation of the liquid crystals at the center of the retarder.

6.2 Mathematical description of coronagraphy

The setup in Figure 6.1 is used to prove the perfect rejection of an optical vortex coronagraph by computing the amplitude of the electric field at each important steps. To simplify the computation, all the lenses are approximated as perfect and are characterized by the same focal length f.

Before the first lens (1), a uniform amplitude is considered, it is given by equation 6.1.

$$\Pi\left(\frac{r_1}{2R_1}\right) \tag{6.1}$$

where r_1 is the radial coordinate in the aperture axes and R_1 is the radius of the circular aperture.
After the first lens and before the coronagraph (2), the amplitude is given by equation 6.2.

$$\int_0^{\infty} \Pi\left(\frac{r_1}{2R_1}\right) \exp \frac{-2\pi\imath}{\lambda f} \left(\rho r_1 \cos(\omega) \cos(\theta_1) + \rho r_1 \sin(\omega) \sin(\theta_1)\right) \tag{6.2}$$

where r_1, θ_1 are the polar coordinates for the aperture and ρ, ω are the polar coordinates for the mask and λ is the incident wavelength. After simplifications, the amplitude is given by equation 6.3.

$$2\pi R^2 \frac{J_1\left(2\pi R_1 \rho / f\lambda\right)}{2\pi R_1 \rho / f\lambda} \tag{6.3}$$

where J_1 is the first order Bessel function.
After the coronagraph (3), the amplitude is given by equation 6.4.

$$2\pi R_1^2 \frac{J_1\left(2\pi R_1 \rho / f\lambda\right)}{2\pi R \rho / f\lambda} e^{\imath 2\alpha} \tag{6.4}$$

where α is the local orientation of the optical axis of the coronagraph, for a vortex retarder with a topological charge of two, $\alpha = \omega$.
Before the Lyot stop: (4), the electric field is given by equation 6.5.

$$\int_0^{\infty} \int_0^{2\pi} 2\pi R_1^2 \frac{J_1\left(2\pi R_1 \rho / f\lambda\right)}{2\pi R_1 \rho / f\lambda} e^{\imath 2\omega} e^{-\frac{\imath 2\pi}{f\lambda} \rho r_2 \cos(\omega - \theta_2)} \rho \, d\rho \, d\omega \tag{6.5}$$

where r_2, θ_2 are the polar coordinates in the Lyot stop axes.

Thanks to the definition of a Bessel function:

$$J_n(z) = \frac{1}{2\pi\imath^{-n}} \int_0^{2\pi} e^{\imath z cos\eta} e^{\imath n\eta} d\eta$$

, the amplitude before the Lyot stop is given by equation 6.6.

$$-\frac{e^{2\imath\theta_2}}{2\pi} 2\pi R_1^2 \int_0^{\infty} \frac{J_1(2\pi R_1 \rho/f\lambda)}{2\pi R_1 \rho/f\lambda} J_2(2\pi\rho r_2/f\lambda)\rho d\rho \tag{6.6}$$

Using the Sonine's integral [16]

$$\int_0^{\infty} y^{1+\mu-\lambda} J_\lambda(ay) J_\mu(by) dy = \left\{ \begin{array}{ll} 0 & 0 < a < b \\ \\ \dfrac{b^\mu (a^2 - b^2)^{\lambda-\mu-1}}{2^{\lambda-\mu-1} a^\lambda \Gamma(\lambda - \mu)} & 0 < b < a \end{array} \right\} \tag{6.7}$$

where Γ is the Γ function:$\Gamma(n) = (n-1)!$.
For a charge two vortex:

$$\left\{ \begin{array}{ll} 0 & 0 < r_2 < R_1 \\ \frac{e^{-2\imath\theta_2} r_1^2 f\lambda}{r_2^2} & 0 < R_1 < r_2 \end{array} \right\} \tag{6.8}$$

. Thus for an ideal vortex, the electric field of a central source can be rejected outside the geometric pupil area.

6.3 Computation of the performances of our retarders

To obtain the coronagraphic performances, the amplitude of the electric field A was computed at each important steps of the Figure 6.1 using Fourier propagation in an IDL code given by D. Mawet.

1. At the beginning of the optical setup A_1,
2. before the coronagraph $A_2 = TF(A_1)$,
3. just after the coronagraph $A_3 = P_M * A_2$
   where P_M is the the phase caused by the vortex retarder $P_M = e^{\imath 2\theta}$,
4. just before the Lyot stop $A_4 = TF(A_3)$,
5. after the Lyot stop $A_5 = LS * A_4$,
6. finally, at the detector $A_6 = TF(A_5)$.

The optical setup and the coronagraphs were simulated with the following characteristics.

- arrays size 1024 × 1024
- size of a pixel in the retarder plane $1.76\,\mu$ m
- incident wavelength 550 nm
- F #: 51.2
- sampling 16 pixels per λF

We computed the intensity at the detector for several coronagraphic setups: the perfect case, the systems proposed in 5.3 ($\mathscr{A}$, $\mathscr{B}$ and $\mathscr{C}$ Figure 6.4) and several rotation centers obtained from the simulation of the experimental setups (a, b, c and d see Figures 6.5 and 6.6).

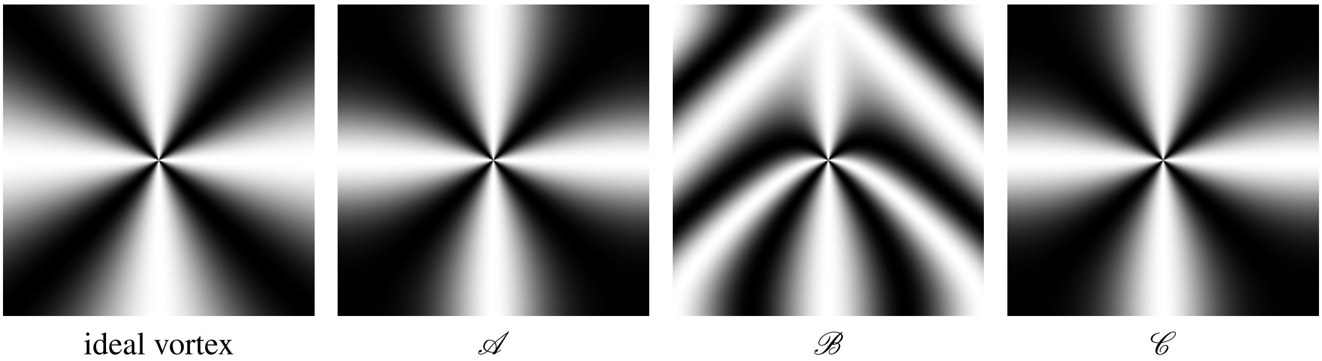

ideal vortex $\mathscr{A}$ $\mathscr{B}$ $\mathscr{C}$

Figure 6.4: Representation of the transmitted intensity of charge 2 vortex with for the centers used to compute the coronagraphic performances.

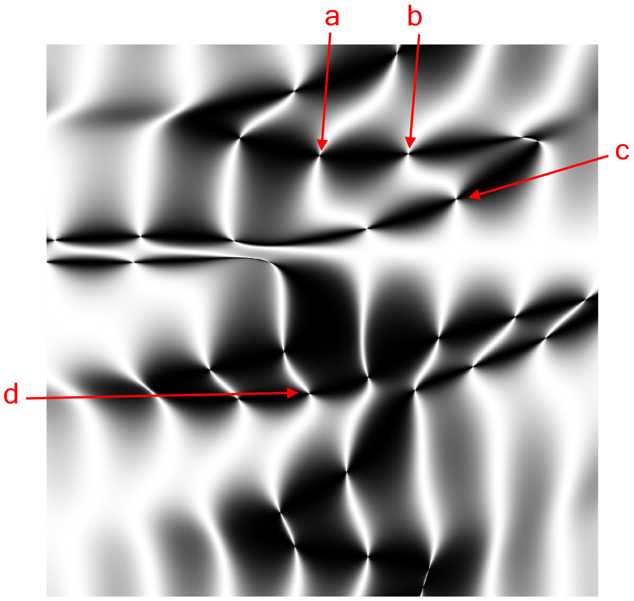

Figure 6.5: Position of the centers (a, b, c and d) chosen to compute the coronagraphic performances.

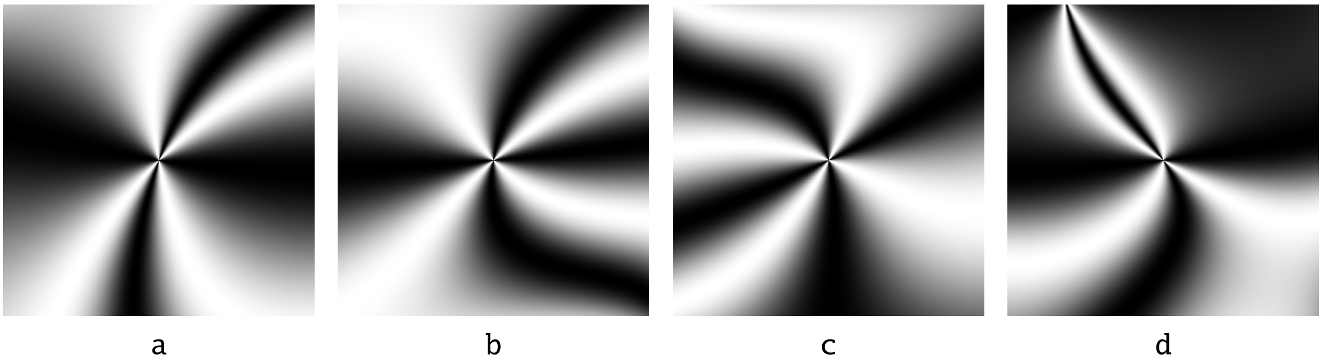

Figure 6.6: Representation of the transmitted intensities for the centers chosen to compute the coronagraphic performances.

Since misorientation of the liquid crystals may appear, we decided to compute the performances for three configurations.

1. The liquid crystals are perfectly oriented everwhere inside the retarder (see Figure 6.7 (a)). Two cases are computed: one with the retarder and one without the retarder. The attenuation Att is computed as the intensity at the detector obtained with the retarder I_A divided by the maximum of the intensity at the detector without the retarder I_B (see Figure 6.8).
2. The liquid crystals exhibit areas of misorientation. A circular obstruction O is added on the retarder to hide the area of misorientation (see Figure 6.7 (b)). An extra way is computed: it consists in the attenuation produced only by the opaque circle. The intensity at the detector is I_C. The attenuation produced by the opaque circle is also computed Att_O like the previous case and the contribution of the retarder to the attenuation is computed as $Contr = \dfrac{Att}{Att_O}$ (see Figure 6.9).
3. The retarder also presents a misorientation area of the liquid crystals but its radius is reduced by 15 μm due to the presence of neighbors receiving the appropriate electric field (see Figure 6.7 (c)). The computation is the same as the previous point except it takes into account a smaller obstruction O.

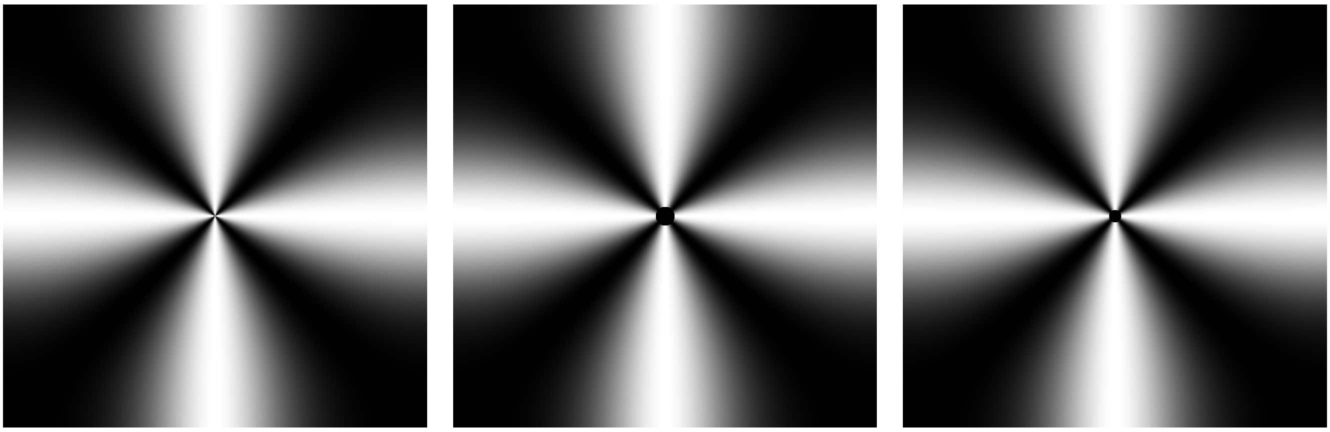

(a)
perfect orientation of the LC

(b)
complete area of misorientation

(c)
reduced area of misorientation

Figure 6.7: Transmitted intensities for the retarder produced by $\mathscr{C}$ for the three proposed configurations. The opaque mask is the circular obstruction O which produced the dark circle at the center for the second and third pictures.

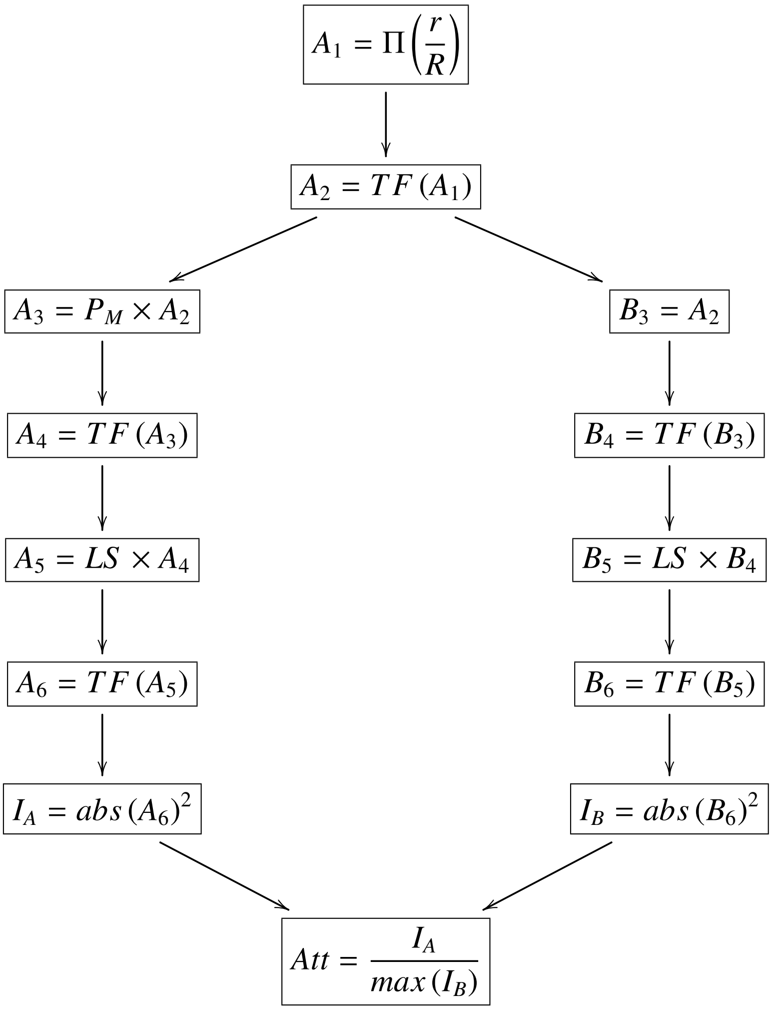

Figure 6.8: Flow chart for the computation of the performances without misorientation area.

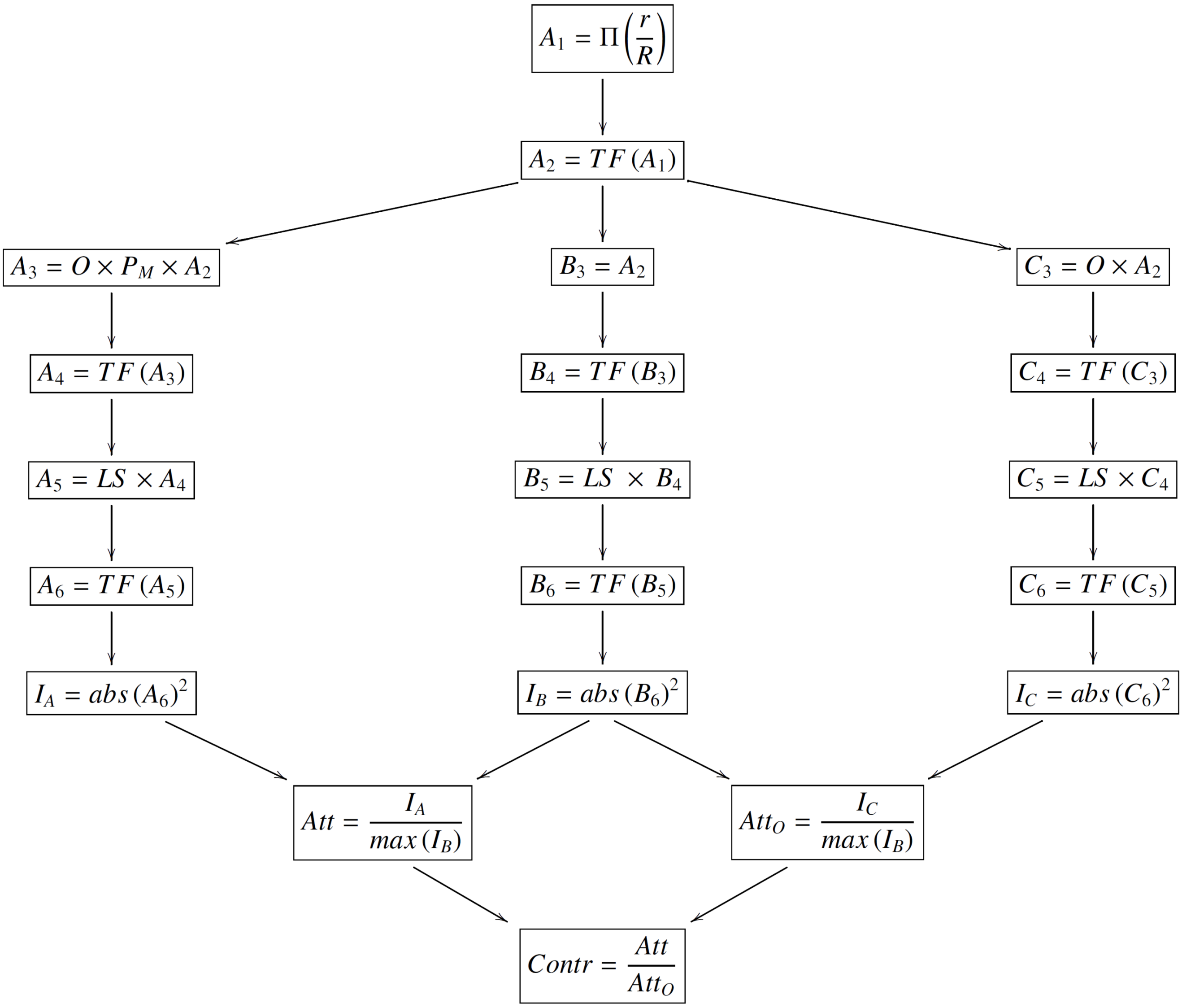

Figure 6.9: Flow chart for the computation of the performances where a misorientation area is present, the differences between the second and the thrid case is the radius of O

In the following tables and figures, the results are summarized and compared to the ideal charge 2 VR (named ideal in the table).

6.3.1 $\mathscr{A}$, $\mathscr{B}$ and $\mathscr{C}$ systems without an area of misorientation

Table 6.1: Table of the peak to peak attenuation.

	peak to peak attenuation
ideal	9.42e-6
$\mathscr{A}$	9.42e-6
$\mathscr{B}$	8.93e-6
$\mathscr{C}$	9.42e-6

Table 6.2: Table of the attenuation for several concentric circles with a radius in λ/d units.

	0.25	0.5	1	1.5	2	3	5	7	10	15
ideal	8.86e-6	7.40e-6	3.82e-6	1.79e6	1.06e-6	4.95e-7	1.87e-7	9.86e-8	5.02e-8	2.38e-8
$\mathscr{A}$	8.86e-6	7.40e-6	3.81e-6	1.78e-6	1.06e-6	4.95e-7	1.87e-7	9.86e-8	5.01e-8	2.38e-8
$\mathscr{B}$	8.37e-6	7.02e-6	3.67e-6	1.73e-6	1.02e-6	4.78e-7	1.82e-7	9.61e-8	4.91e-8	2.37e-8
$\mathscr{C}$	8.86e-6	7.40e-6	3.81e-6	1.78e-6	1.06e-6	4.95e-7	1.87e-7	9.86e-8	5.01e-8	2.38e-8

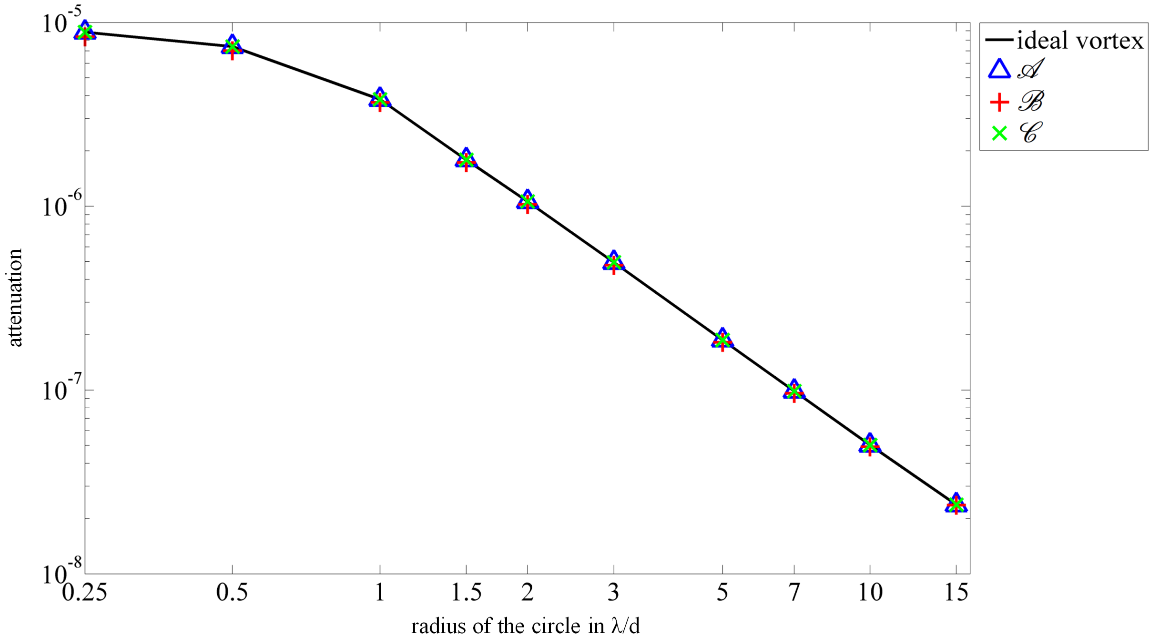

Figure 6.10: Variation of the attenuation for the three systems, for several concentric circles. The ideal vortex being the ideal charge 2 VR.

We can observe that the attenuations for these systems are extremely close to the ideal charge two vortex. It was expected since the orientation of the fast axis is also close to the ideal orientation near the vortex centers and there is no misorientation area is present.

6.3.2 $\mathscr{A}$, $\mathscr{B}$ and $\mathscr{C}$ systems with an area of misorientation

The values of the radius of the misorientation areas in pixels are presented in table 6.3

Table 6.3: Table of the radius of the misorientation area in pixel size.

$\mathscr{A}$	$\mathscr{B}$	$\mathscr{C}$
87	23	23

Table 6.4: Table of the peak to peak attenuation.

	peak to peak attenuation
ideal	7.96e-7
$\mathscr{A}$	1.01e-4
$\mathscr{B}$	7.74e-3
$\mathscr{C}$	7.12e-3

Table 6.5: Table of the attenuation for several concentric circles with a radius in λ/d units.

	0.25	0.5	1	1.5	2	3	5	7	10	15
ideal	9.30e-11	1.15e-9	8.53e-9	1.08e-8	6.96e-9	8.17e-9	6.51e-9	5.13e-9	3.88e-9	3.05e-9
$\mathscr{A}$	1.82e-7	2.47e-6	2.06e-5	3.22e-5	2.14e-5	1.85e-5	1.99e-5	2.59e-5	1.35e-5	6.16e-6
$\mathscr{B}$	2.42e-5	2.78e-4	2.45e-3	4.80e-3	4.20e-3	2.10e-3	8.24e-4	4.38e-4	2.21e-4	1.00e-4
$\mathscr{C}$	1.86e-5	2.57e-4	2.40e-3	4.74e-3	4.17e-3	2.08e-3	8.18e-4	4.35e-4	2.19e-4	9.93e-5

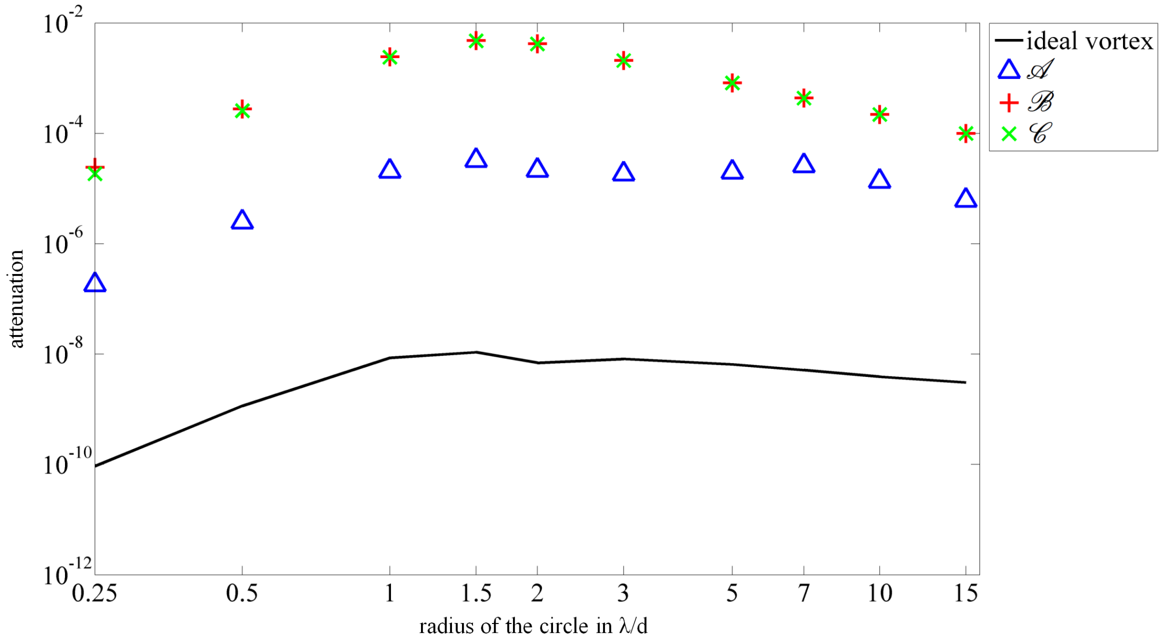

Figure 6.11: Variation of the attenuation for the three systems, for several concentric circles. The ideal case vortex being the ideal charge 2 vortex retarder with a misorientation area masked by an opaque circle of 5 μm diameter.

Table 6.6: Table of the vortex retarder contribution to the attenuation for several concentric circles with a radius in λ/d units.

	0.25	0.5	1	1.5	2	3	5	7	10	15
ideal	1.05e-10	1.55e-9	2.23e-8	6.04e-8	6.59e-8	1.67e-7	3.60e-7	5.48e-7	8.37e-7	1.47e-6
$\mathscr{A}$	8.86e-4	1.68e-2	4.13e-1	8.33e-1	7.28e-1	8.13e-1	8.88e-1	9.12e-1	9.16e-1	9.19e-1
$\mathscr{B}$	4.69e-3	8.78e-2	1.77e0	1.25e0	1.01e0	9.67e-1	9.32e-1	9.18e-1	9.09e-1	9.03e-1
$\mathscr{C}$	3.59e-3	8.14e-2	1.73e0	1.23e0	1.00e0	9.60e-1	9.26e-1	9.12e-1	9.02e-1	8.97e-1

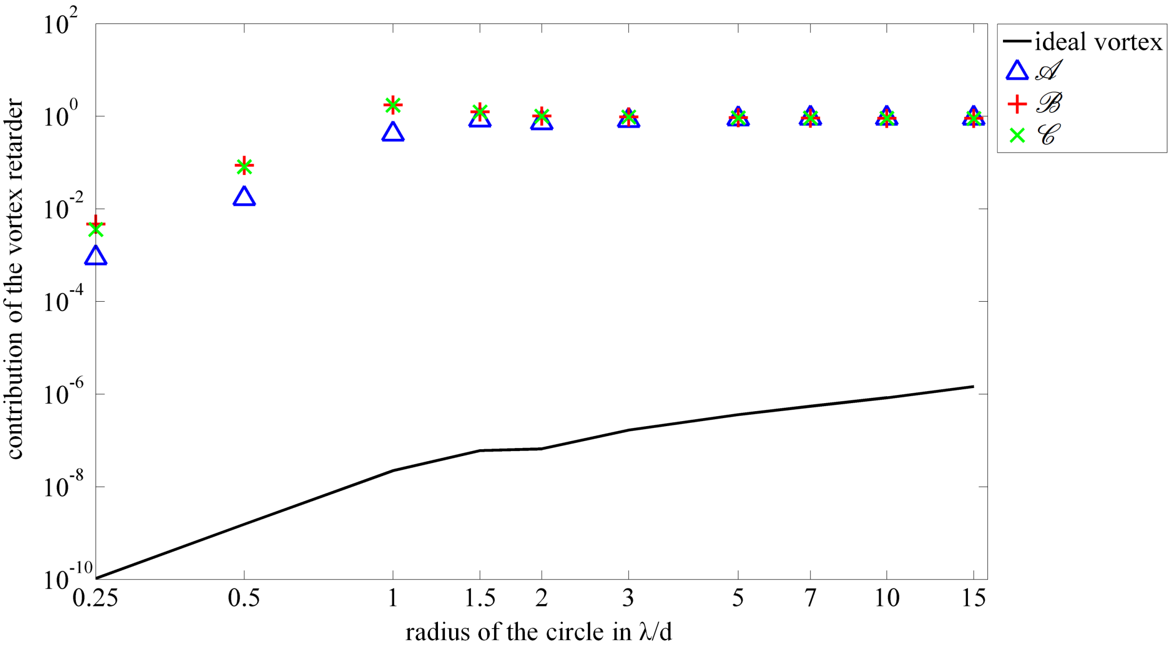

Figure 6.12: Variation of vortex retarder contribution to the attenuation for the three systems, for several concentric circles. The ideal case vortex being the ideal charge 2 vortex retarder.

Once the area of misorientation is introduced, differences appear between the configurations.
We can observe that the attenuations produced by our systems are weaker than the attenuation produced by the perfect case with a misorientation area of 5 μm. Moreover the attenuation produced by $\mathscr{A}$ is approximately hundred times stronger than the attenuation produced by $\mathscr{B}$ and $\mathscr{C}$. However, a strong attenuation of the central source does not necesserily means a performant coronagraphic setup. For example, a large opaque mask alone will produce a high attenuation of the central source but it may also produce high attenuation of the off-axis sources which is an important obstacle to the visual detection of these off-axis sources. Therefore, after the computation of the attenuation for the central source the attenuation of off-axis sources will be computed for several cases (see subsection 6.3.7) to compare the systems.

6.3.3 $\mathscr{A}$, $\mathscr{B}$ and $\mathscr{C}$ systems with a reduced area of misorientation

Table 6.7: Table of the radius of the misorientation area in pixel size.

$\mathscr{A}$	$\mathscr{B}$	$\mathscr{C}$
80	15	15

Table 6.8: Table of the peak to peak attenuation.

	peak to peak attenuation
ideal	7.96e-7
$\mathscr{A}$	1.00e-4
$\mathscr{B}$	6.01e-3
$\mathscr{C}$	5.49e-3

Table 6.9: Table of the attenuation for several concentric circles with the radius in λ/d units.

	0.25	0.5	1	1.5	2	3	5	7	10	15
ideal	9.30e-11	1.15e-9	8.53e-9	1.08e-8	6.96e-9	8.17e-9	6.51e-9	5.13e-9	3.88e-9	3.05e-9
$\mathscr{A}$	1.70e-7	2.33e-6	1.94e-5	3.15e-5	2.12e-5	1.86e-5	1.88e-5	2.60e-5	1.36e-5	6.20e-6
$\mathscr{B}$	1.82e-5	2.11e-4	1.87e-3	3.67e-3	3.23e-3	1.61e-3	6.29e-4	3.34e-4	1.68e-4	7.62e-5
$\mathscr{C}$	1.40e-5	1.96e-4	1.83e-3	3.63e-3	3.20e-3	1.60e-3	6.25e-4	3.32e-4	1.67e-4	7.56e-5

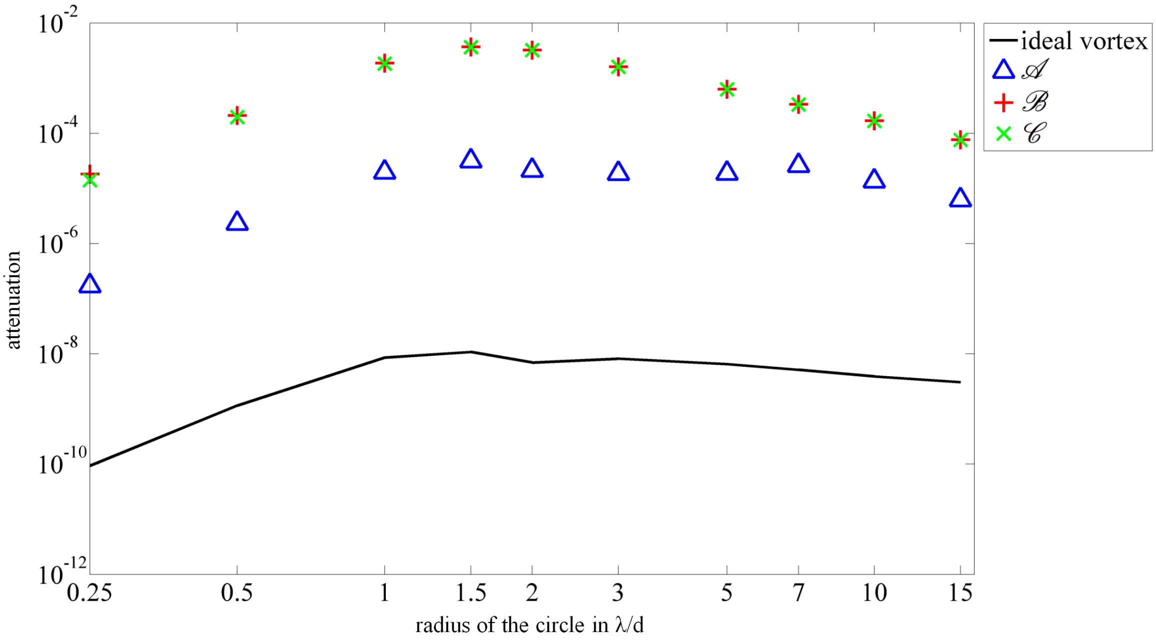

Figure 6.13: Variation of the attenuation for the three systems, for several concentric circles. The ideal case vortex being the ideal charge 2 vortex retarder with a misorientation area masked by an opaque circle of 5 μm diameter.

Table 6.10: Table of the vortex retarder contribution to the attenuation for several concentric circles with the radius in λ/d units.

	0.25	0.5	1	1.5	2	3	5	7	10	15
ideal	1.05e-10	1.55e-9	2.23e-8	6.04e-8	6.59e-8	1.67e-7	3.60e-7	5.48e-7	8.37e-7	1.47e-6
$\mathscr{A}$	8.29e-4	1.57e-2	3.90e-1	8.12e-1	7.81e-1	7.96e-1	8.66e-1	9.91e-1	9.14e-1	9.18e-1
$\mathscr{B}$	1.38e-3	2.26e-2	6.06e-1	1.01e0	8.23e-1	7.81e-1	7.49e-1	7.35e-1	7.26e-1	7.21e-1
$\mathscr{C}$	1.06e-3	2.10e-2	5.91e-1	9.99e-1	8.16e-1	7.75e-1	7.43e-1	7.30e-1	7.21e-1	7.15e-1

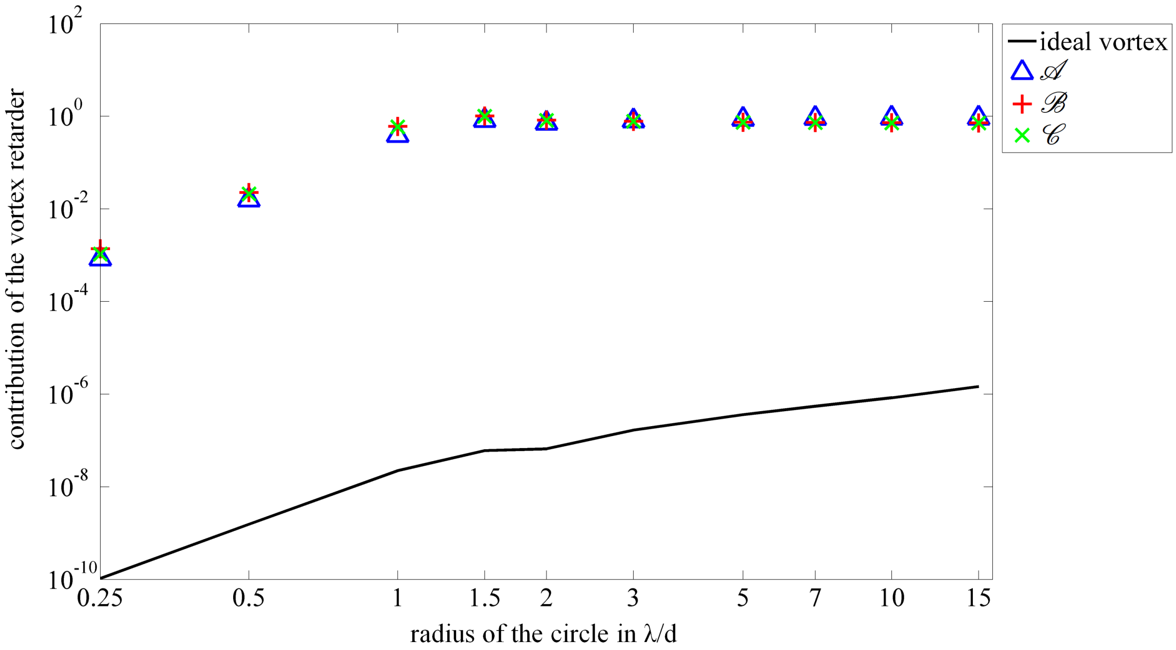

Figure 6.14: Variation of the vortex retarder contribution to the attenuation for several concentric circles. The ideal case vortex being the ideal charge 2 vortex retarder.

We can observe that the $15\,\mu$m decrease of the radius of the misorientation area leads to small modifications of the performances for the 3 systems. The modifications of the attenuation are different for $\mathscr{A}$ compared to $\mathscr{B}$ and $\mathscr{C}$.

For $\mathscr{A}$ the attenuation is sometimes stronger and sometimes weaker than the attenuation for the whole misorientation area, the ratio between the reduced one and the whole one oscillates about 1.03.

For $\mathscr{B}$ and $\mathscr{C}$ the reduced attenuation is always stronger than the whole one. The reduced attenuations oscillates around 1.31 for the two systems. Therefore, we can conclude that the smaller the ratio of the reduced radius on the initial one is, the stronger is the attenuation with the reduced misorientation area.

It can also be observed that the reduction of the misorientation area will also improve the contribution of the vortex retarder on the attenuation and that the increase of the retarder contribution is also stronger for $\mathscr{B}$ and $\mathscr{C}$ than $\mathscr{A}$.

Finally, we can confirm that for these systems, the smaller the misorientation radius is, the smaller is the deviation from the ideal performances.

6.3.4 a, b, c and d centers without an area of misorientation

Table 6.11: Table of the peak to peak attenuation.

	peak to peak attenuation
ideal	9.42e-6
a	1.08e-1
b	1.69e-2
c	1.67e-2
d	1.04e-1

Table 6.12: Table of the attenuation for concentric circles with the radius in λ/d units.

	0.25	0.5	1	1.5	2	3	5	7	10	15
ideal	8.86e-6	7.40e-6	3.82e-6	1.79e6	1.06e-6	4.95e-7	1.87e-7	9.86e-8	5.02e-8	2.38e-8
a	1.02e-1	8.51e-2	4.37e-2	2.04e-2	1.21e-2	5.58e-3	2.07e-3	1.07e-3	5.30e-4	2.37e-4
b	1.58e-2	1.32e-2	6.83e-3	3.20e-3	1.89e-3	8.76e-4	3.25e-4	1.68e-4	8.33e-5	3.73e-5
c	1.57e-2	1.31e-2	6.74e-3	3.15e-3	1.86e-3	8.60e-4	3.19e-4	1.65e-4	8.18e-5	3.66e-5
d	9.85e-2	8.23e-2	4.23e-2	1.97e-2	1.17e-2	5.40e-3	2.00e-3	1.04e-3	5.13e-4	2.29e-4

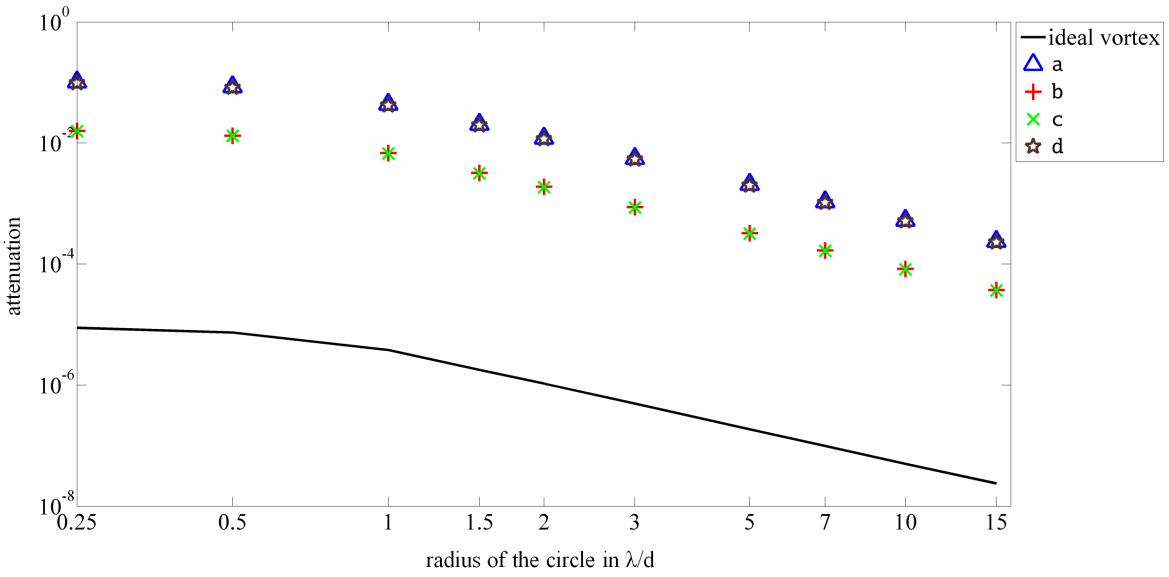

Figure 6.15: Variation of the attenuation for the four rotation centers for several concentric circles. The ideal case vortex being the ideal charge 2 vortex retarder.

This time, the attenuations produced by the retarders are different even for the case of a perfect orientation of the liquid crystals. The attenuation achieved with our systems are always weaker than the ideal charge 2 vortex due to the deviation of the orientation of the fast axis. Besides, differences between our retarders also exist. The attenuation produced by b and c is always stronger than the attenuation produced by the other systems. When the intensities presented in Figure 6.6 are examined, it can be observed that the fast axis patterns of these centers are closer to the ideal charge two pattern than the other center. Consequently, we can assume that the closer the fast axis pattern is to the ideal charge two vortex, the stronger the attenuation achieved by the retarder.

6.3.5 a, b, c and d centers with an area of misorientation

Table 6.13: Table of the peak to peak attenuation.

	peak to peak attenuation
ideal	7.96e-7
a	8.90e-5
b	8.63e-5
c	8.61e-5
d	8.65e-5

Table 6.14: Table of the attenuation for several concentric circles with the radius in λ/d units.

	0.25	0.5	1	1.5	2	3	5	7	10	15
ideal	9.30e-11	1.15e-9	8.53e-9	1.08e-8	6.96e-9	8.17e-9	6.51e-9	5.13e-9	3.88e-9	3.05e-9
a	1.84e-5	1.49e-5	2.03e-5	2.66e-5	1.78e-5	1.45e-5	1.24e-5	2.39e-5	1.32e-5	6.03e-6
b	2.71e-6	4.17e-6	1.95e-5	2.76e-5	1.77e-5	1.45e-5	1.24e-5	2.40e-5	1.33e-5	6.07e-6
c	3.69e-6	4.16e-6	1.95e-5	2.77e-5	1.78e-5	1.45e-5	1.24e-5	2.41e-5	1.33e-5	6.07e-6
d	1.64e-5	1.33e-5	1.85e-5	2.44e-5	1.64e-5	1.34e-5	1.16e-5	2.35e-5	1.31e-5	6.00e-6

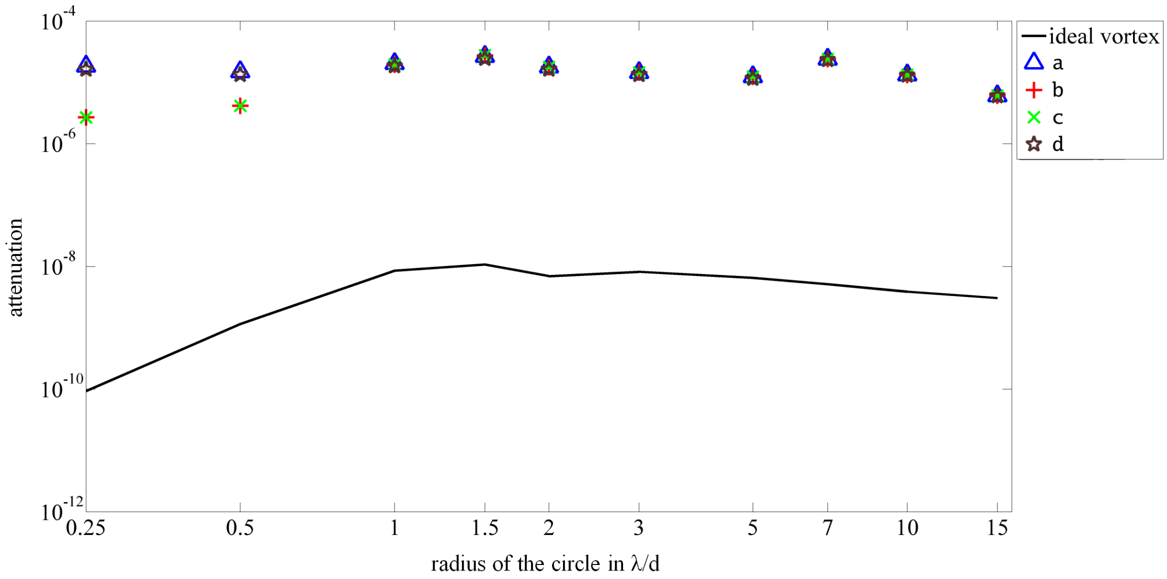

Figure 6.16: Variation of the attenuation for the four rotation centers for several concentric cricles. The ideal case vortex being the ideal charge 2 vortex retarder with a misorientation area masked by an opaque circle of 5 μm diameter.

Table 6.15: Table of the vortex retarder contribution to the attenuation for several concentric circles with the radius in λ/d units.

	0.25	0.5	1	1.5	2	3	5	7	10	15
ideal	1.05e-10	1.55e-9	2.23e-8	6.04e-8	6.59e-8	1.67e-7	3.60e-7	5.48e-7	8.37e-7	1.47e-6
a	1.09e-1	1.25e-1	5.13e-1	8.40e-1	7.84e-1e	8.52e-1	9.10e-1	9.33e-1	9.28e-1	9.27e-1
b	1.59e-2	3.49e-2	4.93e-1	8.72e-1	7.81e-1	8.59e-1	9.90e-1	9.37e-1	9.33e-1	9.34e-1
c	1.58e-2	3.48e-2	4.94e-1	8.73e-1	7.82e-1	8.55e-1	9.10e-1	9.38e-1	9.33e-1	9.34e-1
d	9.64e-2	1.11e-1	4.69e-1	7.70e-1	7.19e-1	7.87e-1	8.52e-1	9.15e-1	9.17e-1	9.21e-1

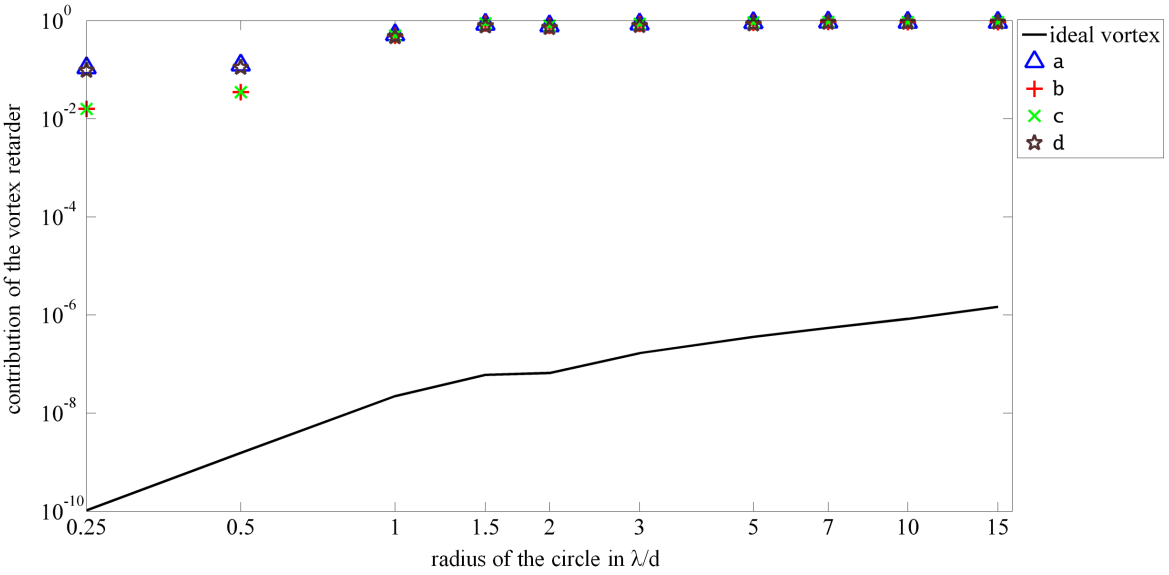

Figure 6.17: Variation of the vortex retarder contribution to the attenuation for the four rotation centers for several concentric circles. The ideal case vortex being the ideal charge 2 vortex retarder.

For this configuration, the introduction of the misorientation areas results in stronger attenuations. The attenuations with the combination vortex retarders and opaque mask are thousand times stronger than the previous case.

The contribution of the vortex retarder on the attenuation is quite weak compared to the cases presented before. It was expected due to the facts that the radius of the misorientation is quite large and the fast axis patterns deviate from the ideal case.

It can also be observed that for circles with a radius smaller than $1\lambda/d$, the attenuation and the contribution of the retarder are stronger for b and c than the other centers while the characteristics of the centers are equivalent for larger radii. This variation could be explained by the fast axis pattern which is closer to the perfect case at a small distance of the center for b and c while it deviate like the other two at larger distance. Other simulations with different fast axis pattern should be completed to check this hypothesis.

6.3.6 a, b, c and d centers with a reduced area of misorientation

Table 6.16: Table of the peak to peak attenuation.

	peak to peak attenuation
ideal	7.96e-7
a	5.98e-5
b	5.71e-5
c	5.72e-5
d	5.82e-5

Table 6.17: Table of the attenuation for for several concentric circles with the radius in λ/d units.

	3	4	5	6	7	8	9	10	15	20
ideal	9.30e-11	1.15e-9	8.53e-9	1.08e-8	6.96e-9	8.17e-9	6.51e-9	5.13e-9	3.88e-9	3.05e-9
a	1.75e-5	1.41e-5	1.87e-5	2.48e-5	1.67e-5	1.36e-5	1.17e-5	1.80e-5	9.94e-5	4.55e-6
b	2.55e-6	3.85e-6	1.77e-5	2.56e-5	1.66e-5	1.37e-5	1.17e-5	1.81e-5	1.00e-5	4.60e-6
c	2.53e-6	3.84e-6	1.77e-5	2.57e-5	1.67e-5	1.37e-5	1.17e-5	1.81e-5	1.00e-5	4.59e-6
d	1.55e-5	1.26e-5	1.70e-5	2.27e-5	1.53e-5	1.26e-5	1.10e-5	1.76e-5	9.94e-6	4.54e-6

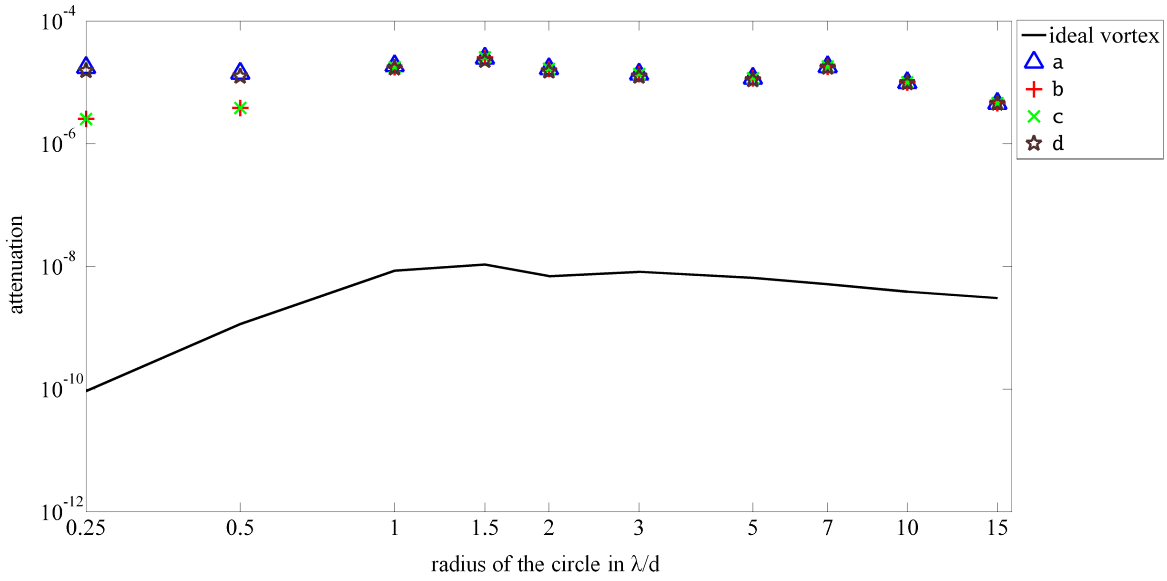

Figure 6.18: Variation of the attenuation for the four rotation centers for several concentric circles . The ideal case vortex being the ideal charge 2 vortex retarder with a misorientation area masked by an opaque circle of 5 μm diameter.

Table 6.18: Table of the vortex retarder contribution to the attenuation for several concentric circles with the radius in λ/d units.

	3	4	5	6	7	8	9	10	15	20
ideal	1.05e-10	1.55e-9	2.23e-8	6.04e-8	6.59e-8	1.67e-7	3.60e-7	5.48e-7	8.37e-7	1.47e-6
a	1.08e-1	1.23e-1	4.92e-1	8.21e-1	7.60e-1	8.30e-1	8.89e-1	9.11e-1	9.91e-1	9.91e-1
b	1.58e-2	3.36e-2	4.67e-1	8.51e-1	7.58e-1	8.33e-1	8.89e-1	9.17e-1	9.16e-1	9.18e-1
c	1.16e-2	3.36e-2	4.68e-1	8.52e-1	7.59e-1	8.34e-1	8.90e-1	9.17e-1	9.16e-1	9.18e-1
d	9.61e-2	1.01e-1	4.48e-1	7.53e-1	6.98e-1	7.67e-1	8.34e-1	8.93e-1	8.99e-1	9.07e-1

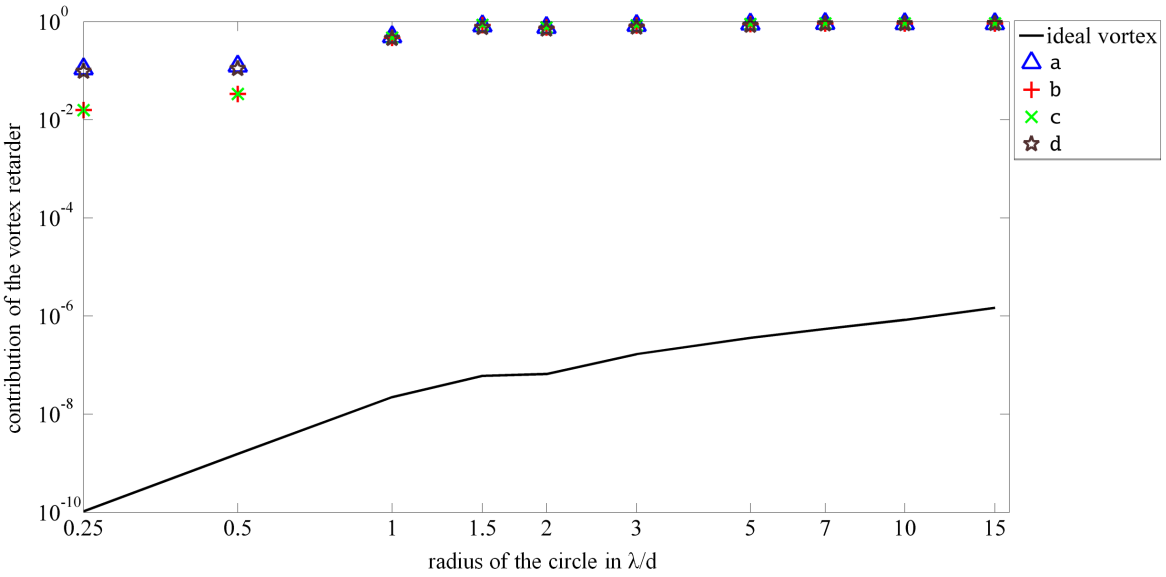

Figure 6.19: Variation of the vortex retarder contribution to the attenuation for the four rotation centers for several concentric circles. The ideal case vortex being the ideal charge 2 vortex retarder.

It can be noticed that the reduction of the area causes small variations on the attenuation and the contribution of the retarder. This is deductible since the variation of the misorientation area is quite small only 7 pixels of difference on an initial value of 103 pixels compared to the variation from 23 to 15 for the $\mathscr{B}$ and $\mathscr{C}$ systems. The stronger efficiency of b and c for radii smaller than $1\lambda/d$ is also observed for this case.

6.3.7 Attenuation for off-axis sources

Since large portions of the retarder are hidden by an opaque mask, off-axis sources could also be cancelled. Therefore, we decided to compute the peak to peak attenuation for them with various configurations of the retarder and the average attenuation for several circles. To compute the attenuation, other retarders were computed with their rotation centers shifted about a multiple of λ/d [17, 18]. We chose to compute $\mathscr{A}$ and $\mathscr{C}$ systems and the c center with their appropriate reduced misorientation areas and the ideal charge two vortex with its opaque mask.

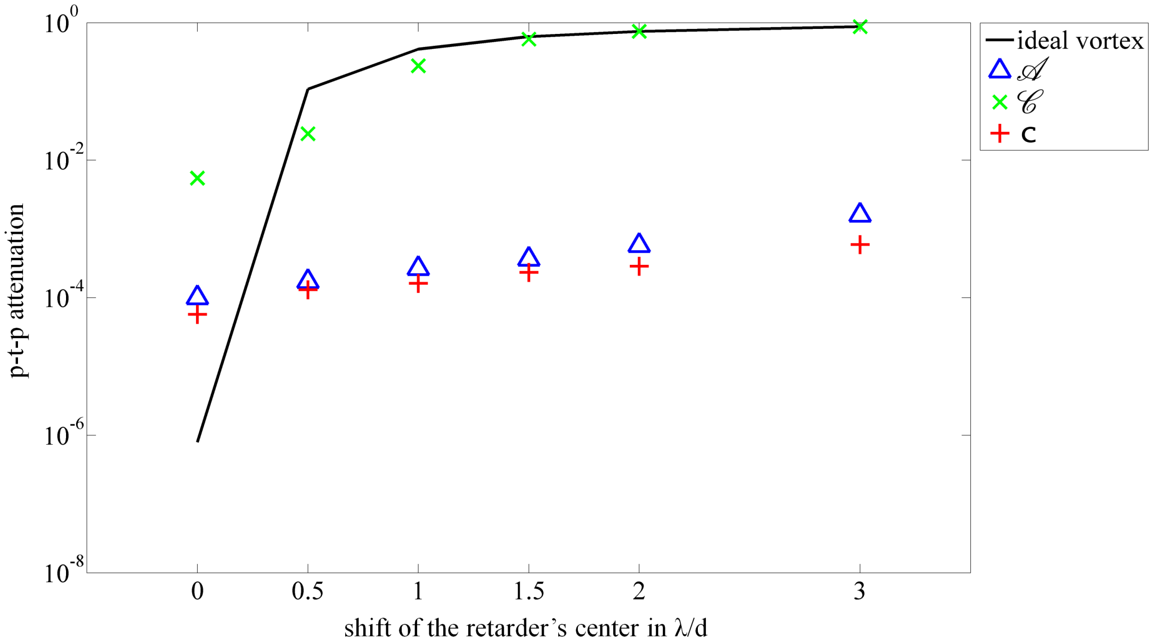

Figure 6.20: Variation of the peak to peak attenuations as functions of the shift of the retarder.

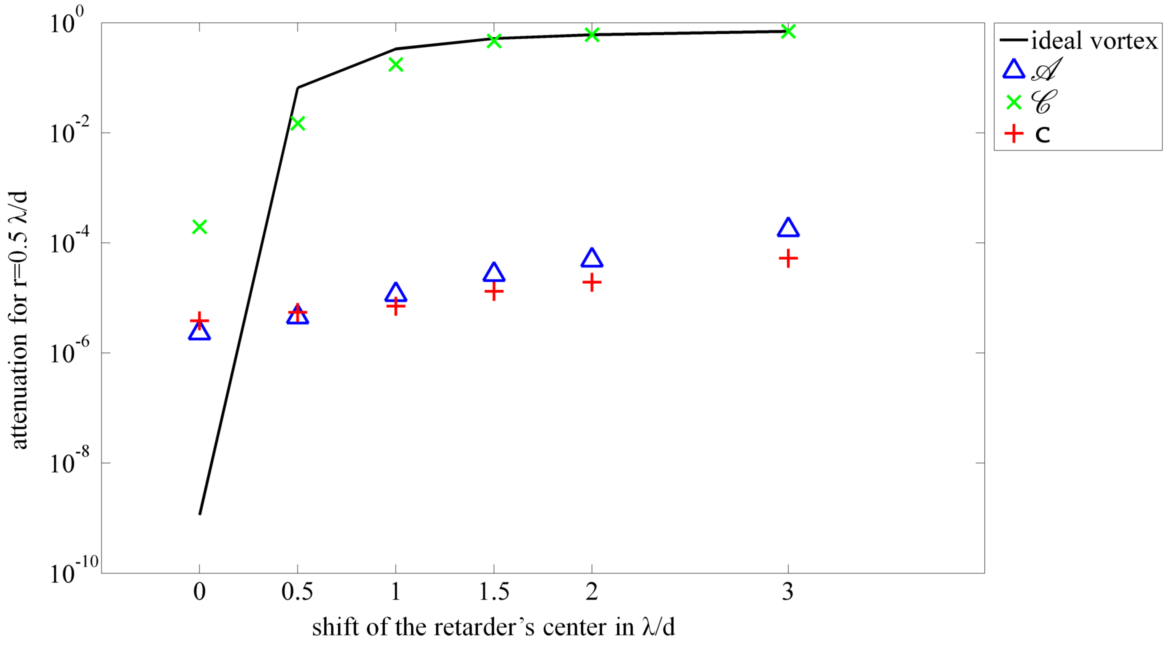

Figure 6.21: Variation of the average attenuation of circles with a center of $0.5\lambda/d$ as functions of the shift of the retarder.

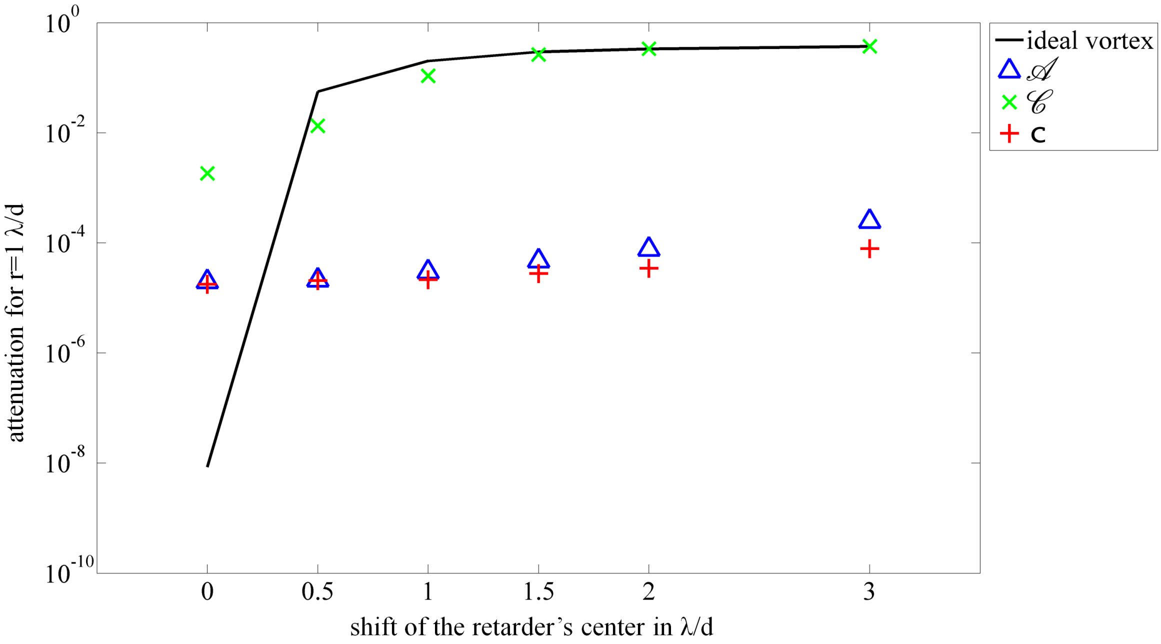

Figure 6.22: Variation of the average attenuation of circles with a center of $1\lambda/d$ as functions of the shift of the retarder.

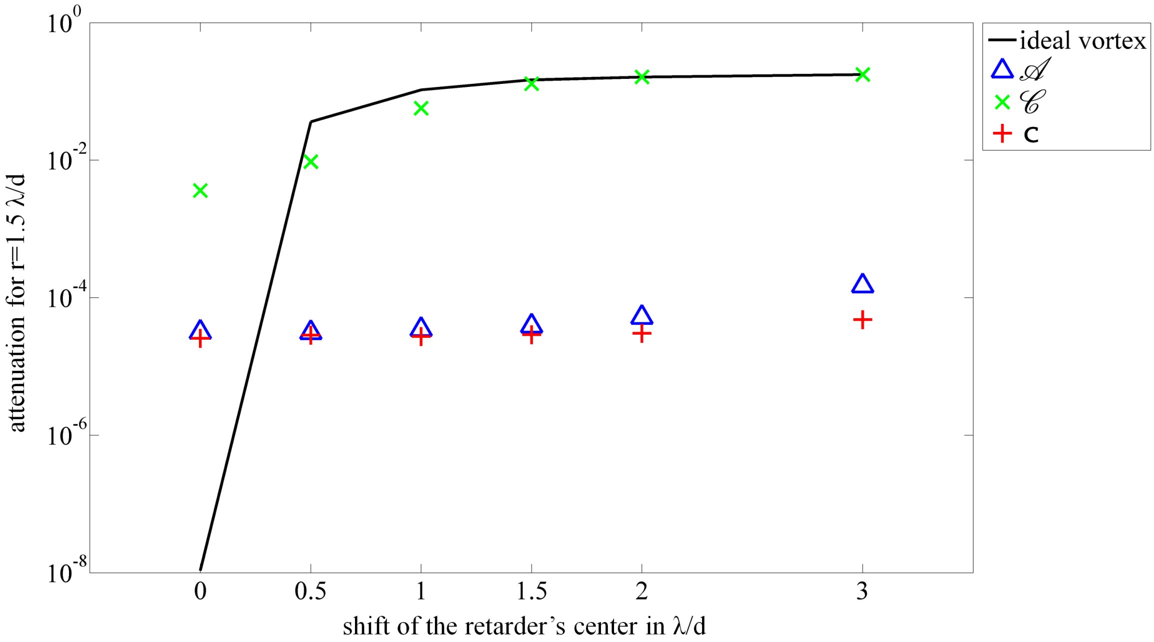

Figure 6.23: Variation of the average attenuation of circles with a center of $1.5\lambda/d$ as functions of the shift of the retarder.

We can observe that the system $\mathscr{C}$ presents the largest variation with the shift of the rotation centers while the experimental center c is less sensitive to the shift. It is due to the size of the opaque mask. The larger the opaque mask is, the less sensitive is the attenuation to the shift of the rotation center.

We can observe that the performances of our experimental retarders are relatively poor but several solutions exist to improve their performances. For example, with c, a reduction of approximately 50 μm of the misorientation area's radius will decrease the average attenuation of approximately 15 for off-axis sources. Therefore the intensity will be 15 times stronger and the contrast between off-axis and on-axis sources will be improved.

As expected, two criteria are important:

1. the orientation of the fast axis which must be closer as possible to the ideal pattern to achieve a high attenuation of on-axis sources,
2. the misorientation area must be as small as possible to achieve the detection of the off-axis sources.

Thus, to improve the coronagraphic performances of our vortex retarders recorded by polarization holography, we must

1. get closer to perfect alignment of the polarization optics to achieve a more regular rotation of the fast axis,
2. achieve a better alignment of the beam expander to reduce the area of misorientation of the liquid crystals.

6.4 Conclusions

In this chapter, coronagraphy was discussed. The goal of a coronagraph is to cancel the light of a central star to see its faint companions. Several retarders used for coronagraphy were exposed. We presented the computation process of the performances of our retarders and the results. The performances of the systems shown in [19] are really close to the ideal charge two vortex but they decrease when the misorientation areas are introduced. The performances of our experimental retarders are weak compared to the ideal case but they could be improved using a better recording process to reduce the misorientation areas and to order the fast axis pattern.

Chapter 6 references

[1] B.Lyot, "The study of the solar corona and prominences without eclipses," *Monthly Notices of the Royal Astronomical Society* **99**, 580 (1939).

[2] C.Delacroix, *Exoplanet imaging with mid-infrared vector vortex coronagraphs: design, manufacture, validation and first light of the annular groove phase mask*, PhD thesis, University of Liège (2013).

[3] D.Mawet, P.Riaud, O.Absil, and J.Surdej, "Annular groove phase mask coronagraph," *Astrophys. J.* **633**(2), 1191–1200 (2005).

[4] D.Mawet, P.Riaud, A.Boccaletti, P.Baudoz, J.Baudrand, O.Absil, J.L.Beuzit, P.Labeye, and J.Surdej, "Optical vortex coronagraph with subwavelength gratings." `http://exep.jpl.nasa.gov/TPF/tpfcDocs/27c+Optical+vortex+coronagraph.ppt` (2006). Accessed: 2013-05-04.

[5] F.Roddier and C.Roddier, "Stellar coronagraph with phase mask," *Publications of the Astronomical Society of the Pacific* **109**(737), 815–820 (1997).

[6] D.Rouan, P.Riaud, A.Boccaletti, Y.Clénet, and A.Labeyrie, "The four-quadrant phase-mask coronagraph. i. principle," *Publications of the Astronomical Society of the Pacific* **112**(777), 1479–1486 (2000).

[7] P.Riaud, A.Boccaletti, J.Baudrand, and D.Rouan, "The four-quadrant phase mask coronagraph. iii. laboratory performance," *Publications of the Astronomical Society of the Pacific* **115**(808), 712–719 (2003).

[8] S.R.Nersisyan, N.V.Tabiryan, D.Mawet, and E.Serabyn, "Improving vector vortex waveplates for high contrast coronagraphy," *Opt. Express* **21**(7), 8205–8213 (2013).

[9] A.Boccaletti, P.Riaud, P.Baudoz, J.Baudrand, D.Rouan, D.Gratadour, F.Lacombe, and A.M.Lagrange, "The four-quadrant phase mask coronagraph. iv. first light at the very large telescope," *Publications of the Astronomical Society of the Pacific* **116**(825), 1061–1071 (2004).

[10] D.Mawet, E.Serabyn, K.Liewer, R.Burruss, J.Hickey, and D.Shemo, "The vector vortex coronagraph : laboratory results and first light at palomar observatory," *Astrophys. J.* **709**(1), 53–57 (2010).

[11] D.Mawet, P.Riaud, J.Surdej, and J.Baudrand, "Subwavelength surface-relief gratings for stellar coronagraphy," *Appl. Opt.* **44**(34), 7313–7321 (2005).

[12] D.Mawet, P.Riaud, O.Absil, and J.Surdej, "Annular groove phase mask coronagraph," *Astrophys. J.* **633**(2), 1191–1200 (2005).

[13] D.Mawet, P.Riaud, C.Hanot, D.Vandormael, J.Loicq, J.Baudrand, J.Surdej, and S.Habraken, "The annular groove phase mask coronagraph : an achromatic optical vortex," in [*Proc. SPIE*], **6693**, 66931M–66931M–9, Society of Photo-Optical Instrumentation Engineers SPIE (2007).

[14] D.Mawet, E.Serabyn, K.Liewer, C.Hanot, S.McEldowney, D.Shemo, and N.O'Brien, "Optical

vectorial vortex coronagraphs using liquid crystal polymers theory, manufacturing and laboratory demonstration," *Opt. Express* **17**(3), 1902–1918 (2009).

[15] D.Mawet, N.Murakami, C.Delacroix, E.Serabyn, O.Absil, et al., "Taking the vector vortex coronagraph to the next level for ground-and space-based exoplanet imaging instruments: review of technology developments in the usa, japan, and europe," in [*Proc. SPIE*], **8151**, 815108–815108–14, Society of Photo-Optical Instrumentation Engineers SPIE (2011).

[16] I.N.Sneddon, [*Fourier Transforms*], New York, McGraw-Hill (1951).

[17] P.Riaud and C.Hanot, "Combining coronagraphy with interferometry as a tool for measuring stellar diameters," *Astrophysical Journal, Letters* **719**(1), 749–762 (2010).

[18] C.Delacroix, O.Absil, P.Forsberg, D.Mawet, V.Christiaens, M.Karlsson, A.Boccaletti, P.Baudoz, M.Kuittinen, I.Vartiainen, J.Surdej, and S.Habraken, "Laboratory demonstration of a mid-infrared agpm vector vortex coronagraph," *Astron. & Astrophys.* **553** (2013).

[19] P.Piron, P.Blain, S.Habraken, and D.Mawet, "Polarization holography for vortex retarders recording," *Appl. Opt.* **52**(28), 7040–7048 (2013).

Conclusions and perspectives

Objectives and results

In the present thesis, our goal was the recording of space-variant retarders in liquid crystal polymers for coronagraphy using polarization holography to avoid mechanical actions. Several retarders and applications were investigated.

The first part of this work introduced the space-variant retarders, the polarization holography concept and our material the liquid crystal polymers.
The first chapter presented the different kind of retarders, several applications and three bulding methods.

Chapter 2 introduced the concept of polarization holography, the generic recording process of a retarder and the first retarders. These retarders were recorded using only one linearly polarized beam. Theye retarders are characterized by a uniform orientation of their fast axis. They were measured on the polarimetric bench of Hololab. They induce a phase retard of approximately 87° with small variations inside the retarder.

The second part is dedicated to retarders recorded using the superimposition of two circularly polarized beams of opposite handedness and their applications. The retarders are characterized by a variation of their fast axis orientation in one dimension. Depending on their period and the incident wavelength, they can be used as polarization analyzers or polarization states separators.

- Chapter 3 focuses on the polarization analyzer. The period of the retarder is approximately ten thousand times larger than the wavelength. The retarder transforms a uniformly polarized beam into a space-variant one and a linear polarizer converts the polarization into an intensity variation. By recording the intensity variation, the Stokes parameters of the incident beam can be computed. Numerical simulations were performed to test the method in the ideal conditions, several retarders were recorded and tested with different linearly polarized beams. The computed parameters exhibit a ten percent difference with the real ones. A short sensitivity analysis allowed us to determine the origins of the error which are the speckle phenomenon, the error on the orientation of the lines of same intensity and the variation of the phase retard inside the retarder. Several clues were given to reduce the errors.

- Chapter 4 is centered on the polarization states separator. The period is only thirty times larger than the wavelength. The retarder diffracts the incident beam into maximum three orders, each with their own polarization state. It was shown that depending on the retarder characteristics and the incident polarization state, the number of diffracted beams and the diffraction angle change. The application to shearography was presented. It aims to detect defaults under a diffusive surface. The separator will diffract the incident beam into two superimposed circularly polarized beams of opposite handedness. A linear polarizer after the retarder will convert the polarization variation into an intensity one. By studying the change of the intensity pattern during a deformation, defaults can be observed. The method principle was exposed as well as numerical simulations. The results of the first tests as well as an analysis of the experimental limits were exposed. Finally, several improvements of the method were mentioned.

The third part cares about 2D space-variant retarders and their application to coronagraphy.
Chapter 5 presents the exapansion of polarization holography to a four-beam superimposition to achieve 2D space-variant retarders. A particular case was studied the vortex retarders. They are characterized by a rotation of their fast axis. The mathematical model for the retarders was exposed and several recording systems were presented and analyzed. The resulting fields deviate from the ideal ones: they exhibit decreases of intensity or directionality near a rotation center resulting in an eventual misorientation area of the liquid crystal. To determine the experimental limits, several simple retarders were recorded using elliptically polarized beams. Then, retarders were recorded using the four beams superimposition. The retarders present the expected rotation of their fast axis and a first estimation of their quality was also computed. Finally, a short sensitivity analysis was performed to determine the modifications required for a quality improvement.

In the last chapter, we came back to our original goal: coronagraphy. The principle behind the attenuations computation was explained and the performances of our retarders were computed for several systems in different configurations. It was observed that two factors limit the efficiency of the retarders: the deviation of the fast axis orientation from the ideal charge 2 vortex and the size of the misorientation area. Due to this factors, the effects of our actual retarders are weak compared to the other realizations but they could be improved by minimizing these factors.

Perspectives

In the future, several improvemennts could be realized to increase the quality of our retarders and their efficiency. Other applications of our retarders could also be investigated.

Improvements of the present applications

Polarization anaysis
The polarization analysis suffers from errors mainly due to the phase retard variation, the speckle and the error on the orientation of the same intensity lines ζ.
Several ways exist to reduce them:

- Measuring the whole retarder with the polarimetric bench will provide a phase retard map. Using this map in the fitting algorithm will improve the results quality.
- Rotating a transparent glass disk at high speed should reduce the importance of the speckle phenomenon by performing a temporal averaging. Then the performances will be improved
- Changing the computation algorithm of the lines of same intensity will decrease the error on ζ and will increase the accuracy of the computation.

Polarization states separator
The first results are promising. Several other tests will be performed and several upgrades are possible like the recording of achromatic separators. They will achieve the half-wave plate condition in a large bandwidth. Therefore, only two circularly polarized beams with equal intensity will be diffracted for an incident linearly polarized one. This will allow the use of the same retarder with several wavelength depending on the reflection spectrum of the surfaces. Moreover, it will allow to easily change the resolution by switching from one source to the other with series of fibered sources.

Vortex retarders
The intensity and directionality limits depend on the collimating process. By upgrading the expanding process, using for example a UV wavefront sensor to check the wavefront quality, the ratio between the radius of the misorientation area on the distance between two rotation centers should be reduced. Moreover, a better alignment of the expanding setup should reduce the wavefront aberrations and results in the recording of VR closer to the ideal case. Several retarders will be recorded with the improved recording setup. By measuring the Stokes parameters of the recording field one can compute the radius of the misorientation areas for the retarders and by measuring the retarders with a polarizing microscope, the size of these areas could be computed and compared to the expected value.

Coronagraphy
For coronagraphy, the performances will be computed for the retarders realized with the improved recording setup. The new retarders will be characterized by a fast axis pattern closer to the ideal charge 2 vortex and a smaller area of misorientation of the liquid crystals. So the performances should approach the ideal case.

Other applications

In the future, other aplications of space-variant retarders could be investigated.

Polarization scrambler

The first one is based on several 1D continuous SR. It is polarization scrambling. It consists in the simulation of an unpolarized beam from an incident polarized one. It is required by polarization sensitive gratings where the diffracted orders depend on the polarization of the incident beam to cancel this dependence. A simple method consists of several birefringent pates: a quarter-wave plate followed by a half-wave plate and another quarter-wave plate. The orientation of the fast axes is quickly made to change in order to achieve a large spectrum of polarization states. By performing a temporal average during the variation, one can simulate the effect of an unpolarized beam [1, 2]. We proposed a series of 1D SR with same phase retard and different direction of variation with two different configurations.

- A large collimated beam will be transmitted by the different retarders, inside the beam a large spectrum of different polarization states will be completed and by performing a spatial mean on the beam an unpolarized beam can be simulated.
- A small beam will be transmitted by the retarders by moving the spot on different parts of the retarders the resulting polarization state will change and by performing a temporal normalization an unpolarized beam can be simulated.

Polarization converters

The other applications come from the usage of charge one vortex. As stated before, the retarder converts a uniformly linearly polarized beam into a radially or azimuthally polarized one. Three applications can be cited: tighter focalization, surface plasmon excitation by a focusing beam and enhanced optical tweezers.

- It has been mathematically demonstrated that under certain conditions a radially polarized beam can be focused into a tighter spot than a uniformly linearly polarized one. Specifically, a radially polarized beam focused by a high numerical aperture with a central obstruction results in a smaller spot than a uniformly polarized beam [3, 4, 5].

- Surface plamons are collective oscillations of electrons, in the most widely used configuration they can only be excited by a p polarization [6]. To obtain a confined plasmonic field, a highly focusing beam could be used. Unfortunately, with a uniformly polarized beam, the optimal excitation is not achieved everywhere inside the spot since the beam is not p polarized everywhere. To obtain the optimal excitation, a radial polarization is mandatory. This polarization could be achieved thanks to a charge one VR [6, 5].

- Optical tweezers use forces originating from electric field gradients in strongly focused beam to trap and move microscopic volume of matter [7, 8]. Two kinds of forces are implied: the gradient forces proportional to the gradient of the electric field and the scatering forces on the particles. The first ones tend to stabilize the trap by putting the particle at the center of the beam while the second ones weaken the trap by moving the particles centered on the focus of th ebeam. Radial polarization allows the tighter focusing and increases the gradient forces while reducing the scattering forces along the optical axis. This combination increases the efficiency of optical tweezers allowing the trapping of larger particles [5, 9].

Conclusions and perspectives references

[1] G.Biener, A.Niv, V.Kleiner, and E.Hasman, “Computer-generated infrared depolarizer using space-variant subwavelength dielectric gratings,” *Opt. Lett.* **28**(16), 1400–1402 (2003).

[2] M.Honma and T.Nose, “Liquid-crystal depolarizer consisting of randomly aligned hybrid orientation domains,” *Appl. Opt.* **43**(24), 4667–4671 (2004).

[3] Lerman, G. and U.Levy, “Effect of radial polarization and apodization on spot size under tight focusing conditions,” *Opt. Express* **16**(7), 4567–4581 (2008).

[4] R.Dorn, Quabis, S., and G.Leuchs, “Sharper focus for a radially polarized light beam,” *Phys. Rev. Lett.* **91**, 2339011–2339014 (2003).

[5] Q.Zhan, “Cylindrical vector beams: from mathematical concepts to applications,” *Adv. Opt. Photon.* **1**(1), 1–57 (2009).

[6] W.Chen, R.L.Nelson, D.C.Abesysinghe, and Q.Zhan, “Optimal plasmon focusing with spatial polarization engineering,” *Optics and Photonics News* **20**(10), 36–41 (2009).

[7] J.E.Curtis, B.A.Koss, and D.G.Grier, “Dynamic holographic optical tweezers,” *Opt. Commun.* **207**, 169–175 (2002).

[8] N.B.Simsona, D.Mcgloin, K.Dholakia, L.Allen, and M.J.Padgett, “Optical tweezers with increased axial trapping efficiency,” *J. Mod. Opt.* **45**(9), 1943–1949 (1998).

[9] Q.Zhan, “Trapping metallic rayleigh particles with radial polarization,” *Opt. Express* **20**(6), 6058–6059 (2012).

Appendix

A

Jones and Stokes formalism

During the writing of the thesis, we discovered that we continuously switch between the Stokes and Jones formalisms. To make the reading easier, we will sum up these formalisms in this annex.
The Jones formalism is used to describe the electric field in terms of amplitude and phase, while the Stokes formalism is more used to describe intensity or partial polarization [1].

Jones formalism
The Jones formalism is based on the electric field of the incident beam, it can only described fully polarized beam. The electric field E is described by its horizontal and vertical components [1]:

$$E = \begin{pmatrix} E_{0x} \exp^{\imath\phi_x} \\ E_{0y} \exp^{\imath\phi_y} \end{pmatrix} \tag{A.1}$$

where E_{0x} and E_{0y} represent the amplitude for the horizontal and vertical components of the electric field and ϕ_x, ϕ_y the phase of these components.

In the Jones formalism, a polarization element is represented by a 2×2 matrix and a generic birefringent plate is given by [2]:

$$\begin{pmatrix} \cos(\phi/2) + \imath\cos(2\alpha)\sin(\phi/2) & -\imath\sin(2\alpha)\sin(\phi/2) \\ -\imath\sin(2\alpha)\sin(\phi/2) & \cos(\phi/2) - \imath\cos(2\alpha)\sin(\phi/2) \end{pmatrix} \tag{A.2}$$

where α is the fast axis orientation and ϕ is the phase retard between the two polarization components.

Stokes-Mueller formalism

The Stokes parameters: S_0, S_1, S_2, S_3 are defined by the transmitted intensities after polarizers in several configurations [3]:

$$S = \begin{pmatrix} S_0 \\ S_1 \\ S_2 \\ S_3 \end{pmatrix} = \begin{pmatrix} I_0 + I_{90} \\ I_0 - I_{90} \\ I_{45} - I_{135} \\ I_R - I_L \end{pmatrix} \tag{A.3}$$

I_0, I_{45}, I_{90} and I_{135} represent the intensities measured after a linear polarizer with its transmission axis forming the corresponding angle with the horizontal. I_R and I_L stand for the intensities transmitted by a right and left circular polarizer.

In the Stokes formalism, a polarization element is represented by a 4×4 matrix and a generic birefringent plate is given by

$$BP = \begin{pmatrix} 1 & 0 & 0 & 0 \\ 0 & 1 - 2\sin^2(2\alpha)\sin^2(\phi/2) & 2\cos(2\alpha)\sin(2\alpha)\sin^2(\phi/2) & -\sin(2\alpha)\sin(\phi) \\ 0 & 2\cos(2\alpha)\sin(2\alpha)\sin^2(\phi/2) & 1 - 2\cos^2(2\alpha)\sin^2(\phi/2) & \cos(2\alpha)\sin(\phi) \\ 0 & \sin(2\alpha)\sin(\phi) & -\cos(2\alpha)\sin(\phi) & \cos(\phi) \end{pmatrix} \tag{A.4}$$

where α is the fast axis orientation and ϕ is the phase retard.

B

Retarders in liquid crystals

As stated in chapter 2, other retarders in liquid crystals exist. Two characteristics are possible: the possibility to dynamically control the orientation of the LCs in the retarder and a variation of the LCs orientation along the thickness of the retarder.

The most simple retarders made from LCs are characterized by a frozen orientation of the LCs.
After a specific recording process, even if the LCs submitted to an electromagnetic field, they do not move and conserve their orientation.
However, some retarders allow a dynamical modification of their LCs orientation changing the phase retard induced by the retarder. These retarders contain controllable electrodes [4] generating an electric field to modify the LC orientation. The electrodes are located at the two interfaces of the retarders. Submitted to an electric current, the LC will change their orientation to align with the electric field; from a director aligned with the incident beam to a pattern when the director is perpendicular to the incident beam (see Figure B.1). Changing the tilt of the LC changes the indexes of the medium containing the LC and the phase retard becomes controllable (see Figure B.2). These retarders are used for several applications in our everyday life such as liquid crystal display on alarm clock [1], a more industrial application is their use for the phase shifting technique used in shearography [5, 6] to allow phase shifting techniques.

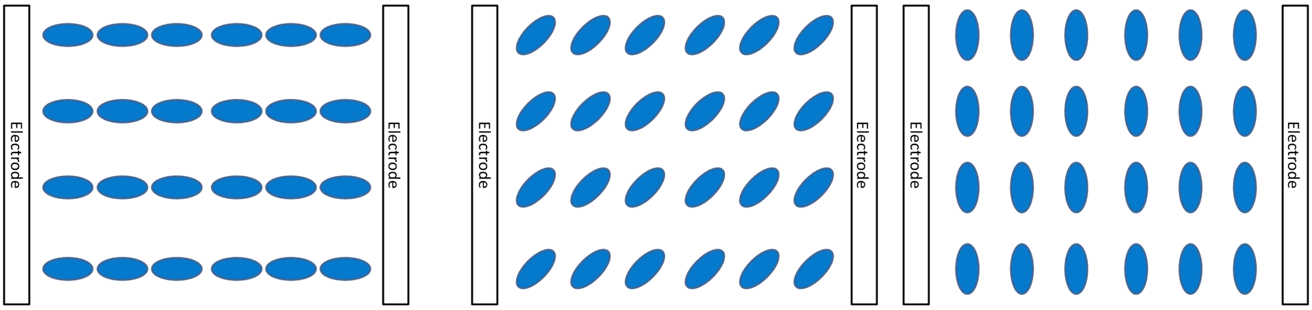

(a) (b) (c)

Figure B.1: (a), (b), (c) Representation of a retarder with a controllable retard for several positions of the liquid crystals.

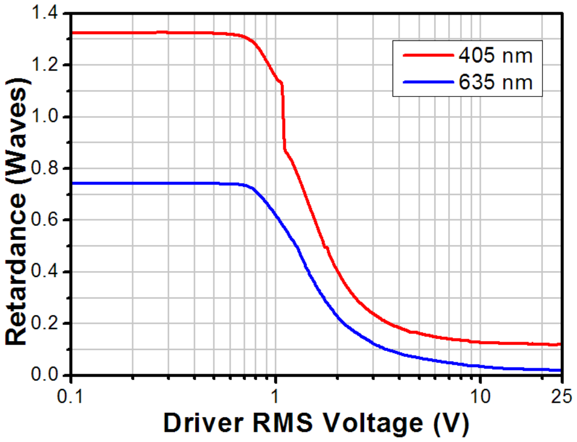

Figure B.2: Represention the phase retard as a multiple of the wavelength for a commercial retarder (LCC1111-A from Thorlabs) [4], when the applied voltage is changed, the retard produced by the retarder is modified.

The other kind concerns the variation of the LC orientation along the thickness of the retarder.

Most retarders are characterized by a uniform orientation of their LC along their thickness while several retarders exhibit a variation of their LC orientation along the thickness.

The retarders can be viewed as a stack of horizontal planes, the orientation of the LC changes from one plane to the next one (see Figure. B.3).

These retarders exhibit achromatic properties. For example the phase retard between the polarization component changes less than the uniform case for a large range of wavelengths [7]. To realize retarders with a variation along the thickness a regularly used method implies two alignment layers differently prepared and a LC cell containing LC able to exhibit that twisting property [8, 9]. The LC is sandwiched between the two substrates with the alignment layers facing each other. The LC near the layers will orient according to them and the LC between them will continuously rotate from one orientation to the other one (see Figure B.4).

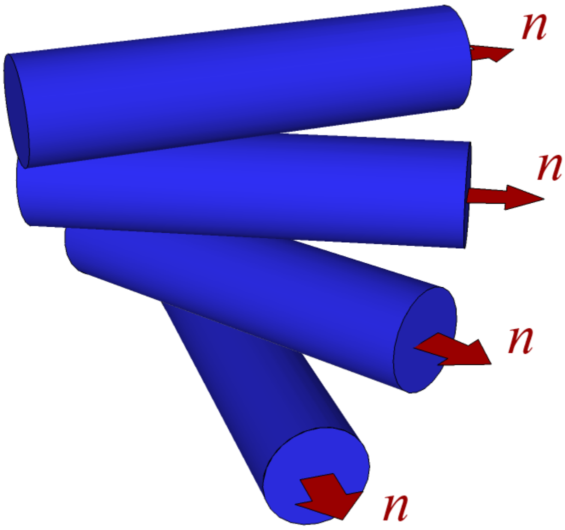

Figure B.3: Representation of the LC orientation of one retarder along the thickness, the LCs are pictured by blue cylinders.

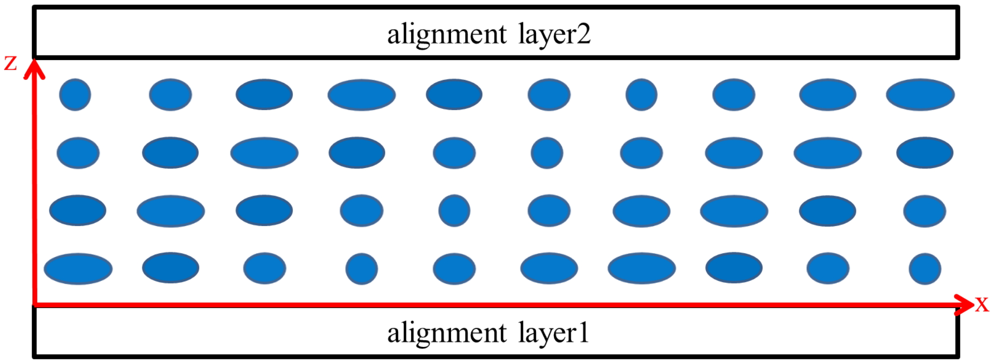

Figure B.4: Profile representation of a 1D SR with a variation of the LC orientation along its thickness, the 1D variation is in the x direction while the variation along the thickness is in the z direction.

C

Cleaning and recording process

This annex will detail the cleaning and recording process presented in 2.2.1. The recording process can be summed up in seven points:

1. Preparation of the substrate
2. Spin-coating of the first layer
3. First heating
4. First exposure
5. Spin-coating of the second layer
6. Second heating
7. Second exposure

1. Preparation of the substrate

Our substrates are microscope slides. The slides are cut to obtain square slides of approximatly 1.5 cm large. They are washed in a bleach solution and to perform a first cleaning then they are rinsed with bi-distilled water. Afterwards they are placed in a solution of Caro acid a.k.a. "piranha solution". It is typically a solution of 5 ml of H_2O_2 at 30% with $15 ml$ of H_2SO_4 at 90%. The substrate stays in the solution for 15 minutes, then it is rinsed with bi-distilled water, acetone and isopropanol. Next, the substrate is glued to another clean larger square glass sheet of $8cm$ large. Finally, it is placed on the spin-coater.

2. Spin-coating of the first layer

When the substrate is on the spin-coater, drops of $ROP - 103$ are deposed on the substrate. The goal of the spin-coating is to achieve a fixed homogenous thickness of the layer by rotating the substrate. A spin-coating process consists in two regimes: the first one is a short one with a slow speed and the second one is longer with a higher speed. The parameters are:

- a time of 15 s and a rotation speed of 800 rpm,
- a time of 60 s and a rotation speed of 3000 rpm.

With this set of parameters, a thickness of approximately 50 nm is expected.

3. First heating

After the spin-coating, the retarder is placed on a heating plate to remove the residual solvents. It will stay for 5 minutes at a temperature of 180°C.

4. First exposure

After that, the retarder is placed on the first exposure setup. This exposure will align the polymers of the first layer, their orientation will define the orientation of the fast axis in the finished retarder.

The retarder is vertically placed to be illuminated by the beam or the superimposed beams. The exposure time is computed to allow an energy of 200mJ/cm^2. It may vary according to the expanding process from 15 minutes to one hour. The first uniform retarders and the first 1D SR had longer exposure time. However, several modifications of the expanding setup were performed and the exposure time was reduced to twenty minutes for the vortex retarders. To control the exposure an optical shutter is programmed with the appropriate exposure time and a twenty minutes delay is added to allow the cooling of the retarder after the heating and the manipulations to place it.

5. Spin-coating of the second layer

After the first exposure, the retarder is placed on the spin-coater and drops of $ROF - 5103$ are deposed on top of the first layer. Only a high speed regime exists:

- a time of $60s$ and a rotation speed of $1600rpm$.

With this regime we are able to achieve nearly half-wave plate at $532nm$ [5]. The absence of a slow regime is due to the spin-coater parameters, one a previous spin-coater we were able to achieve the retarders presented in chapters 2 and 3 with the same set of parameters for the low and high speed regimes

- a time of $60s$ at a rotation speed of $800rpm$.

6. Second heating

Since the second layer reacts with the oxygen of the air, once the spin-coating is finished, the retarder is moved to a glove box where a nitrogen flush is present. The retarder is directly put under the nitrogen entry to avoid oxidations. After 15 minutes, the retarder is placed on a heating plate at a temperature of 50° for 3 minutes. The second heating will also remove the solvents of the second layer and it will anneal the LCPs [10, 11].

7. Second exposure of the retarder

After the heating, still inside the glove box, the retarder is placed vertically just after a UV source with a spectrum contained in 380 − 420 nm [12]. After a 10 minutes delay to allow the cooling of the retarder, it will be exposed during approximately 3 minutes to achieve an energy of 1J/cm^2. Then the retarder is finished, the liquid crystals will not move if exposed to visible light.

Appendix references

[1] E.Hecht, [*Optique*], Pearson Education France, Paris, fourth ed. (2005).

[2] S.Huard, [*Polarisation de la lumière*], Masson, 1 ed. (1993).

[3] M.Bass and Optical Society of America, "polarimetry," in [*Handbook of Optics: devices, measurement and properties*], McGraw-Hill, ed., *Handbook of Optics*(vol. 2), McGraw-Hill, 2 ed. (1994).

[4] "Thorlabs: Half-wave liquid crystal variable retarders/ wave plates web page." `http://www.thorlabs.de/NewGroupPage9.cfm?ObjectGroup_ID=6179` (2013). Accessed: 2013-05-31.

[5] P.Blain, P.Piron, Y.Renotte, and S.Habraken, "An in-line shearography setup based on circular polarization gratings," *Optics and Lasers in Engineering* **51**, 1053–1059 (2013).

[6] P.Blain, F.Michel, P.Piron, Y.Renotte, and S.Habraken, "Combining shearography and interferometric fringe projection in a single device for complete control of industrial applications," *Optical Engineering* **52**(8), 084102–084102 (2013).

[7] C.Oh and J.Escutti, "Achromatic diffraction polarization gratings with high efficiency," *Opt. Lett.* **33**, 2287–2289 (2008).

[8] G.P.Crawford, J.N.Eakin, M.D.Radcliffe., A.Callan-Jones, and R.A.Pelcovits, "Liquid-crystal diffraction gratings using polarization holography alignment techniques," *J. Appl. Phys.* **98**(12) (2005).

[9] M.Stalder and M.Schadt, "Linearly polarized light with axial symmetry generated by liquid-crystal-polarization converters," *Opt. Lett.* **21**(23), 1948–1950 (1996).

[10] "Linearly photo-polymerisable polymer (lpp) as alignment layer for liquid crystals and retardation film coatings rolic rop-103." technical data sheet (2006).

[11] "Liquid crystal pre-polymer (lcp) for retardation film coatings rolic rop-103." technical data sheet (2006).

[12] Phoseon technology, "Rx firefly series user manual." technical data sheet (2008).